# Modelling and Numerical Simulation of Flows with Evaporation and Condensation

Modelling and Numerical Simulation of Flows with Evaporation and Condensation
K.M. Wróbel

Cover: K.M. Wróbel

Printed by PrintPartners Ipskamp

Thesis University of Twente, Enschede - With ref. - With summary in Dutch.
ISBN 90-365-2387-7

# MODELLING AND NUMERICAL SIMULATION OF FLOWS WITH EVAPORATION AND CONDENSATION

PROEFSCHRIFT

ter verkrijging van
de graad van doctor aan de Universiteit Twente,
op gezag van de rector magnificus,
prof. dr. W.H.M. Zijm,
volgens besluit van het College voor Promoties
in het openbaar te verdedigen
op vrijdag 1 september 2006 om 15:00 uur

door

Krzysztof MichałWróbel

geboren op 12 september 1975
te Poznań

Dit proefschrift is goedgekeurd door de promotoren:

prof. dr. ir. H.W.M. Hoeijmakers,
prof. dr. -ing. habil. G.H. Schnerr

*To my wife Agnieszka*

# TABLE OF CONTENTS

# INTRODUCTION

CHAPTER 1

## 1.1 General features of multiphase flows

A multiphase flow is a flow in which more than one fluid phase is present in the same flow system at the same time. The most common multi-phase flows include two phases namely gas (vapour) and liquid. In general a multi-component fluid may consist of various species, where each species is in some state of aggregation, e.g. gas, liquid or solid. In the latter case the solid bodies in the form of small particles are dispersed in a liquid and travel subjected to the forces exerted by the flow on the particles, which the particles influence the flow. Two-phase flows play a significant role, however, three-phase flows occur also quite often especially in chemical industry in processes of mixtures separation or in petrochemical industry where crude oil, transported from the place of exploration, contains water and natural gas. Aside from the mentioned multiphase flow configurations one can also find more complex occurrences where even more than three phases are present, but those are not considered in the present work.

The main difficulty in the study of multiphase flows, is the existence of an interface between the phases, which represent a discontinuity of the value of or gradient of the flow field quantities. The magnitude of this discontinuity depends on the sort of phases. Clearly, it is the largest for the case of a gas-liquid flow. The discontinuity is difficult to handle for standard numerical approaches useful in single phase flows. Complexity of the problem increases with increasing interface deformation. This does not allow the use of a single universal model for all multiphase flows, but rather leads to a variety of approaches applicable to a specific phase configuration. Therefore, scientists have classified flows, through for example ducts, with respect to the distribution of the phases, which is a function of flow parameters and the duct shape. This classification will be briefly discussed in Chapter (2). However, a large number of flows cannot be assigned to any class, particularly flows in geometrically very complex systems.

## 1.2 Overview of research program

Since one does not know the shape of the interface *a priori*, it has to be calculated along with other parameters of the flow. The shape changes are not only due to convection and forces, but also due to thermodynamic effects, such as phase transition. Consequently, this study considers changes in the distribution of the interface alignment and the changes in the flow simultaneously. The algorithm used is based on a mathematical model of the flow. Clearly, since the governing equations and closure relations, are not exact, the resulting solution departs from that in the real world. Another source of error, is that caused by the numerical approach. This thesis aims also at showing how improvements in the numerical approach affect the quality of the results.

The basis of this research is the computational method CAVKA developed at Technical University of Karlsruhe in Germany for simulation of cavitating flows (Sauer, 2000). The method is a tool comprising the basic calculation algorithms that have been improved and developed further in the current project. The main extension is that CAVKA handles pressure driven phase transition, i.e. cavitation. In CAVKA the temperature is assumed to be constant. The extended method includes the energy equation and therefore can treat temperature driven phase transition.

The algorithm assumes a single-field approach in the form of the Volume-of-Fluid (VOF) method. Thus, the distribution of the phases is to be calculated along with other parameters of the flow and constitutes part of the solution. VOF is coupled with the Energy of Fluid (EOF) method which allows for the evaluation of the divergence of the velocity field, caused by the gas-liquid phase transition. This sort of the transition assumes, in contrast to cavitation, the temperature as the driving force. Consequently, the algorithm employs the distribution of energy or rather the temperature itself.

The algorithm can handle physical phenomena appearing in a multi-phase flow in which phase transition takes place. The test cases discussed in this thesis concern flows of a single component that is in liquid or in vapour phase. However, assumptions have to be made that do not allow for a detailed quantitative evaluation of the result. The assumptions are that the problem is two dimensional, that the phases are incompressible and that effects due to surface tension can be neglected. Also it is assumed that effects due to turbulent diffusion may be neglected. These assumptions affect not only the kinematics of the flow, but also the distribution of the phasic structures in the domain. In conclusion, it must be emphasized, that the algorithm should be regarded as a step towards a comprehensive solution of the flow problem. Thus, at this stage of the development, the model is applicable only to a limited range of flows.

## 1.3 Overview of thesis

This thesis describes details of multi-phase flows, and will discuss the variety of possible approaches towards the numerical simulation of these flows. Amongst these approaches the VOF method is a method within the category of single field approaches. This review is given in Chapter (2) titled 'Review of approaches for multi-phase flows'. Subsequently, the physics of the gas-liquid phase transition is discussed in Chapter (3): 'Physics of gas-liquid phase transition'. This chapter considers the situation in which for example surface tension plays a role, and highlights the thermodynamics of the process. Chapter (4) treats the mathematical model of the flow. The set of governing equations is discussed and the Energy of Fluid method is employed to evaluate the divergence of the velocity field. In the Chapter (5), 'Numerical approach', the governing equations are discretised. Here, amongst others, the procedure of pressure correction is discussed. Aside from this, the construction of the system of discretized equations is shown as well as the method of its solution. Chapter (6), 'Interface capturing', is devoted to the numerical method used to determine the phasic distribution. Additional improvements and interface sharpening algorithms are discussed there as well. Chapter (7), 'Results', presents the results of the numerical simulations. The validation of these results is provided utilizing experimental data from the literature or, when possible, a theoretical consideration of the problem. The last chapter, 'Discussion', discusses advantages and disadvantages of the used computational method and gives some recommendations for further development.

# REVIEW OF APPROACHES FOR MULTIPHASE FLOWS

CHAPTER 2

In the present study, two-phase gas(vapour)-liquid flows are considered. This kind of flow occurs in a broad variety of industrial devices and system elements such as vapor condensers, vapor generation systems and mass transfer equipment. All of these devices need to be properly designed according to the type of flow and the range of operational flow parameters. In general, one can distinguish three categories of operation of industrial systems. The first category are systems in which heat and mass transfer occurs in a steady-state process, at least at normal operation conditions. The next category is formed by systems operating in a transient state, which occurs during emergency events in a plant as well as start-up and shut-down. The last category of operation applies to the situation in which the flow parameters attain their limits e.g. a critical heat flux in nuclear reactors threatening integrity of cooling water ducts, critical mass flux at which the mass flow becomes independent of downstream pressure (choking). To predict the flow there are a number of approaches that have been developed over the past decades. One can distinguish methods based on:
- empirical correlations,
- phenomenological models,
- multi-fluid models,
- single-fluid models.
Each of them will be briefly described in the next section with emphasis on the latter two.

## 2.1 Empirical correlations

The prediction method is based on data collected from results of experiments for a particular category of flows. The data are for example the pressure gradient, or mass transition between phases, obtained for a range of flow conditions such as the mass flux, initial flow quality, heat exchange between the system and its surroundings and geometry of the flow channel. The database provides correlations between independent and dependent parameters resulting in empirical or semi-empirical relations.

The next step is the application of the established correlations to predict flow parameters required in an industry applied system. However, if correlations are purely empirical it is preponderantly inaccurate to extrapolate data relations out of the range covered by the data from experiments. Such operation is unlikely to be successful even if correlations are semi-empirical thus partially based on mathematical models well describing some physical phenomena.

Even if calculations are carried out for conditions within the experimental range, some significant inaccuracies may arise in the result. This is caused by biases having influence on the accuracy of the correlation procedure. The main problem appears in obtaining a fully-developed flow which, in case of multiphase flows, is unreachable even at a long distance from the inlet of an experimental setup. While in a single phase flow fully developed flow can be obtained just after tens of duct diameters, in two-phase flow the distance may extend up to hundreds of diameters, hence, in most cases it is out of reach of the setup. In this context the pressure gradient, which is mostly the desirable parameter, that is expected to be constant or varying gradually, may have a significant error. Moreover, not fully-developed flows are often coupled with a lack of thermal equilibrium, which importance is difficult to evaluate due to unsteadiness and unknown dynamic conditions. In the process of developing correlations, unrecognized factors may play an important role, e.g. the effect of surface tension on local pressure gradients. The influence of these factors may not be taken into account entirely because of difficulties concerning the shape of the interface on conditions of the not fully-developed flow. The gas-liquid interface brings about other unresolved questions concerning local physical parameters within an interfacial region. Experimental data sampled from a flow duct may also possess an inherent error of the measuring device or that due to difficulties in the measurement of gas-liquid flows. In summary, empirical correlations may be useful for well-known conditions, but fail relatively often when trying to apply them outside the established range of applicability. This has led to attempts to find better approaches described in the following subsections.

## 2.2 Phenomenological models

The class of phenomenological models considers a two-phase flow in detail based on experimental observation of a given type of flow, which is dependent on the topology of the interface in a duct. These models not only provide global parameters such us the pressure gradient or void fraction, but also give information about local phasic structures, e.g. liquid film thickness at the duct wall, bubble/droplet distribution and their average radius, frequency and size of gaseous slugs, etc. The obtained database allows for evaluation of physical processes, such us interfacial heat transfer and momentum transfer, interfacial mass exchange, wall heat transfer, etc., associated with

the flow and influencing its global parameters. The interfacial transfers are given in the form of closure relations that are required in the multi-fluid approach to be discussed later.

Hence, the conclusion is that the foundation of phenomenological models lies in the classification of the flow geometry. In a single phase flow this is relatively easy, because one knows the geometry *a priori* - e.g. the shape of the channel. In such situation global parameters of the flow may be empirically or theoretically assessed without large effort. However, evaluation of the geometry in two phase flows constitutes a major difficulty, because of the presence of the gas-liquid interface. Its geometry becomes part of the solution. The interface position is then one of dependent flow parameters, which has influence on others such as the velocity gradient or the pressure drop. Thus, without determining the interface geometry there is no way to compute flow quantities that are essential from the engineering point of view. In order to overcome this problem researchers have developed so-called flow regimes that use certain dynamic parameters to describe how the phases are distributed. However, one should keep in mind that the databases underlying flow regimes are limited to data for relatively simple channel geometries. Thus, there are many engineering application for which it is not possible to predict precisely the interface shape.

The empirical correlations described in the preceding section, do not take into account flow regimes and this is the main reason of their failure in the prediction of flow parameters. In many cases attempts of data correlation for the pressure drop or the flow quality generate an error typical of a magnitude of about 30%, whereas in some ranges correlations are over or underpredict experimental data by a factor of two. Only limited ranges of data give a deviation of an acceptable level. Because of the above the flow regimes method, considered here, enjoys greater interest.

In the course of this thesis the multi-field approach will be highlighted. In general, the method utilizes a separate set of governing equations for each of the phases assumed separated from each other by the interface. In order to implement the model an assembly of closure relations is required to describe for example the heat and mass exchange across the interface. It is well known that flow parameters are strongly dependent on the interface geometry, thus the flow regime. For instance, it is not difficult to realize, that an interface heat flux in the case of bubbly flow is diametrically different from the one in the case of annular flow, leading to differences in mass transfer between phases during phase transition. In this situation recognition of the flow regime as the first step of the approach is a necessity for identifying the appropriate constitutive relations.

Flow patterns (regimes) are significantly affected by many factors and one of the most influencing ones is the geometry of the duct and its inclination. As an example of the variety of regimes the flow patterns in a horizontal pipe is illustrated in Fig.2.1 where the pipe transports a co-current flow. In the horizontal flow shown in Fig.2.1

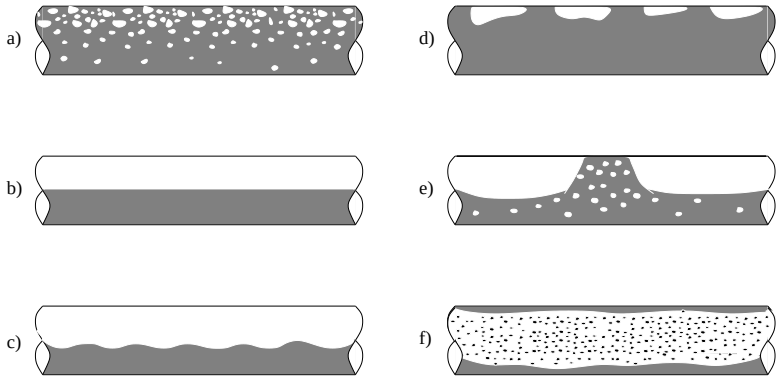


FIGURE 2.1: *Flow patterns in horizontally placed pipe; a) Dispersed bubbly flow; b) Stratified flow; c) Stratified wavy flow; d) Plug flow; e) Slug flow; f) Annular dispersed flow. Figure reproduced from (Banerjee, Hewitt, Zaleski, Tryggvason, Koumoutsakos, Yadigaroglu and Ishii, (2004)).*

the distribution of the interface is strongly affected by gravity. Dominance of gravitation will decrease with increasing kinetic energy of the flow, which is manifested by the magnitude of the phasic velocities. In bubbly flow gas structures are dispersed in the continuous bulk of the liquid, but their concentration tends to higher values at the top of the duct than near the bottom of the duct. However, the bubble distribution may become more uniform in the case of a higher flow speed. The stratified flow is characterised by the liquid flowing along the bottom of the duct and the gas along the top. In general, this kind of flow occurs at low velocity of the two phases, however, depending on the speed the flow pattern is divided into two subregimes, namely smooth stratified and wavy stratified. The amplitude and frequency of the waves appearing in the latter flow regime, are influenced by the relative velocity between the gas and the liquid. Obviously, physical properties of the phases such as density and surface tension are important in this regime. For increasing liquid flux rate one obtains the plug flow, also called the elongated bubble flow. The pattern configuration consists of relatively large, bubble free waves which originate from the interfacial Kelvin-Helmholtz instability. The plug flow transits into slug flow once the gas accelerates. One can observe the small-scale gas structures in the bulk of the waves. The boundary between the liquid slug regime and the elongated bubble regime is not as sharp as in the case of the plug flow; the entire flow becomes more chaotic. Still higher gas velocities result in annular flow characterized by a liquid film covering the pipe wall. The film tends to be thicker at the bottom of the duct, which is due to gravity. Variation of the liquid layer thickness depends on the gas flux rate. The gas velocity affects also the shape of the interface between the film and the gas. The film is wavy and may or may not be continuous. In annular flow regime, one can

also note intensified mass exchange between the liquid layer and the bulk of the gas, caused not only by phase transition, but also due to deposition of droplets onto the film and their entrainment to the gas. Consequently, the flowing gas core contains liquid structures, which may substantially change the flow behavior.

Observation of the variation of the interface configuration caused by changing flow parameters led to the development of flow pattern maps illustrating the flow regimes as a function of quantities characterizing the flow. These are for instance velocities or mass fluxes of each phase, a flow quality and many other parameters concerning physical properties of the phases. The map is based on experiments for ducts at a prescribed inclination and geometry. An experimental setup is equipped with two valves adjusting flux rates of the gas and liquid phase entering the pipe. The valves are set at a certain position which correspond to known values of the phasic fluxes. For this condition one observes which flow regime appears. The results are presented in the form of a map. An example of such a map is given in Fig.(2.2) from (Manhane, Gregory and Azis, (1974)). In Fig.(2.2) volumetric fluxes are expressed in terms of the superficial velocity, $j$, defined as $j = \dot{V}/A$, where $\dot{V}$ is the volumetric flux of the phase considered and $A$ is the cross sectional area of the duct. Many

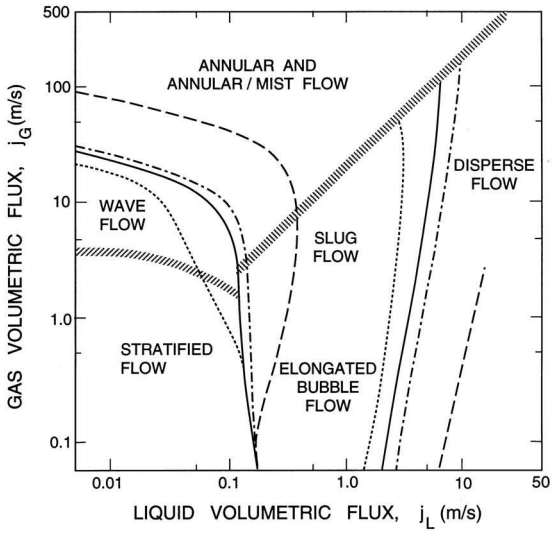


FIGURE 2.2: *Flow regime map of air-water flow in a horizontal pipe at a temperature of* $298.15[K]$ *and pressure of* $1[bar]$ *for various pipe diameters:* $1.25[cm]$ *- dotted line,* $2.5[cm]$ *- solid line,* $5[cm]$ *- dash-dot line,* $30[cm]$ *- dashed line. Figure taken from (Manhane, Gregory and Azis, (1974)).*

attempts have been made to generalize flow regime maps, but it is very difficult because of the large number of parameters influencing the boundaries between different

patterns in the map. Even within a map, for which geometry and inclination of the pipe are constant, regions of regime transitions are difficult to define by any correlation. However, some effort has been made to develop separate models for horizontal and vertical ducts as these find application in most industrial systems. Furthermore, some theories have been proposed for steep and slight inclinations, but the range of inclination angles for which the models are appropriate still remains rather narrow. Barnea (Barnea, (1986); Barnea, (1987)) reviewed the so far existing regime maps. His reevaluation and modification of the flow maps yield the complete model for regime boundaries valid for all angles of a pipe inclination. In spite of this, the feasibility of the approach, particularly for larger pipe diameters and higher pressures, is still to be tested experimentally. It is certain that the method describes quite well the relation between the flow pattern and the angle of inclination in its entire range.

A flow regime map constitutes the foundation for further evaluation of local flow conditions, which are necessary to improve the accuracy of the prediction of essential flow parameters. Local (interfacial) flow behaviour is the basis for assessment of constitutive relations indispensable in the multi-fluid approach discussed in the next section.

## 2.3 Multi-field approach

Multiphase flows and their physics are described in a continuum formulation by partial differential equations for the macroscopic field supplemented by closure relations. During the past couple of decades various methods describing multi-phase flows have been developed, but researchers still encounter difficulties associated with the establishment of constitutive relations, that impose limitations on every flow model. The key issue of a multiphase flow is the gas-liquid interface (a two-phase flow) which appearance is described by flow regimes described in Sec.2.2. However, it may happen that more than one flow pattern occurs simultaneously in a single flow system which increases the complexity of the modelling, in particular when the topography of the interface has to be included in the closure relations.

Detailed observation of multiphase flows shows a number of phasic regions separated by an interface. Theoretically, it would be possible to describe the system by a set of governing equations assigned to each phasic region connected through the boundary conditions for the interface between the regions. However, the phasic variables change in time simultaneously with the change of the interface position. The position is *a priori* unknown i.e. has to be determined as part of the solution. Taking this into account renders the model impractical if not impossible to solve for flows involving more than a small number of (large) regions of one phase embedded in the bulk phase.

The obstacle has been overcome by taking a macroscopic view of the flow. There

are three main formulation regarding gas-liquid flows, which are the basis for further modelling:
a) interacting continua assumption,
b) control volume approach,
c) averaging method.
The above formulation do not consider interfacial transients, consequently information about local transitions is partially eliminated or even lost. Therefore it is very important to consider in detail the local flow behavior at the interface, in order to model the interaction of the two phases and to derive a macroscopic description.

a) The first listed approach assumes similarity with a single-phase flow. In each region of the flow the two phases exist simultaneously and the model includes internal diffusion of the gas and the liquid. Transport properties and thermodynamics of the flow depend on the mixture quality, i.e. the phase concentration in the region considered. In general, the two-phase flow is considered as a mixture described by its averaged properties, together with transfers between phase mass in case of phase transition.

However, if in the two-phase flow a finite volume is occupied by a single phase, this volume is bounded by the moving interface and in continua assumption the discontinuity in the form of the interface (e.g. free surface) has to be taken care of.

This kind of approach does well in case of dispersed two-phase flows such as droplets in a gaseous core or bubbles in a bulk of liquid. It has been successfully applied to gas mixture flows in which a free surface is not present. Later the model has been universalized and adopted to a broader range of mixtures, see (Truesdell and Toupin, (1960)). In spite of the model departure from the description of the discontinuous features of the interface, it possesses a significant advantage, namely only one set of governing equations suffices for the description of the flow of the mixture of the two phases, which substantially simplifies calculations.

b) The control volume approach relies basically on establishing conservation equations for mass, momentum and energy in an arbitrary control volume. The approach applies to a gas-liquid mixture as well as to the individual phases. The method was used extensively in one dimensional or quasi-one dimensional flows. Due to the simplicity of the approach and because quite a wide range of flows present in industrial systems may be regarded as one or quasi-one dimensional, the number of methods that has been developed utilise the control volume approach (Tong, (1965); Brodkey, (1967); Martinelli and Nelson, (1948)). The control volume method predicts flow parameters with quite good accuracy under the condition that the shape of the interface is not too complex, as in a case of annular or stratified flows. Otherwise, interfacial transitions of mass, momentum and energy become difficult to capture and cross-sectional variation of flow parameters does not permit the flow to be regarded as one dimensional any more. In such situation the approach loses its accuracy and

needs to be replaced by a more sophisticated approach.

c) This system is represented by the averaging method, which can be subdivided into two main groups: Eulerian and Boltzmann statistical averages. The most important and widely used is the Eulerian averaging method. The averaging method constitutes the base for the development of multi- (or in case of a single substance, gas-liquid flow, two-) fluid approach.

In the two-fluid model one considers flow phases separately, formulating individual sets of governing equations for each fluid. Consequently, phases do not pass through a duct independently, but they are coupled by closure relations representing interfacial interactions in a macroscopic manner. Constitutive equations are formulated on the basis of appropriate correlations and averaging methods. However, it must be noted, that in many cases experimental data do not provide sufficient information about interfacial transients due to e.g. technical limits of instruments. This implies that for more complex flows such as transitions between flow regimes or complicated channel geometries, considerable uncertainties are present in closure relations for multi-fluid flows. However, one has not discovered yet any alternative for the two-fluid approach, in particular for weakly coupled two-phase flow, which is capable of predicting drift parameters with so high level of accuracy, taking into account many subtleties of local (interfacial) transients.

The very first step in the two-fluid model consists of identification of the flow fields (flow regimes), whose number is affected by the distribution of the phases in the duct. It is assumed that in the flow field is homogeneous. The field is then thought of as a strictly recognizable portion of the flow pattern. An example of the flow field separation is depicted in Fig.2.3. In general, selection of the field should be done

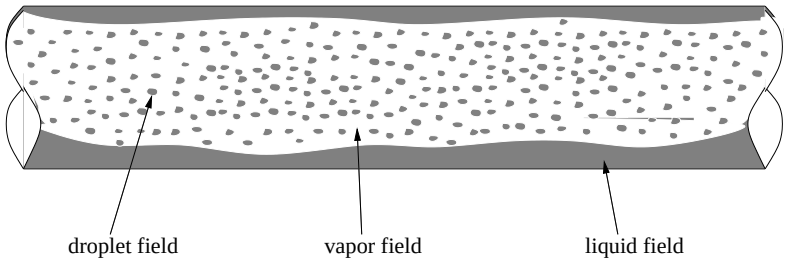


FIGURE 2.3: *Identification of flow fields in an annular flow.*

based on the velocity of each distinguished portion in the flow regime. The velocity within a portion must be as uniform as possible in order to avoid strong variation in the momentum flux. Consider the annular flow sketched in Fig.2.3, where the gaseous core with dispersed droplets has much greater speed than the liquid film at

the pipe periphery. In this situation regarding the flow as consisting of two fields, namely the liquid and the gas phase, would lead to an unsatisfactory representation of the liquid film in the flow. The better choice, for sure, is distinguishing three fields: the liquid film, the gas core and droplets of liquid convected by the gas in the core. In the case one needs to confine the consideration to two fields, the best manner to tackle the problem is, assuming an approximately equal velocity of the droplets and the gas core flow, to separate the flow into the liquid film as the first field and the gas-droplet mixture as the second one. The important conclusion arising at this point is that the number of fields is not strictly tied to the number of flow phases. One may rather state, that the number of fields witnesses the flexibility of a different flow regime modelling. For instance, a three-field model concerning a liquid, gas and liquid-gas mixture, may be assigned to two patterns; the slug flow (the stream of the liquid at the duct bottom, the pure gas structures at the top and a gas-liquid mixture of the slugs) and the annular flow (the liquid layer at the duct periphery, the gas core and the droplets in the core flow), see Fig.2.1.

The next step of the modelling procedure is averaging the governing equations assigned to each of the flow fields. There exist many methods for averaging in time and space or both of them, e.g.(Banerjee and Chan, (1980); Drew, (1983); Panton, (1978)). This averaging procedure allows easy handling of the problem, however, the exchange of momentum, mass and energy at interfacial regions is basically lost. Thus, additional information needs to be specified in the form of closure relations. The quality of these relations is a measure of the accuracy of the result obtained from flow calculations. In the averaging approach one can distinguish common methods, namely Euler and Boltzmann.

### 2.3.1 Euler-Euler approach

The most widely used approach for loosely coupled flows is the Euler-Euler method also called the interpenetrating continua formulation. The Eulerian space and time averaging, which has been extensively used for single phase turbulent flows, has become the tool for modelling of three-dimensional two-phase flows as well. In order to formulate the set of conservation equations one begins with the volume averaging procedure followed by the so-called ensemble averaging. The volume average is a mean value of an instantaneous flow variable averaged over a certain finite volume of the flow e.g. over a cross-section of a channel. Still, for unsteady flow conditions, the values of averaged quantities can differ when measured at the same instant in several flows started from the same initial conditions. This is the effect of the statistical behavior of the flow. In order to avoid the ambiguity of the results one needs to take the mean of the volume-averages of flow quantities. This operation is commutative and has been named double averaging. It ensures continuity of derivatives, which might otherwise be discontinuous. The considered control volume is shown in Fig.2.4, in which all necessary variables are revealed. The volume is just inside the

solid boundary in order to illustrate all possibilities. Nevertheless, the control volume may also be a part of the internal flow, which does not include physical boundaries of the duct. The formulation of the appropriate form of the governing equation requires

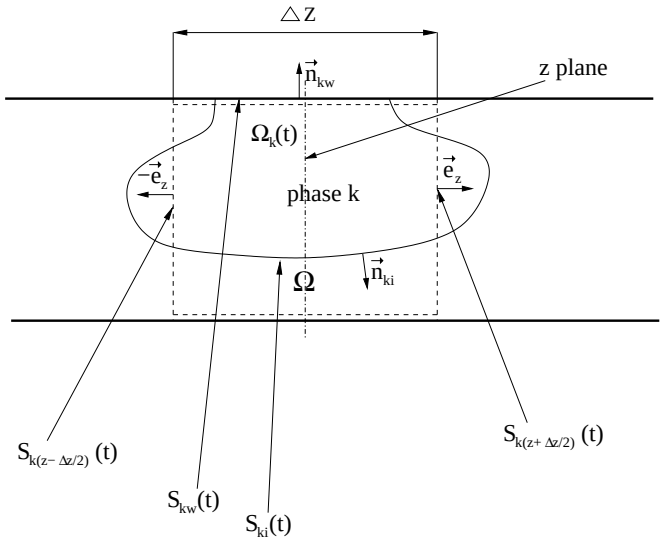


FIGURE 2.4: *Control volume (dashed line) in the channel; non stationary $S_{ki}$ - interfacial surface within the control volume, $S_{kw}$ - surface of the stationary wall wetted by phase (field) $k$ within the control volume, $S_{k(z\pm\Delta z/2)}$ - surface at the control volume boundaries with phase (field) $k$, $\vec{n}_{ki}$ - outward directed normal unit vector at the interface, $\vec{n}_{kw}$ - outward directed normal unit vector on wall $S_{kw}$, $\Omega$ - control volume, $\Omega_k$ - volume of phase (field) $k$ in the control volume $\Omega$; $k \in \mathbb{N}$.*

the use of Gauss' theorem. Consider the control volume shown in Fig.(2.4). Using Gauss'theorem the gradient of quantity $\phi_k = \phi_k(x, y, z, t)$ in control volume $\Omega_k$ is expressed as

$$\int\limits_{\Omega_k} \vec{\nabla}\phi_k \, d\Omega = \int\limits_{S_{kw}} \phi_k \vec{n}_{kw} \, dS + \int\limits_{S_{ki}} \phi_k \vec{n}_{ki} \, dS + \vec{e}_z I, \tag{2.1}$$

with $\vec{e}_z$ the unit vector in $z$ direction and $\phi_k$ a variable of the phase (field) $k$. The rest of notations including subscripts have been explained in the caption of Fig.(2.4). The last term at the right-hand side of (2.1) reads

$$I = \int\limits_{S_k\left(z+\frac{\Delta z}{2}\right)} \phi_k \left(\tilde{x}, \tilde{y}, z + \frac{\Delta z}{2}, t\right) \, dS\left(\tilde{x}, \tilde{y}\right) - \int\limits_{S_k\left(z-\frac{\Delta z}{2}\right)} \phi_k \left(\tilde{x}, \tilde{y}, z - \frac{\Delta z}{2}, t\right) \, dS\left(\tilde{x}, \tilde{y}\right), \tag{2.2}$$

where $\tilde{x}$ and $\tilde{y}$ are coordinates defining the position of points on boundary $S_{k(z\pm\Delta z/2)}$, given by the plane $z = constant$ of the control volume. Now one can express (2.2) as

$$I = \frac{\partial}{\partial z} \int_{z-\frac{\Delta z}{2}}^{z+\frac{\Delta z}{2}} \left[ \int_{S_k(\tilde{z})} \phi_k \left(\tilde{x}, \tilde{y}, \tilde{z}, t\right) \, dS \left(\tilde{x}, \tilde{y}\right) \right] d\tilde{z}, \tag{2.3}$$

which follows directly from Leibnitz'rule. So it follows that

$$I = \frac{\partial}{\partial z} \int_{\Omega_k} \phi_k \left(\tilde{x}, \tilde{y}, \tilde{z}, t\right) \, d\Omega \left(\tilde{x}, \tilde{y}, \tilde{z}\right). \tag{2.4}$$

Substitution of (2.4) in (2.1) shows that for control volume $\Omega_k$ centered around $z = constant$, which is infinitesimal in $z$-direction

$$\int_{\Omega_k} \vec{\nabla} \phi_k d\Omega = \vec{e}_z \frac{\partial}{\partial z} \int_{\Omega_k} \phi_k d\Omega + \int_{S_{ki}} \phi_k \vec{n}_{ki} dS + \int_{S_{kw}} \phi_k \vec{n}_{kw} dS \tag{2.5}$$

For control volume $\Omega_k$ at $(x, y, z)$, that is infinitesimal in each direction, it then follows that

$$\int_{\Omega_k} \vec{\nabla} \phi_k d\Omega = \vec{\nabla} \left( \int_{\Omega_k} \phi_k d\Omega \right) + \int_{S_{ki}} \phi_k \vec{n}_{ki} dS + \int_{S_{kw}} \phi_k \vec{n}_{kw} dS. \tag{2.6}$$

For the divergence theorem one can derive a similar expression, again for infinitesimal volume $\Omega_k$

$$\int_{\Omega_k} \vec{\nabla} . \vec{A}_k \, d\Omega = \vec{\nabla} . \left( \int_{\Omega_k} \vec{A}_k \, d\Omega \right) + \int_{S_{ki}} \vec{A}_k . \vec{n}_{ki} \, dS + \int_{S_{kw}} \vec{A}_k . \vec{n}_{kw} \, dS. \tag{2.7}$$

Leibniz' rule for variable $\phi_k = \phi(x, y, z, t)$ in control volume $\Omega_k = \Omega_k(t)$, not necessarily infinitesimal, reads

$$\int_{\Omega} \frac{\partial \phi_k}{\partial t} \, d\Omega = \frac{\partial}{\partial t} \int_{\Omega_k} \phi_k \, d\Omega - \int_{\partial S_{ki}} \phi_k \left( \vec{u}_{ki} . \vec{n}_{ki} \right) \, dS, \tag{2.8}$$

where $u_{ki}$ denotes the relative velocity of the interface. An infinitesimal volume-averaged variable of phase (field) $k$ is defined as

$$\overline{\phi}_k = \frac{1}{\Omega_k} \int_{\Omega_k} \phi_k d\Omega. \tag{2.9}$$

In order to express a volume-averaged quantity in terms of variables in control volume $\Omega$, one needs to define the volume fraction $\alpha_k$ in an infinitesimal control volume $\Omega$ as

$$\alpha_k = \frac{\Omega_k}{\Omega}. \tag{2.10}$$

The volume-averaged form of a quantity is then

$$\alpha_k \overline{\phi}_k = \frac{1}{\Omega} \int_{\Omega_k} \phi_k d\Omega. \tag{2.11}$$

The local instantaneous conservation equation for field $k$ reads

$$\frac{\partial \rho_k \psi_k}{\partial t} + \vec{\nabla}. \left(\rho_k \vec{u}_k \psi_k\right) = -\vec{\nabla}.\vec{J}_k + \rho_k \Phi_k, \tag{2.12}$$

where $\rho_k \psi_k$ denotes any conserved flow variable, $\vec{J}_k$ is the external flux term and $\Phi$ indicates a source term. Integration of (2.12) over infinitesimal control volume $\Omega_k$, using (2.6), yields

$$\begin{aligned} &\int_{\Omega_k} \frac{\partial \left(\rho_k \psi_k\right)}{\partial t} \, d\Omega + \vec{\nabla}. \left( \int_{\Omega_k} \rho_k \psi_k \vec{u}_k \, d\Omega \right) + \int_{S_{ki}} \rho_k \psi_k \left(\vec{u}_k.\vec{n}_{ki}\right) \, dS = \\ &- \vec{\nabla}. \left( \int_{\Omega_k} \vec{J}_k \, d\Omega \right) - \int_{S_{ki}} \vec{J}_k.\vec{n}_{ki} \, dS - \int_{S_{kw}} \vec{J}_k.\vec{n}_{kw} \, dS + \int_{\Omega_k} \rho_k \Phi_k \, d\Omega. \end{aligned} \tag{2.13}$$

Leibniz' rule (2.8) employed in (2.13) to the unsteady term then gives

$$\begin{aligned} &\frac{\partial}{\partial t} \int_{\Omega_k} \rho_k \psi_k \, d\Omega + \int_{S_{ki}} \left(\rho_k \psi_k \left(\vec{u}_k - \vec{u}_{ki}\right)\right) .\vec{n}_{ki} \, dS + \vec{\nabla}. \left( \int_{\Omega_k} \rho_k \psi_k \vec{u}_k \, d\Omega \right) = \\ &- \vec{\nabla}. \left( \int_{\Omega_k} \vec{J}_k \, d\Omega \right) - \int_{S_{ki}} \vec{J}_k.\vec{n}_{ki} \, dS - \int_{S_{kw}} \vec{J}_k.\vec{n}_{kw} \, dS + \int_{\Omega_k} \rho_k \Phi_k \, d\Omega. \end{aligned} \tag{2.14}$$

Finally, implementation of (2.9) in (2.14) yields the volume averaged form of the general conservation equation for field $k$

$$\begin{aligned} &\frac{\partial \alpha_k \overline{\rho_k \psi_k}}{\partial t} + \vec{\nabla}. \left(\alpha_k \overline{\rho_k \psi_k \vec{u}_k}\right) = -\vec{\nabla}. \left(\alpha_k \overline{\vec{J}_k}\right) + \\ &\alpha_k \overline{\rho_k \Phi_k} - \frac{1}{\Omega} \left( \int_{S_{ki}} \left(\rho_k \psi_k \left(\vec{u}_k - \vec{u}_{ki}\right)\right) .\vec{n}_{ki} dS + \int_{S_{ki}} \vec{J}_k.\vec{n}_{ki} dS + \int_{S_{kw}} \vec{J}_k.\vec{n}_{kw} dS \right), \end{aligned} \tag{2.15}$$

where a bar over the terms, similarly to (2.9), denotes averaged quantities. In the derivation of (2.15) one assumed that at the solid surface, $S_{kw}$, the normal component of the velocity equals zero. Note that the last term on the right-hand side of (2.15) can be interpreted as follows:

$$-\frac{1}{\Omega}\int\limits_{S_{ki}} \rho_k \psi_k \left(\vec{u}_k - \vec{u}_{ki}\right).\vec{n}_{ki}\, dS$$

is the term that represents the increase of $\psi_k$ in control volume $\Omega_k$ because of the motion of the interface $S_{ki}$ relative to the motion of the phase $k$ of the fluid. This term is not present in case the interface is not convected with the fluid of phase $k$;

$$-\frac{1}{\Omega}\int\limits_{S_{ki}} \vec{J}_k.\vec{n}_{ki}\, dS$$

is the term that represents the contribution to phase $k$ of the fluid through a flux into $\Omega_k$ through the interface $S_{ki}$;

$$-\frac{1}{\Omega}\int\limits_{S_{kw}} \vec{J}_k.\vec{n}_{kw}\, dS$$

similar for the flux across the solid surface.

Ensemble-averaging requires replacing the right hand side of Eq.(2.9) by the summation average of a quantity which volume-averaged values are probed from a certain number of identical experiments at the same instant from their beginning. For example, volume fraction $\alpha_k$ of phase $k$ represents a value of an averaged ensemble of fractions which appeared at the same moment since initiation of experiments carried out under the same conditions. Nevertheless, the ensemble-averaging procedure yields exactly the same form of the equations, consequently ensemble-averaging signs have been omitted and only the volume-averaging is marked explicitly. In the following all averaged variables will be regarded as double-averaged quantities, i.e. the average over infinitesimal control volume $\Omega_k$ plus the ensemble-average.

In order to obtain the equations for the conservation of mass, momentum and energy one needs to individualize Eq.(2.15). This is obtained by substituting for $\psi_k$, $\vec{J}_k$ and $\Phi_k$ the expressions relevant for each of the conservation equations. The appropriate form of the above three quantities is given in Tab.(2.1).
In Tab.(2.1) one has: $e_k$ internal energy $[J/kg]$, $\vec{g}$ body force acceleration [N/kg], e.g. gravitation, $p_k$ pressure $[N/m^2]$, $\vec{q}_k$ heat flux vector $[J/m^2 s]$, $\dot{Q}_k$ volumetric heat source $[J/m^3 s]$ e.g. from radiation and $\overline{\overline{\tau}}_k$ stress tensor $[N/m^2]$.

The derived set of equations operates on averages of products, which is not equal to products of averages. This very important aspect of an averaged formulation has

| **Conservation equation** | $\psi_{\mathbf{k}}$ | $\tilde{\mathbf{J}}_{\mathbf{k}}$ | $\mathbf{\Phi_k}$ |
|---|---|---|---|
| Mass | $1$ | $0$ | $0$ |
| Momentum | $\vec{u}_k$ | $p_k\overline{\overline{I}} - \overline{\overline{\tau}}_k$ | $\vec{g}$ |
| Energy | $e_k + \frac{\lvert\vec{u}_k\rvert^2}{2}$ | $\left(p_k\overline{\overline{I}} - \overline{\overline{\tau}}_k\right).\vec{u}_k + \vec{q}_k$ | $\vec{u}_k.\vec{g} + \dot{Q}_k$ |

TABLE 2.1: *Formulas for conserved quantities.*

been defined as a covariance and some have attempted to model the effect of this difference (Zuber and Findlay, (1965); Bankoff, (1960)).

The right-hand side of Eq.(2.15) contains integrals over the interface surface and the wall bounding the duct. They involve mass, momentum and heat exchange between phases (fields) and on absence of wall effects one may express them as given in Tab.(2.2).

| **Conservation equation** | **Formulation** |
|---|---|
| Mass $\Gamma_k$ | $\frac{1}{\Omega}\int_{S_{ki}} \rho_k \left(\vec{u}_k - \vec{u}_{ki}\right).\vec{n}_{ki}dS$ |
| Momentum $\vec{M}_k$ | $\frac{1}{\Omega}\left(\int_{S_{ki}} \rho_k\vec{u}_k[(\vec{u}_k - \vec{u}_{ki}).\vec{n}_{ki}]\,dS + \int_{S_{ki}}\left(p_k\overline{\overline{I}} - \overline{\overline{\tau}}_k\right).\vec{n}_{ki}dS\right)$ |
| Energy $E_k$ | $\frac{1}{\Omega}\int_{S_{ki}}\left(\rho_k\left(e_k + \frac{\lvert\vec{u}_k\rvert^2}{2}\right)(\vec{u}_k - \vec{u}_{ki}) + \vec{u}_k\left(p_k\overline{\overline{I}} - \overline{\overline{\tau}}_k\right) + \vec{q}_k\right).\vec{n}_{ki}dS$ |

TABLE 2.2: *Interfacial relations for the Euler approach.*

The interfacial quantities, the quantities with the $ki$ subscript, appearing in (2.15) and Tab.(2.2) need further modelling. Differences between the averaged variables and those at the interface originate, in the case of the pressure and the stress tensor, from the flow dynamics of the bulk of the flow. Suppose a gaseous bubble or a droplet in the bulk of a liquid or a gas, respectively. The curved interface of these objects causes an increment of the velocity of the bulk in the vicinity of the bubble

or droplet, decreasing simultaneously the static pressure. Consequently, there are additional effects of drag and lift acting on the field. The heat flux at the interface also demands attention, because it is driven by the temperature difference across the interface. The temperature is continuous across the interface because of the thermal diffusive nature of fluids. Thus, the temperature in the region adjacent to the interface will differ in comparison to the averaged one in the bulk of the field, consequently the heat flux will assume other values than in the case of a temperature discontinuity between flow fields. Developing the above closure relations constitutes considerable difficulty, in particular in a flow of high complexity of the interface. Constitutive equations and requirements for them will be discussed below.

### 2.3.2 Boltzmann statistical average

Another important scheme of the multi-field approach in the framework of the averaging method is the Boltzmann probability distribution. The method is mainly applicable for problems involving highly dispersed phases. It is based on the Eulerian approach applied to a continuous phase (field) and the Boltzmann probability distribution formulation, which considers other phases sprayed in the bulk of a continuous phase. A dispersed phase is described by a distribution function, which gives information about number or concentration of phasic structures, their velocity and probable size, thus actually the formulation represents the multi-field model of a sprayed phase consisting of a large number of fields. The approach, similar to that of (Williams, (1959)), considers a two-phase flow and defines the quantity

$$f_{k+1}\left(r,\Omega,\vec{u}_{k+1},t\right)dr_{k+1}\,d\Omega\,d|\vec{u}|_{k+1}\,,$$

which represents the probable number of discrete spherical phasic structures of radius between $r$ and $r+dr$, placed in the control volume $d\Omega$ and moving with a phasic velocity in the range $|\vec{u}|_{k+1}$ and $|\vec{u}|_{k+1}+d|\vec{u}|_{k+1}$. In other words $f_{k+1}$ is the number of phasic particles per unit range of radius, velocity and volume. The change of quantity $f_{k+1}$ in time is defined as

$$\frac{\partial f_{k+1}}{\partial t}=-\frac{\partial\left(\dot{r}_{k+1}f_{k+1}\right)}{\partial r}-\vec{\nabla}.(f_{k+1}\vec{u}_{k+1})-\vec{\nabla}_{u_{k+1}}.(f_{k+1}\vec{a}_{k+1})+\dot{Q}_{k+1}+\sigma_{k+1}. \quad (2.16)$$

The derivatives $\vec{\nabla}$, $\vec{\nabla}_{u_{k+1}}$ are with respect to the spatial and velocity of the phasic structure coordinates, respectively. The term $\dot{Q}_{k+1}$ represents a source of the dispersed phase, whereas $\sigma_{k+1}$ denotes the change of $f_{k+1}$ as the effect of the coalescence and break-up of structures, which change their size and dynamics. The quantity $\dot{r}$ is the growth rate of a phasic particle and $\vec{a}_{k+1}$ its acceleration due to forces acting on the structure. The term involving the acceleration represents the change of $f_{k+1}$ caused by forces which change the velocity such that it is out of the range $\langle\vec{u}_{k+1},\vec{u}_{k+1}+d\vec{u}_{k+1}\rangle$, whereas $\vec{\nabla}.\left(f_{k+1}\vec{u}_{k+1}\right)$ represents the divergence of

structures in the control volume. The acceleration of structures is due to the sum of forces, such as hydrostatic ones, drag or gravitation, that particles are subjected to. In order to arrive at the general equation of interfacial transport one needs to multiply (2.16) by the surface area of the phasic structures in the control volume and integrate over their velocity and radius. If $\dot{r}$ is known, the source term $\dot{Q}_{k+1}$ and $\sigma_{k+1}$ are evaluated, then $f_{k+1}$ can be assessed. If a spray is diluted enough, statistical fluctuations of the dispersed phase is negligible and the equations of motion of the continuous field are coupled with (2.16) through the variables $\dot{r}$ and $\vec{a}_{k+1}$.

The averaged terms of the governing equation (2.15) written for the continuous phase remain essentially unchanged, see Tab.(2.1), however, the volume fraction, $\alpha_k$, is defined according to the statistical nature of the model. For a two-phase flow it is expressed as

$$\alpha_k = 1 - \iint \frac{4}{3}\pi r^3 f_{k+1}\, dr\, d\,|\vec{u}|_{k+1}\,. \tag{2.17}$$

The interfacial relations for mass, momentum and energy transport between the phases (fields) are tabulated in Tab.(2.3). The relation for the continuity equation in Tab.(2.3)

| **Conserv. equation** | **Formulation** |
|---|---|
| Mass $\Gamma_k$ | $-\iint \rho_{k+1} 4\pi r^2 \dot{r} f_{k+1}\, dr\, d\,|\vec{u}|_{k+1}$ |
| Momentum $\vec{M}_k$ | $-\iint \rho_{k+1} \frac{4}{3}\pi r^3 \vec{a}_{k+1} f_{k+1} dr d|\vec{u}|_{k+1} - \iint \rho_{k+1} 4\pi r^2 \dot{r}(\vec{u}_k - \vec{u}_{k+1}) f_{k+1} dr d|\vec{u}|_{k+1}$ |
| Energy $E_k$ | $-\iint \rho_{k+1} \frac{3}{4}\pi r^3 \vec{a}_{k+1}.\vec{u}_{k+1} f_{k+1} dr d|\vec{u}|_{k+1} - \iint \rho_{k+1} 4\pi r^2 \dot{r}\left(e_{k+1} + \frac{|\vec{u}_k|^2}{2}\right) f_{k+1} dr d|\vec{u}|_{k+1}$ |

TABLE 2.3: *Interfacial relations for the Boltzmann approach.*

reveals a mass transfer between phases. The first term of the expression for momentum represents forces of the continuous field acting on the discrete phase, whereas the second term shows the average momentum added to the continuous flow, which is the effect of the phase transition in the fields. The two terms for the energy equation account for the work done on phase $k$ (continuous field) and total internal energy transferred during the phase transition, respectively. Obviously, above relations, as in the case of the Eulerian constitutive equations, require additional modelling effort.

The above discussion of the Boltzmann-type equations assumes a spherical shape of the dispersed droplets or gaseous bubbles, nevertheless the model can be extended to non-spherical sprayed structures by implementing appropriate shape factors. Moreover, implementation of the shape distribution function brings information about the shape and size of the dispersed phase, thus allows for describing the evolution of the interfacial area. Consequently, detailed insight in the interfacial geometry is possible, which makes modelling of closure relations easier and more accurate than the Euler approach, specifically in case of complex topologies of the interface.

### 2.3.3 Closure relations for multi-field approaches

The last step of the procedure of modelling are the closure relations for interfacial exchange of mass, momentum and energy. The relations of the type given by $\Gamma_k$, $\vec{M}_k$ and $E_k$ are integrated over the interface surface or eventually a physical boundary of a channel wetted by the considered phase, consequently values of the integrals are strongly dependent on the interface topology. Prediction of the interface shape is the central difficulty, which is partially overcome by employment of flow regimes, that allow for at least a prediction of interfacial area $s_{ki}$ in the considered control volume. The interfacial area is defined as the interfacial surface area within the control volume per unit volume. Accuracy of prediction of the area depends on the size of the control volume. However, it is theoretically possible to achieve constitutive relations that are independent of the size of the control volume (Nigmatulin, (1979)). For well-dispersed phasic structures in a continuous flow this is feasible, nevertheless, for larger structures such as slugs or plugs the difficulty arises that the control volume cannot be sufficiently large to contain a sufficient number of representative phasic elements.

The general requirements for the constitutive relations may be classified with respect to the kind of the field boundary, namely whether it is an interface or a wall intersected by the field. Essentially, both of them demand similar quantities to model, as will be briefly described. The most difficult issue is establishing $s_{ki}$. Information about a current flow pattern is certainly helpful, however, the matter is more complex for a two-phase flow if there is an additional field running through the duct, e.g. the dispersed phase in the annular dispersed flow. For the interpenetrating continua model the problem arises how to determine which portion of the interface is part of the liquid film and which part is the dispersed phase. Separation of this contribution is the major difficulty in multi-field modelling.
The other necessary quantity is the scalar heat transfer coefficient $\lambda_{ki}$, which is a function of the fluid physical properties and of the interfacial or wall shear stress. The factor is indispensable for the prediction of $\Gamma_k$ and $E_k$. The interfacial mass transfer caused by a phase transition, with negligence of kinetic energy and surface

tension effects, obeys the equation

$$\Gamma_k \cong \frac{\frac{1}{\Omega}\int_{S_{ki}} \vec{q}_k.\vec{n}_{ki}\, dS}{l_k}, \tag{2.18}$$

where the numerator represents the heat flux through the interface and the denominator is the latent heat of vaporisation. The numerator may be expressed as

$$\frac{1}{\Omega}\int_{S_{ki}} \vec{q}_k.\vec{n}_{ki}\, dS \cong \lambda_{ki} s_{ki} \left(T_k - T_{ki}\right), \tag{2.19}$$

where $T$ denotes the temperature and the subscripts $k$ and $ki$ denote a point in the bulk field and at the interface, respectively. Quantity $s_{ki}$ is defined as area of the interface per volume of the control volume. Interfacial temperature $T_{ki}$ is assumed to be that in equilibrium with the pressure $p_{ki}$ for a single-component, two-phase flow. Multiplication of $\Gamma_k$ by the heat of vaporization of the phase is the contribution of $E_k$, revealing the amount of latent heat converted to sensible heat in the phase.

For the momentum closure, $\vec{M}_k$, one needs to evaluate the drag coefficient for the dispersed phase, a friction coefficient for the continuous interface or the channel wall and additionally a mass coefficient for the dispersed structures coexisting in the flow with the same continuous phase at the duct wall. In the situation of the latter, under appropriate conditions, e.g. dispersed annular flow, one observes deposition of phasic structure on the liquid film and the entrainment of the liquid into the gas, that demands additional effort to find the rate of deposition or entrainment. Detailed analysis of $\Gamma_k$ and $E_k$ will not be carried out here since this is not the scope of the present work.

At this point it is concluded that unless the closure terms are not sufficiently accurately modelled the superiority of the multi-field approach over the single-fluid (mixture) method vanishes, however, due to conservation of the interfacial discontinuity in a loosely coupled flow there is not an alternative for the multi-field procedure, that allows a high accuracy prediction.

On the other side of the spectrum, from the point of view of the macroscopic flow field treatment, one finds the single-field flow models. This group of models will be discussed in the following section.

## 2.4 Single-field approach

The single-field approach differs from the multi-field approaches from the point of view of the treatment of the phases in the computational domain. The single-field method regards a multi-phase flow as a single computational field in which more than one phase may exist and the interface between two phases is solved as a part of

the solution. In this kind of scheme, one set of governing equations suffices to calculate all essential flow field variables. This simplifies the process of computation and is the reason why the method raised so much interest of researchers. In the light of difficulties in formulating the closure relations in the multi-field approach, especially in the transition regions of the flow pattern map, single-field schemes reveal their superiority. The method does not demand an approximate predefinition of the interface geometry since this is part of the solution, thus the interface locus becomes the parameter and a flow regime map is redundant. Nevertheless, it still serves as source of information necessary for evaluation of the accuracy of the calculation result.

The problem, which arises in the approach consists in the failure of the governing equations of the handling by multiphase flow discontinuities. In order to overcome this problem, the interface is not assumed as a boundary of continuous flow properties any more, but it is discarded and replaced by a continuous transition between phases. Consequently, the interface loses its sharpness and is diffused in space, that causes the flow dynamics to depart from that existing in reality. The interface possesses thus a finite thickness, its value indicating the solution accuracy. Since the time of the first attempts of the application of the single-field approach, many methods of interface sharpening have been developed. The large variety of methods does not allow to give a detailed review, but some of the best-known sharpening schemes will be discussed in the following paragraphs of this section. The method that has been utilized in the present research is discussed in detail in Chapter (5). The interface spatial diffusion constitutes an obstacle in weakly coupled flows, but in the case of coupled flows such as bubbly flow with vapor structures concentrated in patches or dispersed ones where droplets are suspended and convected in the bulk of the flowing gas, the single-field approach appears to be the ideal solution. However, the obvious shortcoming of the method is that one loses some information about interfacial interactions, which might be incorporated by additional closures.

The single-field approach, due to the condition of smooth transition between phasic physical properties, may be regarded as a member of the interacting continua assumption mentioned in the beginning of Sec.(2.3). The main consequence of the method is that with the assumption of incompressibility of the fluid mixture phases, the mixture behaves as a quasi-compressible flow. This feature allows a single set of equations for the whole domain. In order to formulate the equations one needs the averaged phasic quantities of (2.15), namely $\overline{\rho_k \psi_k}$, $\overline{\rho_k \vec{u}_k \psi_k}$, $\overline{\vec{J}_k}$ and $\overline{\rho_k \Phi_k}$ in terms of the averaged mixture quantities. This is performed by summation of the phasic terms over the number of phases existing in the flow. Consequently,

$$\sum_{k=1}^{k=N} \overline{\rho_k \psi_k}, \quad \sum_{k=1}^{k=N} \overline{\rho_k \vec{u}_k \psi_k}, \quad \sum_{k=1}^{k=N} \overline{\vec{J}_k}, \quad \sum_{k=1}^{k=N} \overline{\rho_k \Phi_k}$$

lead to the general conservation equation for the single-field approach, which as-

sumes the form of (2.15)

$$\frac{\partial\overline{\rho\psi}}{\partial t} + \vec{\nabla}.\left(\overline{\rho\vec{u}\psi}\right) + \vec{\nabla}.\overline{\vec{J}} = \overline{\rho\Phi}. \tag{2.20}$$

Because of the mixture character of (2.20) the subscript $k$ present in (2.15) has been left out. The individual form of the mass, momentum and energy equation are derived based on expansion of the terms in (2.20) which assume the form given in Tab.(2.1). The quantities referring to the interfacial relations, being at the right-hand side of (2.15) need also to be summed. However, for the mass, momentum and energy conservation law, one has that

$$\begin{aligned} \sum_{k=1}^{k=N} \Gamma_k &= 0, \\ \sum_{k=1}^{k=N} \vec{M}_k &= 0, \\ \sum_{k=1}^{k=N} E_k &= 0, \end{aligned} \tag{2.21}$$

thus the right-side hand of (2.20) is simplified considerably. In (2.21) $N$ denotes the number of phases that exist in the mixture.

The solution of the set of the governing equations consists of the flow variables such as pressure, velocity and internal energy, however, it does not provide the geometry of the phase interface. Due to that, values of the time and space dependent physical properties of the flow, namely $\rho$, $\mu$ (dynamic viscosity) and $\lambda$ (heat conductivity), cannot be assessed without introducing a quantity indicating the position of the phases in space. This term is a scalar representing the phase distribution, which may be the argument of a steep function or may itself be the value of this function, that depends on the assumed model. In general, the quantity, say $\phi$, must obey the transport equation

$$\frac{\partial\phi}{\partial t} + \vec{\nabla}.\left(\vec{u}\phi\right) = \vec{\nabla}.\vec{J}, \tag{2.22}$$

where $\vec{J}$ represents the source of $\phi$, e.g. in the case of phase transition. The equation results in the distribution of $\phi$ in space, which subsequently results in the physical properties of the mixture in the domain. The properties are usually estimated using a weighting function, where the weighting factor is equal to $\phi$, i.e.

$$\gamma = \phi\gamma_k + (1-\phi)\,\gamma_{k+1}, \tag{2.23}$$

where $\gamma$ represents a relevant physical property.

Many ways of the interpretation of the interface have been developed, which represents a variety of ideas. Nevertheless, they may be divided in two basic groups distinguished by the character of the spatial discretizing of the computational domain, namely the fixed- and the moving-grid. The first one is predefined and is not convected together with the interface which intersects the grid arbitrarily. The latter appears in the domain as a subgrid describing the shape and position of the interface dividing the domain in subdomains each assigned to a phase. However, the scheme still remains a member of the single-phase approach. A comprehensive review of methods of interface description is beyond the scope of this work, consequently only a couple of widely used approaches will be highlighted, namely:
- Level-Set Method,
- Embedded Interface Method,
- Volume of Fluid Method (VOF).

### 2.4.1 Level-Set approach

In the level set approach, the interface is a surface in three-dimensional space or a contour in two-dimensional space, defined by some function $R(\vec{x},t)$. Additional surfaces, parallel to the interface are constructed by defining their coordinates as offset from the interface by a given distance in the direction normal to the interface. For example, consider the following function in the Cartesian coordinate system

$$R(x,y,z) = \sqrt{x^2+y^2+z^2} - r. \tag{2.24}$$

The surface $R(x,y,z) = 0$ represents a sphere of radius $r$, centered at the origin. A level set of the relation is the set of points placed at a certain constant distance from the considered sphere, consequently, it is represented by another sphere of a smaller or larger radius than $r$.

The level set procedure may also be employed for positioning of the interface in a domain. The representation of

$$R(\vec{x},t) = |\Delta\vec{r}| \tag{2.25}$$

in space is the shape of the interface at a given time under the condition that the parameter $|\Delta\vec{r}|$ is equal to 0. If $|\Delta\vec{r}|$ differs from 0 the level set appears as the contour at distance $|\Delta\vec{r}|$ away from the interface and parallel to it. Thus, $R(\vec{x},t)$ has the meaning of the distance function from the interface (Osher and Sethian, (1988)). In order to recognize a phase, the distance from the interface needs to be indicated by a sign, say, negative for the gas phase and positive for the liquid phase. Assuming this notation and a closed surface for the interface forming the boundary of a gas structure, all distances at the gaseous side will be negative. At time $t = 0$, the position of the interface is known, so it is the moment the initialization of the function $R(\vec{x},t)$ takes place. It lies in the choice of the lowest value of the distance between each point

in the domain and points on the interface, that allows to assess the position of the isospheres. Because of convection the interface changes its position in time, so the obvious consequence of that is updating the distribution of the distance function, which is the next step of the procedure. This operation is performed using (2.22).

The distance function constitutes the basis for evaluation of physical properties of the flow, which are in turn used in the set of governing equations. Values of the function $R(\vec{x},t)$ can be used as the argument in the Heaviside function such that

$$H(R)=\begin{cases} 0 & R(\vec{x},t)\in(-\infty,0) \\ 1 & R(\vec{x},t)\in(0,\infty)\,. \end{cases} \tag{2.26}$$

The distance function remains continuous in the entire domain, however, the argument of (2.26) provides the discontinuity of the Heaviside function at the interface. This feature makes (2.26) a very convenient tool for expressing a sudden jump of values of the physical properties at the interface. Hence, the physics of the interface is described correctly, nonetheless the mathematical model consisting of the equation set is not able to accommodate discontinuities. Consequently, an alternative solution has been employed (Sussman, Smereka and Osher, (1994); Sussman, Fatemi and Smereka, (1998)) which assigns a finite thickness to the interface. The thickness remains in proportional relation to the grid size used to discretize the computational space. Now the Heaviside function assumes the form of the $C^2$ function

$$H(R)=\begin{cases} 0 & R(\vec{x},t)\in(-\infty,-\varepsilon) \\ \frac{1}{2}\left[1+\frac{R}{\varepsilon}+\frac{1}{\pi}\sin\left(\frac{\pi R}{\varepsilon}\right)\right] & R(\vec{x},t)\in\langle-\varepsilon,\varepsilon\rangle \\ 1 & R(\vec{x},t)\in(\varepsilon,\infty)\,, \end{cases} \tag{2.27}$$

where $2\varepsilon$ denotes a measure for the thickness of the interface. This form of the function allows for a smooth transition of the property values through the phase boundary. Values are found using (2.23), with the adjusted version of the Heaviside function serving as the weighting factor $\phi$. When the governing equations together with (2.22) are solved, contours of $R(\vec{x},t)$ deform and depart from the parallel alignment with the interface. This provides nonuniformity in the physical properties of the phases. It follows from (2.27), that the thickness of the interface is $2\varepsilon/\left|\vec{\nabla}R\right|$. To keep the thickness uniform along the phase boundary the gradient of the level set function must satisfy the relation

$$\left|\vec{\nabla}R\right|=1. \tag{2.28}$$

The gradient of $R$ may depart from unity, thus function $R(\vec{x},t)$ needs to be re-initialized. The process of re-initialization is considered out of the scope of this work and it will not be discussed any further.

### 2.4.2 Embedded interface method

The Level-Set Method introduces an interface thickness of the dimension of the grid size, so the finer the mesh the lower the level of diffusion of the phase boundary and the better the description of the real nature of the jump in the fluid properties. However, the mathematical model still features this smooth transition. In the literature there are methods of exact interface positioning with simultaneous conservation of the diffusion of the physical properties. An example of this approach is the embedded interface method mainly developed by Tryggvason (Unverdi and Tryggvason, (1992); Tryggvason, Bunner, Esmaeeli, Juric, Al-Rawahi, Tauber, Han, Nas and Jan, (2001)). The method is a hybrid method. It couples an interface tracking and an interface capturing method. The single set of equations of motion is used for all phases employing a fixed grid in the computational domain. Then a mesh of finer resolution is utilized in order to track the convected interface. This grid moves with the phase boundary and its resolution adjusts dependent on the complexity of the geometry of the interface.

Similarly to the Level-Set Method the phases are distinguished through the Heaviside function given by (2.26), which values are computed in the whole domain by transport equation (2.22). The interface is described by a moving subgrid consisting of triangular elements describing surface $S_{ki}$, or in a case of a two-dimensional scheme consisting of segments. Each element stores information about its corner or vertex points and adjacent elements, see Fig.(2.5). Elements of the front are oriented and those representing a given interface must have the same orientation. Every oper-

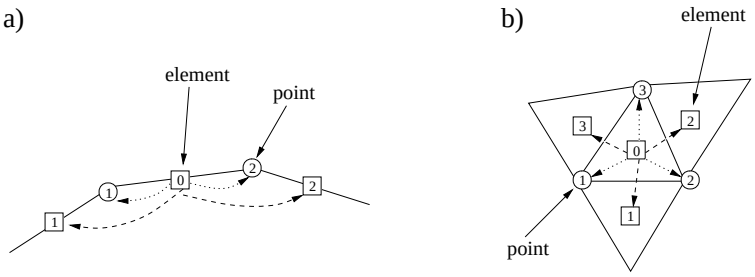


FIGURE 2.5: *Structure of the front; a) two-dimensional scheme, b) three-dimensional scheme; dashed line - pointer to adjacent element, dotted line - pointer to a corner/end point. Figure reproduced from (Banerjee, Hewitt, Zaleski, Tryggvason, Koumoutsakos, Yadigaroglu and Ishii, (2004)).*

ation carried out on the front begin from the first numbered object (element) and then through stored pointers to the others it propagates until all objects have been visited.

Once the interface moves it deforms changing its geometry. Consequently, the

initial number of elements may not be sufficient to reflect properly the shape of the front. Therefore the discretization of the interface is adapted to reflect the complexity of its shape. The surface grid is adapted separately from the fixed volumetric grid in such a way that the interface has a sufficient fine discretization.

Since the governing equations result in the distribution of the velocity in the domain the interface is advanced as an effect of the new time-progressed velocity field. The central challenge in this step of the model is to find the velocity at points of the interface. This is achieved by interpolation of velocities from nodes of the fixed volumetric grid at the points of the interface. Once the interpolated velocity has been found a new position of the point on the interface is obtained by integration. The integration may be performed in the simple way

$$\Delta r_{ki_{i,j,k}} = \int u_{ki_{i,j,k}} dt, \tag{2.29}$$

where $\Delta r_{ki_{i,j,k}}$ denotes the distance, which the convected interface node covers in time $dt$. The advection of the front is performed, unlike the momentum equation, in a nonconservative form, that may result in an error. This error corresponds to an artificial sink or source of mass. Thus the accuracy of the front convection is the crucial issue of the approach. It may be improved by employing a higher-order temporal integration. Another source of error is the interpolation procedure. Even if the velocities at the fixed volumetric grid points are, for an incompressible flow, divergence free, this may not be the case for interpolated velocities at the front. Thus, a higher order interpolation could alleviate this problem.

Once the front is reconstructed it is also desirable to convert quantities at points on the front to volume grid nodes neighbouring those on the interface. Often a smoothing procedure must be performed in order to smear out the flow properties discontinuity and make their distribution tractable for the governing equations. The front represents the Dirac delta function, $\delta$, consequently the procedure uses an approximation of this function on the volume grid. This creates a smooth transfer of quantities. The quantities such as phasic difference of density or heat conductivity gradient are usually of dimension unit per unit length or area for a two or three dimensional system, respectively. The global value of a quantity will be assured if the following equation is satisfied

$$\int_{S_{ki}} \Delta\gamma_{S_{ki}} dS = \int_{\Omega} \Delta\gamma_{\Omega} d\Omega, \tag{2.30}$$

where $\Delta\gamma$ denotes a phasic difference of a quantity. Its volume and surface character is denoted by $\Omega$ and $S_{ki}$ subscripts, respectively. Averaging expression (2.30) leads to the value of the fixed volume grid quantity

$$\overline{\Delta\gamma}_{\Omega} = \sum_{i=1}^{i=n} \overline{\Delta\gamma}_{S_{ki}} \phi \frac{S_{ki}}{\Omega}, \tag{2.31}$$

where $n$ denotes the number of interface elements contained in the control volume, whereas $\phi$ denotes the weighting factor. The factor satisfies the condition

$$\sum_{P}^{N} \phi_{P_{i,j,k}} = 1 \tag{2.32}$$

for each direction of interpolation. The form of the interpolation function depends on the number of volume grid points involved. However, the weighting function consists very often of the product of one dimensional functions such that

$$\phi_{i,j,k} = \phi_i \phi_j \phi_k, \tag{2.33}$$

where $i, j, k$ indicate each individual direction of interpolation. The simplest weighting function for a direction reads

$$\phi_i = \begin{cases} \frac{|\Delta r|_{PN_i} - |\Delta r|_{S_{ki_i}}}{|\Delta r|_{PN_i}} & \Delta r_{S_{ki_i}} \in \langle 0, \Delta r_{PN_i}) \\ \frac{|\Delta r|_{PN_i} - \left(|\Delta r|_{PN_i} - |\Delta r|_{S_{ki_i}}\right)}{|\Delta r|_{PN_i}} & \Delta r_{S_{ki_i}} \in (-\Delta r_{PN_i}, 0\rangle \\ 0 & |\Delta r|_{S_{ki_i}} \geq |\Delta r|_{PN_i}, \end{cases} \tag{2.34}$$

where $|\Delta r|_{PN_i}$ denotes the distance between nodes of the fixed volume grid in the $i$ direction and $|\Delta r|_{S_{ki_i}}$ is the distance from a front node to the considered point of the volume grid. The distances on both sides of the interface may be regarded as the distance function $R$ discussed in the preceding paragraph, thus they assume opposite signs, that allows for proper evaluation of physical property differences.

Summarizing the above approach, it is applicable to problems in which clearly separated phasic structures occur in the surrounding bulk of another phase. An example of this case is the bubbly flow in which separated structures are convected by the bulk of the liquid, while coalescence and break-up appear in the process. Nonetheless, for flows where e.g. bubbly patches containing a large number of interacting gaseous phases appear, this approach is not feasible due to the costs of the interface reconstruction. The method next to be discussed, termed Volume of Fluid (VOF) appears to be a better choice for these flows.

### 2.4.3 Volume of Fluid method

The Volume of Fluid approach is based on the steep function indicating that there is more than one phase in a given control volume. The function is defined such that it assumes values of unity for one phase occupying the volume and zero otherwise. Consequently, it is clear that a phase distribution may also be defined by the Heaviside function given by (2.26). In the Eulerian representation, that is considered here, the grid remains fixed and the flow is convected through the fixed control volume

boundaries. The calculation of the flow requires averaging of flow parameters over fluid elements, which is done for a given control volume. The disadvantage of this procedure is the tendency of smoothing of all gradients in the flow quantities. This applies also to the discontinuity of the physical properties across the interface. Thus the interface itself loses its sharpness, being smeared out in space. The averaging operation allows the use of the partial-differential equation form of the governing equations. Consequently, the Heaviside function also requires smoothing. For the VOF method, the Heaviside function assumes the form

$$H\left(x_{l,m,n}\right) = \begin{cases} 0 & k = 0 \\ \frac{\Omega_k}{\Omega} & k \in (0,1) \\ 1 & k = 1, \end{cases} \tag{2.35}$$

where $x_{l,m,n}$ denotes a point in the domain identified by the coordinates $l, m, n$ of the mesh and $k$ denotes a given phase. Equation (2.35) reveals that the Heaviside function may be represented by the volume fraction given by (2.10). The volume fraction, or the so-called void fraction if one considers a gas-liquid flow, assumes values of $0$ and $1$ for opposite phases and values in between these two for the interfacial region. The field of the volume fraction is convected with the velocity field and obeys transport equation (2.22), repeated here in terms of the volume fraction and with the absence of volumetric effects, e.g. phase transition

$$\frac{\partial \alpha_k}{\partial t} + \vec{\nabla}.\left(\alpha_k \vec{u}\right) = 0. \tag{2.36}$$

The transport equation is solved along with the governing equations and results in a distribution of $\alpha$ which reveals the interface of a certain finite thickness which is not necessarily of the dimension of the grid size. The diffusion of the phasic boundary may exceed the mesh size particularly in regions of high complexity of the interface. Since such smooth transition of flow parameters is not desirable, the scheme needs to be improved. In order to do this some algorithms have been proposed. The step character of the Heaviside function allows using models approaching its discontinuous character. These methods, referred to as donor-acceptor schemes, rely essentially on an appropriate manner of approximation of the convective term present in (2.36) at control volume boundaries (Hirt and Nichols, (1981); Leonard, (1997); Leonard, (1979)). The algorithms require a higher order interpolation of variables at the control volume face, incorporating parameters permitting treatment of the unsteady nature of the flow. It is not intended to review the variety of interpolation models, however, those that have been used in the present research, namely ULTIMATE, QUICKEST and CICSAM, will be described in detail in Chapter (6).

Since the velocity field in the domain has been evaluated, advection of phasic regions needs to be carried out. This operation is performed in two ways. The first, the so-called split operator or fractional step method updates an $\alpha$ field propagating the

variable along each spatial direction in time. This is done separately, thus estimation of an $\alpha$ distribution along one direction results in intermediate alpha values. The process is accomplished when advection along the last coordinate is performed, which gives the final $\alpha$ field. In most cases the convection process is commutative from the point of view of the choice of direction. The detailed explanation of the procedure will be given in Chapter (5). The other group of advection algorithms is the group of unsplit methods (Collea, (1990); Bell, Dawson and Shubin, (1988); Pukett, Almgren, Bell, Marcus and Rider, (1997)). These methods are geometrically complex since they require employment of fluxes along the transverse directions of the control volume. The description of these algorithms is beyond the scope of the present study.

Once the distribution of the volume fraction at a certain time has been obtained one needs to evaluate the physical properties of the phasic flow. The volume fraction plays the role of the weighting factor and contributes in (2.23), which is repeated below in terms of $\alpha$

$$\gamma = \alpha_k \gamma_k + (1 - \alpha_k)\, \gamma_{k+1}, \tag{2.37}$$

where $\gamma$ denotes a given physical property.

The Heaviside function in the form of the volume fraction distributed in the domain gives the base for attempts of interface reconstruction. The phase boundary is considered as a continuous line (2D) or surface (3D) deforming in space during convection. The central difficulty in the reconstruction process lies in the approximation of the position of each section of the interface in the considered control volume, knowing only values of the volume fraction therein and in control volumes in its neighborhood. The simplest type of these methods is the Simple Line Interface Calculation (SLIC) or SOLA-VOF (Hirt and Nichols, (1981)). The reconstruction is relatively crude and outlines the phase boundary as the assembly of segments aligned with grid faces, see Fig.(2.6). Advection of the interface generates a number of spurious regions of phase $k$ detached from the bulk of phase $k$. The improved algorithm is given by the Piecewise Linear Interface Construction (PLIC) (Scradovelli and Zaleski, (2001); Scradovelli and Zaleski, (2003); Rider and Kothe, (1998)), in which the interface is visualized as a chain of discontinuous segments with finite discontinuities, Fig.(2.6), which disappear when the radius of interface curvature assumes larger and larger values.
The effort of reconstruction has not been taken in the present study, thus the subject will not be discussed any further.

In general, the Volume of Fluid approach preserves mass in a natural way due to the advection algorithm which utilizes the conservation law in the form of (2.36). The entire scheme is local from the point of view of convection. Solely values of $\alpha$ in adjacent control volumes are necessary in order to perform the procedure of advection. However, the number of volumes being used depends on the chosen order of interpolation. Results of computations utilizing VOF and generating the motion of

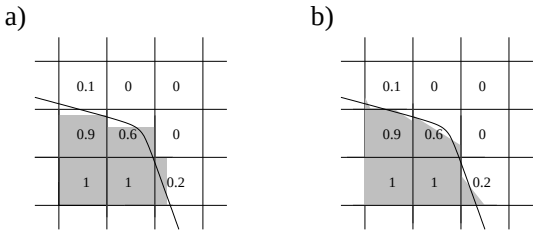


FIGURE 2.6: *Reconstruction algorithms results; a) SLIC, b) PLIC. Figure reproduced from (Banerjee, Hewitt, Zaleski, Tryggvason, Koumoutsakos, Yadigaroglu and Ishii, (2004)).*

interface will be described in the following chapters.

# PHYSICS OF GAS-LIQUID PHASE TRANSITION

CHAPTER 3

## 3.1 p-v-T relation

In this chapter thermodynamic relations are reviewed, that play a role in multi-phase flows with phase transition. The discussion is kept general, in the sense that the fluids are assumed to be compressible. However, in the rest of the thesis it is assumed that the gas and liquid phases are incompressible.

Each pure substance may be described by thermodynamic variables that determine its thermodynamic state. The primitive, basic variables are the pressure, $p$, temperature, $T$, and volume, $v$ or $V$, occupied by the substance. The volume may be given in the extensive or intensive form. The extensive form, $V$, depends on the system size. The intensive form, $v$, is the variable related to a unit of mass, thus is a system size independent quantity.

The above three quantities are linked to each other by the equation of state which, for example, for a perfect gas assumes the form

$$pv = RT, \tag{3.1}$$

where $R$ represents the specific gas constant and $v$ is the specific volume. Real gases behave as perfect gases at not too high temperatures, pressures and densities (dilute gases in which intermolecular forces are negligible). At higher pressures and densities the ratio between the right and left side of (3.1) departs from unity and its deviation is expressed by the compressibility factor $Z$, i.e.

$$Z = \frac{pv}{RT}. \tag{3.2}$$

Based on kinetic theory the viral equation of state has been derived, which assumes the form of a series in the reciprocal of the specific volume

$$Z\left(T, s\right) = 1 + \frac{B}{v} + \frac{C}{v^2} + \frac{D}{v^3}, \tag{3.3}$$

where $B$, $C$, $D$ denote functions of temperature and are named the first, second an third viral coefficient, respectively, which represent interactions between gas particles

on the molecular level. Obviously, once a gas particle is assumed to behave independently on its surrounding, thus when one considers a perfect gas, the right hand side of (3.3) reduces to 1. The determination of the viral coefficients requires information about the intermolecular forces between particles. Models for these forces have been applied successfully for the two or three first factors and for gases of a relatively simple molecular structure (Kandlikar, Shoij and Dhir, (1999)).

Other attempts of obtaining an appropriate equation of state for real gases involve semi-empirical relations, such as proposed by van der Waals (van der Waals, 1873)

$$p = \frac{RT}{v-b} - \frac{a}{v^2}, \tag{3.4}$$

where $b$ denotes the constant accounting for the finite volume occupied by the gas molecules, whereas $a/v^2$ represents attraction forces present between the molecules. Equation (3.4) has been further modified by other researchers, that has led to the two models which are considered as the best amongst those containing two constants, namely

$$p = \frac{RT}{v-b} - \frac{a}{v\,(v+b)\,T^{0.5}} \tag{3.5}$$

and

$$p = \frac{RT}{v-b} - \frac{a}{v^2+2bv-b^2} \tag{3.6}$$

These two relations were proposed by Redlich and Kwong (Redlich and Kwong, (1949)) and Peng and Robinson (Peng and Robinson, (1976)), respectively. These or similar equations are often used as basis for mixture $p$-$v$-$T$ relationships, from which equilibrium diagrams have been determined with reasonable success (Kandlikar et al., (1999)).

At present there is no equation of state, covering the full range of the variables involved, that reflects the nature of a pure substance. Consequently, the equation must be adopted for each state of aggregation and for the regions of coexistence in which two or three phases remain in equilibrium. Fitting the constants present in the equation of state is usually carried out by employing empirical data. The graphical representation of the equation of state is a surface in the space defined by coordinates each assigned to the three primitive variables. Such a graph is given in Fig.(3.1) where relations for two pure substances have been plotted. One of them contracts during solidification, whereas the second expands; this may be, for example, water. In Fig.(3.1) one can distinguish three regions of coexistence, namely liquid-vapour, vapour-solid and solid-liquid. These surfaces are separated by two important isotherms: the triple point temperature and the critical temperature isotherm. The triple point isotherm indicates the thermodynamic condition allowing simultaneous existence of the three phases in thermodynamic balance. The critical point isotherm is the isotherm above which there is no observable difference between the liquid and the vapour phase. At

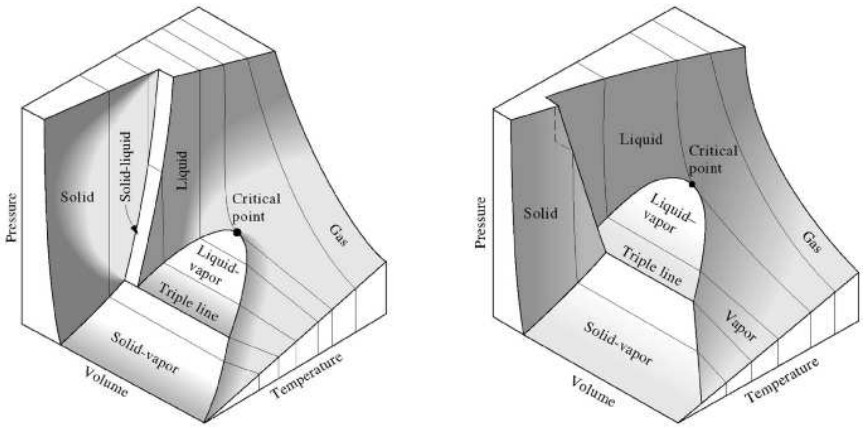


FIGURE 3.1: *p-v-T surfaces; a) substance contracting during solidification, b) substance expanding during solidification. Figure taken from (http://highered.mcgraw-hill.com, n.d.).*

such conditions one cannot observe a sudden jump in volume or specific volume due to evaporation or condensation. The increase of volume with decreasing pressure is monotonic. The critical isotherm passes through the point of inflection of the curve limiting the region of liquid-vapour coexistence. The point called critical determines where the slope of the curve and its derivative is zero i.e.

$$\left(\frac{\partial p}{\partial v}\right)_{T_c} = 0, \qquad \left(\frac{\partial^2 p}{\partial v^2}\right)_{T_c} = 0. \tag{3.7}$$

With the definition of the critical point one is able to express the constants $a$ and $b$ of the van der Waals relation, (3.4), which become

$$a = \frac{9RT_c v_c}{8}, \qquad b = \frac{v_c}{3}, \tag{3.8}$$

where the subscript $c$ indicates the critical condition. With $P_c = 3RT_c/8v_c$, substitution of the constants in (3.4) yields the equation of van der Waals in terms of reduced variables

$$p_r = \frac{8T_r}{3v_r - 1} - \frac{3}{v_r^2}, \tag{3.9}$$

where $r$ is the subscript denoting a reduced variable expressed by

$$\frac{\phi}{\phi_c}, \tag{3.10}$$

with $\phi$ indicating any primitive thermodynamic quantity. The pressure, specific volume and temperature for water in the critical state read (Schmidt, (1982))

$$p_c = 221.2[bar], \quad v_c = 0.00317[m^3/kg], \quad T_c = 674.30[K].$$

These values define the constants in the van der Waals relation, (3.4), for water, namely

$$a = 1109.83[Jm^3/kg^2] \quad b = 0.00106[m^3/kg].$$

## 3.2 Two-phase equilibrium

Generally, the definition of a system isolated from its surroundings and being in thermodynamic equilibrium states that all forces in the system must be balanced and that the temperature is uniform. These conditions exist on the $p$-$v$-$T$ surface which, for convenience and clearness, is projected on the $p$-$v$ plane, see Fig.(3.2). The region of the gas-liquid equilibrium is depicted by the limiting (saturation) curve with its maximum at the critical point. Isotherms for a temperature below the critical value are monotonic for the parts not inside the envelope of the saturation curve. At the saturation curve, however, there is a discontinuity in the slope, such that inside the envelope isotherms are lines $p = const.$ Below the critical value, on the left side of the saturation curve, one finds subcooled liquid. The region to the right of the saturation curve is the vapour region. The projection of the $p$-$v$-$T$ surface onto the

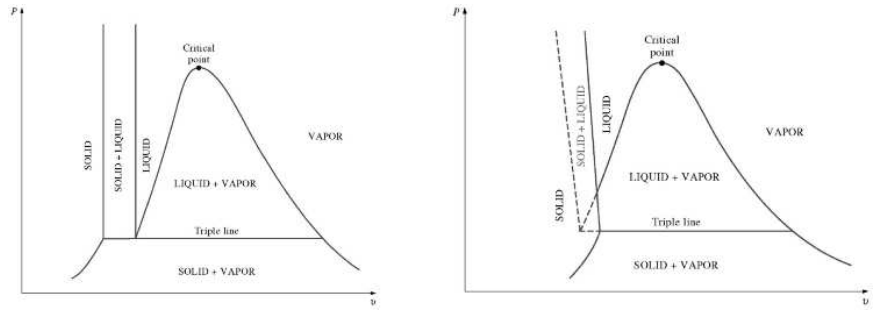


FIGURE 3.2: *p-v diagram; a) substance contracting during freezing, b) substance expanding during freezing. Figure taken from (http://highered.mcgraw-hill.com, n.d.).*

$p$-$T$ plane, Fig.(3.3), shows that the saturation curve terminates at the left at the triple point and at the right at the critical point. The area between the saturation curve and the 'melting' curve, represents the liquid phase, whereas a vapour appears below the saturation curve. The equilibrium conditions allowing for coexistence of the gas and liquid phases, exist only at the saturation curve.

Equilibrium of the system may be also determined by a function of state, e.g. the Gibbs function defined as

$$G = H - TS, \tag{3.11}$$

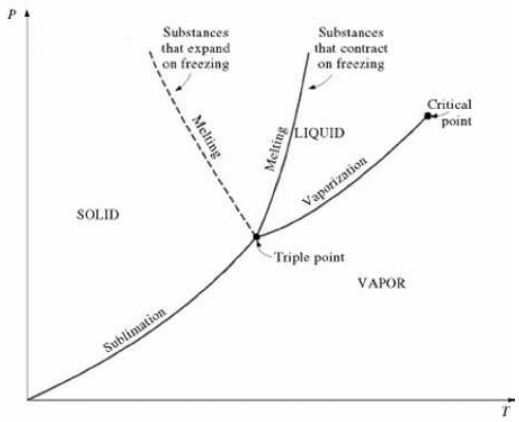


FIGURE 3.3: *p-T diagram. Figure taken from (http://highered.mcgraw-hill.com, n.d.).*

where $H$ denotes enthalpy $[J]$, $S$ entropy [J/K] and $T$ absolute temperature [K]. In the state of equilibrium $G$ is constant, i.e.

$$\delta G_{p,T} = 0. \tag{3.12}$$

In a system of a pure substance where the gas and the liquid phases are present the Gibbs function depends, aside from temperature and pressure, also on the amount of phases present. Thus any change in $G$ is determined by

$$\delta G = \left(\frac{\partial G}{\partial T}\right)_{p,n} \delta T + \left(\frac{\partial G}{\partial p}\right)_{T,n} \delta p + \left(\frac{\partial G}{\partial n_l}\right)_{T,p,n_g} \delta n_l + \left(\frac{\partial G}{\partial n_g}\right)_{T,p,n_l} \delta n_g = 0, \tag{3.13}$$

where the notation $n_l$ and $n_g$ indicate a molar or mass amount of the liquid and the gas in the system, respectively. Since the pressure and temperature are constant and assuming a closed system in which $n = n_l + n_g$ is constant, (3.13) can be reduced to the form

$$\delta G_{p,T} = \left(\frac{\partial G}{\partial n_l}\right)_{T,p,n_g} \delta n_l + \left(\frac{\partial G}{\partial n_g}\right)_{T,p,n_l} \delta n_g. \tag{3.14}$$

Assuming an equilibrium state the left hand side of (3.14), accordingly (3.12), is zero. Consequently, with $\delta n = \delta n_g + \delta n_l = 0$, one finds

$$\left(\frac{\partial G}{\partial n_l}\right)_{T,p,n_g} = -\left(\frac{\partial G}{\partial n_g}\right)_{T,p,n_l}. \tag{3.15}$$

Statement (3.15) reveals the macroscopic nature of an equilibrium state, which does not provide observable changes of system parameters. It does not apply to a microscopic scale for which the phase transition occurs but its rate in both directions is the same, thus the amount of a given phase remains unchanged.

At the state of equilibrium the change in the Gibbs energy of the liquid equals that of the vapour, so that

$$\delta g_l\left(p,T\right)=\delta g_g\left(p,T\right), \tag{3.16}$$

where $g$ is the intensive form of $G$. Taking $g$ as a function of $T$ and $p$ leads to a relation between $p$ and $T$, i.e.

$$\left(\frac{\partial g_l}{\partial p}\right)_T dp+\left(\frac{\partial g_l}{\partial T}\right)_p dT=\left(\frac{\partial g_g}{\partial p}\right)_T dp+\left(\frac{\partial g_g}{\partial T}\right)_p dT. \tag{3.17}$$

Using the definition of internal energy and enthalpy, the increment in the Gibbs free energy in its intensive variable form may be expressed in the form

$$dg=vdp-sdT, \tag{3.18}$$

where $s$ denotes entropy in the form of an intensive variable. Taking $g$ as a function of $(T,p)$ one obtains

$$\left(\frac{\partial g}{\partial p}\right)_T=v, \qquad \left(\frac{\partial g}{\partial T}\right)_p=-s. \tag{3.19}$$

Substitution of (3.19) in (3.17) yields

$$-s_l+v_l\left(\frac{dp}{dT}\right)=-s_g+v_g\left(\frac{dp}{dT}\right). \tag{3.20}$$

According to (3.12)

$$h_l-Ts_l=h_g-Ts_g, \tag{3.21}$$

where $h$ denotes the intensive form of the enthalpy. Rearrangement and combination of (3.20) and (3.21) results in

$$\frac{dp}{dT}=\frac{h_g-h_l}{T\left(v_g-v_l\right)}=\frac{l}{T\left(v_g-v_l\right)} \tag{3.22}$$

which is known as the Clapeyron equation and relates the pressure and temperature at a state of equilibrium with the specific heat of vaporisation $l$ and the specific volumes of the two phases. In case the system is subjected to not too high pressures the gas may be regarded as perfect and its specific volume equals $RT/p$. Furthermore in that case the specific volume of the liquid, $v_l$, is negligible in comparison to that of the gas. Then relation (3.22) reduces to

$$\frac{d\,ln\left(p\right)}{dT}=\frac{l}{R_gT^2} \tag{3.23}$$

known as the Clausius-Clapeyron equation (Kandlikar et al., (1999)). The above equation is the base for the consideration leading to the relation for the latent heat of evaporation of water as a function of temperature,

$$\frac{l\,(T)}{l\,(T_{ref})} = 1+\hat{A}_1\left(\frac{T}{T_{ref}}\right)+\hat{A}_2\left(\frac{T}{T_{ref}}\right)^2+\hat{A}_3\left(\frac{T}{T_{ref}}\right)^3+\hat{A}_4\left(\frac{T}{T_{ref}}\right)^4+\hat{A}_5\left(\frac{T}{T_{ref}}\right)^5, \tag{3.24}$$

which will be used in the further part of this work. The dimensionless constants in (3.24) originate from

$$\hat{A}_i = \frac{A_i (T_{ref})^i}{l(T_{ref})}, \tag{3.25}$$

with following $A_i$ dimensional constants:

$$\begin{aligned} A_5 &= -3.320494\,E-07, & A_2 &= 6.487444\,E-04,\\ A_4 &= -5.184260\,E-01, & A_1 &= 2.068768\,E+02,\\ A_3 &= -4.313656\,E+04, & l(T_{ref}) &= 6.308721\,E+03. \end{aligned}$$

Relation (3.24) remains in good agreement with the distribution of the latent heat as measured (Schmidt, (1982)), see Fig.(3.4).

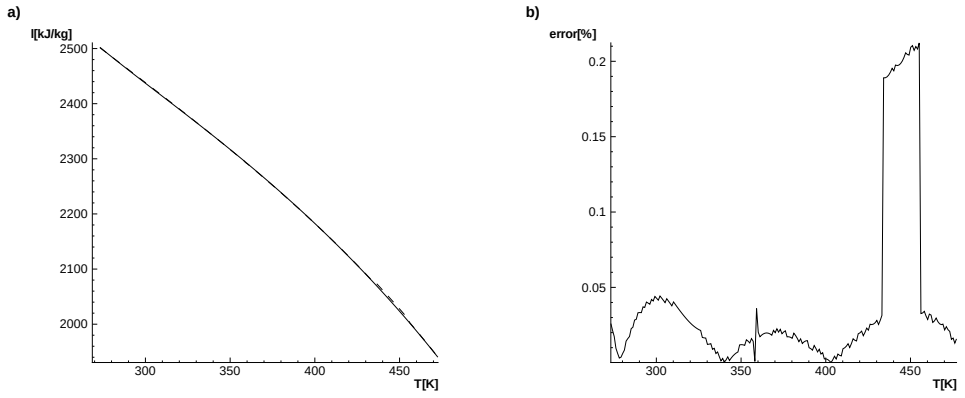


FIGURE 3.4: *a) heat of evaporation for water as function of temperature: solid line - relation (3.24), dashed line - experimental relation (Schmidt,(1982)); b) relative error between experimental and approximate function.*

In order to determine the equilibrium state of a gas-liquid mixture of a pure substance the equation relating the pressure and temperature of saturation is required.

Many efforts have been taken to find a reliable formula, which would be valid for a range of temperatures as wide as possible. The Clausius-Clapeyron equation, (3.23), yields, under the assumption of constant latent heat in a given range of temperatures,

$$ln\,(p) = A - \frac{l}{R_g T}, \tag{3.26}$$

where $A$ is a constant. Equation (3.26) implicates that the pressure-temperature relation is a straight line over the range of temperatures where the heat of vaporization remains constant. Consequently, relation (3.26) may assume the form

$$ln\,(p) = A - \frac{B}{T}, \tag{3.27}$$

where $B$ is the latent heat at a given temperature. Equation (3.27) can be derived from the Clausius-Clapeyron equation, (3.23), by integration. In the present method the result is truncated to the form (3.27). The accuracy of (3.27) suffices for the purpose of this study. For the normal boiling point, taken as the reference value, constants $A$ and $B$ assume values

$$A = 24.9015726[ln(N/m^2)], \quad B = 4991.043497[ln(N/m^2)K],$$

where $A$ and $B$ are temperature independent. Comparison of the measured distribution and relation (3.27) is depicted in Fig.(3.5), in the form of $T = T(p)$.

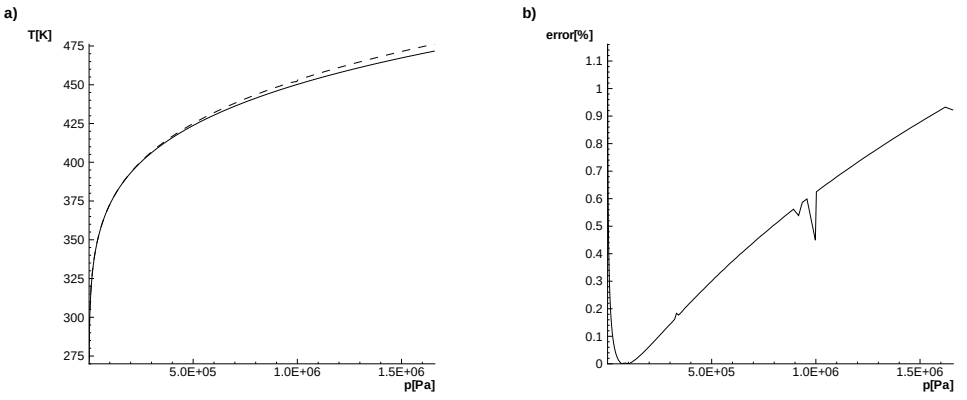


FIGURE 3.5: *a) saturation curve: solid line - relation (3.27), dashed line - experimental data (Schmidt,(1982)); b) relative error between experimental data and relation (3.27).*

For many purposes more accurate data of thermodynamic variables are required and

formula (3.27) does not suffice. A more satisfactory relation has been proposed by Antoine (Antoine, (1888)):

$$ln\,(p) = A - \frac{B}{T+C}. \tag{3.28}$$

In (3.28) $A$, $B$ and $C$ are constants. For a wider range of temperatures or pressures and for demanded high accuracy, it is difficult if not impossible to fit data on experimental saturation values utilizing a relatively simple formula such as that of Antoine. One of the equations satisfying this requirement is

$$ln\,(p) = A - \frac{B}{T+C} + DT + E\,ln\,(T)\,, \tag{3.29}$$

where $A$, $B$, $C$, $D$ and $E$ are constants (Kandlikar et al., (1999)).

Summarizing, the approximate relation for the saturation pressure, all involve empiricism and non of them has a thermodynamic basis that would ensure appropriate values of the constants present in the relations.

In the situation discussed so far, the gas-liquid interface is ideally flat thus there are no additional forces contributing to the mechanical balance that ensures a state of equilibrium of the system. However, many cases of two-phase flow concern curved interfaces. Taking into account surface tension in a two-phase flow, the mechanical balance at the interface reads

$$p_g = p_l + \frac{2\sigma}{r}, \tag{3.30}$$

where $\sigma[N/m]$ denotes the surface tension and $r$ is the radius of the curvature of the interface, e.g. a vapour bubble submerged in a liquid. Suppose that the pressure and the temperature of saturation for flat interfaces is the point $c$ in Fig.(3.6).
The temperature of saturation is associated with vapour pressure $p_g$, however, this pressure is lower than the pressure of saturation for the flat interface, $p_{sat}$; the $p_g$ isobar meets the $T_{sat}$ isotherm at point $b$. Condition of phasic equilibrium demands uniformity of the temperature and equality of the Gibbs energy, see (3.12) and (3.15), consequently the difference between the pressure of the vapour in the bubble and that in the surrounding liquid is the vertical line of constant $g$ from point $b$ to $a$. However, due to the equilibrium condition of uniform temperature, pressure $p_{sat_l}$ is associated with temperature $T_{sat}$, but not with temperature $T_{sat_l}$ which would be the temperature of saturation in case of a flat interface and pressure $p_{sat_l}$. It is concluded that the system contains a superheated liquid and although the temperature is higher than that of the saturation state for the liquid, a phase transition is not observed. This situation is referred to as the metastable state. It is also possible to show points $a$, $b$ and $c$ in a $p - v$ plot, see Fig.(3.7). This figure shows isotherm $T_{sat_l}$ which is divided in segments. Segment $AB$ indicates subcooled liquid which without interface curvature evaporates at point $B$ and becomes a pure vapour at point $E$. Further decrease of

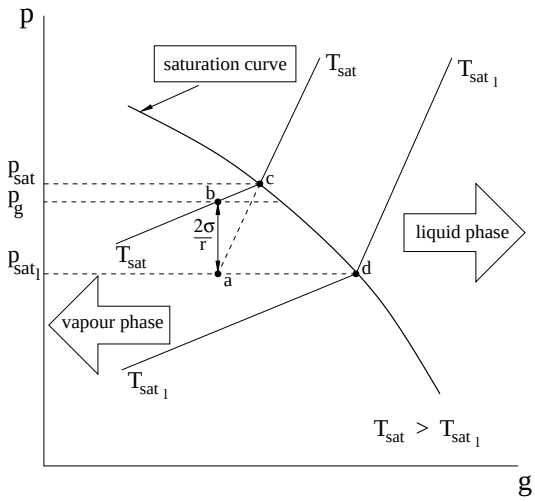


FIGURE 3.6: *Equilibrium diagram of pressure, p, as function of Gibbs free energy, g, for a gaseous bubble submerged in a liquid.*

pressure causes a rise of the specific volume of the vapour and finally one reaches point $F$. Nevertheless, as shown above, it is possible to superheat a liquid above the temperature of saturation without phase transition, i.e. it is given by segment $BC$. Metastable state is also possible for the vapour once its specific volume is decreased along $DE$. Any thermodynamic process occurring along segment $BC$ as well as $DE$ is accessible because it does not violate the stability criterion, $(\partial p/\partial v)_T \leq 0$, which is indispensable from the point of view of mechanical stability of the condensation and evaporation process. It is not the case for segment $CD$ for which the stability rule is violated and $(\partial p/\partial v)_T$ becomes positive.

The curve connecting point $C$, the critical point, and $D$, that bounds the metastable regime, is termed the liquid spinodal and vapour spinodal at the left and right side of the critical point, respectively.

## 3.3 Non-equilibrium state

Phase transition begins when the thermodynamic condition passes the saturation envelope depicted in Fig.(3.2) and Fig(3.7). The first step of the process occurs when the excess of the temperature over the temperature of saturation is large enough to reduce the nucleation barrier, which is the starting point of nucleation. Nucleation relies on the clustering of substance molecules on micro-size objects suspended in the bulk of the substance. This process is named heterogeneous nucleation. The other known way of the nucleation process is termed homogeneous nucleation, which is the spontaneous condensation of molecules, that creates phasic clusters. Existence

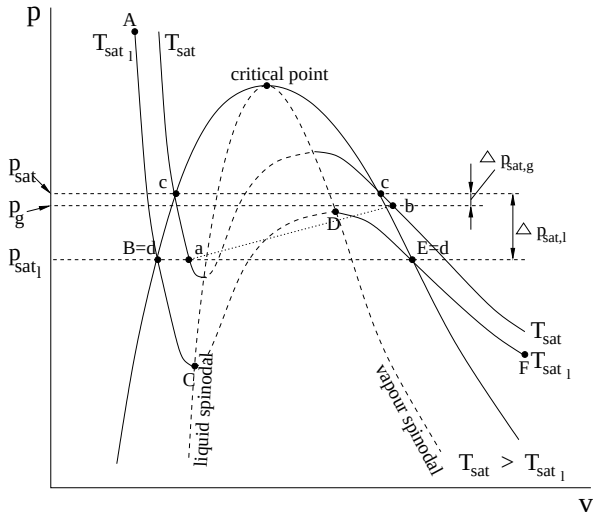


FIGURE 3.7: *p-v graph illustrating metastable state of a pure substance.*

of these clusters in a system provides a metastable state described in the preceding section. Any change of thermodynamic conditions in the direction in which the phase transition is favourable invokes this process immediately. Then the transition occurs until the moment of a new thermodynamic balance in which phasic clusters play the role of aggregation nuclei. The two types of nucleation may occur simultaneously in the same system. The dominance of the nucleation of one type is a matter of concentration of nuclei in the bulk of a substance. It may happen that in real-life fluids with impurities, phase transition originating from homogeneous nucleation dominates due to the higher concentration of nuclei generated by homogeneous nucleation compared to the concentration of impurities. The time scale of homogeneous or heterogeneous phase transition differs. The homogeneous one, once it occurs, is much faster than the heterogeneous phase change, thus effects of homogeneous nucleation dominate in very fast processes.

Assuming a constant pressure of the system in which the liquid is expected to undergo boiling, the required difference between the temperature of the superheated liquid and the temperature of saturation, necessary to form a cluster, is given by

$$T - T_{sat_l} = \frac{2\sigma}{r} \frac{T_{sat_l} \left(v_g - v_l\right)}{l}, \tag{3.31}$$

where $r$ denotes the cluster radius. The equation has been derived from the Clapeyron equation, (3.22), with the assumption that the pressure of a foreign gas can be neglected (Banerjee, Hewitt, Zaleski, Tryggvason, Koumoutsakos, Yadigaroglu and Ishii, (2004)). The temperature difference is shown in Fig.(3.8), where experimental results and the van der Waals prediction, (3.4), are depicted. At a temperature within

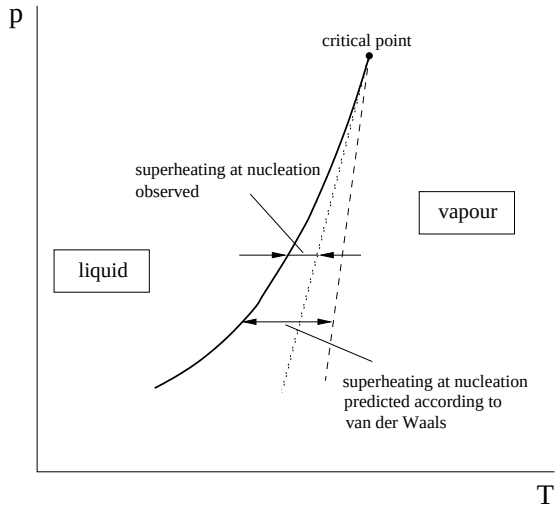


FIGURE 3.8: *Superheating: liquid temperature higher than temperature of saturation; solid line - saturation curve, dotted line - experimental data (Volmer, (1939)), dashed line - van der Waals equation (3.4).*

the range of the metastable state, given by (3.31), any increment of the system heat would bring about growth of the gaseous cluster, or otherwise, its collapse.

One can distinguish two types of nucleation, namely in the bulk and at the surface. For a pure liquid, the bulk nucleation is a homogeneous process due to the low number of foreign bodies suspended in the bulk of the substance. In this sense *pure* indicates that the number of foreign bodies suspended in the bulk of the liquid is considerably smaller than required for the heterogenous nucleation. An absolutely pure substance is technically difficult to produce, if it is possible at all. Considering the homogeneity of the process the superheating temperature, at which the process begins, is higher than in the case of surface nucleation. This is also the reason of the rather explosive nature of homogeneous bulk nucleation. In practice it occurs as the effect of a sudden pressure change e.g. in nozzles or in the case of a shock wave; it is also observable during heating up a liquid in a microwave oven. Surface nucleation is a process of great importance in practice because it forms the foundation for the theory describing the most common boiling mechanism. This kind of phase transition occurs on a heated surface and begins in tiny cavities which are present in a surface even if it is regarded as smooth. Cavities usually trap a foreign, non-condensable gas at their bottom. This gas acts as a site of nucleation. The initial radius of the foreign gas is regarded as that of the nucleation cluster. Thus, neglecting the pressure of this gas, the superheating temperature necessary for the beginning of the process of nucleation is given by (3.31). An example of such a situation is shown in Fig.(3.9). The presence of the initial nucleus constitutes the metastable state and if the temperature

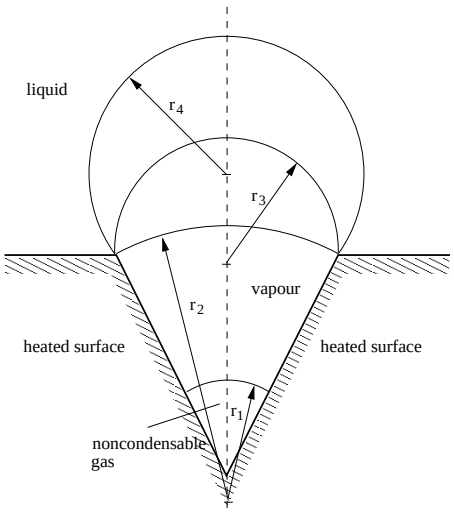


FIGURE 3.9: *Stages of vapour bubble growth in a cavity of a superheated surface. Figure reproduced from (Banerjee, Hewitt, Zaleski, Tryggvason, Koumoutsakos, Yadigaroglu and Ishii, (2004)).*

of the liquid layer above the initial gaseous structure inside the cavity exceeds the saturation threshold, the bubble will increase in size up to the moment of its detachment from the surface.

From the point of view of the behaviour of an industrial system and its prediction, it is essential to be able to predict the amount of a substance phase that is generated as the effect of the gas-liquid phase transition. Initial data for this are thermodynamic conditions of the system and the thermodynamic requirements necessary for carrying out the phase transition process. The basic assumption that simplifies the process is neglecting the surface tension effects. Consequently, one also drops the contributing surface tension which causes the phase transition to be limited by the saturation line but not by the gas-liquid spinodal. In the $p - v$ plane, Fig.(3.7), a transition of this kind is depicted by the isothermal, and simultaneously isobaric, line between points $B$ and $E$. Therefore a metastable state is not considered.

First the amount of heat necessary to accomplish the phase transition is required. Completion of the process means that the entire amount of a given substance, contained in the system, will change its state of aggregation. It is assumed that the initial state is a state of saturation, thus either point $B$ or $E$, depending on the direction of the transition.

In order to evaluate the amount of energy needed for the transition, one needs to split the process in two parts, namely the isochoric heat transfer to the substance and subsequently its adiabatic expansion.

The considered process applies to evaporation. Condensation can be considered

analogously. In the first part of the process one supplies a portion of heat to a closed vessel filled with liquid. The heat supplied reads

$$dq = Tds + sdT. \tag{3.32}$$

The Gibbs-Duhem relation, see (Kuiken, (1994)), shows that

$$sdT = vdp. \tag{3.33}$$

The amount of heat is exactly such that it allows to evaporate the entire content of the system considered, e.g. a vessel. According to Gibbs' equation the change of internal energy reads

$$(de)_{dv=0} = (Tds)_{dv=0} - p\underbrace{dv}_{0} = (Tds)_{dv=0}\,, \tag{3.34}$$

where $e$ denotes the specific internal energy. The change in enthalpy at constant volume $v$ reads

$$(dh)_{dv=0} = (Tds)_{dv=0} - p\underbrace{dv}_{0} + p\underbrace{dv}_{0} + vdp = (Tds)_{dv=0} + vdp. \tag{3.35}$$

Interpretation of enthalpy in a system of fixed volume provides problems. The change in enthalpy of a system is nearly singularly meaningful for systems at constant pressure, when the change in enthalpy is equivalent to heat delivered. Otherwise, there is no easily-interpreted meaning for this state function. Nevertheless, the enthalpy is put forward as the sum of the heat that cannot be transferred to mechanical work, $(Tds)_{dv=0}$, and the thermodynamic potential, $vdp$, which could possibly be turned to work. Equation (3.35) can be quantitatively evaluated using specific heats. Employing the Maxwell relations one obtains

$$(dh)_{dv=0} = (Cv_l dT)_{dv=0} + vdp = Cp_l\, dT, \tag{3.36}$$

where $Cv$ and $Cp$ are the specific heats at constant volume and constant pressure, respectively. For a liquid their values are nearly the same. Thus, an increment of the enthalpy at constant volume is equivalent to the product of the specific heat at constant pressure and the change in temperature.

The following step concerns adiabatic expansion. One may imagine, that one of the vessel boundaries is released and the superheated liquid expands. In the standard case of a gas expansion, the thermodynamic potential, $vdp$, would be entirely transferred to mechanical work. However, in this particular case, due to physical properties of the substance, causing phase transition, only a part of the potential will turn to work. The rest will be used to overcome the attraction forces between particles of the liquid. The attraction forces consume the majority of the energy used for the transition. For water at a pressure of $1[atm]$ the amount of energy transferred into

the work is only about $7.51\%$. Since aside from the mechanical work, the potential is used for increasing the system disorder, the system rises further its entropy, in spite of the process being adiabatic. The mechanical work done by the system induces the change of the internal energy $de$, such that

$$(de)_{exp} = (Tds)_{exp} - pdv. \tag{3.37}$$

Since the process is adiabatic and $dq = 0$, then according to (3.32)

$$TdS = -sdT. \tag{3.38}$$

Bearing in mind (3.33) the change of the enthalpy of the expansion is equal to zero, namely

$$(dh)_{exp} = \left( \underbrace{Tds}_{-vdp>0} \right)_{exp} - pdv + pdv + v \underbrace{dp}_{<0} = 0. \tag{3.39}$$

If one assumes that the mass of the system is $1[kg]$, then the intensive quantities are equivalent to extensive ones and $h$, $e$ and $s$ become additive variables. Thus, the entire process of transition can be described as the sum of changes of quantities, namely

$$de = (de)_{dv=0} + (de)_{exp} = (Tds)_{dv=0} + (Tds)_{exp} - pdv = Tds - pdv. \tag{3.40}$$

and

$$dh = \left( T \underbrace{ds}_{>0} \right)_{dv=0} + v \underbrace{dp}_{>0} + \left( \underbrace{Tds}_{-pdv>0} \right)_{exp} + v \underbrace{dp}_{<0} = Tds = Cp_l \, dT. \tag{3.41}$$

Suppose that heat $Cp_k \, dT$, delivered to the substance being in the state of saturation, is not sufficient to change the state of aggregation of the entire content of the considered system. In this situation, only a part of the substance, of volume $\Omega_{e,c}$, will undergo the transition, whereas the rest remains in the same state of aggregation. In order to transit the entire content the latent heat

$$L = l\rho_k\Omega \tag{3.42}$$

is necessary, with $\Omega$ the volume of the system. The subscript $k$ denotes the phase considered. Transition of the substance contained in $\Omega_{e,c}$ requires

$$Cp_k \, dT\rho_k\Omega = l\rho_k\Omega_{e,c}. \tag{3.43}$$

The relation between the delivered heat and the latent heat yields

$$\frac{Cp_k \, dT\rho_k\Omega}{L} = \frac{l\rho_k\Omega_{e,c}}{l\rho_k\Omega} = \frac{\Omega_{e,c}}{\Omega}. \tag{3.44}$$

From (3.44) the volumetric portion of the substance that will undergo the transition can be found. It reads

$$\Omega_{e,c} = \frac{Cp_k\, dT}{l}\Omega. \tag{3.45}$$

The fraction at the right-hand side of (3.45) is called the energy fraction. It is the basic quantity for the EOF method. The mechanical work $pdv$ causes $\Omega_{e,c}$ to increase or decrease, depending on the direction of the process. Since the transition is isothermal and isobaric a volume change depends on the difference between phasic densities in the state of saturation. The volume of the substance resulting from the phase transition obeys the relations

$$\Omega_g = \frac{\rho_l}{\rho_g}\Omega_e, \qquad \Omega_l = \frac{\rho_g}{\rho_l}\Omega_c \tag{3.46}$$

for evaporation and condensation, respectively. Equation (3.46) leads immediately to the formulation for the volume increment or decrement:

$$\Delta\Omega_e = \left(\frac{\rho_l}{\rho_g} - 1\right)\Omega_e, \qquad \Delta\Omega_c = \left(\frac{\rho_g}{\rho_l} - 1\right)\Omega_c \tag{3.47}$$

for evaporation and condensation, respectively. Volume change of the substance during evaporation is positive, whereas during condensation it is negative, which indicates the direction of the process.

The gas-liquid phase transition from a quantitative point of view, as presented here, constitutes the base for the Energy of Fluid (EOF) method useful for modelling of the phase transition process. Details of this approach will be described in Chapter (5).

# MATHEMATICAL MODEL

4 CHAPTER

The main goal of this thesis, is the development of a suitable CFD algorithm for the prediction of the flow of two immiscible fluids, separated by an interface. The field of interest concerns gas(vapour)-liquid flows, so the jump of the value of the flow quantities over the interface is large. The fluids considered represent a single substance and are assumed incompressible, i.e. their density does not change because of changes in pressure or temperature. The temperature-driven phase transition is also incorporated in the method. This chapter describes the mathematical basis of the method.

The fluids are considered as continua. The flow is modelled by the standard mathematical approach considering the mechanical and thermodynamic balance of flow field quantities (Ramshaw and Trapp, (1976)). Regions occupied by fluids are indicated by the Heaviside function (2.35), see Sec.(2.4.3), with as argument the volume fraction defined as the ratio between the volume occupied by a phase and that of the control volume considered, (2.10). In expression (2.10) volume fraction denotes a gaseous volume fraction, consequently it is termed the void fraction. The Heaviside function is approximated by its smoothed version, so that the interface does not form a sudden jump in fluid properties, but a monotonic transition of these properties result in space. This allows to regard a two-phase substance as a continuous medium and although the phases of the substance are incompressible, the flow behaves as quasi-compressible.

The model is suited for turbulent as well as laminar flows, however, the first one requires the modelling of the influence of turbulence on the mean flow quantities. Several turbulent flow schemes have been developed e.g. (Wilcox, (1993)), nevertheless since the flow motion in the model is dominated by the pressure and inertia forces the problem of turbulence is not to be considered within the scope of this study.

## 4.1 General equation of motion

The local instantaneous conservation equation given by (2.12) describes the three conservation laws, namely conservation of mass, momentum and energy. Equation (2.12) applies to a single phase of a multi-phase system, marked by subscript $k$. Once the single-field approach is considered, the subscript can be omitted, see Sec.(2.4). Since (2.12) has the partial differential equation form, it describes changes of flow field quantities occurring in an infinitesimally small control volume fixed in space. However, due to the discontinuous nature of two-phase flows this type of formulation fails and needs to be replaced by a formulation involving a computational domain consisting of fixed finite volumes inside which all flow variables and properties are volumetrically averaged. This formulation, termed the Finite-Volume approach, uses the general equation of motion in the volume-integrated form of (2.12)

$$\int_{\Omega} \frac{\partial \rho\psi}{\partial t}\, d\Omega + \int_{\Omega} \vec{\nabla}.\left(\rho\vec{u}\psi\right) d\Omega = -\int_{\Omega} \vec{\nabla}.\vec{J} d\Omega + \int_{\Omega} \rho\Phi d\Omega. \tag{4.1}$$

The first term on the left hand side of (4.1) denotes the net change of the time derivative of the quantity $\rho\psi$ contained in the control volume $\Omega$. The quantity $\psi$ represents the conserved intensive property which multiplied by the density and integrated over the control volume appears as the extensive variable,

$$\Psi = \int_{\Omega} \rho\psi d\Omega, \tag{4.2}$$

which constitutes the total content of the physical quantity in the control volume. The second term on the left hand side denotes the change due to a net flux out of the control volume. The term containing $\vec{J}$ represents a surface source, whereas the lats term involving $\Phi$ is the volumetrically distributed source of $\psi$. Summarizing, the above relation is the relation between the convective, the diffusive and the volumetric source terms as the cause of producing the change of $\psi$ in time. The equation constitutes the basis for the formulation of the mass, momentum and energy conservation laws. These laws completely describe the behaviour of the flow, which are to be supplemented by expressions for the physical properties of the fluid such as density, viscosity and heat conductivity.

Employing Gauss' theorem yields

$$\int_{\Omega} \vec{\nabla}\phi\, d\Omega = \int_{\partial\Omega} \phi\vec{n} dS, \tag{4.3}$$

where $\phi$ denotes an arbitrary quantity. The left-hand side of (4.3) is equivalent to the integration of $\phi$ over the closed surface bounding the control volume $\Omega$. Employment

of the Gauss' theorem and Leibniz' rule yields, for a control volume that is fixed in space:

$$\frac{\partial}{\partial t}\int\limits_{\Omega}\rho\psi\, d\Omega+\int\limits_{\partial\Omega}\left(\rho\vec{u}\psi\right).\vec{n}dS=-\int\limits_{\partial\Omega}\vec{J}.\vec{n}dS+\int\limits_{\Omega}\rho\Phi d\Omega. \tag{4.4}$$

The form of (4.4) is convenient for the derivation of the individual conservation equations. The graphic representation of the conservation laws, based on (4.4), is shown in Fig.(4.1).

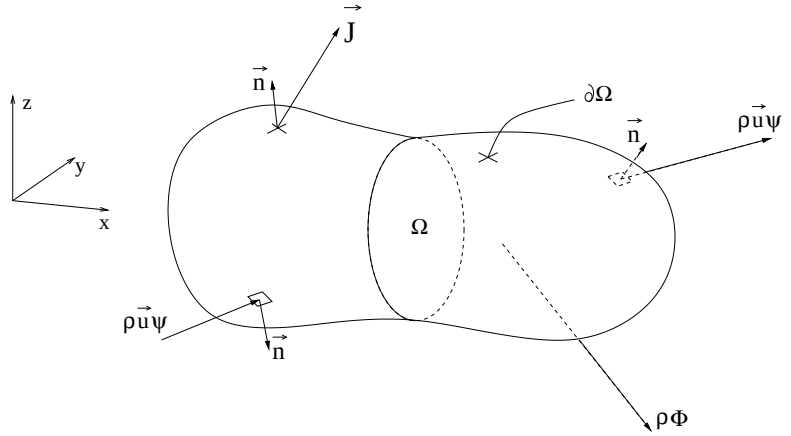


FIGURE 4.1: *Control volume for conservation laws.*

## 4.2 Individual conservation equations

Individual conservation equations are obtained by choosing the quantities $\psi$, $\vec{J}$ and $Q$ in the form given in Tab.(2.1). Each of the conservation equations is given in the following subsections.

### 4.2.1 Conservation of mass

The quantity $\psi$ is chosen as the density of the fluid. This fluid density varies from the value of the liquid to that of the vapour, depending on the vapour-liquid interface location, see Sec.(2.4.3). The equation of conservation of mass reads

$$\frac{\partial}{\partial t}\int\limits_{\Omega}\rho\, d\Omega+\int\limits_{\partial\Omega}\rho\left(\vec{u}.\vec{n}\, dS\right)=0, \tag{4.5}$$

with vapour-liquid mixture density $\rho$ defined as $\rho=\alpha\rho_g+(1-\alpha)\,\rho_l$. Continuity equation (4.5) states that if there is no net mass production in the control volume $\Omega$, the only reason of a mass change in this volume is a flux across its boundaries.

In partial differential form one finds

$$\frac{\partial \rho}{\partial t} + \vec{\nabla}.(\rho \vec{u}) = 0. \tag{4.6}$$

This equation can be rearranged as

$$\frac{\partial \rho}{\partial t} + \vec{u}.\vec{\nabla}\rho + \rho\vec{\nabla}.\vec{u} = 0, \tag{4.7}$$

where the first two terms on the left combine to the substantial derivative of the density, $D\rho/Dt \equiv \partial\rho/\partial t + \vec{u}.\vec{\nabla}\rho$, i.e. the change in $\rho$ of an infinitesimal fluid element moving with the flow. This results in

$$\frac{D\rho}{Dt} + \rho\vec{\nabla}.\vec{u} = 0. \tag{4.8}$$

### 4.2.2 Conservation of momentum

In the momentum equation the quantity $\psi$ is chosen as $\rho\vec{u}$. As seen in Tab(2.1), the external flux term consists of the pressure and the viscous stress tensor. If the fluid is assumed to be Newtonian, the term can be expressed by

$$\vec{J} = \left(p + \frac{2}{3}\mu\vec{\nabla}.\vec{u}\right)\overline{\overline{I}} - 2\mu\overline{\overline{D}}, \tag{4.9}$$

where $\mu$ denotes the temperature-dependent dynamic viscosity coefficient, $\overline{\overline{I}}$ is the unit tensor and $\overline{\overline{D}}$ is the rate of strain (deformation) tensor. In (4.9) use is made of Stokes' hypothesis that the trace of the local stress tensor equals zero. Writing (4.9) in index notation for Cartesian coordinates yields

$$J_{ij} = \left(p + \frac{2}{3}\,\mu\frac{\partial u_k}{\partial x_k}\right)\delta_{ij} - 2\mu D_{ij}, \tag{4.10}$$

where

$$D_{ij} = \frac{1}{2}\left(\frac{\partial u_i}{\partial x_j} + \frac{\partial u_j}{\partial x_i}\right). \tag{4.11}$$

The Kronecker symbol, $\delta_{ij}$, appearing in (4.10), assumes the value 1 if $i = j$ and 0 otherwise. For the viscous part of the external surface flux term one finds

$$\tau_{ij} = 2\mu D_{ij} - \frac{2}{3}\,\delta_{ij}\mu\frac{\partial u_k}{\partial x_k}. \tag{4.12}$$

The second term on the right hand side of (4.12) appears only when any volumetric change in the control volume occurs. This may be a phase transition that changes the volume of the substance and causes a nonzero divergence of the velocity field. The

only volumetric force term considered here is the gravitational force. Thus, the quantity $\Phi$ in the far-right hand side term of (4.1) is replaced by $\vec{g}$ denoting gravitational acceleration.

Substituting all terms in the general equation one obtains the momentum equation as

$$\begin{aligned}&\frac{\partial}{\partial t}\int\limits_{\Omega}\rho\vec{u}\,d\Omega+\int\limits_{\partial\Omega}\rho\,\vec{u}\,(\vec{u}.\vec{n}\,dS)=\\&-\int\limits_{\partial\Omega}p\vec{n}\,dS+\int\limits_{\partial\Omega}\left(2\mu\overline{\overline{D}}-\left(\frac{2}{3}\,\mu\vec{\nabla}.\vec{u}\right)\overline{\overline{I}}\right)\vec{n}\,dS+\int\limits_{\Omega}\rho\vec{g}\,d\Omega.\end{aligned}\tag{4.13}$$

To re-arrange the energy equation later on, it is convenient to obtain the partial differential form of the momentum equation:

$$\frac{\partial}{\partial t}\rho\vec{u}+\vec{\nabla}.\,(\rho\vec{u}\vec{u})=-\vec{\nabla}p+\vec{\nabla}.\overline{\overline{\tau}}+\rho\vec{g}.\tag{4.14}$$

Using the continuity equation the left-hand side of (4.14) can be re-arranged in the form with the substantial derivative, to yield

$$\frac{D\vec{u}}{Dt}=-\vec{\nabla}p+\vec{\nabla}.\overline{\overline{\tau}}+\rho\vec{g}.\tag{4.15}$$

### 4.2.3 Energy

The basic form of the energy equation introduces the specific total energy, $E$, thus in the energy equation the general quantity $\psi$ in (4.4) is $E$. The external energy flux term consists of three terms: the heat flux into the control volume through its boundary; the work done on the system per unit time by the pressure; the work done on the system per unit time by the viscous stress. Taking this together, $\vec{J}$ assumes the form

$$\vec{J}=\vec{q}+p\vec{u}-\overline{\overline{\tau}}\,\vec{u}.\tag{4.16}$$

The volumetric energy source consists of two terms: the work done per unit time of the volumetric force field, and the volumetric heat sources. Here volumetric heat sources are not considered and only the gravitational force does work. Consequently, one obtains

$$\begin{aligned}&\frac{\partial}{\partial t}\int\limits_{\Omega}\rho E\,d\Omega+\int\limits_{\partial\Omega}\rho E\vec{u}.\vec{n}\,dS=\\&-\int\limits_{\partial\Omega}\vec{q}.\vec{n}\,dS-\int\limits_{\partial\Omega}p\vec{u}.\vec{n}\,dS+\int\limits_{\partial\Omega}\left(\overline{\overline{\tau}}\,\vec{u}\right).\vec{n}\,dS+\int\limits_{\Omega}\rho\vec{u}.\vec{g}\,d\Omega\end{aligned}\tag{4.17}$$

The partial differential form of the energy equation is

$$\frac{\partial}{\partial t}\left(\rho E\right)+\vec{\nabla}.\left(\rho\vec{u}E\right)=-\vec{\nabla}.\vec{q}-\vec{\nabla}.\left(p\vec{u}\right)+\vec{\nabla}.\left(\overline{\overline{\tau}}\,\vec{u}\right)+\rho\left(\vec{g}.\vec{u}\right). \tag{4.18}$$

Using the continuity equation the left-hand side can be rearranged into the form with the substantial derivative, resulting in

$$\rho\frac{DE}{Dt}=-\vec{\nabla}.\vec{q}-\vec{\nabla}.\left(p\vec{u}\right)+\vec{\nabla}.\left(\overline{\overline{\tau}}\,\vec{u}\right)+\rho\left(\vec{g}.\vec{u}\right). \tag{4.19}$$

The heat flux vector, $\vec{q}$, may be expressed by Fourier's law as

$$\vec{q}=-\lambda\vec{\nabla}T. \tag{4.20}$$

In the present study the specific internal energy, $e$, is a more convenient quantity to consider, so (4.17) requires rearrangement.

The definition of the total specific energy is

$$E=e+\frac{1}{2}\left|\vec{u}\right|^{2}, \tag{4.21}$$

with the second term on the right representing the kinetic energy per unit mass. Taking the inner product of the velocity vector and the momentum equation (4.13) in the partial differential form gives

$$\rho\frac{D}{Dt}\frac{1}{2}|\vec{u}|^{2}=-\vec{u}.\vec{\nabla}p+\vec{u}.\left(\vec{\nabla}.\overline{\overline{\tau}}\right)+\rho\left(\vec{g}.\vec{u}\right). \tag{4.22}$$

So that combining this mechanical energy equation with (4.19) yields

$$\rho\frac{De}{Dt}=-\vec{\nabla}.\vec{q}-p\vec{\nabla}.\vec{u}+\vec{\nabla}.\left(\overline{\overline{\tau}}\,\vec{u}\right)-\vec{u}.\left(\vec{\nabla}.\overline{\overline{\tau}}\right). \tag{4.23}$$

The last two terms on the right-hand side of (4.23) form Rayleigh's dissipation function, i.e.

$$\vec{\nabla}.\left(\overline{\overline{\tau}}\,\vec{u}\right)-\left(\vec{\nabla}.\overline{\overline{\tau}}\right).\vec{u}=\left(\overline{\overline{\tau}}\,\vec{\nabla}\right).\vec{u}. \tag{4.24}$$

Now, using the continuity equation, the left-hand side of (4.23) can be rewritten in partial differential conservation form, i.e. $\partial\left(\rho e\right)/\partial t+\vec{\nabla}.\left(\rho\vec{u}e\right)$, so that upon integration over the control volume and applying Gauss' theorem one obtains

$$\begin{aligned}&\frac{\partial}{\partial t}\int\limits_{\Omega}\left(\rho e\right)\,d\Omega+\int\limits_{\partial\Omega}\rho e\left(\vec{u}.\vec{n}\right)\,dS=\\&-\int\limits_{\partial\Omega}\vec{q}.\vec{n}\,dS-\int\limits_{\Omega}p\left(\vec{\nabla}.\vec{u}\right)\,d\Omega+\int\limits_{\Omega}\left[\left(\overline{\overline{\tau}}\,\vec{\nabla}\right).\vec{u}\right]\,d\Omega.\end{aligned} \tag{4.25}$$

In a system in which more than one phase of a substance exists, term $\rho e$ consists of many elements. Suppose the system is not in thermodynamic equilibrium. Then term $\rho e$, with the reference energy level at the state of saturation, reads

$$\begin{aligned}\rho e = {} & \rho_l \left(1-\alpha\right) \left(Cv_l T_{sat} + Cv_l \left(T - T_{sat}\right)\right) + \\ & \rho_g \alpha \left(Cv_l T_{sat} + l - p_{sat}(v_{g_{sat}} - v_{l_{sat}}) + Cv_g \left(T - T_{sat}\right)\right).\end{aligned} \tag{4.26}$$

Implementation of this form into the energy equation, (4.25), is avoided by omitting the latent heat and the work $l - p_{sat}(v_{l_{sat}} - v_{l_{sat}})$ from (4.26). Now term $\rho e$ is expressed by

$$\rho e = \rho_l \left(1 - \alpha\right) Cv_l T + \rho_g \alpha C v_g T. \tag{4.27}$$

Since term $l - p_{sat}(v_{l_{sat}} - v_{l_{sat}})$ is eliminated, one needs to model the change of temperature caused by phase transition. Thus, an additional contribution of the surface source, $Q_{trans}$, appears in the energy equation. Now the energy equation reads

$$\begin{aligned}&\frac{\partial}{\partial t} \int\limits_{\Omega} \rho e \, d\Omega + \int\limits_{\partial\Omega} \rho e \left(\vec{u}.\vec{n}\right) \, dS = \\ &- \int\limits_{\partial\Omega} \vec{q}.\vec{n} \, dS - \int\limits_{\Omega} p \left(\vec{\nabla}.\vec{u}\right) \, d\Omega + \int\limits_{\Omega} \left[\left(\bar{\bar{\tau}} \, \vec{\nabla}\right).\vec{u}\right] \, d\Omega + \hat{Q}_{trans}.\end{aligned} \tag{4.28}$$

Now suppose that function $F(t, \psi, \cdots)$ assumes the partial differential form of (4.4), such that

$$F\left(t, \psi, \cdots\right) = \frac{\partial}{\partial t} \left(\rho\psi\right) + \vec{\nabla}. \left(\rho\psi\vec{u}\right) + \vec{\nabla}.\vec{J} - \rho\Phi = 0. \tag{4.29}$$

Function $F(t, \psi, \cdots)$ may be expressed as the sum of two other functions

$$F\left(t, \psi, \cdots\right) = F_1\left(t, \psi, \cdots\right) + F_2\left(t, \psi, \cdots\right). \tag{4.30}$$

Functions $F_1(t, \psi, \cdots)$ and $F_2(t, \psi, \cdots)$ have the same form as $F(t, \psi, \cdots)$, namely

$$F_i\left(t, \psi, \cdots\right) = \frac{\partial}{\partial t} \left(\rho\psi\right)_i + \vec{\nabla}. \left(\rho\psi\vec{u}\right)_i + \vec{\nabla}.\vec{J_i} - \rho\Phi_i = 0, \tag{4.31}$$

where $i = 1, 2$. Expressing function $F(t, \psi, \cdots)$ as the sum of $F_1(t, \psi, \cdots)$ and $F_2(t, \psi, \cdots)$, after rearrangement, yields

$$\begin{aligned}&\frac{\partial}{\partial t} \left(\rho\psi\right)_1 + \vec{\nabla}. \left(\rho\psi\vec{u}\right)_1 = \\ &- \vec{\nabla}.\vec{J_1} + \rho\Phi_1 + \left[-\frac{\partial}{\partial t} \left(\rho\psi\right)_2 - \vec{\nabla}. \left(\rho\psi\vec{u}\right)_2 - \vec{\nabla}.\vec{J_2} + \rho\Phi_2\right].\end{aligned} \tag{4.32}$$

Now, $(\rho\psi_1)$, $\vec{J_1}$ and $\Phi_1$ for the energy equation are:

$$\begin{aligned}
&(\rho\psi)_1 = \rho C v_g T,\\
&-\vec{J_1} = \left(\alpha\lambda_g + \frac{Cv_g}{Cv_l}\,(1-\alpha)\,\lambda_l\right)\left(\vec{\nabla}T\right) + \left(\alpha\mu_g + \frac{Cv_g}{Cv_l}\,(1-\alpha)\,\mu_l\right)\overline{\overline{a}}.\vec{u} + q_1, \quad (4.33)\\
&\rho\Phi_1 = 0,
\end{aligned}$$

where $\overline{\overline{a}} = \overline{\overline{\tau}}/\mu$ and $q$ represent the temperature change due to phase transition. In order to satisfy (4.30) such that $F(t,\psi,\cdots)$ corresponds to (4.28), $(\rho\psi_2)$, $\vec{J_2}$ and $\Phi_2$ are

$$\begin{aligned}
&(\rho\psi)_2 = (1-\alpha)\,\rho_l\,(Cv_l - Cv_g)\,T,\\
&-\vec{J_2} = \left(1-\frac{Cv_g}{Cv_l}\right)(1-\alpha)\lambda_l\left(\vec{\nabla}T\right) + \left(1-\frac{Cv_g}{Cv_l}\right)(1-\alpha)\mu_l\overline{\overline{a}}.\vec{u} + q_2, \quad (4.34)\\
&\rho\Phi_2 = 0,
\end{aligned}$$

Since, according to (4.31), $F_2(t,\psi,\cdots) = 0$, the integral, rearranged form of $F_1(t,\psi,\cdots)$ for the energy equation reads

$$\begin{aligned}
&\frac{\partial}{\partial t}\int_\Omega \rho C v_g T\,d\Omega + \int_{\partial\Omega}\rho C v_g T\,(\vec{u}.\vec{n})\,dS = \int_{\partial\Omega}\left(\alpha\lambda_g + \frac{Cv_g}{Cv_l}\,(1-\alpha)\,\lambda_l\right)\left(\vec{\nabla}T\right).\vec{n}\,dS +\\
&\int_\Omega\left(\left(\alpha\mu_g + \frac{Cv_g}{Cv_l}\,(1-\alpha)\,\mu_l\right)\overline{\overline{a}}\;\vec{\nabla}\right).\vec{u}\,d\Omega + Q_{trans}.
\end{aligned} \quad (4.35)$$

While temperature, $T$, is the same in $F$, $F_1$ and $F_2$, all these functions produce the same temperature distribution. The above consideration has led to the simplified form of the unsteady and convective terms of (4.35), in which the specific heat of liquid does not appear. For the purpose of convenience in implementation, (4.35) will be used further. Discretization of (4.35) is discussed in Chapter (5).

## 4.3 Void fraction transport equation

The Heaviside function, (2.35), describes the distribution of phases in a system. Employing the Heaviside function, the two-fluid system can be modelled as a continuum. The argument of the Heaviside function is the void fraction $\alpha$ defined by (2.10). Time and spatial changes of $\alpha$ are governed by the general conservation equation (4.1), where $\psi$ equals $\alpha$. In the case of phase transition, one finds the surface source $\vec{J}$ at the right side of (4.1), consequently the transport equation for the void fraction assumes the form

$$\frac{\partial}{\partial t}\int_\Omega \alpha\,d\Omega + \int_{\partial\Omega}\alpha\,(\vec{u}.\vec{n})\;dS = \int_\Omega \vec{\nabla}.\vec{J}\,d\Omega. \quad (4.36)$$

In order to evaluate $\vec{J}$ one needs to refer to the continuity equation, (4.5). The averaged density in control volume $\Omega$ is defined by (2.37), where $\alpha$ plays the role of the weighting factor. This ensures the continuous distribution of properties in regions where the interface is present. Equation (2.37) constitutes the closure relation which for the density reads

$$\rho = \alpha\rho_g + (1-\alpha)\,\rho_l \tag{4.37}$$

Substitution of (4.37) in (4.5), with the assumption of incompressibility of the vapour and liquid phases, yields

$$\frac{\partial}{\partial t}\int\limits_{\Omega} \alpha\, d\Omega + \int\limits_{\partial\Omega} \alpha\vec{u}.\vec{n}\, dS = \int\limits_{\Omega} \frac{\rho_l}{\rho_l - \rho_g}\vec{\nabla}.\vec{u}\, d\Omega, \tag{4.38}$$

where the surface flux $\vec{J}$ reads

$$\vec{J} = \frac{\rho_l}{\rho_l - \rho_g}\vec{u}. \tag{4.39}$$

The divergence of the velocity field, appearing at the right hand side of (4.38), will be discussed in the following section.

## 4.4 Energy of Fluid method (EOF).

The divergence of the velocity field is evaluated using the non-conservation form of the continuity equation, (4.8). From this equation one finds $\vec{\nabla}.\vec{u}$ and integration over the control volume, using Gauss' theorem yields

$$\int\limits_{\partial\Omega} \vec{u}.\vec{n}\, dS = -\int\limits_{\Omega} \frac{1}{\rho}\frac{D\rho}{Dt}\, d\Omega. \tag{4.40}$$

The right hand side of (4.40) contains $\rho$ which may be expressed with the help of (4.37). Assuming incompressibility of the phasic densities one obtains

$$\int\limits_{\partial\Omega} \vec{u}.\vec{n}\, dS = \int\limits_{\Omega} \frac{\rho_l - \rho_g}{\rho}\frac{D\alpha}{Dt}\, d\Omega. \tag{4.41}$$

The divergence of the velocity field, appearing in the control volume, is understood as a volume source resulting from the phase transition which occurs inside this control volume. The Volume of Fluid method regards the transition, e.g. evaporation, as the growth of the vapour-liquid mixture volume with simultaneous decrement of the mixture density. This volume growth is represented by the divergence of the velocity field, where the velocity results from the substance expansion or contraction in the

control volume. The velocity can be compared to that of the boundary of a growing or shrinking gaseous bubble during the transition in the two-field approach. The velocity is regarded then as absolute, not relative. Consequently, the divergence of the velocity field in the control volume depends only on the rate of change of the volume, not on the substance motion caused by external forces. Therefore the substantial derivative, $D\alpha/Dt$ in (4.41), reduces to the ordinary time derivative (Sauer, 2000). Finally, one obtains

$$\int_{\partial\Omega} \vec{u}.\vec{n}\, dS = \int_{\Omega} \frac{\rho_l - \rho_g}{\rho} \frac{d\alpha}{dt}\, d\Omega. \tag{4.42}$$

The next step of the procedure is the quantitative evaluation of the term $d\alpha/dt$. This will be done on the basis of the mathematical model of the Energy of Fluid method discussed in Sec.(3.3).

The key of the procedure is the evaluation of the time derivative of $\alpha$. Suppose the phase transition process which occurs in both directions - evaporation and condensation. At time $t = 0$, the beginning of the transition, a substance, a pure liquid or a pure vapor, occupies the control volume $\Omega$. After an infinitesimally small time increment $dt$ the substance will change its volume as the effect of the transition, see Fig(4.2). In reality, one would observe the appearance of phasic structures separated by the

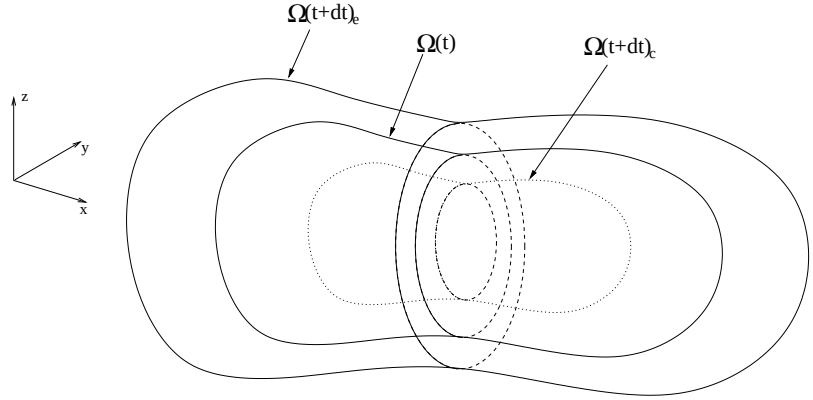


FIGURE 4.2: *Change of the volume of a vapour-liquid mixture at the time t+dt, as the effect of phase transition. Initial volume is* $\Omega$*, volume after condensation is* $\Omega(t+dt)_c$*, volume after evaporation is* $\Omega(t+dt)_e$*.*

interface, i.e. appearing in the bulk. However, in the case of the VOF approach, a substance is regarded as a continuum, where one assumes the change of the averaged density, with simultaneous increment or decrement of the volume. The occupied volumes at time $t + dt$ are $\Omega(t + dt)_e$ and $\Omega(t + dt)_c$ for evaporation and condensation,

respectively. Their values are obtained based on the procedure described in Sec.(3.3). By combination of (3.45) and (3.47) one obtains

$$\begin{aligned}\Omega(t+dt)_e &= \Omega(t) + d\Omega_e = \Omega(t) + \left(\frac{\rho_l}{\rho_g} - 1\right)\frac{Cp_l dT}{l}\Omega(t)\,,\\ \Omega(t+dt)_c &= \Omega(t) + d\Omega_c = \Omega(t) + \left(\frac{\rho_g}{\rho_l} - 1\right)\frac{Cp_g dT}{l}\Omega(t)\,,\end{aligned} \tag{4.43}$$

where $Cp\,dT$ denotes the heat excess over or below the state of saturation. The volume of vapour resulting from the evaporation and the volume of condensing vapour is

$$\begin{aligned}\Omega(t+dt)_{e,g} &= \frac{\rho_l}{\rho_g}\frac{Cp_l\,dT}{l}\Omega\,(t)\,, \quad \text{and}\\ \Omega(t+dt)_{c,g} &= \left(1 - \frac{Cp_g\,dT}{l}\right)\Omega\,(t)\,,\end{aligned} \tag{4.44}$$

for the evaporation and condensation, respectively. According to the definition of the void fraction, (2.10), the relation between (4.44) and (4.43) gives the void fraction in the volumes $\Omega(t+dt)_e$ and $\Omega(t+dt)_c$, namely

$$\begin{aligned}\alpha(t+dt)_e &= \frac{\Omega(t+dt)_{e,g}}{\Omega(t+dt)_e},\\ \alpha(t+dt)_c &= \frac{\Omega(t+dt)_{c,g}}{\Omega(t+dt)_c}.\end{aligned} \tag{4.45}$$

Since the control volumes considered are fixed, it is necessary to assume, that the void fraction in the volumes $\Omega(t+dt)$ is the same as that in $\Omega$ at time $t+dt$. This leads to the statement

$$\alpha(t+dt)_\Omega = \alpha(t+dt)_{\Omega(t+dt)_{e,c}}. \tag{4.46}$$

The void fraction in $\Omega$, resulting from the transition, reads

$$\alpha(t+dt)_\Omega = \alpha(t) + d\alpha, \tag{4.47}$$

where $\alpha(t) = 0$ for the case of evaporation and $\alpha(t) = 1$ for the case of condensation. Expressing $\alpha(t+dt)_\Omega$ using (4.43) and (4.44) and further rearrangement leads to the formula for $d\alpha$, namely

$$\begin{aligned}d\alpha_e &= \frac{\rho_l}{\rho_g}\frac{Cp_l\,dT}{l + \left(\frac{\rho_l}{\rho_g} - 1\right)Cp_l\,dT},\\ d\alpha_c &= -\frac{\rho_g}{\rho_l}\frac{Cp_g\,dT}{l + \left(\frac{\rho_g}{\rho_l} - 1\right)Cp_g\,dT}.\end{aligned} \tag{4.48}$$

Finally, for the time-derivative of $\alpha_e$ and $\alpha_c$ one finds for (4.48)

$$\begin{aligned}
&\left(\frac{d\alpha}{dt}\right)_e = \lim_{dt\to 0}\frac{d\alpha_e}{dt} = \\
&\lim_{dt\to 0}\frac{\rho_l}{\rho_g}\frac{Cp_l}{l+\left(\frac{\rho_l}{\rho_g}-1\right)Cp_l\,\left(\frac{dT}{dt}\right)_e dt}\left(\frac{dT}{dt}\right)_e = \frac{\rho_l}{\rho_g}\frac{Cp_l}{l}\left(\frac{dT}{dt}\right)_e, \\
&\left(\frac{d\alpha}{dt}\right)_c = \lim_{dt\to 0}\frac{d\alpha_c}{dt} = \\
&\lim_{dt\to 0}-\frac{\rho_g}{\rho_l}\frac{Cp_g}{l+\left(\frac{\rho_g}{\rho_l}-1\right)Cp_g\,\left(\frac{dT}{dt}\right)_c dt}\left(\frac{dT}{dt}\right)_c = -\frac{\rho_l}{\rho_g}\frac{Cp_g}{l}\left(\frac{dT}{dt}\right)_c.
\end{aligned} \tag{4.49}$$

Substitution of (4.49) in (4.42) gives an estimate of the net velocity divergence in a control volume.

The above discussion applies to the situation that the transition begins for the case volume $\Omega(t)$ contains a single phase. A more complex scheme involving a vapour-liquid mixture as start will be discussed in Chapter (5).

## 4.5 Physical properties of phases

The vapour and liquid densities are assumed to be constant throughout the numerical simulation. They are evaluated at the start of calculations on the basis of initial pressure and temperature, on the condition that both variables are uniformly distributed in each phase. If this is not the case, an average temperature and pressure is chosen. For the gas (steam) the density is estimated according to formulae used by (Sauer, 2000)

$$\rho_g(T) = 10^{-3}\exp\left(-A_0+A_1T-A_2T^2+A_3T^3-A_4T^4+A_5T^5\right)[kg/m^3], \tag{4.50}$$

where

$$\begin{aligned}
&A_5 = 1.759194E-12, \quad A_4 = 4.293708E-09, \quad A_3 = 4.313782E-06, \\
&A_2 = 2.258077E-03, \quad A_1 = 6.383280E-01, \quad A_0 = 7.099724,
\end{aligned}$$

with dimension $[A_i] = [1/K^i]$. The value of the density of the liquid (water) is obtained from

$$\rho_l(T) = A_0 - A_1T + A_2T^2 - A_3T^3 + A_4T^4 - A_5T^5\,[kg/m^3], \tag{4.51}$$

where

$$\begin{aligned}
&A_5 = 1.336940E-13, \quad A_4 = 2.337246E-10, \quad A_3 = 1.582645E-07, \\
&A_2 = 4.854679E-05, \quad A_1 = 6.496841E-03, \quad A_0 = 7.188601,
\end{aligned}$$

with dimension $[A_i] = [kg/m^3K^i]$.

The specific heat for the phases are also assumed constant. They are evaluated as a function of an initial, averaged temperature. The temperature is averaged for each phase separately. The specific heat of the gas (steam) at constant pressure obeys

$$Cp_g(T) = A_0 - A_1T + A_2T^2\,[J/kgK], \tag{4.52}$$

where

$$A_2 = 1.5643478E - 02, \quad A_1 = 1.5543478, \quad A_0 = 4.217E + 03, \tag{4.53}$$

with the dimension $[A_i] = [J/kgK^{i+1}]$. The specific heat of steam at constant volume is obtained from

$$Cv_g(T) = Cp_g(T) - R\,[J/kgK], \tag{4.54}$$

The parameter $R$ is the specific gas constant which for steam equals

$$R = 461.519\,[J/kgK].$$

The specific heat capacity for liquid (water) is assumed to have the same value at constant pressure and volume. It reads

$$Cp_l(T) = A_0 - A_1T + A_2T^2 - A_3T^3 + A_4T^4 - A_5T^5\,[J/kgK], \tag{4.55}$$

where

$$\begin{array}{lll} A_0 = 3.46362E - 09, & A_1 = 6.004644E - 06, & A_2 = 4.01443E - 03, \\ A_3 = 1.311501, & A_4 = 2.09999E + 02, & A_5 = 1.504741E + 04, \end{array}$$

with the dimension $[A_i] = [J/kgK^{i+1}]$

The dynamic viscosity is a function of the temperature. Its value is updated after each time step of the simulation. For vapour the viscosity coefficient reads (Schmidt, (1982))

$$\mu_g(T,v) = \mu_0(T)\exp\left(\frac{v^*}{v}\sum_{i=0}^{5}\sum_{j=0}^{4} b_{ij}\left(\frac{T^*}{T}-1\right)^i\left(\frac{v^*}{v}-1\right)^j\right)[kg/ms], \tag{4.56}$$

with

$$\mu_0(T) = \left(\frac{T}{T^*}\right)^{1/2}\left(\sum_{k=0}^{3} a_k\left(\frac{T^*}{T}\right)^k\right)^{-1}\cdot 10^{-6}\,[kg/ms]. \tag{4.57}$$

The quantities $T^*$ and $v^*$ are the absolute temperature and the specific volume, respectively, at the critical point. For steam, their values are

$$T^* = 647.27[K], \qquad v^* = 3.147 \cdot 10^{-3}[m^3/kg].$$

The quantities $b_{ij}$ and $a_k$ are constants which values are given in Tab.(1.1) and Tab.(1.3), respectively. The reader can find the tables in App.(A). For the liquid, the dynamic viscosity assumes the form

$$\mu_l(T) = 10^{-3} \exp\left(-A_0 + A_1 T^{-1} + A_2 T - A_3 T^2\right) \, [kg/ms], \tag{4.58}$$

where

$$\begin{array}{ll} A_0 = 2.471E + 01, & A_1 = 4.209E + 03\,[K], \\ A_2 = 4.527E - 02\,[K^{-1}], & A_3 = 3.376E - 05\,[K^{-2}], \end{array}$$

The heat conductivity coefficient, just like the dynamic viscosity, is updated every time step of the calculation. Its estimate is a function of temperature and density. The density is temperature dependent only for the purpose of the evaluation of the heat conductivity coefficient. The density is obtained from (4.50) and (4.51).The relation for the heat conduction coefficient is common for steam and water. It assumes the form (Schmidt, (1982))

$$\lambda(T, \rho) = \lambda_0 + \overline{\lambda} + \Delta\lambda \, [J/msK], \tag{4.59}$$

where

$$\lambda_0(T) = \left(\frac{T}{T^*}\right)^{1/2} \sum_{i=0}^{3} a_i \left(\frac{T}{T^*}\right)^i \, [J/msK], \tag{4.60}$$

$$\overline{\lambda}(\rho) = b_0 + b_1 \left(\frac{\rho}{\rho^*}\right) + b_2 \exp\left(B_1 \left(\frac{\rho}{\rho^*} + B_2\right)^2\right) [J/msK] \tag{4.61}$$

and

$$\begin{aligned} \Delta\lambda(T, \rho) = &\left(d_1 \left(\frac{T^*}{T}\right)^{10} + d_2\right) \left(\frac{\rho}{\rho^*}\right)^{1.8} \exp\left(C_1 \left(1 - \left(\frac{\rho}{\rho^*}\right)^{2.8}\right)\right) + \\ &d_3 S \left(\frac{\rho}{\rho^*}\right)^Q \exp\left(\frac{Q}{\hat{R}} \left(1 - \frac{\rho}{\rho^*}\right)^{\hat{R}}\right) + d_4 \exp\left(C_2 \left(\frac{T}{T^*}\right)^{1.5} + C_3 \left(\frac{\rho^*}{\rho}\right)^5\right), \end{aligned} \tag{4.62}$$

with dimension $[J/msK]$. The variables, appearing in (4.60), (4.61), (4.62), are as

follows

$$\begin{aligned} Q &= 2 + C_5 \left(\Delta T^*\right)^{-0.6}, \\ \hat{R} &= Q\left(\frac{T}{T^*}\right) + 1, \\ S &= C_6 \left(\Delta T^*\right)^{-0.6}, \\ \Delta T^* &= \left|\frac{T}{T^*} - 1\right| + C_4. \end{aligned} \tag{4.63}$$

The constants $a$, $b$, $B$, $C$ and $d$ are given in Tab.(1.2) in App.(A). The term $\rho^*$ represents the density at the critical point. For water the critical density amounts

$$\rho^* = 317.7[kg/m^3].$$

## 4.6 Boundary conditions

The set of governing equations, including the transport equation for the void fraction and the relations for the physical properties, is associated with a single control volume. The assembly of control volumes constitutes the computational domain, i.e. system. It is possible to solve the system only if the number of unknown elements is equal to the number of equations. The formulation of the model is completed by specifying boundary and initial conditions.

### 4.6.1 Initial conditions

The initial conditions require physical consistency of all flow variables at the start of the simulation. For an incompressible flow it is sufficient to set an initial velocity and void fraction distribution in the computational domain. The level of the pressure is irrelevant for the further evolution of the flow, thus any initial level of its distribution is theoretically satisfactory. However, due to the fact, that the simulation algorithm uses the pressure distribution associated with a previous time step, it is required to initialize the pressure in accordance with velocity and density (if the gravitational force is present). This will decrease the computational effort at the beginning of the simulation (Ubbink, 1997). Since the flow is incompressible, the temperature remains independent of the pressure or density, thus its initial distribution may be arbitrary. Nevertheless, if one intends to simulate additional, temperature driven processes, such as a phase transition, it is clear, that the value of the temperature must correspond to that of the real system.

### 4.6.2 Physical boundaries

From the mathematical point of view there are two types of physical boundary conditions, namely Dirichlet and von Neumann conditions. The first applies to specifying

the value of the variable at the boundary and the second condition represents specifying the normal component of the gradient of the variable. However, in the light of the complex behaviour of gas-liquid flows, these straightforward conditions do not suffice. It is preferable to define conditions that depend on the sort of boundaries and physical characteristics of the flow in the neighbourhood of the boundary.

At an inflow boundary of the computational domain the distribution of the velocity is specified. The pressure is unknown and its boundary value is obtained from extrapolation from the interior of the domain. For the void fraction, one uses the Dirichlet condition, which implies that at the inlet one needs to specify $\alpha$ (Renardy and Renardy, (1991); Ubbink, 1997). The temperature is extrapolated from the interior of the domain using of the zero-gradient boundary condition.

The outflow boundary should be positioned as far from the region of interest of the flow as possible. In general, variables at the outlet need to be defined in such a way, that overall mass conservation is satisfied. There are two schemes used in this research, which fulfil this restriction. The choice of the approach depends on the case studied.
The first scheme assumes a fixed or averaged pressure at the outlet, with the zero-gradient (Versteeg and Malalasekera, (1995)) condition for the velocity. Nevertheless, this approach may be used only if one is certain, that there is no large velocity variation at the outflow boundary or that the pressure distribution is approximately constant. This restriction excludes the case of e.g. a fluid of high density with the gravitational force acting; if for example the outlet is a vertical plane the influence of the hydrostatic force will distort the constant pressure distribution so much, that the fixed pressure type of the boundary condition cannot be used.
The second scheme employes the extrapolation of flow quantities from the interior of the domain to the boundary. Thus, the velocity at the outflow has the same direction at the internal side of the domain, next to the boundary. Subsequently, the velocity at the outlet is scaled in such a way, that the overall mass in the system is conserved.
For the temperature the zero-gradient boundary condition is used. The void fraction, assuming small variations of the flow at the boundary, is extrapolated in the same manner as the temperature.

For solid boundaries, such as walls, a commonly utilised assumption has been implemented. The approach, termed zero slip condition, sets the flow velocity equal to the velocity of the boundary (Richardson, (1989)). Moreover, due to wall impermeability, there is no convection through the boundary. These assumptions cause, that the wall contributions in the convective terms of the governing equations disappear. The consequences of the no-slip boundary conditions appear also in the viscous term, namely

$$\tau_{nn} = 2\mu \left( \frac{\partial u_n}{\partial n} \right)_{wall} = 0 \tag{4.64}$$

and

$$\tau_{nt} = \mu \left( \frac{\partial u_t}{\partial n} \right)_{wall} \neq 0, \tag{4.65}$$

where the subscripts $n$ and $t$ indicate the normal and tangential direction to the boundary.
It suffices, that the no-slip boundary condition is applied to other flow variables, such as the void fraction (Kothe and Mjolsness, (1992)) or the temperature.
However, the pressure boundary condition requires consistency with velocity. For a fluid remaining at rest, in case the gravitational force acts, the momentum equation reduces to

$$\int_{\partial\Omega} p\vec{n}\, dS = \int_{\Omega} \rho\vec{g}\, \Omega. \tag{4.66}$$

Equation (4.66) imposes the gradient boundary condition related to the gravitational acceleration (Ubbink, 1997).

The last category of boundaries is the symmetry plane. The plane assumes the mirror counterpart of flow parameters at the other side of the plane. Consequently, at the plane of symmetry the normal component of the gradient of scalar quantities and of tangential components of the velocity are zero while the normal component of the velocity equals zero. There is no a flux across the plane of symmetry. The contribution of the symmetry plane to the convective terms in the conservation equations vanishes. The mirror condition also implies that the tangential gradient of the normal component of velocity component is zero, thus the viscous term reads

$$\tau_{nn} = 2\mu \left( \frac{\partial u_n}{\partial n} \right)_{sym} \neq 0 \tag{4.67}$$

and

$$\tau_{nt} = \mu \frac{\partial u_t}{\partial n} = 0, \tag{4.68}$$

where the subscripts $n$ and $t$ indicate the normal and tangential direction at the boundary.

# NUMERICAL APPROACH


To solve the set of governing equations, one needs to carry out their discretization preserving the conservation laws underlying them.

The present implicit discretization of the equations has been developed for a two-dimensional, structured grid. The discretized equations are collected in a matrix equation type of form representing the set of equations for the computational domain considered. The matrix equation is subsequently solved by the so-called Incomplete LU (Lower Upper) Decomposition. This method is also known as the Strongly Implicit Procedure (SIP) proposed by (Stone, (1968)).

Considered is two-phase, vapour-liquid flow consisting of constant-density phases. Since flow quantities are averaged over a given control volume using the Finite Volume method (Sec.(4.1)) combined with the Volume of Fluid approach (Sec.2.4.3), the flow is regarded as a mixture of a vapour and a liquid. Consequently, the flow behaves as quasi-compressible, in spite of the velocity field having a zero divergence in absence of a phase transition. To tackle this kind of flow problems, the solution algorithm, termed Semi Implicit Method for Pressure Linked Equations (SIMPLE), has been chosen (Caretto, Gosman, Patankar and Spalding, (1972)). The algorithm requires linearisation of the momentum equation, consequently it constitutes an iterative scheme. This approach is described in detail in (Perić and Ferziger, (1996)), where the method is used for a single-phase, incompressible flow. In this research the approach has been adapted to vapour-liquid flows in which phase transition occurs. SIMPLE has been coupled with the Energy of Fluid method (EOF) ((Anghaie and Ding, (1996); Anghaie and Ding, (1997))), which is used for the evaluation of the divergence of the velocity field.

As mentioned in Sec.(3.3), EOF operates on the enthalpy of the flow. The method utilizes the so-called energy fraction defined as the ratio of the enthalpy contained in one of the phase of the vapour-liquid mixture and the latent heat necessary to change the state of aggregation of the entire amount of that phase present in the control volume, see (3.45). The mentioned enthalpy applies to the heat exceeding the enthalpy at the state of thermodynamic equilibrium. The energy fraction assumes values between minus one and plus one. Negative values are associated with condensation

and, in particular, the minimum value, minus one, appears when the entire vapour content in the control volume transfers to liquid. Positive values of the fraction apply to evaporation. A value of zero corresponds to the situation of thermodynamic equilibrium, i.e. no phase transition. The problem of the phase change and its consequences for the model has been described in Chapter (4). However, in Chapter (4) the discussion has been confined to the situation in which the phase transition occurs in a control volume containing pure vapour or pure liquid. In this section the model is generalized to cases in which transition appears in a control volume containing a vapour-liquid mixture.

The Volume of Fluid method uses the void fraction as the indicator for the distribution of the phases in the computational domain. The equation for the transport of the void fraction, (4.36), is treated in a special way which includes some additional numerical procedures. These procedures increase the resolution of the interface. The discretization of the transport equation for the void fraction is discussed in Chapter (6).

As mentioned in Sec.(4.5), the physical properties of the vapour are those of steam, whereas these for liquid represent water.

## 5.1 Spatial discretization

The Finite-Volume method averages values of flow variables and properties over a given control volume. The averaged value is associated with the value of the flow variable at the centre of gravity of the computational cell. In case all variables and properties are taken as the spatially centred values, one deals with a so-called co-located grid discretization scheme ((Perić and Ferziger, (1996))). The grid utilized in the present research is structured, which means that each cell has four neighbours and a grid line of a given direction can intersect a grid line in the other direction only once in the entire computational domain. The co-located grid arrangement has significant consequences for the discretization procedure, namely it necessitates approximating the flux terms at the boundaries of the control volume. Variables at such a cell face are interpolated (in the interior of the domain) or extrapolated (at domain boundaries). Due to the interpolation, additional problems arise associated with unphysical oscillations of variables, termed odd-even decoupling (Perić and Ferziger, (1996); Banerjee, Takahira and Takahashi, (2004); Banerjee, Takahira and Horiuchi, (2003)). To overcome this problem, some additional, numerical procedures have been implemented which improve the interpolation schemes, substantially damping the oscillations. The basic interpolation scheme has second-order accuracy in space, but the mentioned improvements use higher-order approximations. The exception is made for the energy equation, where for the purpose of smoothness of the solution first-order accurate interpolation in space has been used. Thus, formally, the global spatial accuracy of

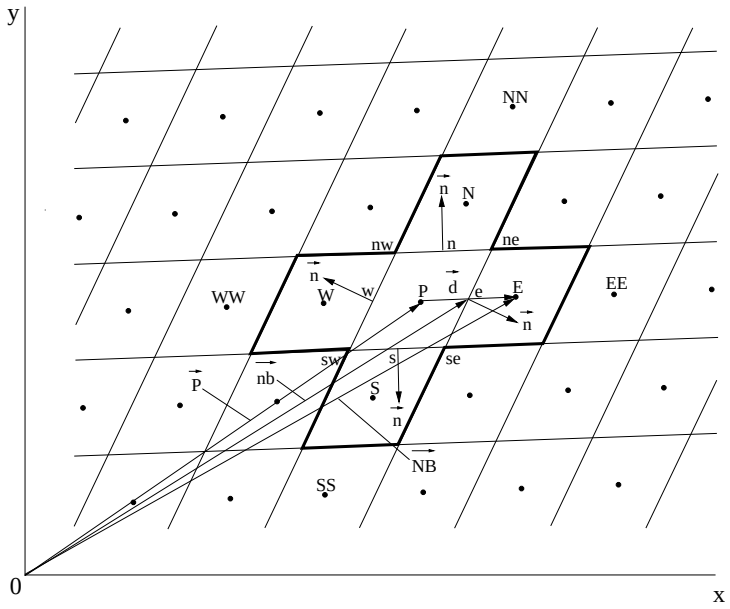


FIGURE 5.1: *Computational molecule in case of a two-dimensional, structured grid.*

the scheme is first-order. The scheme is designed such that it uses only five points in its computational molecule, see Fig.(5.1). This substantially simplifies constructing the matrix equation of the discretized equations.

### 5.1.1 Basic geometrical quantities

All flow variables are cell-averaged quantities positioned at mid point $\vec{P}$ of the cell. The mid point is the position vector

$$\vec{P}= \frac{1}{4}\left(\vec{x}_{ne}+\vec{x}_{nw}+\vec{x}_{se}+\vec{x}_{sw}\right), \tag{5.1}$$

where $\vec{x}_{ab}$ denotes the corner points of the cell. For the purpose of interpolation the vector between node $P$ and the neighbouring nodes, at $\vec{NB}$, is required, see Fig.(5.1) where $NB = E$. This vector is obtained from

$$\vec{d} = \vec{NB} - \vec{P} = \vec{x}_{NB} - \vec{x}_P. \tag{5.2}$$

A surface vector, normal to the cell face, the $e$ face, reads

$$\vec{n}S_e = \left(S_{x_n},\ \ S_{y_n}\right)^T = \vec{e}_z \times \left(\vec{x}_{ne} - \vec{x}_{se}\right). \tag{5.3}$$

The area of the face of the control volume is

$$S_{nb} = \sqrt{S_{x_{nb}}^2 + S_{y_{nb}}^2}. \tag{5.4}$$

The last important geometrical quantity is the volume of cell $P$, given by

$$\Omega_P = \frac{1}{2}\left(\vec{S}_w \times \vec{S}_s + \vec{S}_e \times \vec{S}_n\right).\vec{e}_z, \tag{5.5}$$

where $\vec{S}$ is the surface vector of a cell face. This vector, for one of the faces, e.g. $e$, reads

$$\vec{S}_e = (S_x,\ S_y)^T = \vec{x}_{ne} - \vec{x}_{se}. \tag{5.6}$$

### 5.1.2 Basic terms of spatial discretization

There are two types of terms in the governing equations, namely volume and surface integrals.

The volume integrals are approximated as the value of the variable $\phi$ averaged over the control volume, multiplied by the volume of the control volume. For control volume $P$ the integral reads, dividing the equation by $\Omega_P$

$$\frac{1}{\Omega_P}\int\limits_{\Omega_P} \phi\, d\Omega \cong \phi_P, \tag{5.7}$$

which constitutes a second-order accurate approximation.

The approximation of the surface integral is taken as the sum of products of the variable value interpolated to the cell face and the vector normal to the cell face.

$$\frac{1}{\Omega_P}\int\limits_{\partial\Omega_P} \vec{f}\,(\phi).\vec{n}\, d\Omega \cong \frac{1}{\Omega_P}\sum_{nb} \vec{f}_{nb}\,(\phi).\vec{n}S_{nb}, \tag{5.8}$$

with $\vec{f}$ denoting the flux vector. The basic interpolation scheme is of second order. The interpolation procedure employs the spatial weighting factor $\zeta$, such that the variable $\phi$ at face $nb$ is computed as

$$\phi_{nb} = \zeta_{nb}\phi_P + (1-\zeta_{nb})\,\phi_{NB}, \tag{5.9}$$

where

$$\zeta_{nb} = \frac{\left|\vec{NB} - \vec{nb}\right|}{\left|\vec{d}\right|}, \tag{5.10}$$

with the vectors $\vec{NB}$ and $\vec{nb}$ the position of the neighbouring node and the position of the point at the center of the cell face positioned in between $P$ and $NB$, respectively, see Fig.(5.1). In the case of a uniform mesh $\zeta_{nb} = 1/2$. Some face values are approximated by an interpolation of higher order. This will be discussed later.

## 5.2 Discretization of governing equations

### 5.2.1 Unsteady term

In the formulation used in this research the unsteady term has the same form for each equation. The spatial discretization leads to an ordinary differential in time, such that

$$\frac{\partial \phi}{\partial t} = f\left(t, \phi\left(t\right)\right). \tag{5.11}$$

The left-hand side of (5.11) is approximated by a first-order scheme. The unknown value of $\phi$, at a subsequent time step, is obtained from

$$\phi^{n+1} = \phi^{n} + f\left(t_{n+1}, \phi^{n+1}\right)\Delta t + O\left(\Delta t^{2}\right), \tag{5.12}$$

where superscript $n+1$ is the shorthand notation of time $t + \Delta t$, whereas $n$ denotes previous time $t$. The function $f$ at time $t + \Delta t$ is estimated using the value of $\phi$ at the subsequent time $t + \Delta t$ ((Perić and Ferziger, (1996))). The graphical representation of the approach is shown on Fig.(5.2). This time-discretization scheme is

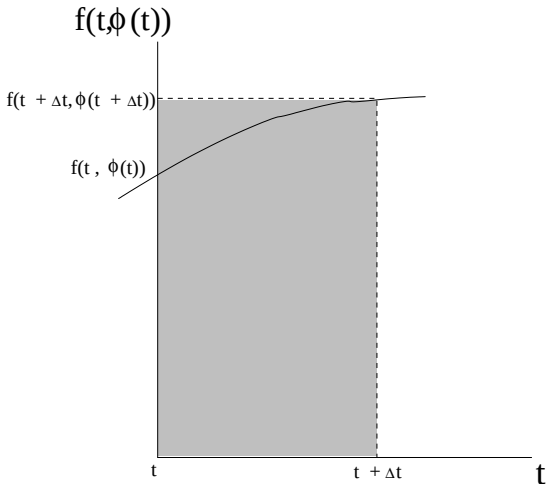


FIGURE 5.2: *Graphical representation of the Euler implicit approximation of a time derivative.*

termed implicit or backward Euler. Finally, averaging of the time derivative yields the discretised unsteady term

$$\Omega_P \frac{\partial}{\partial t}\frac{1}{\Omega_P}\int\limits_{\Omega_P} \phi \, d\Omega \cong \frac{\phi_P^{n+1} - \phi_P^{n}}{\Delta t}\Omega_P = A_{u_P}\phi_P^{n+1} - S_{u_P}, \tag{5.13}$$

where

$$A_{u_P} = \frac{\Omega_P}{\Delta t}, \qquad S_{u_P} = \frac{\phi_P^n}{\Delta t}\Omega_P. \tag{5.14}$$

The process is iterative, the variable $\phi_P^{n+1}$ the result of the present iteration. In this case, if it is necessary for the sake of clearness, the variable $\phi^{n+1}$ will be replaced by $\phi^{*+1}$.

### 5.2.2 Convective term

For every governing equation, the convective term is treated implicitly. Thus, the value of the variables in the flux terms is unknown and appears as part of the solution. The implicit scheme increases the numerical stability of the calculation process (Perić and Ferziger, (1996)). Approximations for the flux term, used for the momentum and the energy equations are not the same. The choice of two different schemes is motivated by characteristic features of the equations. These features will be discussed in the subsequent paragraphs.

The convective term, contributing to the momentum equation, is discretised by the Central Difference Scheme (CDS) which requires the addition of so-called artificial dissipation terms. The scheme has second-order accuracy and is used in simulations of multi-phase as well as single-phase flows. It obtains the variable at the cell face by linear interpolation using (5.9). However, the second-order accuracy of the scheme is deteriorated by the oscillatory behaviour of the result (Perić and Ferziger, (1996); Banerjee, Takahira and Takahashi, (2004)). Suppose an equidistant, one-dimensional, co-located grid, for which a discretised surface integral is computed, see (5.8). The approximation of the variable at the cell face is performed by (5.9). Then, the summation over the two boundaries of the cell, cancels the contribution of the variable at point $P$. Consequently, effectively the scheme uses a grid twice as coarse. Moreover, the scheme for the variable at the central node involves contributions from two neighbouring control volumes, without contribution from the central one itself. Thus, the result shows a decoupled solution characterised by oscillations, see Fig.5.3. Implementation of artificial dissipation terms, involv-

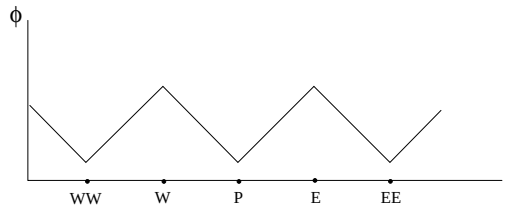


FIGURE 5.3: *Decoupled behaviour of the CDS solution on one dimensional scheme.*

ing the second and fourth derivative of $\phi$, cures the problem. Originally, the method

has been utilized for damping unphysical oscillations of variables, which occur as the result of the sharp discontinuity e.g. a shock wave, (Pulliam, (1986); Beam and Warming, (1976); Steger, (1986)). In the scheme used for the present research, the velocity field, from the point of view of the mathematical model, is continuous everywhere in the domain. However, the control-volume averaging in the discretization results in an artificial discontinuity at the boundaries of each control volume. The higher the velocity gradient, the larger the discontinuity in the control-volume averaged velocity. Taking this into account, implementation of artificial dissipation seems to be a suitable solution. Hence, the flux term of the momentum equation, for a given iteration, reads

$$\int_{\partial\Omega} \rho u \left(\vec{u}.\vec{n}\right) \, dS \cong \sum_{nb} \left[\rho^*_{nb} u^{*+1}_{nb} \left(\vec{u}^*_{nb}.\vec{n}\right) S_{nb} + D^{(2)} + D^{(4)}\right]. \tag{5.15}$$

In this scheme, the density and the normal component of velocity are evaluated at the previous time (iteration) all at the face of the control volume and are assumed known. The unknown component of the face velocity, $u^{*+1}_{nb}$, is given by

$$u^{*+1}_{nb} = \zeta_{nb} u^{*+1}_P + \left(1 - \zeta_{nb}\right) u^{*+1}_{NB}. \tag{5.16}$$

The term $D^{(2)}$ is the second-order artificial dissipation, which reads

$$D^{(2)} = -\epsilon^{(2)} \left|\dot{m}^*\right| \left(u^{*+1}_{NB} - u^{*+1}_P\right), \tag{5.17}$$

where $\epsilon^{(2)}$ is the dimensionless pressure-controlled parameter discussed later. The term $\dot{m}^*$ represents the mass flux defined as

$$\dot{m}^* = \rho^*_{nb} \vec{u}^*_{nb}.\vec{n} S_{nb}. \tag{5.18}$$

The second-order artificial dissipation has the implicit form. The second-order artificial dissipation term, when summed over all faces, results in a term proportional to the Laplacian of $u$. The fourth order dissipation term, $D^{(4)}$, is explicit and reads

$$D^{(4)} = \epsilon^{(4)} \left|\dot{m}^*\right| \left(u^*_{NNB} - 3u^*_{NB+1} + 3u^*_P - u^*_{NB-1}\right), \tag{5.19}$$

where subscript $NNB$ denotes the node positioned next to $NB + 1$, such as $EE$, $WW$, $NN$ and $SS$; see Fig(5.1). If subscript $NB + 1$ indicates node $E$, then $NB - 1$ denotes $W$ and the other way round. The same rule applies to $N$ and $S$. The fourth-order artificial dissipation term, when summed over all faces, results in a term proportional to the bi-harmonic of $u$. The factor $\epsilon^{(4)}$ reads

$$\epsilon^{(4)} = MAX\left(0, b_1 - b_2 \epsilon^{(2)}\right), \tag{5.20}$$

where

$$\epsilon^{(2)} = MIN\left(a_1, a_2 \frac{\left|p^*_{NB+1} - 2p^*_P + p^*_{NB-1}\right|}{|4p_{init}|}\right), \tag{5.21}$$

with the initial pressure, $p_{init}$, which is the constant initial pressure set at the start of the computation. Parameters $a_1$, $a_2$, $b_1$ and $b_2$ are constants. Typically, it is a matter of experience how to define $\epsilon^{(2)}$ and $\epsilon^{(4)}$ or how to select proper values of the constants. However, it is important to realise, that the artificial dissipation terms modify the original flux term, thus they should be kept as small as possible while still maintaining stability (Pulliam, (1986)). The general form of the convective term now reads

$$\sum_{nb} \dot{m}^*_{nb} u^{*+1}_{nb} = A_{c_P} u^{*+1}_P + \sum_{NB} A_{c_{NB}} u^{*+1}_{NB} - S_{c_P}, \tag{5.22}$$

where

$$\begin{aligned} A_{c_P} &= \sum_{nb} \left[\dot{m}^*_{nb}\zeta + |\dot{m}^*|_{nb}\,\epsilon^{(2)}\right], \\ A_{c_{NB}} &= \dot{m}^*_{nb}\,(1-\zeta) - |\dot{m}^*|_{nb}\,\epsilon^{(2)}, \\ S_{c_P} &= -D^{(4)}. \end{aligned} \tag{5.23}$$

The convective term contributing to the energy equation employs the first-order approximation of the flux, namely the Upstream Differential Scheme (UDS). The choice of this scheme has been dictated by the requirement to obtain a smooth solution for the energy. Unlike CDS, the monotonicity of the solution is independent of the magnitude of the gradient of the flow variable. This is an essential feature required for handling additional, temperature driven occurrences in the flow, such as phase transition. The disadvantage of UDS is its dissipative character which causes an underprediction of gradients of the solution.

The specific internal energy of a mixture, present in the equation, is defined as the sum of the energy of the vapour and the liquid within the control volume. The sum is obtained employing (2.37). The energy of an individual phase of the mixture is defined as the product of the specific heat at constant volume and temperature. However, the specific heats of steam and water differ substantially and implementation of the mixture energy involving different specific heats is avoided by taking the specific heat of water equal to that of steam, while the right-hand side of the equation has been rearranged maintaining the correct form of the equation, see Sec.(4.2.3). The convective term of the energy equation for a given iteration reads

$$\int_{\partial\Omega} \rho C v_g T\,(\vec{u}.\vec{n})\; dS \cong \sum_{nb} \dot{m}^*_{nb} e^{*+1}_{nb}, \tag{5.24}$$

where, according to UDS, the face value of the energy is approximated by

$$e_{nb}^{*+1} = Cv_g T_{nb}^{*+1} = \begin{cases} Cv_g T_P^{*+1} & \text{if } \dot{m} \geq 0, \\ Cv_g T_{NB}^{*+1} & \text{if } \dot{m} < 0. \end{cases} \tag{5.25}$$

The general form of the term is given by

$$\sum_{nb} \dot{m}_{nb}^{*} Cv_g T_{nb}^{*+1} = A_{c_P} T_P^{*+1} + \sum_{nb} A_{c_{NB}} T_{NB}^{*+1}, \tag{5.26}$$

where

$$\begin{aligned} A_{c_P} &= \sum_{nb} \dot{m}_{nb}^{*} Cv_g \quad \text{for } \dot{m} \geq 0, \\ A_{c_{NB}} &= \dot{m}_{nb}^{*} Cv_g \qquad \text{for } \dot{m} < 0. \end{aligned} \tag{5.27}$$

### 5.2.3 Surface source terms

**Momentum equation**

The momentum equation contains the surface integral associated with the surface force, namely the pressure and the viscous stress.
The term containing the pressure is discretized using

$$-\int_{\partial\Omega} p\vec{n}\, dS \cong -\sum_{nb} p_{nb}^{*} \vec{n} S_{nb}, \tag{5.28}$$

where $p_{nb}^{*}$ is evaluated using the standard CDS. Consequently, the general form of the term reads

$$-\sum_{nb} p_{nb}^{*} \vec{n} S_{nb} = -\sum_{nb} \left(\zeta_{nb} p_P^{*} + (1-\zeta_{nb})\, p_{NB}^{*}\right) \vec{n} S_{nb} = S_{p_P}. \tag{5.29}$$

The diffusive term in the momentum equation is

$$\int_{\partial\Omega} \bar{\bar{\tau}}\vec{n} dS = \vec{e}_x \int_{\partial\Omega} \left(\tau_{xx} n_x + \tau_{xy} n_y\right) dS + \vec{e}_y \int_{\partial\Omega} \left(\tau_{yx} n_x + \tau_{yy} n_y\right)\, dS, \tag{5.30}$$

where $\vec{e}$ is the unit vector in the x-direction or y-direction. Here one considers the x-component of the momentum equation. This contribution consists of two parts, the contribution due to $\tau_{xx}$ and $\tau_{xy}$. Consider the contribution due to $\tau_{xx}$ first.

$$\int_{\partial\Omega} \tau_{xx} n_x\, dS = \int_{\partial\Omega} \left[2\mu \frac{\partial u}{\partial x} - \frac{2}{3}\mu \left(\vec{\nabla}.\vec{u}\right)\right] n_x\, dS. \tag{5.31}$$

In the discretization the integral is replaced by a summation over the four faces of the control volume, i.e.

$$\begin{aligned}
&\int_{\partial\Omega} \tau_{xx} n_x \, dS \cong \sum_{nb} \left[ 2\mu \frac{\partial u}{\partial x} - \frac{2}{3}\mu \left( \vec{\nabla}.\vec{u} \right) \right]_{nb} (S\vec{n}.\vec{e}_x) = \\
&\sum_{nb} \left[ 2\mu_{nb} \left( \frac{\delta u^*}{\delta x} \right)_{nb} - \frac{2}{3}\mu_{nb} \left( \vec{\nabla}.\vec{u} \right)^*_{nb} \right] S_{x_{n,nb}} + \\
&\sum_{nb} \left[ \mu_{nb} \left( \frac{\left( \vec{\nabla} u^{*+1} \right).\vec{d}}{\left| \vec{d} \right|} \right)_{nb} - \mu_{nb} \left( \frac{\left( \vec{\nabla} u^{*} \right).\vec{d}}{\left| \vec{d} \right|} \right)_{nb} \right] S_{x_{n,nb}}
\end{aligned} \tag{5.32}$$

The last term has been added in order to introduce partly implicit discretization. The final result is

$$\begin{aligned}
&\int_{\partial\Omega} \tau_{xx} n_x \, dS \cong \sum_{nb} \left( \mu_{nb} \frac{u^{*+1}_{NB} - u^{*+1}_{P}}{\left| \vec{d} \right|} \left| \vec{n} S_{nb} \right| + \mu_{nb} \left( \frac{\delta u^*}{\delta x} \right)_{nb} S_{x_{n,nb}} \right) + \\
&\sum_{nb} \mu_{nb} \left( \left( \frac{\delta u^*}{\delta x} \right)_{nb} S_{x_{n,nb}} - \left( \left( \frac{\delta u^*}{\delta x} \right)_{nb} d_{x_{nb}} + \left( \frac{\delta u^*}{\delta y} \right)_{nb} d_{y_{nb}} \right) \frac{\left| \vec{n} S_{nb} \right|}{\left| \vec{d} \right|} \right) - \\
&\sum_{nb} \mu_{nb} \frac{2}{3} \left( \vec{\nabla}.\vec{u} \right)^*_{nb} S_{x_{n,nb}},
\end{aligned} \tag{5.33}$$

Terms of the form $(\delta\phi/\delta x)_{nb}$ are the face value of the gradient of $\phi$ in $x$ direction. The gradient is first evaluated using (5.8) and then interpolated to the face by (5.9), namely

$$\left( \frac{\delta \phi}{\delta x} \right)_{nb} = \zeta_{nb} \frac{\left( \sum_{nb} \phi_{nb} S_{x_{n,nb}} \right)_P}{\Omega_P} + (1 - \zeta_{nb}) \frac{\left( \sum_{nb} \phi_{nb} S_{x_{n,nb}} \right)_{nb}}{\Omega_{NB}}. \tag{5.34}$$

The subscript $x_{n,nb}$ next to the face notation, $S$, denotes the component of the vector normal to cell face $nb$, in direction $x$. The discretization of the velocity divergence, present in (5.33), will be discussed in Sec.(5.3). The divergence at the cell face is approximated by equation (5.9). The term before the last term of the right hand side of (5.33) is the so-called Deffered Correction (Perić and Ferziger, (1996); Khosla and Rubin, (1974)) which provides the correction associated with non-orthogonality between vector $\vec{d}$ and face normal $\vec{n}S$. The general form of (5.33) reads

$$\int_{\partial\Omega} \tau_{xx} n_x \, dS \cong -A_{d1_P} u^{*+1}_P - \sum_{nb} A_{d1_{NB}} u^{*+1}_{NB} + S_{d1_P}, \tag{5.35}$$

where

$$
\begin{aligned}
A_{d1_P} &= \sum_{nb} \mu_{nb} \frac{|\vec{n} S_{nb}|}{\left|\vec{d}\right|}, \\
A_{d1_{NB}} &= -\mu_{nb} \frac{|\vec{n} S_{nb}|}{\left|\vec{d}\right|}, \\
S_{d1_P} &= \sum_{nb} \mu_{nb} \left( 2 \left( \frac{\delta u^*}{\delta x} \right)_{nb} S_{x_{n,nb}} - \left( \left( \frac{\delta u^*}{\delta x} \right)_{nb} d_{x_{nb}} + \left( \frac{\delta v^*}{\delta y} \right)_{nb} d_{y_{nb}} \right) \frac{|\vec{n} S_{nb}|}{\left|\vec{d}\right|} \right) - \\
&\sum_{nb} \mu_{nb} \frac{2}{3} \left( \vec{\nabla} . \vec{u} \right)^*_{nb} S_{x_{n,nb}}.
\end{aligned}
\tag{5.36}
$$

The contribution due to $\tau_{xy}$ is discretized explicitly. For the $x$-direction it reads

$$
\int_{\partial\Omega} \tau_{xy} n_y \, dS \cong \sum_{nb} \mu_{nb} \left( \left( \frac{\delta u^*}{\delta y} \right)_{nb} + \left( \frac{\delta v^*}{\delta x} \right)_{nb} \right) S_{y_{n,nb}} = S_{d2_P} \tag{5.37}
$$

**Energy equation**

The source term in the energy equation is associated, as discussed in Sec.(4.2.3), with the amount of energy contained in one of the phase of a vapour-liquid mixture, that will be converted from sensible heat into latent heat or the other way around, depending on the direction of the phase transition.
The discretised energy equation assumes, that a phase change may begin in a control volume that is filled by pure vapour or, by pure water, or by a mixture of these two. In the case of a mixture, the amount of energy associated with latent heat, and released or absorbed during a phase transition, is dependent on the content of water or steam. In order to evaluate this energy in a quantitative way, one needs to consider the system separately, for the substance undergoing the transition and for the substance generated in the phase transition.

In the case of the medium undergoing the phase change, one may assume that when the process is accomplished the temperature of the substance will be the saturation value. Thus, the amount of exchanged energy reads

$$
-S_{p_{P1}} = \begin{cases} \alpha_P^n \rho_g C v_g \left( T_P^n - T_{sat_P}^n \right) \frac{\Omega_P}{\Delta t} & \text{condensation,} \\ \left( 1 - \alpha_P^n \right) \rho_l \frac{C v_g}{C v_l} C v_l \left( T_P^n - T_{sat_P}^n \right) \frac{\Omega_P}{\Delta t} & \text{evaporation.} \end{cases} \tag{5.38}
$$

Like the medium undergoing phase change, the generated substance will have the temperature of saturation at the moment the phase transition is accomplished. However, one may not assume that in the control volume the newly produced phase will

occupy the same volume as this before the transition. Suppose the case of evaporation. The generated vapour will in general not fill the entire space that was occupied by the vapour at the initial instant. Consequently, when the evaporation is accomplished, the vapour content of the control volume will consist of the newly generated vapour and the vapour that already existed before the evaporation began. Thus, the energy content will be somewhere between that of the state of saturation and that of the vapour before the transition. The difference between the new energy state and that at the beginning of the process gives the energy exchange (temperature drop) for the vapour.
The first step to find the difference is the evaluation of the relation between the volume of the generated substance and the volume of the phasic content of the substance in the control volume. The relation is given by

$$\begin{aligned} \frac{\Omega_l}{\Omega_{l_{CV}}} &= \frac{\left(1-\alpha_P^n\right)\frac{\rho_l}{\rho_g}\frac{q_P^n}{l_P^n}\Omega_P}{\left(\alpha_P^n+\left(1-\alpha_P^n\right)\frac{\rho_l}{\rho_g}\frac{q_P^n}{l_P^n}\right)\Omega_P} \quad \text{evaporation,} \\ \frac{\Omega_g}{\Omega_{g_{CV}}} &= \frac{\alpha_P^n\frac{\rho_g}{\rho_l}\frac{q_P^n}{l_P^n}\Omega_P}{\left(\left(1-\alpha_P^n\right)+\alpha_P^n\frac{\rho_g}{\rho_l}\frac{q_P^n}{l_P^n}\right)\Omega_P} \quad \text{condensation.} \end{aligned} \tag{5.39}$$

The derivation of the forms of the numerators and denominators can be found in Sec.(5.3), see (5.50) and the relevant part of (5.51). The term $q_P^n/l_P^n$ denotes the relation between superheating or super-cooling energy and the latent heat, see(5.49). The volumetric amount of the generated substance in the control volume reads

$$\begin{aligned} &\frac{\Omega_l}{\Omega_{l_{CV}}}\left(\alpha_P^n+\delta\alpha\right)\Omega_P = \\ &\frac{\left(1-\alpha_P^n\right)\frac{\rho_l}{\rho_g}\frac{\delta q_P^n}{l_P^n}}{\left(\alpha_P^n+\left(1-\alpha_P^n\right)\frac{\rho_l}{\rho_g}\frac{\delta q_P^n}{l_P^n}\right)}\left(\alpha_P^n+\delta\alpha\right)\Omega_P \quad \text{evaporation,} \\ &\frac{\Omega_g}{\Omega_{g_{CV}}}\left(\alpha_P^n+\delta\alpha\right)\Omega_P = \\ &\frac{\alpha_P^n\frac{\rho_g}{\rho_l}\frac{\delta q_P^n}{l_P^n}}{\left(\left(1-\alpha_P^n\right)+\alpha_P^n\frac{\rho_g}{\rho_l}\frac{\delta q_P^n}{l_P^n}\right)}\left(\alpha_P^n+\delta\alpha\right)\Omega_P \quad \text{condensation.} \end{aligned} \tag{5.40}$$

The term $\delta\alpha$ denotes the change of the void fraction in the control volume caused by the phase transition. For details, see Sec.(5.3), equation (5.54). Finally, the difference

of energy brought about by the appearance of generated substance is defined by

$$-S_{p_{P2}} = \begin{cases} \rho_g C v_g \left(T_P^n - T_{sat_P}^n\right) \dfrac{\left(1-\alpha_P^n\right)\frac{\rho_l}{\rho_g}\frac{\delta q_P^n}{l_P^n}}{\left(\alpha_P^n + \left(1-\alpha_P^n\right)\frac{\rho_l}{\rho_g}\frac{\delta q_P^n}{l_P^n}\right)} \left(\alpha_P^n + \delta\alpha\right)\frac{\Omega_P}{\Delta t}, \\ \rho_g \frac{Cv_g}{Cv_l} C v_l \left(T_P^n - T_{sat_P}^n\right) \dfrac{\alpha_P^n \frac{\rho_g}{\rho_l}\frac{\delta q_P^n}{l_P^n}}{\left(\left(1-\alpha_P^n\right) + \alpha_P^n \frac{\rho_g}{\rho_l}\frac{\delta q_P^n}{l_P^n}\right)} \left(\alpha_P^n + \delta\alpha\right)\frac{\Omega_P}{\Delta t}. \end{cases} \tag{5.41}$$

The upper line of (5.41) applies to evaporation, whereas the lower one applies to condensation. Summation of (5.41) and (5.38) gives the rate of the energy change in the control volume during the phase transition, see Sec.(4.2.3). The energy source term present at the right hand side of the energy equation is now

$$Q_{trans} = -\left(S_{p_{P1}} + S_{p_{P2}}\right). \tag{5.42}$$

As seen, the void fraction $\alpha$, the temperature $T$ and the temperature of saturation $T_{sat}$ in (5.38-5.41) originate from the previous time step, because they represent the initial conditions of the phase change.
The diffusion term in the energy equation consists of heat conduction and the work done by the viscous stresses. The heat conduction term is discretized in an implicit form with the Deffered Correction term accounting the non-orthogonality between the vector $\vec{d}$ and the normal to the cell face. The conduction term reads

$$\int_{\partial\Omega} \lambda \left(\vec{\nabla} T\right).\vec{n}\, dS \cong \sum_{nb} \lambda_{nb} \frac{T_{NB}^{*+1} - T_P^{*+1}}{\left|\vec{d}\right|} \left|\vec{n}S\right| + \sum_{nb} \lambda_{nb} \left( \left( \left(\frac{\delta T^*}{\delta x}\right)_{nb} S_{x_{n,nb}} + \left(\frac{\delta T^*}{\delta y}\right)_{nb} S_{y_{n,nb}} \right) - \left( \left(\frac{\delta T^*}{\delta x}\right)_{nb} d_x + \left(\frac{\delta T^*}{\delta y}\right)_{nb} d_y \right) \frac{\left|\vec{n}S\right|}{\left|\vec{d}\right|} \right). \tag{5.43}$$

The last term of the right hand side of (5.43) is the Deffered Correction.
The general form of (5.43) reads

$$\int_{\partial\Omega} \lambda \left(\vec{\nabla} T\right).\vec{n}\, dS = -A_{d1_P} T_P^{*+1} - \sum_{nb} A_{d1_{NB}} T_{NB}^{*+1} + S_{d1_P}, \tag{5.44}$$

where

$$
\begin{aligned}
A_{d1_P} &= \sum_{nb} \lambda_{nb} \frac{|\vec{n}S|}{\left|\vec{d}\right|}, \\
A_{d1_{NB}} &= -\lambda_{nb} \frac{|\vec{n}S|}{\left|\vec{d}\right|}, \\
S_{d1_P} &= \sum_{nb} \lambda_{nb} \left( \left( \left( \frac{\delta T^*}{\delta x} \right)_{nb} S_{x_{n,nb}} + \left( \frac{\delta T^*}{\delta y} \right)_{nb} S_{y_{n,nb}} \right) - \left( \left( \frac{\delta T^*}{\delta x} \right)_{nb} d_x + \left( \frac{\delta T^*}{\delta y} \right)_{nb} d_y \right) \frac{|\vec{n}S|}{\left|\vec{d}\right|} \right).
\end{aligned}
\tag{5.45}
$$

The detailed derivation of the form of (5.43) is given in App.(B.2.1).
The second part of the diffusion term is associated with the work done by viscous stresses. This part of the energy equation is discretized explicitly. The discretised term assumes the form

$$
\begin{aligned}
&\int_{\Omega} \left( \vec{\bar{\tau}} \, \vec{\nabla} \right) . \vec{u} \, d\Omega \cong 2\mu_P \left( \left( \frac{\delta u^*}{\delta x} \right)_P^2 + \left( \frac{\delta v^*}{\delta y} \right)_P^2 \right) \Omega_P + \\
&\mu_P \left( \left( \left( \frac{\delta u^*}{\delta y} \right)_P + \left( \frac{\delta v^*}{\delta x} \right)_P \right)^2 - \frac{2}{3} \left( \left( \frac{\delta u^*}{\delta x} \right)_P + \left( \frac{\delta v^*}{\delta y} \right)_P \right)^2 \right) \Omega_P = S_{d2_P}.
\end{aligned}
\tag{5.46}
$$

The detailed derivation of (5.46) is given in App.(B.2.2).

### 5.2.4 Volume source term

There is only one volume source term appearing in the momentum equation. It is associated with the gravitational force acting volumetrically on the substance contained in the control volume. The discretised volume source term reads

$$
\int_{\Omega} \rho \vec{g} \, d\Omega \cong -\rho_P^* g \Omega_P = S_{g_P}. \tag{5.47}
$$

## 5.3 Discretization of divergence of velocity field

In section (4.4), the derivation of the velocity divergence has been described. However, this mathematical model is limited to cases where a control volume, at the beginning of the phase transition process, is filled by pure steam or pure water. The description in this section includes the situation where the control volume may also be filled by a steam-water mixture. The model will be discussed using the discrete form of the equations.

The volumetric amount of a pure substance that undergoes the phase transition has been defined by (3.45). If the substance occupies only a part of the cell, this amount is equal to

$$\begin{aligned} \Omega_e &= (1-\alpha_P^n)\,\frac{\delta q_P^n}{l_P^n}\Omega_P, \\ \Omega_c &= \alpha_P^n \frac{\delta q_P^n}{l_P^n}\Omega_P, \end{aligned} \tag{5.48}$$

for evaporation and condensation, respectively. The term $\delta q_P^n / l_P^n$ represents the relation between the superheating or the super-cooling energy and the latent heat, namely

$$\frac{\delta q_P^n}{l_P^n} = \frac{Cp_k\left(T_P^n - T_{sat_P}^n\right)}{l_P^n}, \tag{5.49}$$

where subscript $k$ denotes the phase relevant to the direction of the phase transition. The volume of the vapour resulting from evaporation, $\Omega_l$, or the volume of the vapour undergoing condensation, $\Omega_g$, equals

$$\begin{aligned} \Omega_l &= (1-\alpha_P^n)\,\frac{\rho_l}{\rho_g}\frac{\delta q_P^n}{l_P^n}\Omega_P, \\ \Omega_g &= \alpha_P^n \frac{\delta q_P^n}{l_P^n}\Omega_P, \end{aligned} \tag{5.50}$$

where subscripts $l$ and $g$ denote evaporation and condensation, respectively. The volume occupied by the vapour-liquid mixture upon accomplishment of the phase transition equals the sum of $\Omega_P$ and the volume increment or decrement (depending on the direction of the transition) $\delta\Omega_{e,c}$, namely

$$\begin{aligned} \Omega_P + \delta\Omega_e &= (1-\alpha_P^n)\Omega_P - (1-\alpha_P^n)\frac{\delta q_P^n}{l_P^n}\Omega_P + \alpha_P^n\Omega_P + \frac{\rho_l}{\rho_g}\,(1-\alpha_P^n)\frac{\delta q_P^n}{l_P^n}\Omega_P, \\ \Omega_P + \delta\Omega_c &= (1-\alpha_P^n)\,\Omega_P + \frac{\rho_g}{\rho_l}\alpha_P^n\frac{\delta q_P^n}{l_P^n}\Omega_P + \alpha_P^n\Omega_P - \alpha_P^n\frac{\delta q_P^n}{l_P^n}\Omega_P. \end{aligned} \tag{5.51}$$

Rearrangement of (5.51) yields the volume change

$$\begin{aligned} \delta\Omega_e &= \left(\frac{\rho_l}{\rho_g} - 1\right)(1-\alpha_P^n)\,\frac{\delta q_P^n}{l_P^n}\Omega_P, \\ \delta\Omega_c &= \alpha_P^n\left(\frac{\rho_g}{\rho l} - 1\right)\frac{\delta q_P^n}{l_P^n}\Omega_P. \end{aligned} \tag{5.52}$$

The void fraction in volume $\Omega_P + \delta\Omega_e$ and $\Omega_P + \delta\Omega_c$ is equal to the sum of $\alpha_P^n$ and the void fraction change, $\delta\alpha_{e,c}$, and reads

$$\begin{aligned} \alpha_P^n + \delta\alpha_e &= \frac{\alpha_P^n \Omega_P + \Omega_l}{\Omega_P + \delta\Omega_e}, \\ \alpha_P^n + \delta\alpha_c &= \frac{\alpha_P^n \Omega_P - \Omega_g}{\Omega_P + \delta\Omega_c}, \end{aligned} \tag{5.53}$$

for evaporation and condensation, respectively. Assuming that the void fraction in the volume $\Omega_P + \delta\Omega_e$ or $\Omega_P + \delta\Omega_c$ equals that in $\Omega_P$. Rearrangement of (5.53) yields the change of the void fraction, $\delta\alpha_{e,c}$, in the control volume considered, namely

$$\begin{aligned} \delta\alpha_e &= \frac{\alpha_P^n \Omega_P + \Omega_l}{\Omega_P + \delta\Omega_e} - \alpha_P^n, \\ \delta\alpha_c &= \frac{\alpha_P^n \Omega_P - \Omega_g}{\Omega_P + \delta\Omega_c} - \alpha_P^n. \end{aligned} \tag{5.54}$$

The formula for the velocity divergence, (4.42), has been derived in Sec.(4.4). Substitution of (5.54) in (4.42) finally gives the discretised equation for the divergence of the velocity field caused by the evaporation or condensation

$$\int_\Omega \left(\vec{\nabla}.\vec{u}\right) \, d\Omega \cong \frac{\rho_l - \rho_g}{\rho_{e,c}} \frac{\delta\alpha_{e,c}}{\Delta t} \Omega_P, \tag{5.55}$$

where $\rho_{e,c}$ is the density in the control volume resulting from the phase transition. This density is given by

$$\rho_{e,c} = \rho_P^* - (\rho_l - \rho_g)\, \delta\alpha_{e,c}, \tag{5.56}$$

where the term $(\rho_l - \rho_g)\, \delta\alpha_{e,c}$ originates from (4.37).

## 5.4 Pressure correction

The pressure correction procedure belongs to the group of methods termed projection methods. In general, the procedure results in a velocity field that does not satisfy the continuity equation. This field is then corrected by subtracting a term expressed in the form of a pressure gradient.

The general form of the momentum equation is given by employing coefficients derived in the preceding subsections

$$A_P \vec{u}_P^{n+1} + \sum_{nb} A_{NB} \vec{u}_{NB}^{n+1} = \vec{S}_{p_P}^{n+1} + \vec{S}_P^{n+1}, \tag{5.57}$$

where

$$\begin{aligned} A_P &= A_{u_P} + A_{c_P} + A_{d1_P}, \\ A_{NB} &= A_{c_{NB}} + A_{d1_{NB}}, \\ \vec{S}_P &= \vec{S}_{u_P} + \vec{S}_{c_P} + \vec{S}_{d1_P} + \vec{S}_{d2_P} + \vec{S}_{g_P}. \end{aligned} \tag{5.58}$$

The momentum equation is treated implicitly, thus the velocity in some terms of the equation is unknown. The additional complexity is the non-linear character of the equation, since coefficients $A$ and $S$ depend on $u_i^{n+1}$. Solution of the momentum equation of this type, with known value of all velocity independent variables, would give a result satisfying the continuity equation. However, this is not possible because the number of unknowns is larger than the number of equations. To overcome the problem, the values of the variables and dependent flow properties, incorporated in the coefficients, are predicted on the basis of their value at the previous time step. In this way the momentum equation becomes linear, nevertheless, the velocity distribution resulting from the solution does not satisfy the continuity equation. Consequently, computed velocity and pressure constitute an intermediate solution which needs to be corrected. In the light of this, the notation of equation (5.57) must be reconsidered, namely

$$A_P \vec{u}_P^{*+1} + \sum_{nb} A_{NB} \vec{u}_{NB}^{*+1} = \vec{S}_{p_P}^{*} + \vec{S}_P^{*}. \tag{5.59}$$

The corrections change the form of (5.59), such that

$$A_P\left(\vec{u}_P^{*+1} + \vec{u'}_P\right) + \sum_{nb} A_{NB}\left(\vec{u}_{NB}^{*+1} + \vec{u'}_{NB}\right) = -\sum_{nb} p_{nb}^{*} \vec{n} S_{nb} - \vec{\nabla} p' \Omega_P + \vec{S}_P^{*}. \tag{5.60}$$

The relation between the velocity and pressure corrections follows from (5.60) and reads

$$\vec{u'}_P = -\vec{\nabla} p' \frac{\Omega_P}{A_P}, \tag{5.61}$$

where the term $\sum_{nb} A_{NB} \vec{u'}_{NB}$ has been dropped, which is common practice for the SIMPLE method. This is the main reason for the decrease of the convergence rate of the iterative system. There are some procedures which improve the convergence, but description of them is beyond the scope of this study.

The continuity equation imposes the zero velocity divergence in the case phase transition is not present. In presence of phase transition, the discretized divergence is equal to that defined by (5.55). Assuming that the velocity $\vec{u}_P^{*+1} + \vec{u'}_P$ satisfies the continuity equation, one obtains

$$\sum_{nb} \vec{u}_{nb}^{*+1} . \vec{n} S_{nb} = -\sum_{nb} \vec{u'}_{nb} . \vec{n} S_{nb} + S_{div_P}, \tag{5.62}$$

where, according to (5.55)

$$S_{div_P} = \frac{\rho_l - \rho_g}{\rho_{e,c}} \frac{\delta\alpha_{e,c}}{\Delta t}\Omega_P. \tag{5.63}$$

Finally, substitution of (5.61) in (5.62) yields the pressure correction equation,

$$\begin{aligned}&\sum_{nb}\left(\frac{\Omega}{A}\right)_{nb}\left(\frac{p'_{NB}-p'_P}{d_xS_{x_n}+d_yS_{y_n}}\right)_{nb}\left(S^2_{x_n}+S^2_{y_n}\right)_{nb}=\\&\sum_{nb}\vec{u}^{*+1}_{nb}.\vec{n}S_{nb}-S_{div_P}-S_{corr_P},\end{aligned} \tag{5.64}$$

where the face value of $(\Omega/A)_{nb}$ is evaluated using (5.9). The last term at the right-hand side of (5.64) is the correction to the pressure term on the left hand side. The pressure correction gradient is discretized using the standard CDS scheme, which will result in an oscillatory character of the pressure correction. The correction $S_{corr_P}$ corresponds to the central difference approximation of the third derivative of the pressure, namely

$$\begin{aligned}&S_{corr_P}=\\&\sum_{nb}\left(\frac{\Omega}{A}\right)_{nb}\left(\frac{S^2_{x_n}+S^2_{y_n}}{d_xS_{x_n}+d_yS_{y_n}}\right)_{nb}\left((p^*_{NB}-p^*_P)-\left(\left(\frac{\delta p^*}{\delta x}\right)_{nb}d_x+\left(\frac{\delta p^*}{\delta y}\right)_{nb}d_y\right)\right)\end{aligned} \tag{5.65}$$

The detailed derivation of (5.65) and (5.64) is given in App.(B.3). The correction detects oscillations and smoothes them. It may be factorised by a constant without affecting the consistency of the approximation (Perić and Ferziger, (1996)). The magnitude of this factor depends on the flow conditions. The procedure has been devised for improvement of the pressure-velocity coupling on co-located grids (Rhie and Chow, (1983)).
The general form of the pressure correction equation reads

$$A_P p'_P + \sum_{nb} A_{NB} p'_{NB} = S_P, \tag{5.66}$$

where

$$\begin{aligned}A_P &= \sum_{nb}\left(\frac{\Omega}{A}\right)_{nb}\left(\frac{S^2_{x_n}+S^2_{y_n}}{d_xS_{x_n}+d_yS_{y_n}}\right)_{nb},\\A_{NB} &= -\left(\frac{\Omega}{A}\right)_{nb}\left(\frac{S^2_{x_n}+S^2_{y_n}}{d_xS_{x_n}+d_yS_{y_n}}\right)_{nb},\\S_P &= \sum_{nb}\vec{u}^{*+1}_{nb}.\vec{n}S_{nb}-S_{div_P}-S_{corr_P}.\end{aligned} \tag{5.67}$$

The coefficients and unknowns associated with each control volume are assigned in a matrix-vector form solved using the SIP procedure. The pressure correction equation results in the pressure corrections which adjusts the pressure $p^*$ directly, such that

$$p^{*+1} = p^* + p'. \tag{5.68}$$

The volume flux correction is obtained directly from the pressure correction equation. The corrected flux, for an individual cell face, reads

$$\vec{\hat{u}}^{*+1}_{nb}.\vec{n}S = \vec{u}^{*+1}_{nb}.\vec{n}S - \left(\frac{\Omega}{A}\right)_{nb}\left(\frac{p'_{NB} - p'_P}{d_x S_{x_n} + d_y S_{y_n}}\right)_{nb}\left(S^2_{x_n} + S^2_{y_n}\right)_{nb}. \tag{5.69}$$

The velocity correction is estimated based on (5.61) and, like the pressure, the velocity distribution is updated directly as

$$\begin{aligned} \hat{u}^{*+1} &= u^{*+1} + \left|\vec{u'}\right|, \\ \hat{v}^{*+1} &= v^{*+1} + \left|\vec{u'}\right|. \end{aligned} \tag{5.70}$$

The updated velocity distribution satisfies the continuity equation, but not the momentum equation. Hence, the velocity field and adjusted volume fluxes are used again to evaluate the coefficients in the momentum equation and execute the next iteration. In the course of the iterative procedure the numerical error is assumed to tend asymptotically to zero, i.e. machine accuracy. Consequently, values of the pressure correction, hence also the flux and velocity corrections, will decrease to machine-zero. Then the subsequent time step is carried out. The entire procedure is illustrated in the block scheme shown in Fig.(5.6) in Sec.(5.7).

## 5.5 Boundary conditions

The conditions at the physical boundaries have been discussed in Sec.(4.6). The most important numerical approximations will be explained here.

Dirichlet and von Neumann types of conditions do not suffice in all cases. Therefore, an extrapolation procedure is necessary. A second order extrapolation is used in the computational method, which defines the value of variables at the boundary. The value of variables at boundary $B$ is computed from

$$\phi_B = \phi_P + \frac{\left|\vec{d}\right|_{PB}}{\left|\vec{d}\right|_{NP}}\left(\phi_P - \phi_B\right), \tag{5.71}$$

where the subscript $B$ denotes the variable positioned at the boundary node. The notations $\left|\vec{d}\right|_{PB}$ and $\left|\vec{d}\right|_{NP}$ indicate distances between the node $P$ and the boundary

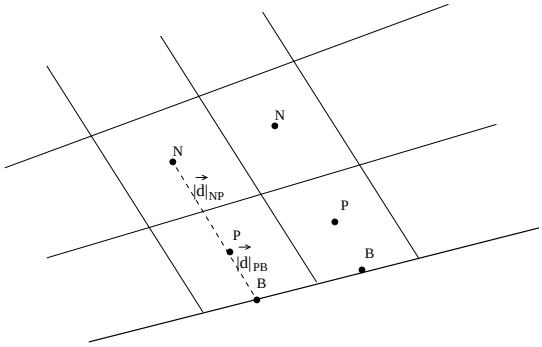


FIGURE 5.4: *Arrangement of control volumes at a domain boundary.*

node and between the node $N$, positioned right behind the node $P$ (see Fig.(5.4)), and the node $P$, respectively. As mentioned in Sec.(4.6), the outflow boundary condition of the momentum equation needs to be treated in a special way in case the pressure distribution departs substantially from constant. The algorithm allows for conservation of mass in the domain. Velocities at the outflow boundary are extrapolated using the von Neumann approach and then scaled, such that

$$u_B^* = u_P^* \frac{\dot{V}_{inl} + S_{div}^{*+1}}{\dot{V}_{out}^*}, \tag{5.72}$$

where $\dot{V}_{inl}$ and $\dot{V}_{out}$ are volume fluxes summed at the inflow and outflow boundaries, respectively, whereas $S_{div}$ is the velocity divergence summed over the whole domain. The algorithm for the velocity in $j$ direction is analogous. The velocity at the boundary is evaluated based on the value of the variables at the previous iteration, thus the contribution of the outflow boundary condition is added to the source term of the momentum equation.

The viscous terms in the momentum equation requires some attention. For a symmetry plane, the algorithm takes into account that velocity at node $P$, adjacent to the boundary, is not always perpendicular to the boundary face. The vector connecting node $P$ and $B$ is also not always normal to the face. Consequently, the formula for the viscous force at the plane of symmetry, for the horizontal direction, reads

$$\begin{aligned}
&\bar{\bar{\tau}}_{nn} S_{x_{n,sym}} = \\
&-\mu_{sym}\left(\frac{u_P^{*+1}}{d_x S_{x_{n,sym}} + d_y S_{y_{n,sym}}} S_{x_{n,sym}}^2 + \frac{u_P^*}{d_x S_{x_{n,sym}} + d_y S_{y_{n,sym}}} S_{x_{n,sym}}^2\right) + \\
&2\mu_{sym}\frac{v_P^*}{d_x S_{x_{n,sym}} + d_y S_{y_{n,sym}}} S_{x_{n,sym}} S_{y_{n,sym}} - \frac{2}{3}\mu_{sym}\left(\vec{\nabla}.\vec{u}\right)_{sym}^* S_{x_{n,sym}}.
\end{aligned} \tag{5.73}$$

Subscript $n$ of $S$ denotes the normal to the boundary. The velocity field divergence has been derived in Sec.(5.3). This term is extrapolated to the boundary using the zero-gradient boundary condition.

In case of a rigid boundary the velocity at node $P$ is first projected onto the direction tangential to the boundary. With the vector $\vec{d}_{PB}$ perpendicular to the rigid wall one finds

$$\begin{aligned}\overline{\overline{\tau}}_{nt}S_{x_{wal}} = -\mu_{wal}\frac{u_P^{*+1}}{d_x S_{x_{n,wal}} + d_y S_{y_{n,wal}}}S_{y_{wal}}^2 - \\ \mu_{wal}\frac{v_P^*}{d_x S_{x_{n,wal}} + d_y S_{y_{n,wal}}}S_{x_{wal}}S_{y_{wal}} - \frac{2}{3}\mu_{wal}\left(\vec{\nabla}.\vec{u}\right)^*_{wal}S_{x_{n,wal}}.\end{aligned} \tag{5.74}$$

The derivation of (5.73) and (5.74) is given in App.(B.1).

## 5.6 Strongly Implicit Procedure (SIP)

### 5.6.1 Matrix arrangement

As shown in the preceding subsections, each of the individual discretized equations can be expressed in a compact form using the coefficients $A$ and the source term $S$, such that

$$A_P\phi_P + \sum_{nb} A_{NB}\phi_{NB} = S_P. \tag{5.75}$$

The number of equations and number of unknowns must be equal in order to be able to solve the system of discretized equations. For each control volume one obtains equations containing unknowns which number depends on the size of the computational molecule. This molecule, for a two dimensional scheme, for the discretization described in the previous subsections, incorporates five nodes, see Fig.(5.1). The equations are collected in a matrix system containing the matrix $A$ for the coefficients, $\phi$ for the unknowns and $S$ for the source term, i.e.

$$A\phi = S. \tag{5.76}$$

The arrangement of matrix $A$ depends on the numbering algorithm for the control volumes in the computational domain. In this study cells are numbered starting from the left lower corner of the domain, proceeding upwards, line after line in a regular manner. This way of labelling is termed lexicographic ordering. For each control volume there is one row of the matrix depending on the number of the control volume and the size of the molecule of the numerical scheme. For the two dimensional case, the five node computational molecule and a structured grid, matrix $A$ has a poly-diagonal, symmetric structure. The example of the matrix generated for a square

computational domain of the dimension $4 \times 4$ control volumes reads

$$A = \begin{bmatrix}
A_P & A_N & 0 & 0 & A_E & 0 & 0 & 0 & 0 & 0 & 0 & 0 & 0 & 0 & 0 & 0 \\
A_S & A_P & A_N & 0 & 0 & A_E & 0 & 0 & 0 & 0 & 0 & 0 & 0 & 0 & 0 & 0 \\
0 & A_S & A_P & A_N & 0 & 0 & A_E & 0 & 0 & 0 & 0 & 0 & 0 & 0 & 0 & 0 \\
0 & 0 & A_S & A_P & A_N & 0 & 0 & A_E & 0 & 0 & 0 & 0 & 0 & 0 & 0 & 0 \\
A_W & 0 & 0 & A_S & A_P & A_N & 0 & 0 & A_E & 0 & 0 & 0 & 0 & 0 & 0 & 0 \\
0 & A_W & 0 & 0 & A_S & A_P & A_N & 0 & 0 & A_E & 0 & 0 & 0 & 0 & 0 & 0 \\
0 & 0 & A_W & 0 & 0 & A_S & A_P & A_N & 0 & 0 & A_E & 0 & 0 & 0 & 0 & 0 \\
0 & 0 & 0 & A_W & 0 & 0 & A_S & A_P & A_N & 0 & 0 & A_E & 0 & 0 & 0 & 0 \\
0 & 0 & 0 & 0 & A_W & 0 & 0 & A_S & A_P & A_N & 0 & 0 & A_E & 0 & 0 & 0 \\
0 & 0 & 0 & 0 & 0 & A_W & 0 & 0 & A_S & A_P & A_N & 0 & 0 & A_E & 0 & 0 \\
0 & 0 & 0 & 0 & 0 & 0 & A_W & 0 & 0 & A_S & A_P & A_N & 0 & 0 & A_E & 0 \\
0 & 0 & 0 & 0 & 0 & 0 & 0 & A_W & 0 & 0 & A_S & A_P & A_N & 0 & 0 & A_E \\
0 & 0 & 0 & 0 & 0 & 0 & 0 & 0 & A_W & 0 & 0 & A_S & A_P & A_N & 0 & 0 \\
0 & 0 & 0 & 0 & 0 & 0 & 0 & 0 & 0 & A_W & 0 & 0 & A_S & A_P & A_N & 0 \\
0 & 0 & 0 & 0 & 0 & 0 & 0 & 0 & 0 & 0 & A_W & 0 & 0 & A_S & A_P & A_N \\
0 & 0 & 0 & 0 & 0 & 0 & 0 & 0 & 0 & 0 & 0 & A_W & 0 & 0 & A_S & A_P
\end{bmatrix}. \tag{5.77}$$

It is easy to estimate, that the matrix for a domain of $n_i \times n_j$ control volumes, would have $n_i^2 \times n_j^2$ elements, hence the amount of necessary storage is substantial. However, one can take advantage of the sparseness of the matrix and of its diagonal structure. Thus, in place of the full matrix containing individual rows of the matrix, five arrays with the diagonal elements suffice. The distance between the central coefficient, $A_P$, and the neighbour coefficients, $A_W$ and $A_E$, in the $i$ direction (horizontal for matrix $A$) is $n_i$ elements, the same as in $j$ direction. This leads to the conversion between the position in the domain, the compass indices of the element and its storage location in the array, see Tab.(5.1)

| **Location in a domain** | **Compass indices** | **Array location** |
|---|---|---|
| $i, j$ | $P$ | $l = (i-1)n_j + j$ |
| $i-1, j$ | $W$ | $l - n_j$ |
| $i, j-1$ | $S$ | $l - 1$ |
| $i, j+1$ | $N$ | $l + 1$ |
| $i+1, j$ | $E$ | $l + n_j$ |

TABLE 5.1: *Conversion between a grid, compass and storage array locations.*

### 5.6.2 Direct solution

The commonly used algorithm for solving a problem involving large matrixes is the decomposition of matrix $A$ in the product of two triangular matrices, namely the

lower $L$ and the upper $U$,

$$A = LU. \tag{5.78}$$

The non-zero elements of the lower matrix are positioned in the area downwards of the main diagonal. The upper matrix is structured the other way round. To render the factorization process unique one demands that the main diagonal of $L$ or alternatively of $U$ consists of unit elements. The algorithm for evaluation of individual elements of both matrixes is straightforward and based on Gauss elimination, see (Perić and Ferziger, (1996)). In general, it assumes that the first row of the upper matrix remains unchanged. With the assumption that the unit elements are positioned on the main diagonal of $L$, one computes individual elements of the matrixes using the relations

$$L_{ij} = \left( A_{ij} - \sum_{k=1}^{j-1} L_{ik} U_{kj} \right) U_{jj}^{-1} \quad \text{for } j \leq i-1 \tag{5.79}$$

and

$$U_{ij} = A_{ij} - \sum_{k=1}^{i-1} L_{ik} U_{kj} \quad \text{for } j \geq i. \tag{5.80}$$

Notation $ij$ refers to the position of an element in the matrix, but not in the grid. According to the terminology used for Gauss elimination, the decomposition will be termed forward elimination, i.e. opposite to the backward substitution which is the final step of the algorithm.

The solution of the set is then split in two stages. The matrix equation may be written as

$$A\phi = L\left(U\phi\right) = LY = S. \tag{5.81}$$

Initially one calculates the variable $Y$ knowing $L$ and $S$. This is performed using backward substitution. Then the sought variable $\phi$ is computed using

$$U\phi = Y \tag{5.82}$$

which, because of the triangular character of $U$, is also computed by backward substitution. Though the described algorithm is straightforward, it cannot take advantage of the sparse, diagonal structure of the original $A$ matrix. Moreover, it requires a large storage effort, because, unlike $A$, matrixes $L$ and $U$ are not sparse, nor diagonal. Thus $LU$-decomposition is more applicable to cases for which the structure of $A$ is not arranged in the way shown in (5.77).

In order to decrease the calculation and storage effort one turns to iterative methods, in which an initial guessed solution leads to the final solution of (5.76).

### 5.6.3 SIP

The iteration method hinges on finding a matrix $M$ which is as good an approximation of $A$ as possible. Additionally, it is required, that the decomposition of $M$ produces two triangular matrixes $L$ and $U$ that are sparse and diagonal. Moreover, the location of their diagonals must be related to that of matrix $A$. The construction of lower and upper matrices saves substantially on computational and storage effort. Thus, the relation

$$M\tilde{\phi} = S \tag{5.83}$$

gives an approximation of $\phi$. The magnitude of the difference between $\tilde{\phi}$ and the solution of (5.76) depends on the difference between $M$ and $A$. The rate of convergence of the iteration procedure is strongly associated with the difference between $M$ and $A$. Consequently, one needs to find an algorithm allowing the fast evaluation of $L$ and $U$ which product gives an excellent approximation to $A$.

The product of the sparse diagonal $L$ and $U$ gives a matrix with seven diagonals. Five of them refer to those of $A$ and the two extra ones correspond to the nodes $NW$ and $SW$, see Fig.(5.5). The location of the nodes in the domain is shown in Fig.(5.1). The matrix $M$ may be expressed as

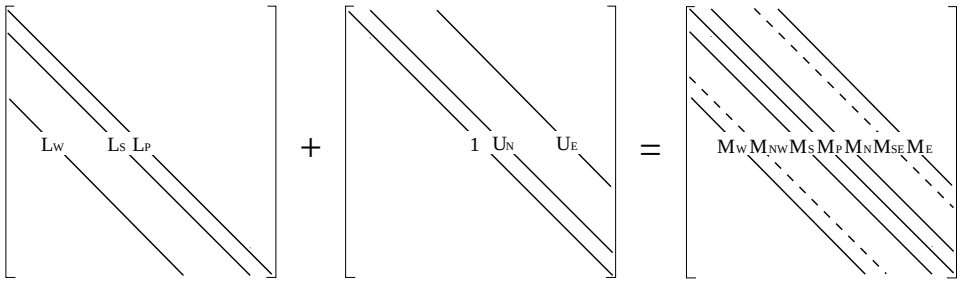


FIGURE 5.5: *Illustration of the product of $L$ and $U$ resulting in $M$.*

$$M = LU = A + N, \tag{5.84}$$

where $N$ is the matrix required to resolve $A$ from $M = LU$, such that $M$ is a good approximation of $A$. The obvious choice for $M$ is that it contains the same elements as those in $A$ plus the two additional diagonals corresponding to nodes $NW$ and $SW$, which are contained in $N$. Consequently, the elements in $M$, according to the

rules of matrix multiplication, can be expressed in terms of elements of $L$ and $U$

$$\begin{aligned}
M_W &= A_W = L_W^l, \\
M_{NW} &= N_{NW} = L_W^l U_N^{l-n_j}, \\
M_S &= A_S = L_S^l, \\
M_P &= A_P = L_W^l U_E^{l-n_j} + L_S^l U_N^{l-1} + L_P^l, \\
M_N &= A_N = U_N^l L_P^l, \\
M_{SW} &= N_{NW} = L_S^l U_E^l, \\
M_E &= A_E = U_E^l L_P^l,
\end{aligned} \tag{5.85}$$

where $l$ indicates the position in the one dimensional arrays in which the elements of each diagonal are stored. Solution of the elements of $L$ and $U$ (5.85) is possible. However, the resulting algorithm does not converges sufficiently fast, because one does not control the influence exerted by $N$ on $\phi$. In order to decrease this impact Stone proposed (Stone, (1968)) an $M$ such, that the five diagonals referring to those in $A$ nearly cancel the extra ones added by $N$. To achieve this objective, values of non-zero elements of $N\phi$ are decreased by subtraction of $\phi'$. The latter is approximated by variables in the vicinity of nodes $NW$ or $SW$. The approximation is of the second order and reads

$$\begin{aligned}
\phi'_{NW} &= \gamma \left( \phi_W + \phi_N - \phi_P \right), \\
\phi'_{SW} &= \gamma \left( \phi_S + \phi_E - \phi_P \right),
\end{aligned} \tag{5.86}$$

where $\gamma$ is a positive constant. The choice of its value is a matter of experience, however, Stone recognised that $\gamma < 1$ ensures stability of the calculation process. Equation (5.86) modifies the general form of the discretized governing equation, (5.75), such that its left hand side reads

$$\begin{aligned}
&A_P\phi_P + A_W\phi_W + A_S\phi_S + A_N\phi_N + A_E\phi_E + \\
&N_{NW} \left( \phi_{NW} - \phi'_{NW} \right) + N_{SW} \left( \phi_{SW} - \phi'_{SW} \right).
\end{aligned} \tag{5.87}$$

Rearrangement of (5.87) using (5.86) yields

$$\begin{aligned}
&\left(A_P + \gamma N_{NW} + \gamma N_{SW}\right) \phi_P + \left(A_W - \gamma N_{NW}\right) \phi_W + \left(A_S - \gamma N_{SW}\right) \phi_S + \\
&\left(A_N - \gamma N_{NW}\right) \phi_S + \left(A_E - \gamma N_{SW}\right) \phi_E + N_{NW}\phi_{NW} + N_{SW}\phi_{SW}.
\end{aligned} \tag{5.88}$$

The form of (5.87) constitutes the basis for constructing the modified $M$, which is now equivalent to the sum of $A$ and the modified $N$. The adjusted matrix $N$ com-

prises now five diagonals instead two, namely

$$\begin{aligned}
M_W &= A_W - \gamma N_{NW} = L_W^l, \\
M_{NW} &= N_{NW} = L_W^l U_N^{l-n_j}, \\
M_S &= A_S - \gamma N_{SW} = L_S^l, \\
M_P &= A_P + \gamma \left(N_{NW} + N_{SW}\right) = L_W^l U_E^{l-n_j} + L_S^l U_N^{l-1} + L_P^l, \\
M_N &= A_N \gamma N_{NW} = U_N^l L_P^l, \\
M_{SW} &= N_{NW} = L_S^l U_E^l, \\
M_E &= A_E - \gamma N_{SW} = U_E^l L_P^l.
\end{aligned} \tag{5.89}$$

Only the two diagonals of $N$, $N_{NW}$ and $N_{SW}$, remain unchanged. Now one can express all elements of $N$ in terms of $L$ and $U$. Consequently, knowing the elements of $A$ the diagonals in $L$ and $U$ can be computed.

The procedure of estimating the lower and upper matrixes is equivalent to the forward elimination in the classical way of the constructing an $LU$ decomposition which leads to a full triangular form of both matrixes.

The lower and upper matrixes are the basis for the iteration algorithm

$$\left(A + N\right)\phi = N\phi + S. \tag{5.90}$$

Further rearrangement of (5.90) leads to

$$\left(A + N\right)\phi = \left(A + N\right)\phi - \left(A\phi - S\right). \tag{5.91}$$

Since the right hand side of (5.90) is assumed to be known, the equation can be solved for $\phi$. The outcome is a subsequent guess for the result, namely

$$\left(A + N\right)\phi^{n+1} = \left(A + N\right)\phi^n - \left(A\phi^n - S\right), \tag{5.92}$$

where superscript $n$ denotes the level of the iteration. The equation (5.92) may be expressed using the difference between the $\phi$ resulting from two subsequent iterations,

$$\delta^{n+1} = \phi^{n+1} - \phi^n \tag{5.93}$$

and the residual,

$$R^n = S - A\phi^n. \tag{5.94}$$

Equation (5.92) using (5.93) and (5.94) reads

$$\left(A + N\right)\delta^{n+1} = R^n \tag{5.95}$$

or

$$LU\delta^{n+1} = R^n. \tag{5.96}$$

The remainder of the algorithm has been described earlier in this section and is similar to the calculation process associated with the standard $LU$ factorisation. At the first step one solves (5.96) for $Y$, namely

$$LU\delta^{n+1} = LY^{n+1} = R^n. \tag{5.97}$$

Subsequently, having $Y$ determined, one proceeds to the final step of the iteration

$$U\delta^{n+1} = Y \tag{5.98}$$

to find $\delta^{n+1}$. Taking advantage of the sparse, diagonal character of $A$, constructing $L$ and $U$ such that they have a similar structure to $A$ and finally, the efficient evaluation of elements in $N$ makes the SIP algorithm an efficient way for solving the large set of equations. The method is characterised by a high rate of convergence, (Perić and Ferziger, (1996)), and within couple of iterations residual $R^n$ obtains an acceptable level.

## 5.7 Block scheme of algorithm

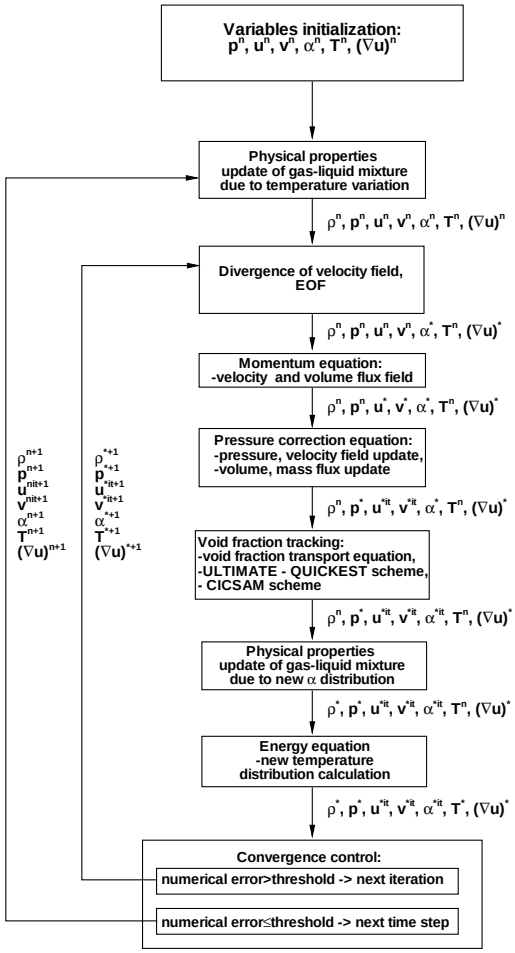


FIGURE 5.6: *Block scheme of the algorithm. Nomenclature: p - pressure, u - horizontal component of velocity, v - vertical component of velocity, $\rho$ - gas-liquid mixture density, T - temperature, $(\nabla u)$ - divergence of a velocity field.*

# INTERFACE CAPTURING

6 CHAPTER

In this chapter the transport equation for the void fraction, (4.38) is discussed in more detail. The algorithm for its solution differs from that used for the other equations in the system. The equation is solved using the split operator scheme. The algorithm assumes (in the case of two dimensions) a two step process of convection of the void fraction within a time step. Each step, termed a sweep, represents advection of the variable along an individual coordinate direction. The first sweep results in an intermediate distribution of the void fraction, whereas the second sweep gives the final result for a given iteration. The process is commutative and leads to accurate mass conservation in the system. In order to satisfy the volume (mass) conservation constraint the Eulerian-Lagrangian scheme has been utilized.

Unlike the other equations, the transport equation for the void fraction is considered in an explicit way. Hence, it is assumed, that all elements of the convective term are known at the iteration considered and follow from the previous iteration. The Volume of Fluid method, implemented in the Finite Volume approach, dissipates the interface in space preserving continuity of flow quantities. However, this scheme deteriorates the physical representation of phasic regions, thus, additional numerical algorithms have been implemented in order to improve the sharpness of the interface. This is done in the framework of the Volume of Fluid method, with conservation of the continuous distribution of flow quantities across the phasic boundary. The algorithms, termed ULTIMATE and QUICKEST, have been initially devised for the one-dimensional case. Since here a two-dimensional flow is considered, these two methods need to be extended. The adaptation was possible employing the CICSAM algorithm. In general, the methods use higher order interpolation algorithms for the convective term present in the transport equation for the void fraction. The influence of the flux rate is also taken into account. The description of the algorithm can be found in Sec.6.2 and Sec.(6.3).

## 6.1 Split operator scheme

For the sake of simplicity, the description is started for the case without phase transition. Thus, the velocity field, for incompressible flows, remains free of divergence, i.e.

$$\int_{\Omega} \vec{\nabla}.\vec{u}\, d\Omega = \int_{\partial\Omega} (\vec{u}.\vec{n})\, dS = 0. \tag{6.1}$$

This condition, for the discretized fluxes associated with a two-dimensional, rectangular control volume, is written as

$$\sum_{nb} (\vec{u}_{nb}.\vec{n})\, S_{nb} = 0. \tag{6.2}$$

Though the integration of the fluxes over all boundaries of the control volume results in zero, this is not necessarily the case for the sum of the contribution of two opposite boundaries, hence

$$\begin{aligned} \sum_{ew} u_{ew} S_{ew} &\neq 0, \\ \sum_{ns} v_{ns} S_{ns} &\neq 0, \end{aligned} \tag{6.3}$$

where the subscripts $ew$ and $ns$ denote, using the compass notation, the east-west and north-south faces of the control volume, respectively. One of the situations described by (6.3) is illustrated in Fig.(6.1). Since volume flux $u_w S_w$ is not equal to $u_e S_e$, according to (6.2), the 'excess', or 'missing' volume flux must leave, or enter, the control volume through the south and north boundary. This volume flux is the sum of $v_n S_n$ and $v_s S_s$. Figure (6.1) also shows the identity

$$\sum_{ew} u_{ew} S_{ew} = -\sum_{ns} v_{ns} S_{ns}, \tag{6.4}$$

which will be used for constructing a separate sweep for each of the two directions. In absence of phase transition, the transport equation for the void fraction $\alpha$ reads, see Sec.(4.3),

$$\frac{\partial}{\partial t} \int_{\Omega} \alpha\, d\Omega + \int_{\partial\Omega} \alpha\, (\vec{u}.\vec{n})\; dS = 0. \tag{6.5}$$

The void fraction transport equation for the first, horizontal direction, in the discretized form, reads

$$(\alpha_P^* - \alpha_P^n)\, \frac{\Omega}{\Delta t} + \sum_{ew} \alpha_{ew}^n u_{ew} S_{ew} = \alpha_P^* \sum_{ew} u_{ew} S_{ew}, \tag{6.6}$$

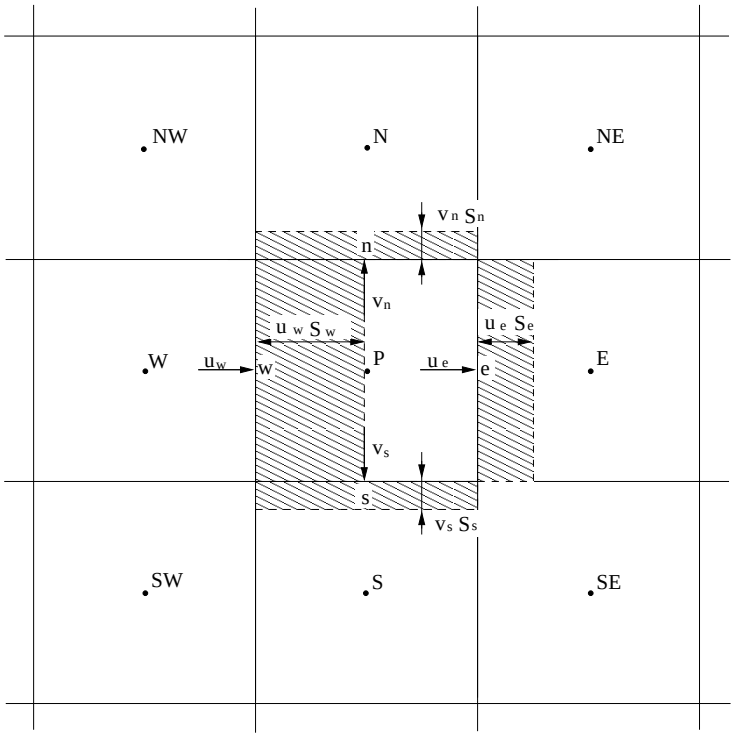


FIGURE 6.1: *Graphical representation of fluxes associated with the control volume.*

where the asterisk denotes an intermediate value of the variable. The right-hand side of (6.6) constitutes the correction source term. Since the left-hand side employs the void fraction, the right-hand side, the net divergence, has the same form, thus, $\alpha$ is also present there. The void fraction at the right-hand side of (6.6) is unknown, thus the first, horizontal sweep is implicit. The intermediate distribution of the variable is the basis for the Lagrangian sweep which is explicit. Its discretised form reads

$$\left(\alpha_P^{*+1} - \alpha_P^*\right) \frac{\Omega}{\Delta t} + \sum_{ns} \alpha_{ns}^* v_{ns} S_{ns} = \alpha_P^* \sum_{ns} v_{ns} S_{ns}. \tag{6.7}$$

Superscript $* + 1$ denotes the void fraction at the subsequent iteration. In case $\alpha$ is the final result for a given time step the subscript is replaced by $n + 1$.

To illustrate how the algorithm works, consider a domain comprising of nine control volumes, see Fig.(6.2). The middle volume is filled by vapour indicated by $\alpha = 1$. The rest of the control volumes are filled by liquid, thus $\alpha = 0$ there. The velocity field for the central control volume is shown in Fig.(6.2). For the sake of simplicity, the area of the faces of the control volumes as well as the time step are

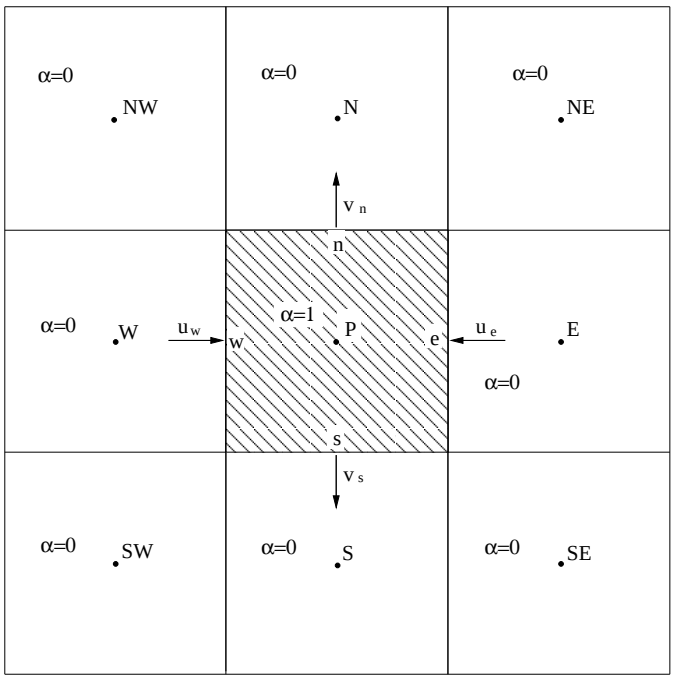


FIGURE 6.2: *Part of the computational domain consisting of nine control volumes.*

set as unity. The Eulerian sweep for the node $P$ results in

$$\alpha_P^* = \frac{1}{1 - \sum_{ew} u_{ew}}. \tag{6.8}$$

Thus, the void fraction $\alpha^*$ in all the control volumes, except the middle one, is zero. In the middle control volume $\alpha$ is less than unity. The subsequent, Lagrangian sweep results in the final distribution all over the domain and gives

$$\alpha_P^{*+1} = \alpha_P^*, \quad \alpha_S^{*+1} = \alpha_P^{*+1} v_s, \quad \alpha_N^{*+1} = \alpha_P^{*+1} v_n. \tag{6.9}$$

Now, the procedure is completed and summation of the void fraction over the domain should give the initial value of $\alpha$. Taking into account (6.8) and (6.9), the summation reads

$$\sum \alpha^{*+1} = \alpha_P^{*+1} + \alpha_S^{*+1} + \alpha_N^{*+1} = \alpha_P^{*+1} \left( 1 + \sum_{ns} v_{ns} \right) = \frac{1 + \sum_{ns} v_{ns}}{1 - \sum_{ew} u_{ew}}. \tag{6.10}$$

Employing the identity (6.4), the last term on the right hand side of (6.11) results in one. Thus, the overall value of $\alpha^{*+1}$ in the domain amounts to this at the beginning. This proves, in the case considered, that the volume of a convected fluid is conserved

in a natural way. This is necessary from the point of view of preserving mass conservation in the system. The reverse order of the sweeps, namely Lagrangian explicit and subsequently Eulerian implicit, will give the same result for the above example. However, in general it is not the case and in terms of mass conservation the combination Eulerian-Lagrangian sweep is better than the reverse one, see (Scradovelli and Zaleski, (2003)).

The procedure results in an accurate conservation of mass, see (Scradovelli and Zaleski, (2003)). Earlier versions of the split operator algorithm for the transport equation did not consider the net divergence, resulting in a distribution of the void fraction after each sweep. This used to cause undershoots or overshoots of the void fraction (Aulisa, Manservisi, Scradovelli and Zaleski, (2003)), i.e. the volume of the flow was not conserved. Missing or exceeding volumes were corrected such that

$$\alpha + (1 - \alpha) = 1. \tag{6.11}$$

If mass is not conserved, one observes unphysical jumps or drops of temperature. This will be shown in Chapter (7), where the two different versions of the split operator algorithm will be applied.

Phase transition modifies the formulas for the two sweeps. In the Eulerian step one needs to add the divergence of the velocity field and take into account the new distribution of $\alpha$ caused by phase transition. Finally, the net divergence resulting from the sweep also requires adjustment. The first step of the algorithm is now formulated as

$$\begin{aligned} &(\alpha_P^* - \alpha_P^n)\,\frac{\Omega}{\Delta t} + \sum_{ew} \left(\alpha^n + \delta\alpha^{*+1}\right)_{ew} u_{ew} S_{ew} = \\ &\alpha_P^* \left( \sum_{ew} u_{ew} S_{ew} + \sum_{ew} (\vec{u}.\vec{n})\, S_{ew} \right) + \left(\vec{\nabla}.\vec{u}\right) \Omega, \end{aligned} \tag{6.12}$$

where the divergence of the velocity field on the right-hand side of (6.12) is evaluated using the EOF method, see Sec.(5.3). The values of the divergence at the boundaries of the control volume, e.g. $(\vec{u}.\vec{n})\, S_{ew}$, are obtained from their approximation at the cell face. The term $\delta\alpha^{*+1}$ denotes the variation in the void fraction caused by the phase transition, see (5.54). Since the Eulerian sweep contains all quantities associated with the divergence due to the phase transition, the resulting intermediate distribution of the void fraction already incorporates the source effects for $\alpha$. Consequently, the form of the Lagrangian sweep remains unchanged, see (6.7).

## 6.2 ULTIMATE QUICKEST scheme

In the past decades much effort has been invested in deriving a proper discretization for the advection of flow quantities. The key problem is the evaluation of flow

field variables at the control volume boundary. In order to increase accuracy of the algorithm, a higher order interpolation appears to be required. However, standard procedures assuming orders higher than one produce spurious oscillations; moreover, increasing the order of interpolation does not guarantee a smoother distribution of the variables. It has been observed that algorithms of odd order of interpolation give better results than these of even order of approximation. Furthermore, there is no interpolation that, regardless of its order, while used without improvements, produces satisfactory output. The widely used procedure is to switch from a higher order interpolation to a first order interpolation or eventually to blend these interpolation schemes in regions of sharp gradients. However, the first order approach is severely dissipative in nature. The effect of dissipation increases proportional to the magnitude of the gradient of the convected variable. To avoid these disadvantages, the algorithms used in the present research have been improved. In the present section the one-dimensional scheme is considered, see Fig.(6.3). The further extension to a

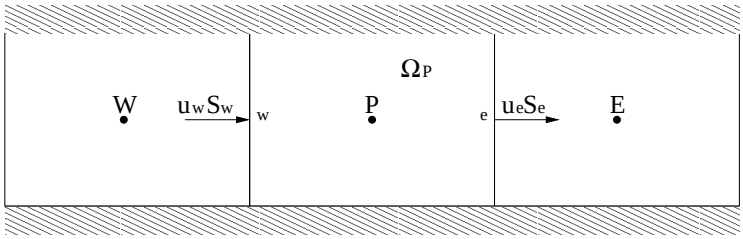


FIGURE 6.3: *One-dimensional arrangement of discretised space.*

two-dimensional arrangement will be discussed later.

### 6.2.1 QUICKEST

According to the advection algorithm (Leonard, (1991)), the control-volume averaged value of $\alpha$ at node $P$, at time step $\Delta t$ is considered as

$$\alpha_P^{n+1} \equiv \alpha\left(P, \Delta t\right) = \alpha\left(P - u\left(P, 0\right)\Delta t, 0\right). \tag{6.13}$$

Expansion of $\alpha_P^{n+1}$ in a series in space gives

$$\alpha_P^{n+1} = \alpha_P^n + f\left(\xi\right), \tag{6.14}$$

where, taking into account the argument of $\alpha$ at the right hand side of (6.13), $\xi$ is also a function of position in space and time, i.e.

$$\xi = g\left(x\left(P\right) - u\left(P, 0\right)\Delta t\right), \tag{6.15}$$

where $x$ denotes the position in one-dimensional space. Further expansion of the function $f$ in terms of a polynomial leads to

$$f(\xi) = \xi\left(\alpha^n_{P+x} - \alpha^n_{P-x}\right) + \frac{1}{2}\xi^2\left(\alpha^n_{P+x} - 2\alpha^n_P + \alpha^n_{P-x}\right) + (\cdots). \tag{6.16}$$

Assuming the second order of the expansion, one obtains

$$\alpha^{n+1}_P = \alpha^n_P + \xi\left(\alpha^n_{P+x} - \alpha^n_{P-x}\right) + (O)^2. \tag{6.17}$$

For a one-dimensional scheme the transport equation for the void fraction, in absence of phase transition, does not have a source term. Unsteady, pure advection of the control-volume averaged value of $\alpha$ may be written as

$$\frac{\partial}{\partial t}\frac{1}{\Omega_P}\int\limits_{\Omega_P}\alpha\, d\Omega = -\frac{1}{\Omega_P}\int\limits_{\partial\Omega}(\alpha\vec{u})\,.\vec{n}\, dS. \tag{6.18}$$

Discretization of (6.18) assumes the form of the second-order approximation for $\alpha^{n+1}_P$, namely

$$\alpha^{n+1}_P = \alpha^n_P - \left(\frac{u_e S_e \Delta t}{\Omega_P}\alpha_e - \frac{u_w S_w \Delta t}{\Omega}\alpha_w\right). \tag{6.19}$$

Now, comparing (6.19) and (6.17), it is easy to recognize links between individual terms of the equations. Notice, superscripts $n$ applying to the face values of $\alpha$ in (6.17) are dropped, because these variables are time dependent. Clearly, higher orders of approximation of (6.17) are also possible, however, Leonard (Leonard, (1991)) recognized that the second order scheme resulted in a low level of error in the distribution of $\alpha$, i.e. also one that is acceptable for the purpose of this research.

The face values of $\alpha$, appearing in (6.19), must be averaged in time, since the transport equation contains an unsteady term. To maintain the second-order accuracy of the scheme in all dimensions, effective cell-face boundary values of the convected variable are estimated from the second-order time averaging. If $\alpha'_{nb}$ is the instantaneous value of the void fraction at a face of the control volume, then the averaged value over time reads, e.g for face $nb$,

$$\alpha_{nb} = \frac{1}{\Delta t}\int\limits_0^{\Delta t}\alpha'_{nb}\, dt \cong \alpha^n_{nb} - \frac{u_{nb}\Delta t S_{nb}}{\Omega_P}\left(\alpha^n_{nb} - \alpha^n_P\right). \tag{6.20}$$

The term in front of the parenthesis at the right hand side of (6.20) is the CFL number. Hereinafter, the notation $c$ will refer to the CFL number, thus (6.20) is rewritten in the form

$$\alpha_{nb} = \alpha^n_{nb} - c_{nb}\left(\alpha^n_{nb} - \alpha^n_P\right) \tag{6.21}$$

or

$$\alpha_{nb} = (1 - c_{nb})\,\alpha^n_{nb} + c_{nb}\alpha^n_P. \tag{6.22}$$

The choice of the spatial approximation for the face value of $\alpha$ is arbitrary, however, as shown in (Leonard, (1991); Ubbink, 1997), the third order quadratic upstream interpolation (QUICK) scheme gives satisfactory results. This interpolation, for the $e$ boundary of the control volume and with the assumption that the flux direction is from $w$ to $e$, assumes the form, see (Leonard, (1997)),

$$\alpha_e = \frac{1}{2}\left(\alpha^n_P + \alpha^n_E\right) + \frac{1}{8}\left(\alpha^n_W - 2\alpha^n_P + \alpha^n_E\right). \tag{6.23}$$

Substitution of (6.23) and a similar expression for the $w$ boundary in (6.21) and subsequently (6.21) in (6.19) gives the value of $\alpha_P$ at the new time. This procedure involves the pure QUICKEST (QUICK with Estimated Streaming Terms) algorithm, however, it does not guarantee an accurate distribution near a region of high gradients. In particular, for shocks, the algorithm cannot handle the compressive character of the distribution while also an oscillatory behaviour results and the scheme is dissipative. Consequently, without additional numerical procedures aiming at improvement of QUICKEST the method is not adequate for the present purpose.

### 6.2.2 Normalized variable

For the evaluation of the face value of the void fraction, two nodes are involved, adjacent to the face, and one additional node positioned right behind the face neighbouring nodes, dependent on the direction of the flow. Variation of flow directions combined with the various possible signs of the gradient in $\alpha$ implies that a large number of cases has to be considered, if one maintains the compass notation. A convenient way to avoid this is to normalize the notation. Simultaneous notation of involved nodes, which indicates their dependence on flow direction rather than their position in the domain, eliminates ambiguity and further limits cases that need to be considered. At this point one introduces the donor-acceptor concept for characterizing the control volumes (nodes). From the donor control volume, $D$, a flux emanates and enters the acceptor cell, $A$. The upstream control volume, $U$, is positioned behind $D$ when looking in downstream direction, see Fig.(6.4). Hence, the notation depends on the flux direction, but not on the orientation of the domain. The normalised value of the void fraction at any point $x$ between the nodes $A$ and $U$ reads

$$\tilde{\alpha}\left(x\right) = \frac{\alpha\left(x\right) - \alpha_U}{\alpha_A - \alpha_U}. \tag{6.24}$$

It is clear, that the normalized values for the upstream and acceptor nodes are

$$\tilde{\alpha}_U = 0, \qquad \tilde{\alpha}_A = 1. \tag{6.25}$$

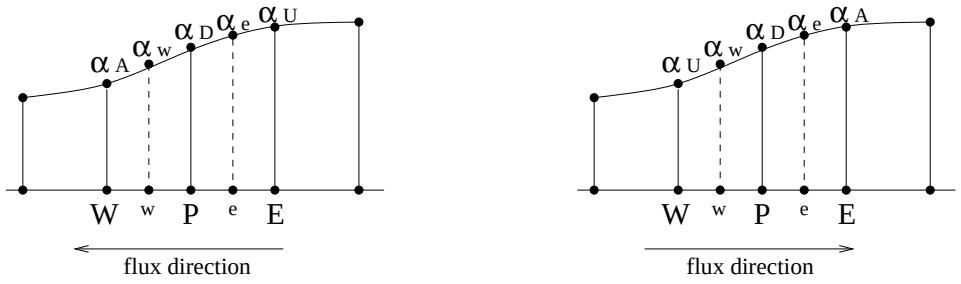


FIGURE 6.4: *Donor-acceptor arrangement. U - upstream cell, D - donor cell, A - acceptor cell.*

The above feature illustrates the useful character of normalized variables, such that whenever a variable assumes a value outside the range between zero and one, it indicates an extremum of the function. Therefore, it is easy to detect oscillatory behaviour of the void fraction.

The effective $\alpha$ face value, given by (6.22), reads in the terms of normalized variables

$$\tilde{\alpha}_{nb} = (1 - c_{nb}) \left( \frac{1}{2} \left( \tilde{\alpha}_D^n + 1 \right) + \frac{1}{8} \left( 1 - 2\tilde{\alpha}_D^n \right) \right) + c_{nb} \tilde{\alpha}_D^n. \tag{6.26}$$

Hence, the normalized face value of $\alpha$ is a function of the normalized void fraction in the donor cell only, while the CFL number appears as a parameter, i.e.

$$\tilde{\alpha}_{nb} = f\left( \tilde{\alpha}_D^n \right) \tag{6.27}$$

The function given in (6.27) may be illustrated in the so-called normalized variable diagram (NVD) which is a convenient tool describing the functioning of the relation. Such diagrams are shown in the following sections.

### 6.2.3 Universal Limiter - Hyper-C

The normalized variable allows for the evaluation of the function relating the effective, time-averaged, normalized face value of the void fraction and the normalized value of $\alpha$ for the donor cell. The method constitutes a convenient and straightforward tool for checking the monotonicity of the void fraction distribution. Universalism of the idea relies on the independency on the order of approximation used for the calculation of the face value $\alpha_{nb}^n$, see (6.22). Nevertheless, the computational molecule involved in an approximation cannot exceed a five node stencil, e.g. an acceptable scheme is the donor-acceptor-upstream scheme. Non-monotonic behaviour of a distribution becomes evident as values of the normalized variable outside the range $[0, 1]$. Clearly, the necessary condition is that the variable is positioned between an acceptor and upstream cell. Thus, the monotonic condition for a donor cell requires

$$\tilde{\alpha}_D^n \in [0, 1]\,. \tag{6.28}$$

The effective, normalized face value at the face between the donor and acceptor, is subject to an additional constraint. This limitation is depicted in Fig.(6.5) which shows the monotonicity-maintenance criteria for the void fraction at the faces of the control volume. For the $e$ face, the constraint of monotonicity imposes

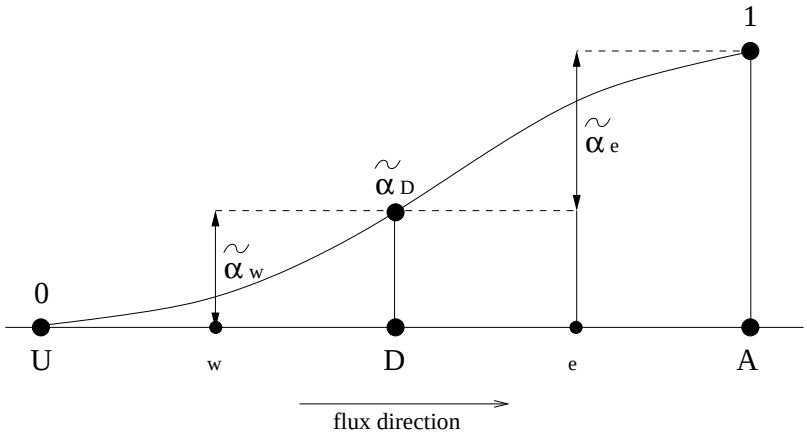


FIGURE 6.5: *Monotonicity-maintenance criteria for the faces of the control volume.*

$$\tilde{\alpha}_D^n \leq \tilde{\alpha}_e \leq 1. \tag{6.29}$$

If a maximum of the void fraction appears in the vicinity of the $e$ face, the value of $\tilde{\alpha}_e$ exceeds one. In the case of a minimum, one observes a negative value of the normalized void fraction. The spurious extremums are effectively eliminated by imposing the constraint

$$\tilde{\alpha}_{nb} = \tilde{\alpha}_D^n \qquad \text{for} \quad \tilde{\alpha}_D^n \notin [0,1]\,. \tag{6.30}$$

This influences the distribution $\tilde{\alpha}_{nb} = f\left(\tilde{\alpha}_D^n\right)$ shown in the NVD. The function passes through points $(0,0)$ and $(1,1)$, regardless of the order of approximation. Beyond the range $[0,1]$, the function is the line given by (6.30), see (6.6) or (6.7).

The QUICKEST algorithm is not able to handle high gradients of the convected variable. The method dissipates artificially a shock-like gradient, thus, the distribution of the variable becomes smooth. With the help of the monotonicity criteria described above, an effective improvement of QUICKEST is constructed. The condition of monotonicity for the face $w$ is written, see Fig.(6.5), as

$$\tilde{\alpha}_w \in [0, \tilde{\alpha}_D^n]\,. \tag{6.31}$$

The equation for the void fraction at the new time, (6.19), normalized and expressed in terms of the donor-acceptor notation, reads

$$\tilde{\alpha}_D^{n+1} = \tilde{\alpha}_D^n - \left(c_e \tilde{\alpha}_e - c_w \tilde{\alpha}_w\right). \tag{6.32}$$

Rearrangement of (6.32) yields the value of $\alpha$ of the $e$ face:

$$\tilde{\alpha}_e = \frac{1}{c_e}\left(\tilde{\alpha}_D^n - \tilde{\alpha}_D^{n+1}\right) + \frac{c_w}{c_e}\tilde{\alpha}_w. \tag{6.33}$$

The monotonicity condition (6.31) shows, that $\tilde{\alpha}_w^n$ will not be negative for the distribution shown in the Fig.(6.5). One can easily imagine that the larger the gradient of the void fraction between nodes $U$ and $D$ the more $\tilde{\alpha}_w^n$ tends to zero. Clearly, an extreme case is the case that $\tilde{\alpha}_w^n = 0$. In such situation, a jump in $\tilde{\alpha}^n$ takes place somewhere between face $w$ and node $D$. This implies that $\tilde{\alpha}_D^{n+1}$ will become zero as the effect of advection. Thus, the jump proceeds towards the $e$ face and the form of (6.33) simplifies to

$$\tilde{\alpha}_e = \frac{\tilde{\alpha}_D^n}{c_e}. \tag{6.34}$$

The approach leading to (6.34) is termed Hyper-C and represents the most compressive method for capturing the shock-like behaviour of flow parameters. In combination with the monotonicity criteria described above, the results remain free of oscillations. The relation $\tilde{\alpha}_{nb} = f\left(\tilde{\alpha}_D^n\right)$ is shown in NVD, Fig.(6.6), with the CFL number as parameter. Although the algorithm allows maintaining a high level of res-

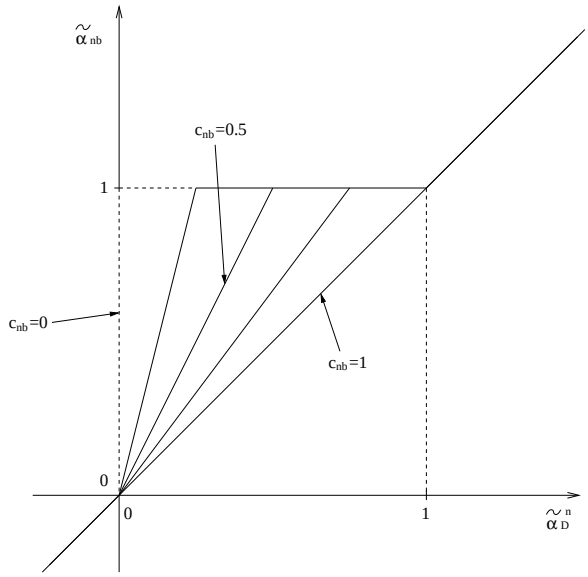


FIGURE 6.6: *NVD for Hyper-C.*

olution, it may not be used on its own. Since it handles very well a step change in variables, it is also responsible for artificial stepping of gradients which are supposed

to be smooth (Lafaurie, Nardone, Scardovelli, Zaleski and Zanetti, (1994); Leonard, (1991)). Hyper-C flattens local extremums, which is known as the 'clipping' defect. Consequently, the algorithm may only be used in combination with other approximation methods, where Hyper-C operates as an universal limiter.

### 6.2.4 ULTIMATE QUICKEST

In this subsection the combination between Hyper-C and QUCKEST will be described. The oscillatory behaviour of the QUICKEST scheme when used alone is effectively damped by the monotonicity criteria incorporated in the construction of Hyper-C. In order to keep a good resolution of a step-like behaviour of a convected variable the QUICKEST algorithm is switched automatically to Hyper-C, if one expects the appearance of high gradients. The combination of the two methods in depicted in the NVD for ULTIMATE QUICKEST, see Fig.(6.7). Figure (6.7) shows,

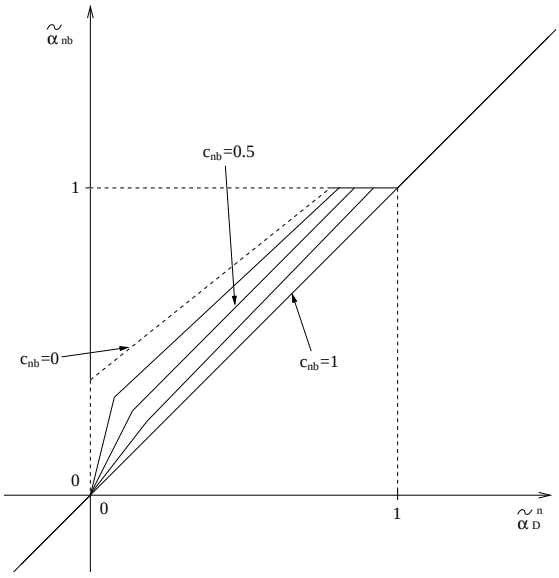


FIGURE 6.7: *NVD for ULTIMATE QUICKEST.*

that for small values of $\tilde{\alpha}_D^n$ Hyper-C is active. According to (6.24), the normalized value for the donor cell denotes the relation between the donor-upstream and acceptor-upstream gradients. If this value is small one may expect a step in the variable. Then, this shock behaviour is conserved by Hyper-C. The higher the value of $\tilde{\alpha}_D^n$ the gentler the distribution of variables, thus, the scheme switches to QUICKEST.

The ULTIMATE QUICKEST algorithm reads

$$\tilde{\alpha}_{nb_{UQ}} \begin{cases} MIN\left(\tilde{\alpha}_{nb_Q}, \tilde{\alpha}_{nb_H}\right) & \text{for } \tilde{\alpha}_D^n \in [0,1], \\ \tilde{\alpha}_D^n & \text{for } \tilde{\alpha}_D^n \notin [0,1], \end{cases} \tag{6.35}$$

where $\tilde{\alpha}_{nb_Q}$ and $\tilde{\alpha}_{nb_H}$ denote the normalized face values of the void fraction evaluated by QUICKEST and Hyper-C, respectively. Leonard (Leonard, (1991)) shows, that the limited QUICKEST algorithm for most practical solutions is the best of the algorithms using a five points upstream-donor-acceptor stencil. Figure (6.8) shows the result of a simulation of a pure advection for different types of the initial distribution. The test cases were carried out by Leonard (Leonard, (1991)) in the one-dimensional domain. The initial distribution of the convected variable assumes one of three shapes, namely the step, sine-squared and semi-ellipse. The figure illustrates the differences in performance between algorithms. It is clear, that the limited QUICKEST is far superior to any other scheme shown.

## 6.3 CICSAM differencing scheme

CICSAM is the acronym of Compressive Interface Capturing Scheme for Arbitrary Meshes. The algorithm adapts the ULTIMATE QUICKEST one-dimensional scheme to a multi dimensional scheme. In the one-dimensional scheme the gradient of the void fraction has only one possible direction. However, in two-dimensional space this is not necessarily true. In such a situation, the direction of the gradient of the void fraction may vary dependently on the orientation of the gas-liquid interface. This is taken into account by the weighting factor $\gamma_{cic}$ which controls the contribution of the ULTIMATE QUICKEST and the pure Hyper-C algorithms in the evaluation process for the normalized face value of $\alpha$. Hence, the value of $\tilde{\alpha}_{nb}$ is found from the relation

$$\tilde{\alpha}_{nb} = \gamma_{cic}\tilde{\alpha}_H + (1 - \gamma_{cic})\,\tilde{\alpha}_{UQ}. \tag{6.36}$$

The weighting factor in (6.36) depends on the angle $\theta$ at which the interface is inclined with respect to the flow direction, see Fig.(6.9). Since one uses a split operator scheme and a uniform grid, the flow direction for each sweep coincides with the direction of the vector connecting the nodes of the donor and acceptor control volumes. This results in

$$\theta = \arccos\left|\frac{\left(\vec{\nabla}\alpha\right)_D . \vec{d}}{\left|\left(\vec{\nabla}\alpha\right)\right|_D \left|\vec{d}\right|}\right|. \tag{6.37}$$

The weighting factor in then computed according to

$$\gamma_{cic} = MIN\left(k_{\gamma_{cic}}\frac{\cos(2\theta)+1}{2}, 1\right), \tag{6.38}$$

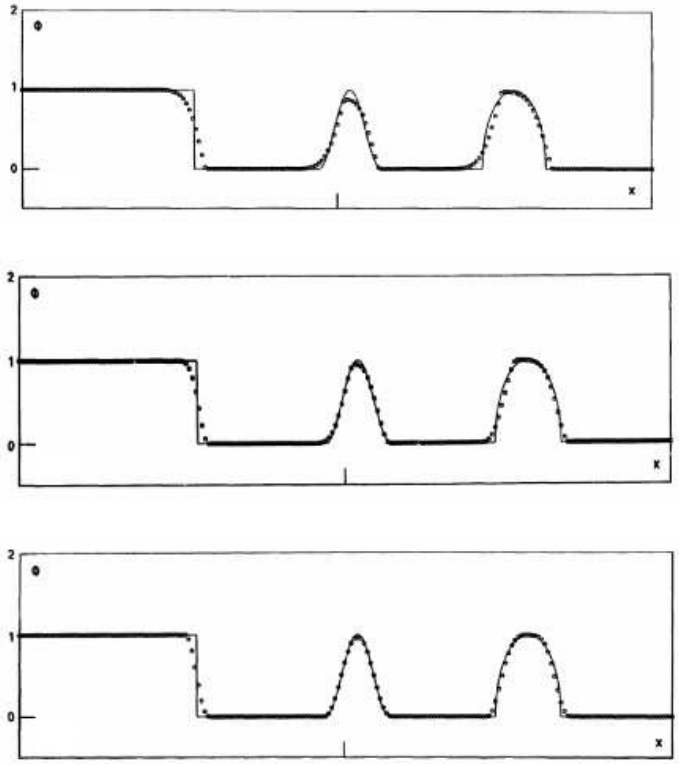

FIGURE 6.8: *Results of one-dimensional advection for different numerical schemes; a) ULTIMATE second-order upwind; b) ULTIMATE Fromm; c) ULTIMATE QUICKEST. The CFL number for all cases: c=0.05. The graphs taken from (Leonard,(1991)).*

where $k_{\gamma_{cic}} \geq 0$ is the factor controlling the contribution of the algorithms in the evaluation of $\tilde{\alpha}_{nb}$. The recommended value of $k_{\gamma_{cic}}$ is 1.0 (Ubbink, 1997), however, it is a matter of experience which value is the most suitable for a particular simulation. Once the interface is parallel or nearly parallel to the flow direction, $\gamma_{cic}$ tends to zero. Consequently, one may expect a mild gradient passing the considered face, thus, the ULTIMATE QUICKEST, with the pure QUICKEST, will play a role. Otherwise, if the interface tends to be perpendicular to the flow direction and the gradient increases its steepness, $\gamma_{cic}$ increases giving priority to Hyper-C.

Since, the normalized, time-averaged, face value of $\alpha$ is known, evaluating its actual value is straightforward. For the normalized value, (6.24), the actual face value yields

$$\alpha_{nb} = \tilde{\alpha}_{nb}\alpha_A^n + (1 - \tilde{\alpha}_{nb})\,\alpha_U^n. \tag{6.39}$$

In order to eliminate $\alpha_U^n$ from (6.39), the same equation, (6.24), but for the donor

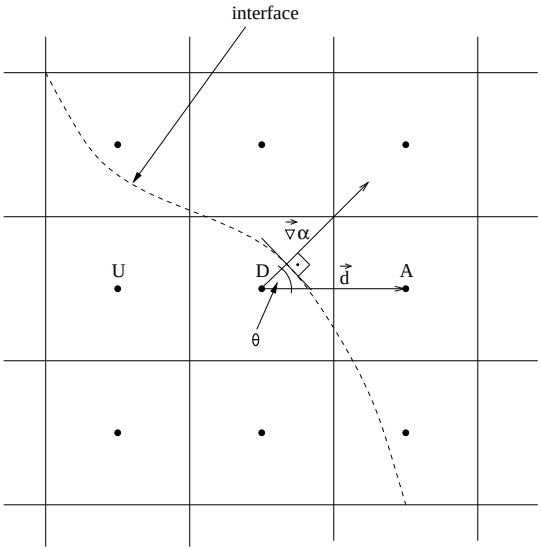


FIGURE 6.9: *The angle theta between the vector connecting the centroids of the donor acceptor cells and the direction of the interface gradient.*

cell, is used. Consequently,

$$\alpha_U^n = \frac{\alpha_D^n - \tilde{\alpha}_D^n \alpha_A^n}{1 - \tilde{\alpha}_D^n}. \tag{6.40}$$

Substitution of (6.40) in (6.39), gives

$$\alpha_{nb} = (1 - \beta_{nb})\, \alpha_D^n + \beta_{nb} \alpha_A^n, \tag{6.41}$$

where

$$\beta_{nb} = \frac{\tilde{\alpha}_{nb} - \tilde{\alpha}_D^n}{1 - \tilde{\alpha}_D^n}. \tag{6.42}$$

In the algorithm the face values of the void fraction are substituted in equation (6.19), where, for a two-dimensional scheme, source terms appear at the right hand side of the equation. These terms are associated with the divergence resulting from the sweep, see (6.1), and if occurring the divergence from the phase transition. The procedure for the evaluation of the void fraction at the face is repeated for each sweep of the Eulerian-Lagrangian algorithm. This finally leads to the new distribution of $\alpha$ at the new time.

# RESULTS

CHAPTER 7

## 7.1 Single phase flow

This section is devoted to results of the flow around hydrofoil NACA 0015 in a channel. The results of the simulation, give insight in effects brought about by various discretization methods for the convective term in the momentum equation. These methods considered are: a blend of UDS (Upstream Differential Scheme) and CDS (Central Differential Scheme) with emphasis on UDS; a blend of UDS and CDS with emphasis on CDS; and, CDS improved by artificial dissipation. The latter has been described in detail in Sec.(5.2.2). Methods with the UDS and CDS blend are first-order accurate schemes in space and time. CDS improved by artificial dissipation is second-order accurate in space and first-order in time. Since the energy equation does not take part in these simulations, the global accuracy in space for the CDS method with artificial dissipation is second-order.

Three test cases are discussed. The calculations have been carried out in the computational domain illustrated in Fig.(7.1). The domain has been split into two blocks. One block wraps around the hydrofoil, the other block, the front block extends between the hydrofoil and the inlet plane. The latter block is necessary in order to minimize the spurious effects of the variation of the pressure at the inlet of the computational domain. Since the inlet of the block around the hydrofoil is too close to the hydrofoil, a constant pressure boundary condition at the inlet of this block would give inaccurate results. Introduction of the front block solves this problem. The front block is discretised with an H-type grid of $16 \times 26$ control volumes, whereas the block around the hydrofoil of $C$ type consists of $134 \times 41$ control volumes, see Fig.(7.2). This is the basic grid. At the end of this section the influence of the grid density on the results is considered.

The flow is assumed incompressible and inviscid. The simulation is carried out neglecting effects of gravity. Inlet velocity, directed horizontally, amounts to $u_\infty = 12[m/s]$. The angle of attack of the hydrofoil is $6^\circ$. At the outlet, a constant pressure boundary condition is imposed. The outlet pressure is taken equal to $p_\infty = 74175[Pa]$. The density is taken equal to $\rho = 999[kg/m^3]$. Phase transition is ab-

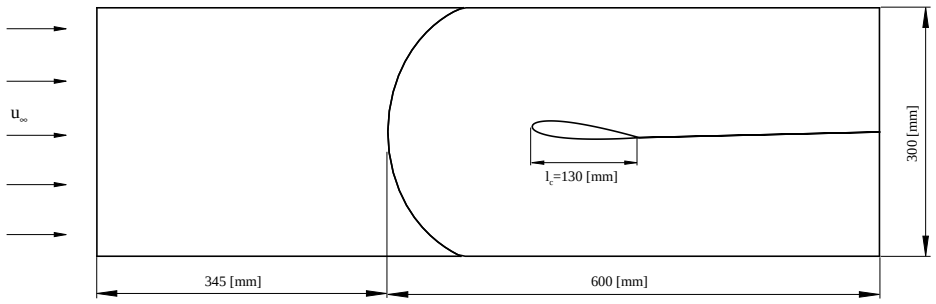


FIGURE 7.1: *Geometry of the computational domain for NACA 0015 at* $6^\circ$ *angle of attack.*

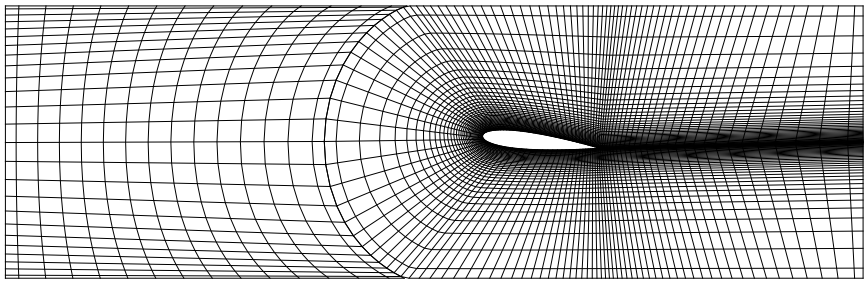

FIGURE 7.2: *Grid. The front block* $16 \times 26$ *cells; the second block* $134 \times 41$ *cells.*

sent.

Since the flow is inviscid and gravitational forces are not present, one may establish criteria that determine the quality of numerical results. The absence of viscous forces implies that the resultant drag force exerted by the flow on the hydrofoil (or any other object) must be zero. Once gravitational forces are neglected, according to the Bernoulli equation, the value of the total pressure must be constant everywhere in the domain. Additionally, following the theory of the flow around a body and employing the Kutta condition, there are two stagnation points, one at the leading and one at the trailing edge. At these points the velocity becomes zero and the value of the static pressure is equal to that of the total pressure.

The following results comprise illustrations of static and total pressure distributions, velocity vectors around the hydrofoil as well as drag and lift forces. Provided

are plots of the pressure coefficient, defined as

$$Cp = \frac{p - p_\infty}{\frac{1}{2}\rho u_\infty^2} \tag{7.1}$$

and the total pressure coefficient, defined as

$$Cp_t = \frac{p_t - p_\infty}{\frac{1}{2}\rho u_\infty^2}, \tag{7.2}$$

with $p_t = p + 1/2\rho\,|\vec{u}|^2$ and distributions of static and total pressure as well as tangential velocity on the hydrofoil surface are also provided.

### 7.1.1 UDS/CDS blend 75%

It is well known, that UDS, which is first order accurate, underestimates the values of the variables. This is caused by the fact that variables which are to be evaluated at the boundary of the control volume are taken equal to those at the centroids of the control volume. Consequently, in a region with high gradients, where the difference between values at adjacent nodes is substantial, one may expect that the difference of the value at the cell face and that at the centroid is also substantial (Leonard, (1979)). Clearly, the coarser the grid, the larger the underestimation of the variable. Refinement of the grid decreases the magnitude of the underestimation. Only infinitesimally small cells would give the exact result. The advantage of UDS is that the scheme provides unconditional numerical stability.

In this test case the UDS scheme is blended with CDS. The approach is constructed such that the contribution of UDS and the part of CDS (the unknown velocity at the considered control volume) is regarded implicitly, whereas the rest of the CDS term (the known velocity at adjacent control volumes) is explicit. The blending parameter is a user controlled coefficient. Here, in order to emphasize the effect of UDS, the contribution of the UDS scheme has been set at 75%.

The underestimation appears in regions of high gradients. For the flow around the hydrofoil this region is positioned at the leading and at the trailing edge of the profile, where the flow stagnates. Underestimation of velocity takes place at the nose, at the second point above the stagnation point. This is the region of the largest changes of the velocity, from about zero to the highest value in the domain. Since, the highest velocity is underestimated and it contributes in the evaluation of the velocities at the subsequent nodes at the suction side, the velocity at neighbouring cells also has a too low magnitude. One can observe this effect comparing Fig.(7.4c) and Fig.(7.6c). The profiles of velocity at the suction side indicate that at a small distance from the surface a stronger dissipation of kinetic energy appears. This numerical dissipation has an effect on the static pressure which is also lower than expected (compare the pressure plots in Fig.(7.4c) and Fig.(7.6c) or Fig.(7.8c)). The underestimation of the

two variables superimposes resulting in a deterioration of the distribution of the total pressure, as well as the total-pressure coefficient. Since in Fig.(7.4) the distribution of the total pressure should be a straight line, the values at the suction side are substantially lower than those at the pressure side, see Fig.(7.4b) and Fig.(7.4c). These losses in the total pressure are also observed in the total pressure isolines, Fig.(7.3b), where the region of dissipated energy is observed at the leading edge and visible far behind the trailing edge. Although, both, the static pressure and the velocity, have a contribution in the total pressure, the velocity plays the major role as it appears as a non-linear term in the Bernoulli equation. The underestimation of the static pressure is also expressed by the drag force which amounts to $351.17[N/m]$, see Fig.(7.4a). Since calculations are carried out in two dimensions, the dimension of the drag and lift force is given in Newton per meter in the third direction. Since the flow is inviscid the value of the drag force should be zero. Since the scheme has a contribution of CDS, the results are not free from oscillatory effects. These are observable in regions of high gradients, i.e. at stagnation points. At the leading edge, one can notice the considerable overshoot in the total pressure, see Fig.(7.4c) and Fig.(7.4b). Since the value of total pressure is more sensitive to changes in the velocity than in the static pressure, one may assume that the reason lies in the overestimation of the velocity. The overestimated value is placed at the neighbour node, towards the suction side. The possible explanation of the effect will be given in the following subsection. Oscillatory behaviour also appears on the lower side of the profile, at the trailing edge, see Fig.(7.4c).

The plots in Fig.(7.4c) for the tangential velocity along the contour of the hydrofoil should show closed lines, whereas at the trailing edge, one can see a discontinuity in the distributions. It results from the way the grid has been constructed. Since the grid is of $C$ type and consists of quadrilateral cells, the two control volumes which boundaries are next to the trailing edge, contact each other only at their two corners. Surface values of variables are obtained from extrapolation from centroids to cell-boundary midpoints. In the cell-centered scheme the flow quantities are not known at the corners, thus the trailing edge value is not included in the plot.

### 7.1.2 UDS/CDS blend 5%

In this test case, the dominant scheme, CDS, is of second order. It produces spurious oscillations in the distribution of the variables due to the odd-even decoupling discussed in Chapter (5) and (Leonard, (1979)). The decoupling results in the so-called checkerboard pattern of the variable distribution. Clearly, the higher the gradients of the variable the stronger the oscillation. In extreme cases, particularly in structured, thus quadrilateral, grids the oscillatory behaviour may result in loss of numerical stability in the course of the calculation. Therefore, in the test case, described in the present subsection, the UDS scheme has been incorporated as a smoother of oscillations, which maintains numerical stability.

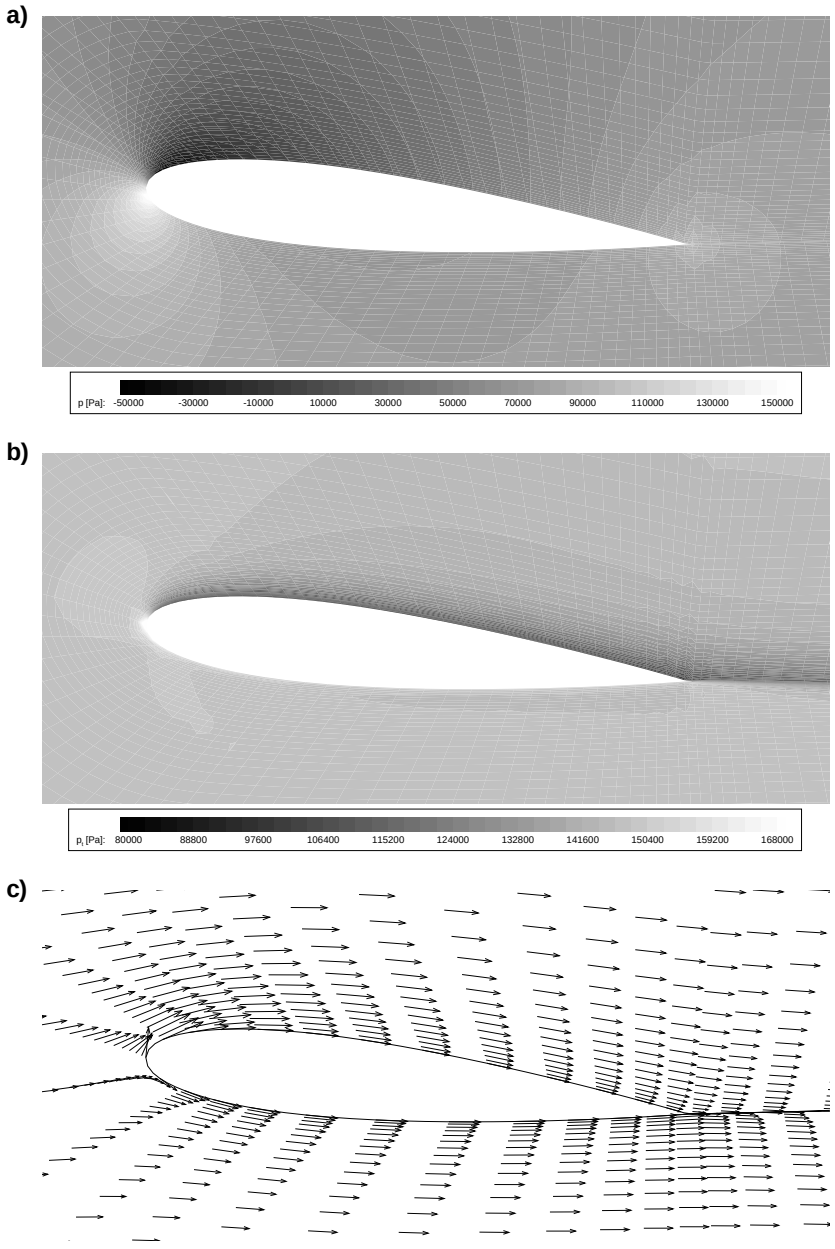


FIGURE 7.3: *Results for flow around the hydrofoil NACA 0015* $u_\infty = 12[m/s]$, $\alpha = 6^\circ$, $p_\infty = 74175[N/m^2]$. *UDS/CDS 75%. C-type grid* $134 \times 41$ *control volumes. The computed total pressure* $p_{t_{comp}} = 1.46103[bar]$. *a) static pressure isolines; b) total pressure isolines; c) velocity vectors.*

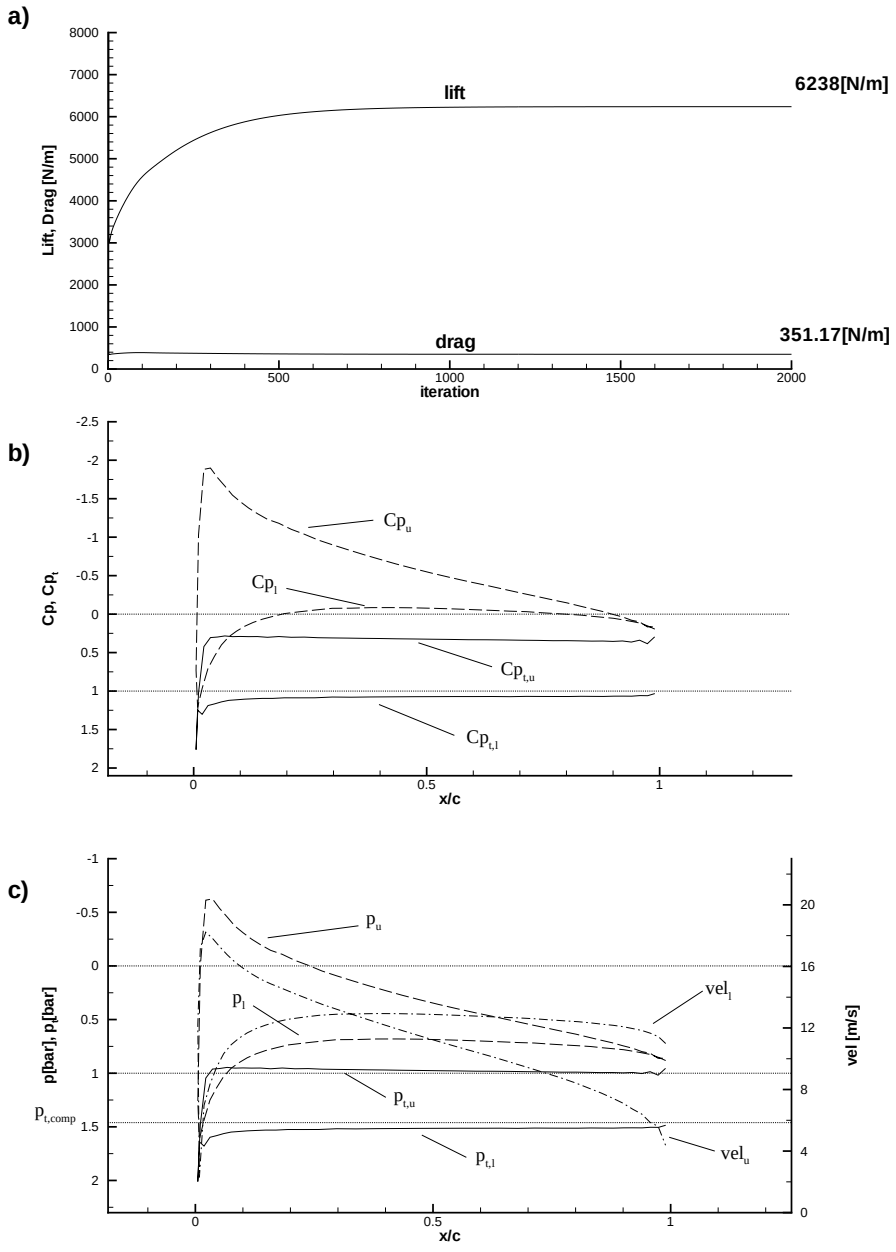


FIGURE 7.4: *Results for flow around the hydrofoil NACA 0015* $u_\infty = 12[m/s]$, $\alpha = 6^\circ$, $p_\infty = 74175[N/m^2]$. *The computed total pressure* $p_{t_{comp}} = 1.46103[bar]$. *UDS/CDS 75%. C-type grid* $134 \times 41$ *control volumes. a) drag and lift force as function of time; b) coefficients of total,* $Cp_t$*, and static pressure,* $Cp$*; c) total pressure,* $p_t$*, static pressure,* $p$*, and tangential velocity,* $vel$.

Oscillations appear in regions of high values of the gradient. This can be observed in Fig. (7.6c) and (7.6b). The oscillations of the velocity at the pressure side begin to appear in the region right downstream of the stagnation point. The shorter the distance to the trailing edge the larger the amplitude of the oscillations, see the velocity plot in Fig.(7.6c). At the leading edge, one can see the unphysical peak in the total pressure and its coefficient. It shows up as the white spot at the nose of the profile in Fig.(7.5b). This extremum is positioned at the node right above the stagnation point. In this region the highest gradient of the velocity appears. Since CDS is the dominant scheme, according to the above discussion on its drawbacks, the contribution of variables at the node just above the stagnation point in the evaluation of the velocity played a minor role. Thus, clearly the velocity has been estimated with variables at the stagnation point and at a point in the region of the highest velocities. Large values of the velocity above the considered node probably led to the overestimation of the variable in the control volume the node belongs to. In two dimensions, CDS forms a checkerboard pattern of values. This means that oscillations propagate in both directions of the grid. This is confirmed by Fig.(7.5b), where the wiggles appear at the suction and pressure side, and propagate in the direction normal to the hydrofoil. The problem associated with the velocity distribution does not affect the pressure. Values of the velocity at peaks and minimums are used in the evaluation of fluxes through the boundaries of the control volume. Assuming second-order interpolation of the variable on the boundary, see (5.9), one obtains the flux estimated on the basis of an averaged velocity which cancels the oscillation. Thus, fluxes are evaluated with good accuracy. Pressure correction is calculated on the basis of integrated fluxes over the boundaries of the control volume, see (5.64). Since the gradient of the correction may cause oscillatory behaviour of the correction distribution, the additional term with the third derivative of the pressure is employed to eliminate this spurious effect, see (5.64). Taking this into account, there is no reason that the pressure correction should depart from a smooth distribution. Therefore the pressure distribution remains smooth, see the static pressure plot in Fig.(7.6c) and the static pressure coefficient in (7.6b). The averaged velocity, particularly at the cell face, is approximately correct, thus the estimation of the pressure leads to a high level of accuracy. This is also evident in the drag force, which amounts to $34.68[N/m]$ only and a substantially higher value of the lift force, see Fig.(7.6a). This is a huge difference in comparison to the outcome described in Sec.(7.1.1). The proper estimation of the velocity also affects the total pressure. In Fig.(7.6c) and (7.6b), one can observe that the distributions are approximately straight lines (except close to the trailing and leading edge), for the total pressure and its coefficient, respectively. Comparing the results of the UDS dominated scheme with the CDS dominated scheme, it is concluded that on the same grid the latter gives substantially better results, much larger tangential velocities, lower static pressure (higher lift, lower drag) and lower values

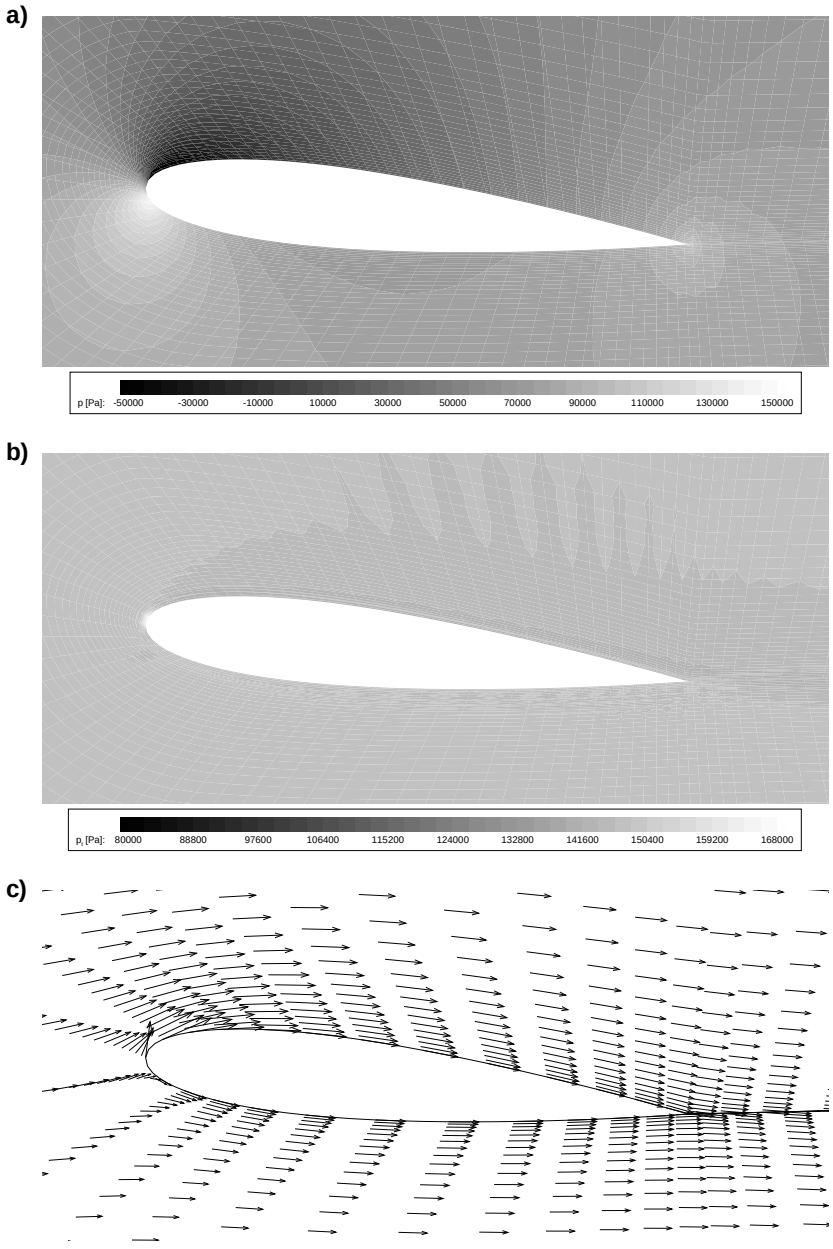


FIGURE 7.5: *Results for flow around the hydrofoil NACA 0015* $u_\infty = 12[m/s]$, $\alpha = 6^\circ$, $p_\infty = 74175[N/m^2]$. *UDS/CDS 5%. C-type grid* $134 \times 41$ *control volumes. The computed total pressure* $p_{t_{comp}} = 1.46103[bar]$. *a) static pressure isolines; b) total pressure isolines; c) velocity vectors.*

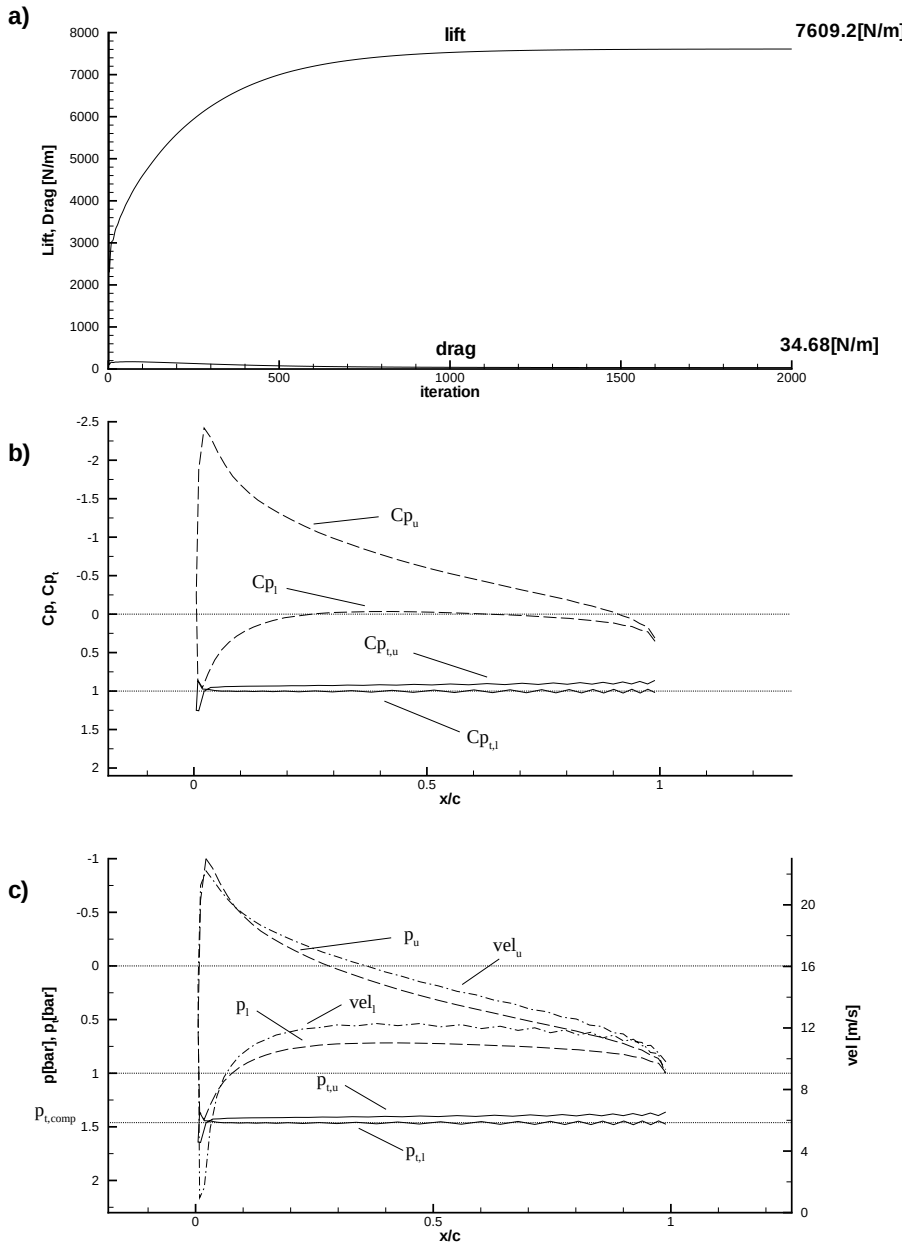


FIGURE 7.6: *Results for flow around the hydrofoil NACA 0015* $u_\infty = 12[m/s]$, $\alpha = 6^\circ$, $p_\infty = 74175[N/m^2]$. *UDS/CDS 5%. C-type grid* $134 \times 41$ *control volumes. The computed total pressure* $p_{t_{comp}} = 1.46103[bar]$. *a) drag and lift force as function of time; b) coefficients of total,* $Cp_t$, *and static pressure,* $Cp$; *c) total pressure,* $p_t$, *static pressure,* $p$, *and tangential velocity,* $vel$.

of the numerics-induced losses/gains of total pressure.

### 7.1.3 CDS and artificial dissipation

To cure the drawbacks associated with the oscillatory behaviour of CDS, an additional term has been added to the convective term of the momentum equation, namely artificial dissipation. The main concept of the method employing CDS with artificial dissipation has been described in (Jameson, Schmidt and Turkel, (1981); Pulliam, (1986)). In the present method the artificial dissipation consists of two terms, the second order implicit and the fourth order explicit dissipation term. The general concept is that the fourth-order dissipation plays the role of the odd-even oscillation damper, whereas the second-order one is supposed to control the stability in regions with large gradients. The dissipation term is constructed such, that the higher the second-order dissipation term the lower the fourth-order one, see (5.20) and (5.21).

The value of the dissipation coefficients depends on the particular simulation. Many test cases has been carried out to determine proper values for the coefficients. For the test case described here the coefficients are chosen as:
- $a_1 = 1/8$,
- $a_2 = 1/8$,
- $b_1 = 1/32$,
- $b_2 = 1.6$.

The first visual effect in the plots of the velocity distribution around the hydrofoil surface, is that of effectively damped oscillations. The oscillations disappeared almost over the whole length of the pressure side, see Fig.(7.8c). However, at the stagnation points, specifically the rear stagnation point, there is still some oscillation present. Nevertheless, at the nose of the profile the magnitude of the peak in the total pressure remained approximately the same as in the case of the dominant CDS method. Since, the second-order dissipation term in the dissipation is responsible for overshoots in regions of very high gradients, it seems to be clear, that increasing the value of this term might improve the result. However, this affects the magnitude of the fourth-order dissipation term which attains lower values and does not perform as well. Clearly, it is also possible to decouple the two terms and let them act separately. Then, although the fourth-order term was set at a proper level, the second-order one, higher than in this simulation, would affect not only the solution in the region of the high gradient, but also in the rest of the domain. This would provide a too large overall dissipation, such as in the case of the dominant UDS. Hence, the current value of the second-order dissipation term is maintained.

The total pressure is influenced by the velocity and the pressure. Since both quantities are represented correctly, the total pressure is a straight line in the regions of smooth velocity distribution, see Fig.(7.8c) and Fig.(7.8b). Moreover, the value of the total pressure approximately coincides with the exact one.

The oscillations of the velocity near the hydrofoil surface have been effectively

removed. The distribution of the static pressure does not have to be affected by the oscillatory behaviour of the velocity. However, values of the pressure can deteriorate if the overall prediction of the velocity departs from the correct one. The artificial dissipation constitutes an additional term, of the same order, or of higher order as the truncation error, which for finite mesh changes the original form of the convective term in the momentum equation. Thus, it is important to realize that this added term modifies the momentum equation and the coefficients used should be kept as small as possible while still maintaining stability (Pulliam, (1986)) and allowing for more realistic distributions of the variables free of oscillations. Apparently, in the case of the present simulation, the artificial dissipation affected the velocity, affecting only slightly the distribution of the static pressure. It is evidently revealed by the value of the drag force, which amounts to $20.67[N/m]$, see Fig.(7.8a). This particular result is not ideal. However, the overall outcome appears as the most accurate one among the three schemes described in this section.

To analyze the influence of the grid resolution, two additional simulations have been performed, one on a coarser grid, one on a finer grid. For the one assuming the coarse discretization, the grid $68 \times 22$ control volumes has been used. The grid with $266 \times 80$ control volumes has been used for the simulation assuming the finer resolution. The results are illustrated in Fig.(7.9) in which for the three schemes the drag force is shown as function of the number of iterations. This figure shows that the finer the grid the lower the value of the drag force. It also shows that the rate of convergence of the method depends on the number of grid points, i.e. the finer the grid the slower the convergence rate of the numerical procedure. The CDS method with artificial dissipation requires an order of magnitude more iterations than the blended schemes. Figure (7.10) shows the relation between numerical error (drag force) and number of control volumes used to discretize the computational domain for the three discretization schemes described above. Figure (7.10) shows that the UDS/CDS 75% scheme features the largest error, which decreases linearly with the average cell size. The UDS/CDS 5% scheme shows a reduced error which still decreases linearly with cell size. The CDS-plus artificial dissipation scheme converges almost quadratically with cell size. The non-linear behaviour of this scheme is caused by the decrease in the grid spacing. The value of the second-order artificial dissipation is controlled by factor $\epsilon^{(2)}$ which is given by the minimum function, see (5.21). Since the size of control volumes tends to zero the second-order derivative of pressure decreases too. Eventually, the second-order derivative has such a small value that it controls the value of $\epsilon^{(2)}$ instead of the constant $a_1$. This situation corresponds to a change of the discretization scheme, therefore the results for the CDS-plus artificial dissipation scheme do not correspond to results for precisely the same scheme.

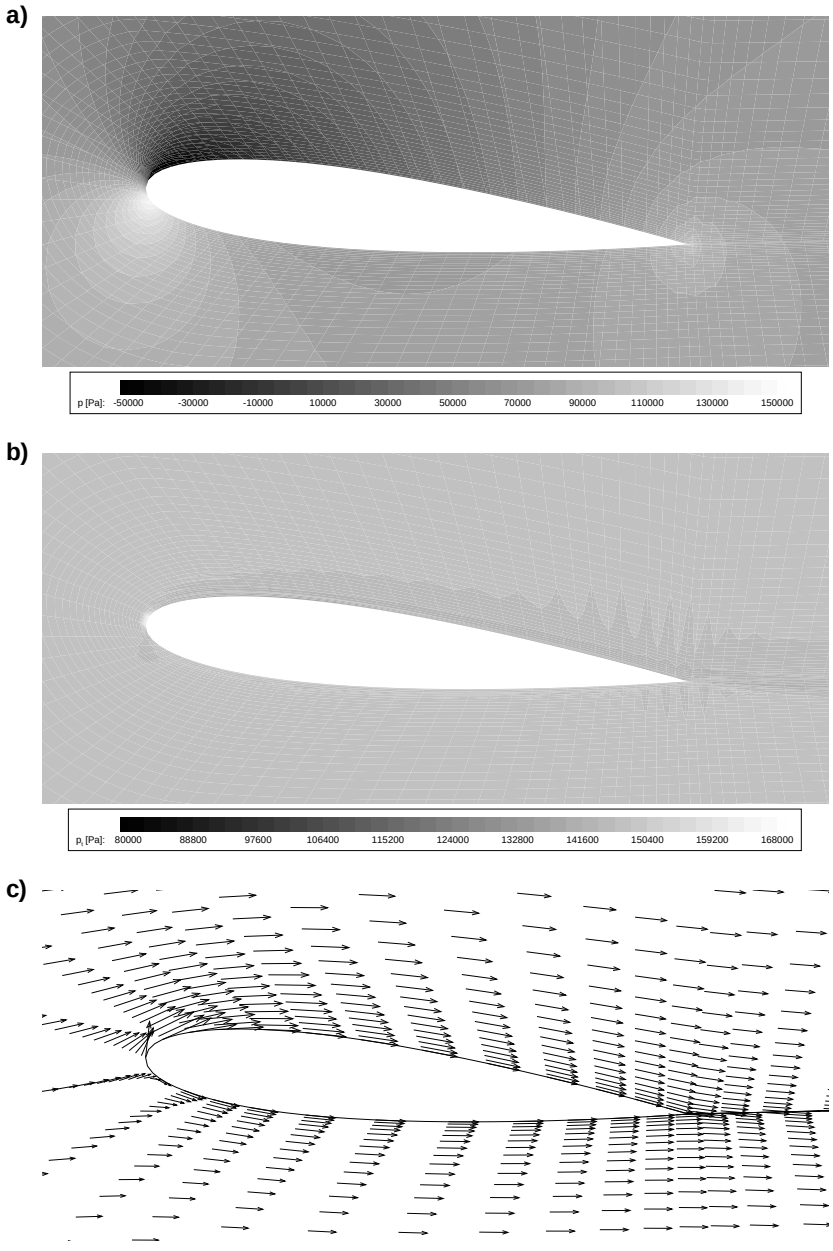


FIGURE 7.7: *Results for flow around the hydrofoil NACA 0015* $u_\infty = 12[m/s]$, $\alpha = 6^\circ$, $p_\infty = 74175[N/m^2]$. *CDS coupled with the artificial dissipation. C-type grid* $134 \times 41$ *control volumes. The computed total pressure* $p_{t_{comp}} = 1.46103[bar]$. *a) static pressure isolines; b) total pressure isolines; c) velocity vectors.*

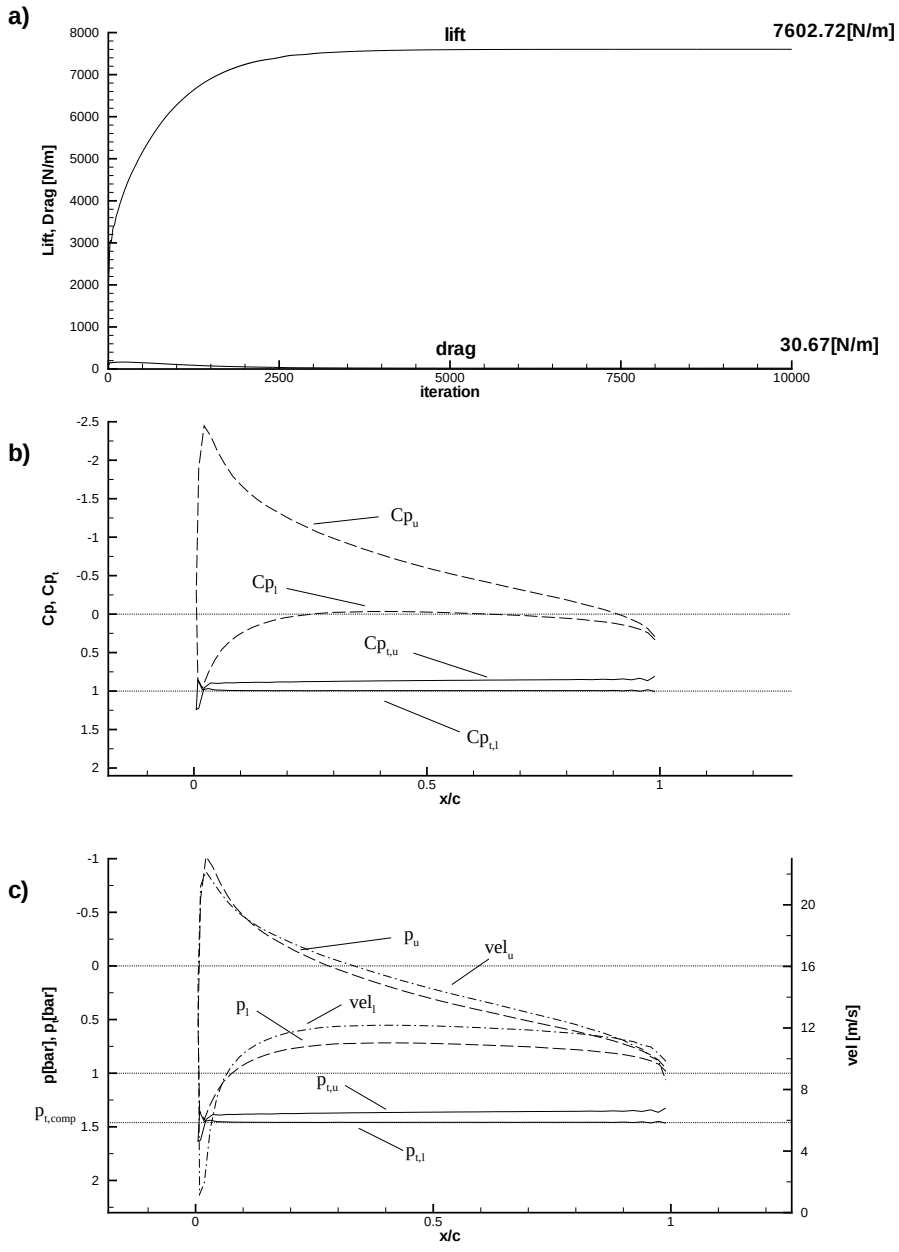


FIGURE 7.8: *Results for flow around the hydrofoil NACA 0015* $u_\infty = 12[m/s]$, $\alpha = 6^\circ$, $p_\infty = 74175[N/m^2]$. *CDS coupled with the artificial dissipation. C-type grid* $134 \times 41$ *control volumes. The computed total pressure* $p_{t_{comp}} = 1.46103[bar]$. *a) drag and lift force as function of time; b) coefficients of total,* $Cp_t$, *and static pressure,* $Cp$; *c) total pressure,* $p_t$, *static pressure,* $p$, *and tangential velocity,* $vel$.

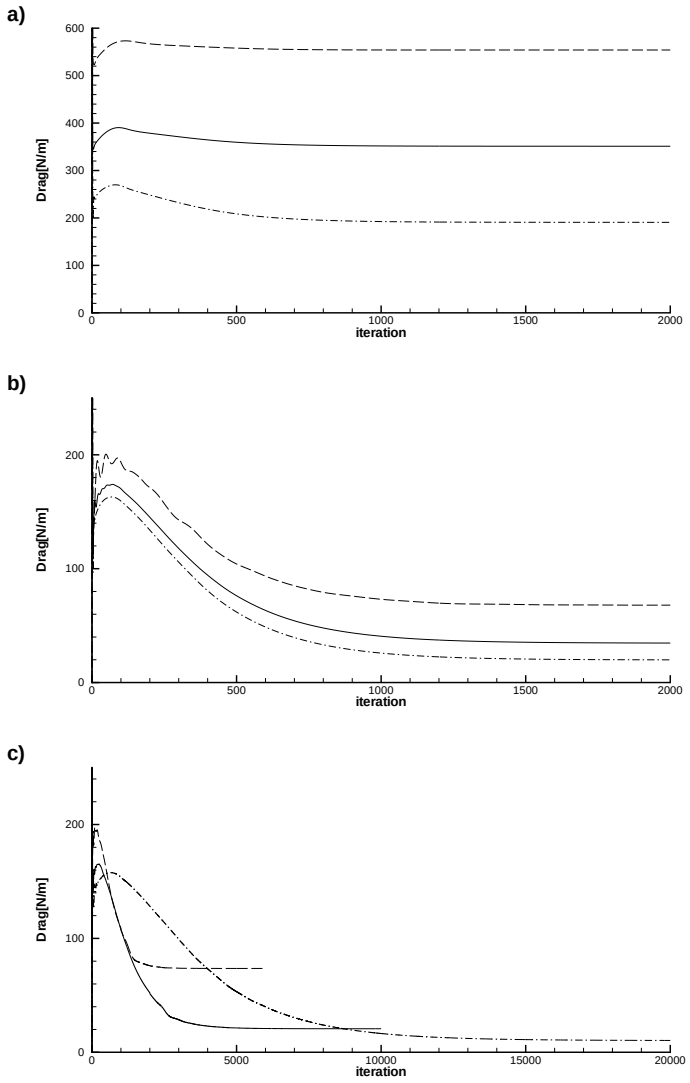


FIGURE 7.9: *NACA 0015. Drag force as function of iteration number. Dashed line - grid* $68 \times 22$*; solid line - grid* $134 \times 41$*; dash-dotted line - grid* $266 \times 80$*. a) UDS/CDS scheme, blend 75[%]; b) UDS/CDS scheme, blend 5[%]; c) CDS with artificial dissipation.*

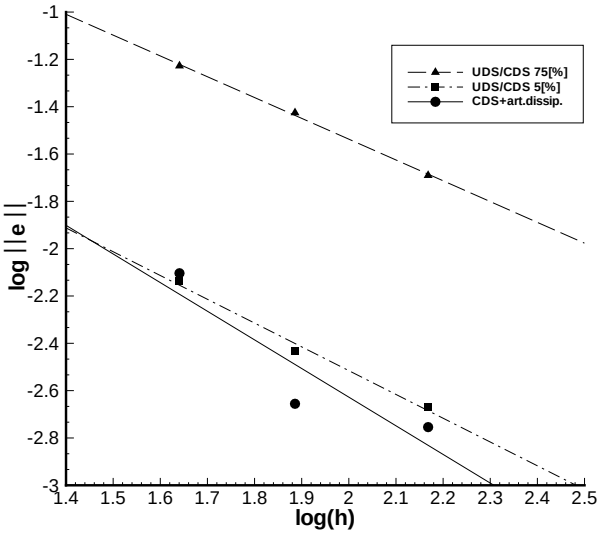


FIGURE 7.10: *Numerical error as function of number of control volumes in the computational domain; dimensionless h is defined as the square root of the number of control volumes in the computational domain,* $\|e\| = D/0.5\rho u_\infty^2 c$*, with D - drag force [N/m] and c - the hydrofoil chord. Dashed line - UDS/CDS scheme, blend 75[%]; dash-dotted line - UDS/CDS scheme, blend 5[%]; c) solid line - CDS with artificial dissipation.*

## 7.2 Free surface capturing

This subsection is devoted to the validation of the mathematical and numerical model for the case in which a gas-liquid interface is present. Phase transition is not active. The flow is incompressible, viscous without effects of turbulence. The gravitational force acts. Physical properties of the liquid phase are those for water at a temperature of $15°C$ and at atmospheric pressure. For the gaseous phase properties are set for air at the same conditions as for water. Properties are shown in Tab.(7.1). In the momen-

| **Phase** | $\boldsymbol{\rho}[kg/m^3]$ | $\boldsymbol{\mu}[kg/ms]$ |
|---|---|---|
| gas | 1.23 | 1.76e-05 |
| liquid | 998.85 | 0.00115 |

TABLE 7.1: *Physical properties for vapour and liquid water at the temperature of* $15°C$.

tum equation the second-order accurate, spatial discretization, CDS with artificial dissipation, has been used. For the energy equation the spatial discretization has first-order accuracy and uses the pure UDS method. First-order accurate discretization in time has been used. For capturing of the free surface the standard VOF technique has been used. The standard test case is considered, namely the collapse of a water column (Harlow and Welch, (1965); Ramaswamy and Kawahara, (1987); Koshizuka and Oka, (1996)). The simulation follows the experiment carried out by Martin and Moyce (Martin and Moyce, (1952)) in which a water column was at one of the narrower sides of a container. At the initial instant, the bulk of the liquid was constrained by a diaphragm. The diaphragm was suddenly lifted to release the column. This was done fast enough to not affect the flow itself. The cross-section of the experimental setup is illustrated in Fig.(7.11) where the water column is set at the left side of the container. The rectangular base of the column has the dimension $a \times a$. The height is $2a$. It has been assumed, that viscous forces associated with the front and rear rigid boundary of the vessel, are neglected. Thus, the experiment provides a two-dimensional situation and due to this it is suitable for the CFD method described in the present work. Martin and Moyce considered the propagation of the front of the column in the horizontal direction (collapse of the top surface of the column was also measured) in a container which is not constrained at the right side. The current simulation, however, assumes the vessel is to be constrained by an impermeable rigid boundary, see Fig.(7.11). The boundary is set at a distance of $4a$ from the left wall of the vessel. It is similar to the experiment of Koshizuka (Koshizuka and Oka, (1996)), which will be used here for qualitative comparison. Until the front of the column impinges on the right boundary, it is assumed that the front and the top of the column will behave in the same way as in the unconstrained vessel. Thus, the experiment carried out by Martin and Moyce serves the quantitative assessment of the quality of the numerical results. The discretised computational domains are shown in Fig.(7.12). The domain on the right consists of $82 \times 82$ control volumes with a column base of $a = 57.15[mm]$, equal to the one of Martin and Moyce. Results for this domain will be used for the quantitative comparison. For the qualitative assessment, the second domain on the left of Fig.(7.12) will be utilized. This consists of $82 \times 52$ control volumes with the column base $a = 146[mm]$, equal to the one of Koshizuka. For the rigid boundaries bounding the domain, the non-slip boundary condition has been applied. At the top of the domain, where the outlet is assumed, the constant pressure boundary condition is applied.

Aside from the quantitative evaluation of the propagation of the column front and qualitative comparison to the results of the experiment of Koshizuka, an assessment with respect to mass conservation has been carried out. In order to achieve the objective, the left and right rigid boundary of the $82 \times 82$ domain has been extended such, that the water arising after the impingement onto the right wall leaves the domain

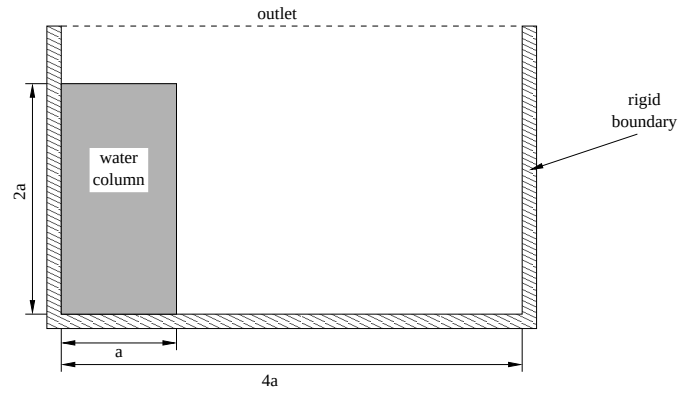


FIGURE 7.11: *Geometry of the experimental setup of Martin and Moyce (Martin and Moyce, (1952)).*

later than in the case of the domain with $82 \times 52$ control volumes. Because of this, the evaluation can be carried on for a longer time. To visualize mass disappearance or production, the energy equation has been employed. The initial temperature is uniform, equal to $15°C$. Each change of this value reflects the loss or appearance of mass in the system. In this way, one reveals the importance of the implementation of the term with the divergence of the velocity field in each step of the split operator method applied to the transport equation for the void fraction, see Sec.(6.1).

First, the qualitative assessment will be shown. The propagation, impinging and deformation of the gas-liquid interface is shown in Fig.(7.13) and (7.14). The time interval between the photographs taken from the experiment of Koshizuka is $0.2[s]$. They correspond to the time intervals of the plots with the computed void fraction distribution.

At the beginning of the flow, gravitational forces make the column to change its shape. The column starts to deform, its bottom part seeking the most stable state. This state will finally be obtained, when the water covers the bottom of the vessel and its kinetic energy lowers allowing the liquid to remain at rest. The observations, as well as calculations have not been carried out until that moment. They are reported up to the first second of the liquid motion. At that stage the liquid has a complicated geometry of its interface and is certainly far from equilibrium. The scale of the experimental setup and the time period for which the liquid motion was observed and calculated, allows neglecting the viscous forces.

At the time $0.2[s]$ the front of the column has progressed to about 75 % of the length of the bottom of the vessel. This result corresponds well with the photograph taken at the same moment. The predicted interface shape is aligned smoothly, thus, the monotonic behaviour of the void fraction is conserved. Also evident is the circulatory flow induced in the air by the motion of the collapsing water column. At

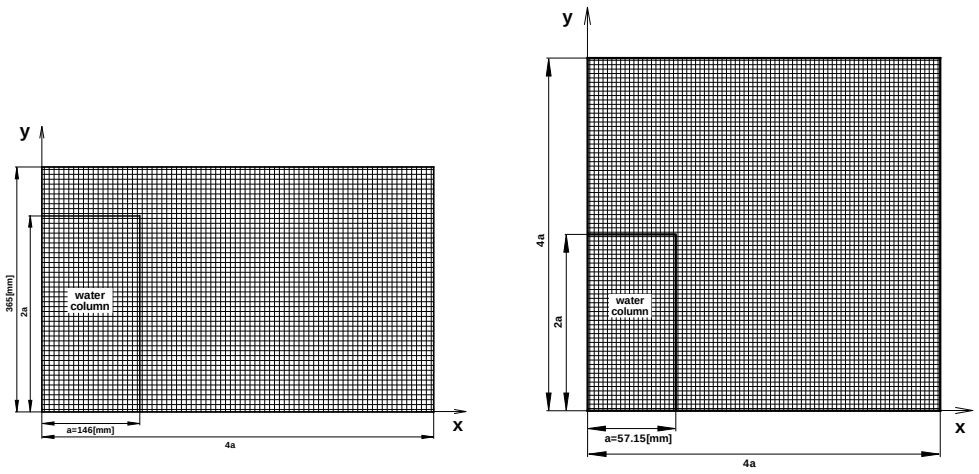


FIGURE 7.12: *Computational domains for collapse of the water column. On the left -* $82 \times 52$ *control volumes, the water column equal to one of Koshizuka (Koshizuka and Oka, (1996)); on the right -* $82 \times 82$ *control volumes, the water column equal to one of Martin and Moyce (Martin and Moyce, (1952)).*

the subsequent stage the water impinges onto the right boundary (this has not been shown in the figures). At this moment the kinetic energy of the water flowing along the bottom transforms into the potential energy associated with the total pressure at the stagnation point positioned somewhere at the location of the impingement. Since there is not any constraint on the top, the liquid begins to rise, acting against gravitational forces and forming the secondary column at the right boundary of the domain. This moment has been captured at time $0.4[s]$ when the free surface of the water is nearly parallel to the domain bottom. The top of the secondary column is elevated such, that the liquid leaves the domain at the right upper corner. The subsequent stage of the flow shows the moment when gravitational forces halt the upward motion of the secondary column. At time $0.6[s]$ the flow nearly stops and the secondary column begins to deform at its side. The formed bump folds down capturing a portion of air. During this process the front of the bump impinges on the gas-liquid surface. The stream reaches the domain bottom, partially transforming its kinetic energy into potential energy. Pressure increases causing the front jet of sprayed water droplets. This has been captured at the time $0.8[s]$. Since the methods for the transport of the void fraction tend to keep the interface sharp, the sprayed droplets accumulate in a structure in which the liquid has a high weight contribution. This affects the position of the jet in the numerical simulation. It is lower than that in the corresponding pho-

tograph (Ubbink, 1997).
Experiment shows, that the trapped gaseous structure, described above, is in the form of a group of bubbles or a foam. The numerical methods tends to increase the resolution of the interface, thus the simulation shows this structure as separated from the bulk of the liquid. However, the contribution of the gas is lower than in the region of the pure gas. The final captured stage, at time $1.0[s]$, shows the impingement of the front onto the left wall. This process encapsulates a large portion of the sprayed droplets. This is also revealed in the experiment. The numerical result corresponds qualitatively well with the result of the experiment, showing the gas-liquid structure. The position of the impingement also resembles that shown in the experiment.

The evaluation of mass conservation of the model will be discussed next. First the quality of the two ways of approximation of the void fraction equation are compared. The first way concerns the implementation of the divergence of the velocity field at each step of the split operator method; the second one omits this. The purpose of this paragraph is to reveal the importance of the divergence implementation in the equation. Furthermore, it will be shown how it affects the numerical stability of the solution and the quality of the results.

The transport equation without the divergence term included, results in problems associated with maintaining the void fraction in the range between zero and one. Each excursion of the value out of this range, corresponds to the existence of holes or excesses of mass in the bulk of the considered phase. Most authors then routinely redistribute the mass in the surrounding cells with some diffusion algorithm or reset the volume fraction to one or zero, thus destroying mass conservation (Aulisa et al., (2003)).
To cure the problem, the divergence is computed in each step of the split operator method, see Sec.(6.1).

The comparison between the two versions of the discretization of the transport equation is carried out for the results achieved up to time t=0.43[s]. For the configuration of the grid and boundary conditions of the domain, the calculations without the divergence become unstable at this time. The instability appears not in the form of numerical divergence, but in the sense, that the value of the CFL number becomes larger than unity.

In the test case of the water column collapse, it turns out, that the change of mass summed up in the domain assumes positive values for the calculation without the divergence. This denotes an increment of the mass of the liquid. The process is shown in Fig.(7.15) where the dashed lines indicate the non-divergence simulation. In the same figure one can see the solid lines representing the change of mass resulting from the transport equation in which the divergence of the velocity field is used. The difference between the results of the method that includes the divergence and the ones of the method without divergence is substantial. It is remarkable, that the divergence

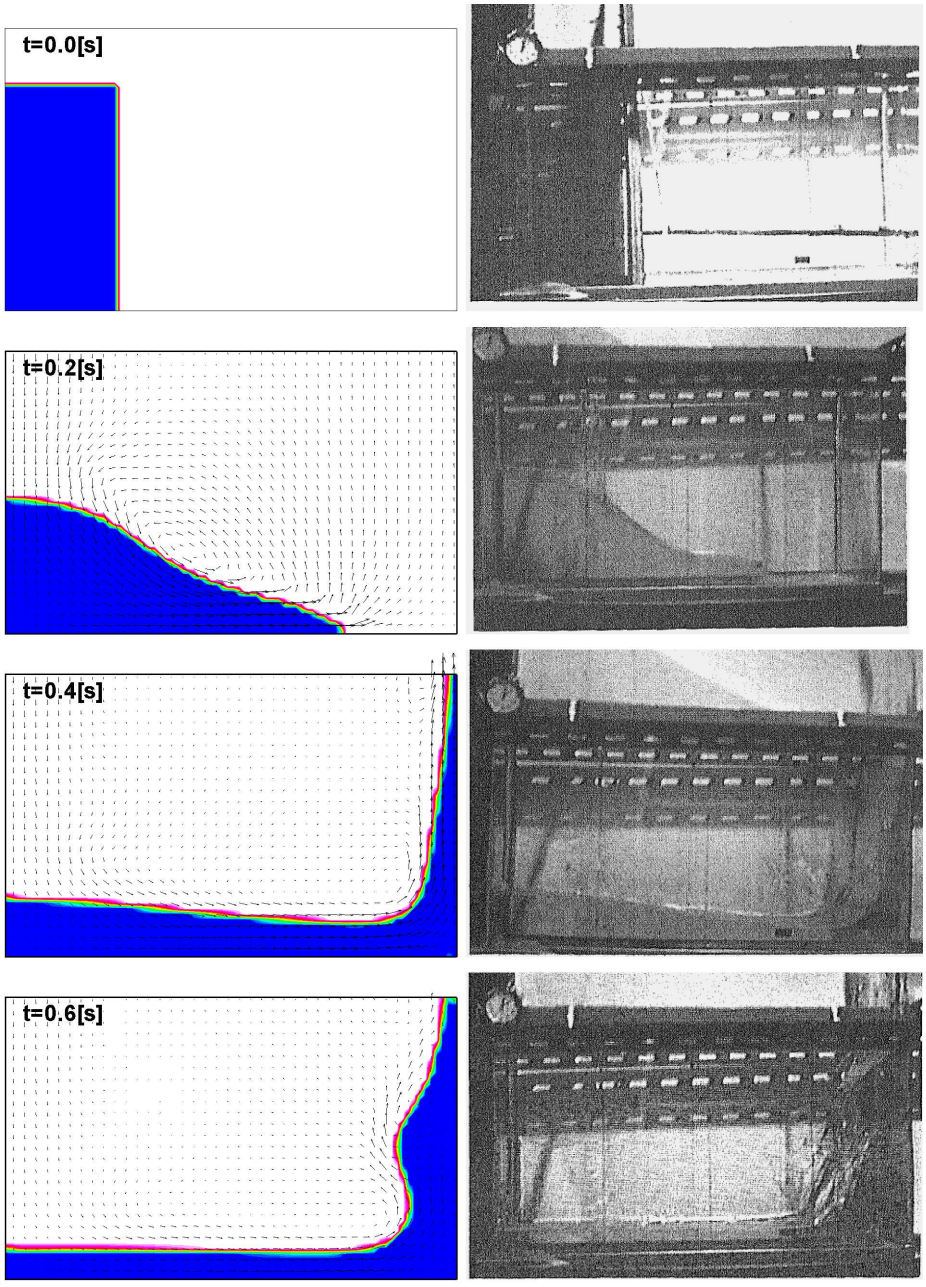


FIGURE 7.13: *Comparison of numerical simulation and experimental results of Koshizuka (Koshizuka and Oka, (1996)). Time frames from* $0.0[s]$ *to* $0.6[s]$. *The numerical result shows the void fraction distribution and velocity vectors.*

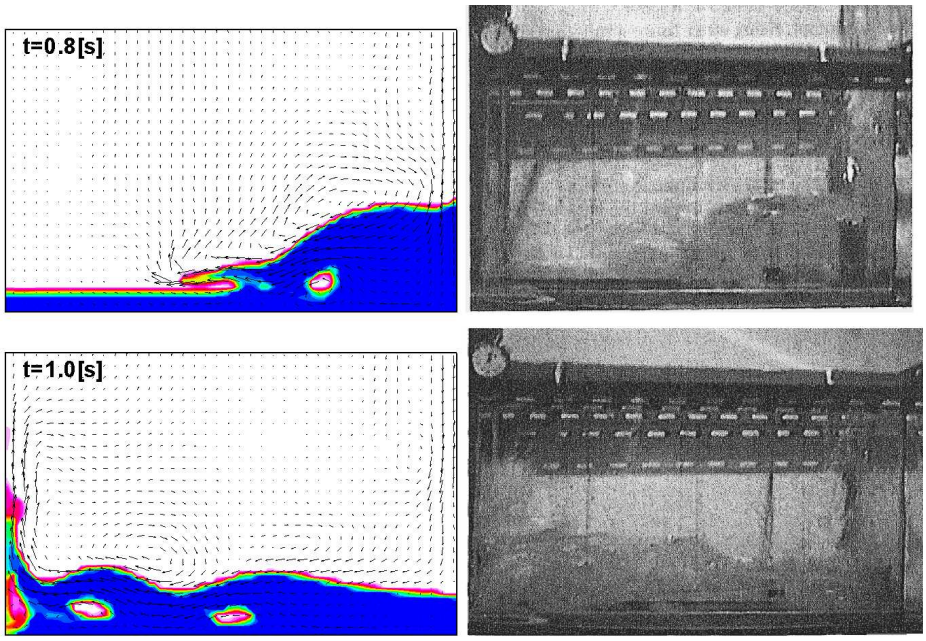


FIGURE 7.14: *Comparison of numerical simulation and experimental results of Koshizuka (Koshizuka and Oka, (1996)). Time frames from* $0.8[s]$ *to* $1.0[s]$. *The numerical result shows the void fraction distribution and velocity vectors.*

version of the transport equation tends to a loss in mass, because $\delta m[kg]$ assumes negative values.

Mass variation can be expressed visually by the distribution of the temperature in the system. This is illustrated for the non-divergence transport equation in Fig.(7.16). Each portion of mass contains a certain amount of energy. In the energy equation, a loss or gain of mass automatically causes a change of energy in the form of a temperature change. This is shown in Fig.(7.16) for three points in time. For the sake of clearness, these time points are also marked in Fig.(7.15) where the vertical, dashed lines indicate the instants at which the distributions of temperature are presented. In Fig.(7.16), one can observe, that the majority of the temperature changes assume values below the initial temperature. This corresponds to a loss of mass. The temperature field outlines the contour of the moving water column. The spots of lower temperature appear in regions of the highest velocity gradients - at the lower part of the column front and at the right upper corner of the column. Since the plot of the mass conservation, given in Fig.(7.15), shows the mass change for the liquid, the change of the temperature in Fig.(7.16) appears in the vapour side of the domain. This is caused by the way in which the liquid mass is computed. This quantity has been computed as the result of differences between the total volume of the domain

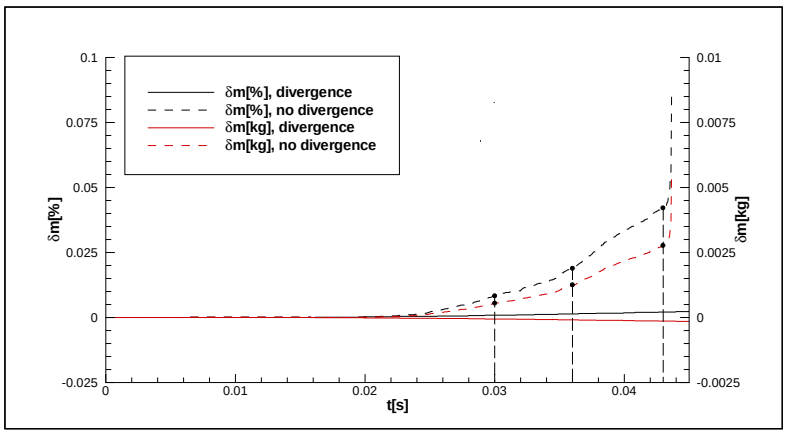


FIGURE 7.15: *Change of mass in the domain vs. time. Dashed lines - the transport equation without the divergence; solid lines - the transport equation with the divergence.*

and the volume of the vapour in it, multiplied by the liquid density. Thus, a loss of vapour mass appears as an increment of the liquid mass, in spite of the liquid mass remaining at an acceptable level of accuracy. Consequently, the plot of the absolute mass change in Fig.(7.15) expresses the equal but opposite drop of mass of the vapour.

Mass conservation in the solution for the case with the transport equation incorporating the divergence is also studied for time up to $t = 0.276[s]$ when the liquid (or rather droplets spread, see Fig.(7.18) at time $t = 0.276[s]$) begins to leave the domain. Figure (7.17) shows the decrease of the liquid mass, which is monotonic up to the instant of the impingement of the water column front on the right boundary. Since the result for the temperature field at $t = 0.165[s]$ in Fig.(7.18) reports regions of higher temperatures, the decrement of the liquid mass may reflect an increment in the mass of the vapour. At the location of the front impingement, one may expect a stagnation point positioned at the right boundary. Such as in the test case concerning the flow around the hydrofoil, see Sec.(7.1.3), the model fails at this point and in the region around it where gradients are high. This failure in the prediction is visible by the sudden drop of the liquid mass at time $t = 0.165[s]$, see Fig.(7.17). Unlike the flow around the hydrofoil (with the artificial dissipation incorporated), the wake of the erroneous distribution develops upwards along the rising water column at the right boundary. This is evident by the steeper slope in the graph of the mass loss of the liquid, see Fig.(7.17), and by the higher temperatures in the region of the evolving liquid front, see Fig.(7.18). Notice, however, that the magnitude of the temperature variation is not as high, as in the case of the transport equation without the divergence incorporated. In the course of the elevation of the water column at the right

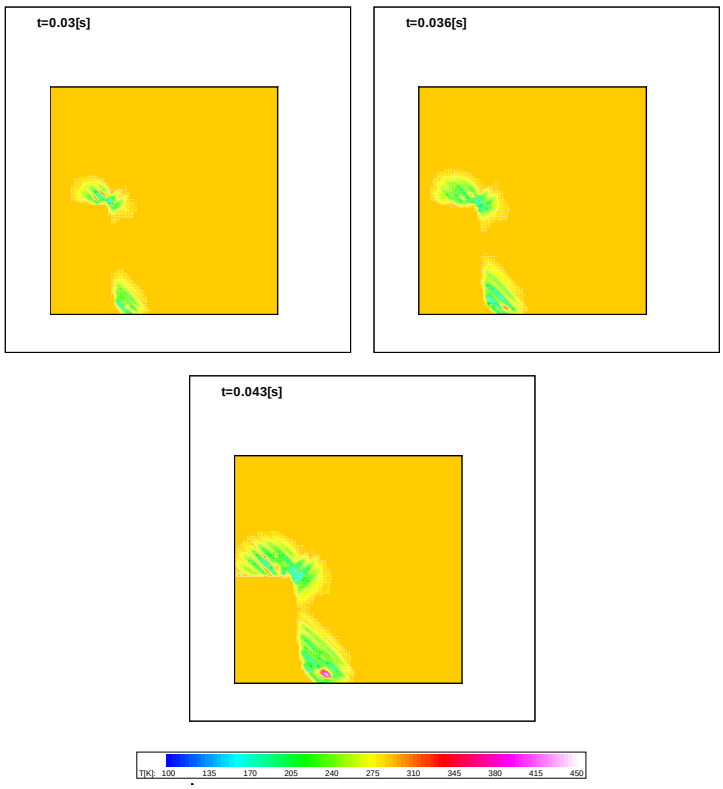


FIGURE 7.16: *Temperature variation caused by the lack of mass conservation. Result for the case of the transport equation without the term with the divergence of the velocity field.*

boundary, its kinetic energy is transformed to potential energy. Thus, the magnitude of the velocity decreases along with the velocity gradient. In these conditions mass is conserved with a higher accuracy. This is clear from the decrement of the slope of the graphs at the time close to $t = 0.276[s]$, see Fig.(7.17).

Further quantitative evaluation follows the experiment carried out by Martin and Moyce (Martin and Moyce, (1952)). In this paragraph, the calculated propagation of the front of the water column is compared to its experimental counterpart. Collapse of the column top is also investigated.

Since the model does not incorporate reconstruction subroutines of the interface, the problem of extraction of data appeared. Since there is not an exact interface, it has been assumed, that the interface is always perpendicular to the rigid boundary. Thus, in the control volume positioned in the neighbourhood of the wall, the position of the interface is determined by the value of the void fraction. Clearly, a lack of exact information on the location of the interface provides an uncertainty in the evaluation.

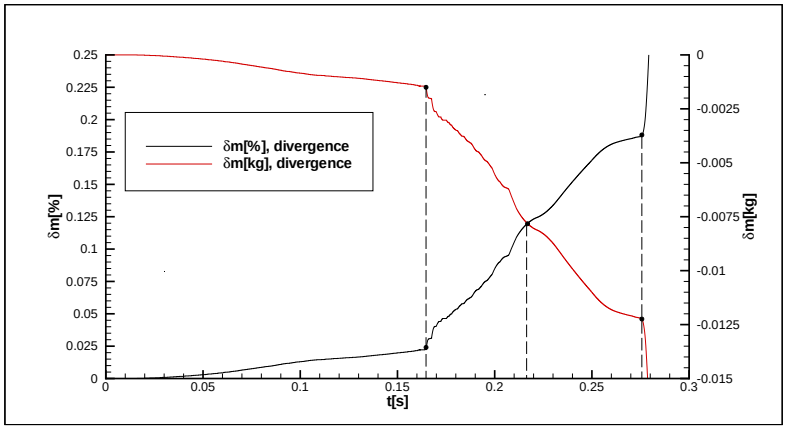


FIGURE 7.17: *Change of mass in the domain vs. time. Results of the method with the transport equation with the divergence included.*

However, because of the methods of interface sharpening, see Sec.(6.2) and Sec.(6.3), the thickness of the free surface is comparable to the mesh size.

The propagation of the column is described by dimensionless parameters. The dimensionless time is defined as

$$T = t\sqrt{2g/a} \qquad \text{or} \qquad \tau = t\sqrt{g/a}, \tag{7.3}$$

where $a$ is the initial width of the column base, $g$ denotes the value of the gravitational acceleration and $t$ is the time. The dimensionless $T$ is used for the front propagation, whereas $\tau$ is used for the top collapse. The spatial parameters are determined as the relation between the actual position of the interface and its initial position. The initial position for the front is the base of the column and for the top, the column height, namely in dimensionless form

$$X = x/a \qquad \text{and} \qquad H = h/2a. \tag{7.4}$$

respectively.

The results are given in Fig.(7.19). The predicted speed of the collapse of the column top corresponds well with the experimental result. However, the front propagation is somewhat overpredicted. This is also reported by Ubbink (Ubbink, 1997). The reason for this is the difficulty to determine the exact position of the leading edge of the front. A thin layer of liquid shoots over the bottom and the rest of the bulk flow follows shortly behind it (Ubbink, 1997).

From a qualitative point of view the test case corresponds with the experiment carried out by Koshizuka. Due to the numerical improvements of the standard VOF approach, the interface is sharp and monotonic. All deformations of the free surface,

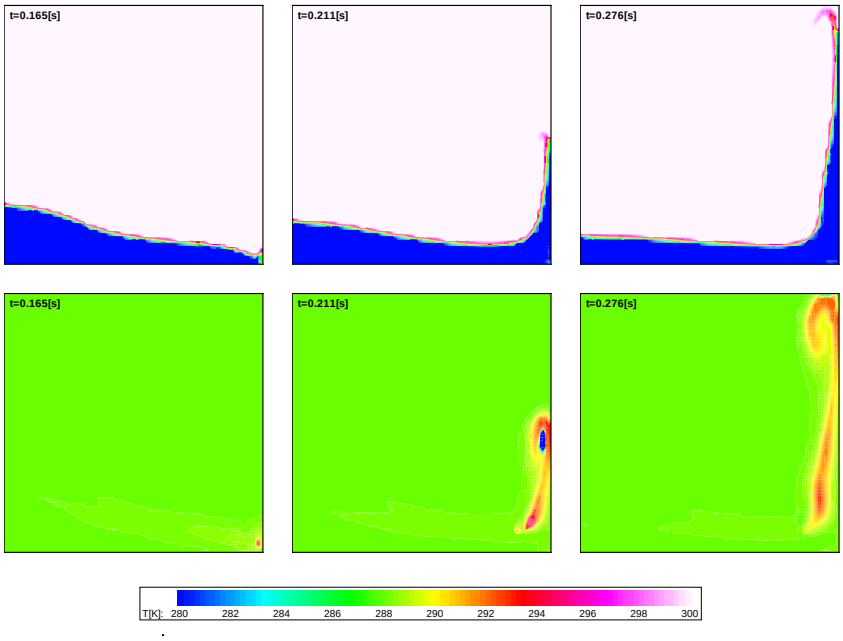


FIGURE 7.18: *Temperature variation in the domain caused by lack of mass conservation. The transport equation with the divergence of the velocity field. The upper row - void fraction distribution; the lower row - temperature distribution.*

observed in the experiment, coincide with the distribution of the void fraction, see Fig.(7.13) and Fig.(7.14). Due to the sharpening tendency of the model some regions of the domain show clusters of the liquid bulk instead of sprayed droplets or foam structures which appear in the experiment.

The quantitative analysis reveals good agreement of the results of the simulation and those of the experiment carried out by Martin and Moyce. As long as high gradients of the flow variables do not appear, accuracy of the numerical outcome remains at an acceptable level. However, sudden changes of parameters, such as in the case of the region close to the stagnation point, cause failures in the prediction. Employment of the term with the divergence of the velocity field in the split operator method decreases the error substantially. Nevertheless, the result still departs from reality, from a point of view of mass conservation. A possible reason of the problem lies in the order of the time discretization used in the model. A higher order discretization for the time dependent terms or at least a decrease of the time step is expected to increase the quality of the results.

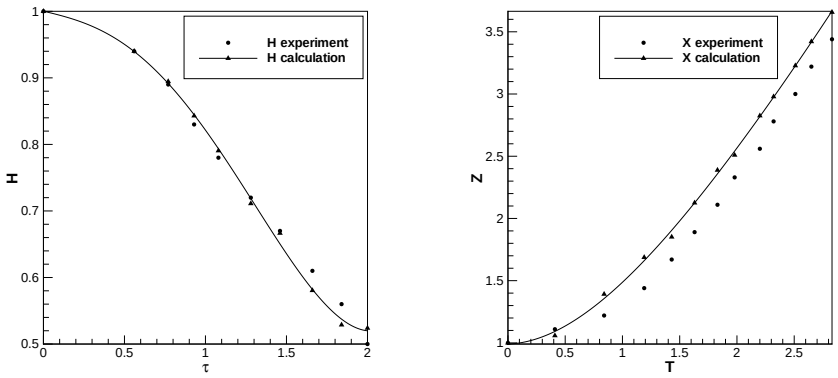


FIGURE 7.19: *Comparison of the experimental results of Martin and Moyce and data extracted from the present calculations.*

## 7.3 Free surface capturing with phase transition incorporated

In many industrial systems, cooling processes play a vital role. A very good example is a power plant system in which partially condensed steam flows out of a steam turbine. In order to increase the efficiency of the thermodynamic cycle, further cooling of the vapour is necessary. This can be carried out in a direct contact mode with various types of equipment, such as a pool condenser or any other device in which direct contact between the two fluids takes place.

In this subsection, a numerical simulation is described which considers the cooling appearing in a system with injection of a liquid coolant into a duct or a pool in which a hot liquid and vapour are present. Thus, it involves the complex dynamic process consisting of injection of the coolant jet; its deformation before impingement on the free surface; the impingement itself; entrainment and encapsulation of large gaseous structures in the bulk of the hot liquid and finally, entrainment of vapour bubbles, caused by viscous forces which drag the vapour below the free surface. All of this is accompanied by thermodynamic processes of condensation and evaporation. Hence, the distribution of the temperature in the system is to be determined as part of the solution. This section considers the physics of the phenomena.

The used model is two-dimensional and assumes some simplifications mentioned in Sec.(1.2). A quantitative comparison with any experiment cannot be carried out, however, a qualitative evaluation of the result is possible. The basis for the assessment is given by the experiment performed by Bonetto and Lahey (Bonetto and Lahey, (1993)) on the impingement of a round jet in a large pool. It was mainly aimed at the evaluation of the velocity and the void fraction (gas) distribution carried by an

impinging jet through the free surface. The jet was generated in a nozzle positioned vertically a short distance above the free surface. The exit velocity of the jet was of the order of $5[m/s]$. The temperature of the jet and the water in the pool were both equal to $90°C$. The authors did not report, however, on the thermodynamic effects of the process. Thus, there is no data on the rate of exchanged mass and energy. The temperature of the water was kept approximately constant, thus the effect of phase transition was kept relatively small. Pressure was set at the atmospheric level. The main objective of the experiment was the better understanding of processes associated with air entrainment into the bulk of the liquid. Air entrainment appears in various phenomena, such as sea surface chemistry, breaking ocean waves, absorption of greenhouse gases into sea water or breaking bow waves of ship hulls. The latter causes a long wake on the sea surface and is obviously undesirable from a naval point of view.

In the numerical simulation the case considered is similar to the one present in the experiment. The computational domain differs from the geometry of the experimental setup. The size of the experimental setup is too large to be fully included in the computational domain because of restrictions associated with the use of CPU time. Thus, the computational domain has been confined to the size given in Fig.(7.20). The flow present in the experiment is axisymmetric flow, whereas the numerical algorithm constitutes the flow to be two-dimensional. Consequently, flow quantities may not be compared quantitatively. However, the experiment provides information on the void fraction propagation in the pool after the impingement of the jet. From this point of view the experiment is relevant to the simulation and constitutes a proper basis for a qualitative comparison of the numerical and experimental result.

In the numerical simulation, the flow is assumed to be incompressible, viscous without effects of turbulence. The gravitational force acts. Phase transition is active. Density of the liquid phase is assumed for water at the temperature of $371.15[K]$ and at the atmospheric pressure. Density for the vapour phase is assumed for steam at the temperature $375.15[K]$ and at the atmospheric pressure. The difference in the density of water for compressible flow for the lowest temperature used in the simulation and the temperature of saturation amounts to $4[\%]$. The difference for steam for the highest temperature used in the simulation and the temperature of saturation is $0.57[\%]$. Temperature dependent properties at the initial stage of simulation have been assumed for water and steam. Temperatures, densities and temperature dependent physical properties for the coolant, hot liquid and vapour are given in Tab.(7.2). The computational domain, given in Fig.(7.20), assumes three rigid boundaries on the top, bottom and right-lower side of the domain, the outlet at the upper right and the inlet at the left upper corner. The computational domain is chosen such that the ratio of diameter to height of the nozzle exit above the free surface in the experiment is about equal to the ratio of the jest width to height above the free surface in

| **Fluid** | $\mathbf{T}_{init}[K]$ | $\boldsymbol{\rho}[kg/m^3]$ | $\boldsymbol{\mu}_{init}[kg/ms]$ | $\boldsymbol{\lambda}_{init}[J/msK]$ |
|---|---|---|---|---|
| vapour | 375.15 | 0.56 | 1.23e-05 | 0.026 |
| hot liquid | 371.15 | 959.76 | 2.96e-04 | 0.68 |
| cold liquid | 283.15 | 959.76 | 1.31e-03 | 0.58 |

TABLE 7.2: *Physical properties for fluids used in the numerical simulation of the jet of coolant injected into the pool filled by the hot liquid and vapour.*

the computational domain. Also the velocity at which the jet hits the free surface is about equal. In the experiment the jet is round and because the pool dimensions are much larger than the jest diameter, the flow will be more or less axi-symmetric, with the axis at the center line of the jet. In the case of the computation the geometry is two dimensional, with the plane of symmetry at the center line of the jet. In Fig.(7.20) the left side of the domain is the plane of symmetry which imposes symmetrical behaviour of the flow. The domain has been discretized with a uniform grid of $100 \times 71$ control volumes, see Fig.(7.20). The inlet (left upper corner) brings the coolant into the domain with a constant velocity of $-1[m/s]$. The void fraction at the inlet is held constant, equal to zero. The no-slip boundary condition is imposed at the rigid boundaries. At the symmetry plane the slip condition is applied. Since one cannot assume a constant distribution of pressure and velocity at the outlet, the outlet velocity is adjusted at each iteration such that overall mass conservation is assured. This outlet boundary condition has been described in detail in Sec.(5.5). The pressure at the top of the domain is the atmospheric pressure. In the momentum equation the second-order accurate, spatial discretization, CDS, improved by artificial dissipation has been used. For the energy equation the spatial discretization has first-order accuracy and uses the pure UDS method. First-order accurate discretization in time has been used. Since the model uses a time discretization of first-order accuracy, the time step used for the calculations is as low as $1 \cdot 10^{-5}[s]$. This diminishes problems associated with mass conservation, reported in Sec.(7.2). The drawback of such a low time step is very long CPU. In the test case discussed, CPU amounts to about two weeks. In a case of a higher number of control volumes than this in this simulation CPU will increase and the computational method loses its practical applicability. Thus, the cure might be increasing the order of accuracy of the time.

For the purpose of qualitative assessment of the result two test cases are considered, both assume the same initial data and boundary conditions. One of the cases assumes that phase transition takes place, whereas the other does not. The first is used for the evaluation of the effects brought about by the phase transition. These effects are visually assessed through the distribution of temperature and void fraction in the domain. Also the rate of vapour production or disappearance will be discussed.

The simulation begins with the assumption of a flat front of the jet. Immediately after the beginning, the jet front starts to push away the bulk of the vapour in front

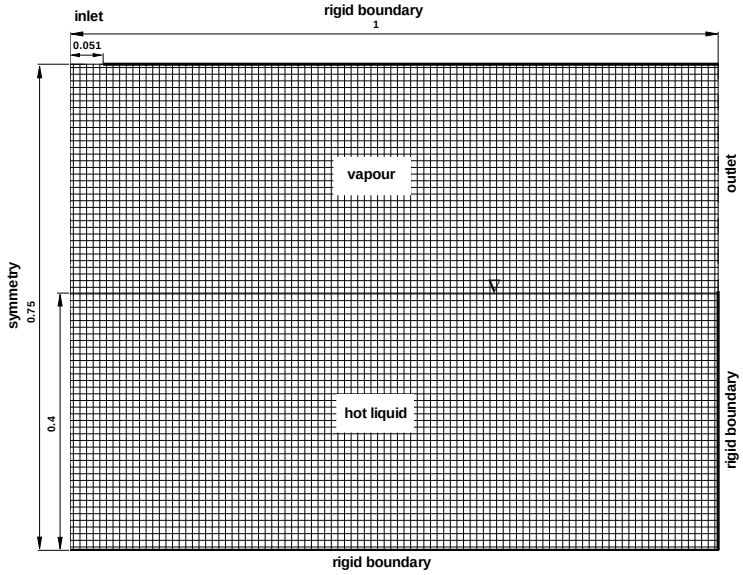


FIGURE 7.20: *Geometry and grid of the calculation domain. All dimensions are given in meters.*

of it. The vapour takes over part of the kinetic energy carried with the bulk of the liquid. Hence, the vapour begins to move downwards and towards the sides of the jet, flowing around the bulk of the coolant. This results in the deformation of the flat surface of the jet. The initial evolution of the deformation of the jet is presented in Fig.(7.21). Shown is the region above the free surface. The figure presents the void fraction distribution and the relative velocity and pressure. The relative variables are helpful in understanding the process. The reference point for the velocity and pressure is the point in the region of the front where the highest pressure appears. From a theoretical point of view this point is in the plane of symmetry. In order to describe the deformation process one needs to imagine a situation of an observer positioned at the reference point moving downwards with the coolant jet. Now, one may consider the situation as the case of the flow around the front of the jet. Hence, the middle of the front is a stagnation point in the relative velocity field and the point with the highest pressure. At the left and right sides of the stagnation point a horizontal velocity component develops, increasing towards the edges of the front. Maximal values

of the velocity are attained the jet edge. The velocity increase induces a decrease of the static pressure. The jet is not a rigid object, and liquid flows from regions of high pressure towards regimes of low pressure. This is the reason why the surface of the front deforms, taking the form of a cavity positioned in the middle of the jet. Once the cavity develops, the flow becomes more complex. In the vapour region two large eddies appear caused by flow separation at the edge of the jet. The eddies are shown in the pictures of the velocity at times $t = 0.1[s]$ and $t = 0.15[s]$.

At a later stage of the deformation process when the jet approaches the free surface, one observes that the tips of the jet edge do not flow along with the main body of the jet, but are slowed down, creating a vortex-like wake of dispersed liquid. In the experimental investigation the reason of this are the effects of viscous forces at the gas-liquid interface. These forces would drag the liquid tips away from the main body of the jet, whereas the relative velocity of the vapour pushes the tips back to the front. In the real situation there is a discontinuity between the liquid jet and the vapour, thus the dragging is caused solely by viscosity of the fluids. However, since the single field model does not assume discontinuities in flow parameters, regardless whether the considered region contains the interface or not, the formation of the vortex-like wakes is reinforced by the averaged velocity of the vapour-liquid mixture in the region of the interface at the edges of the jet. In other words, the horizontal velocity of the liquid tip increases due to the process of averaging. This results in a higher rate of the formation of the vortex-like structures of the vapour-liquid mixture than in case of the two-fluid model.

Further analysis of the evolution of the jet shape concerns the contraction of the jet formed following the initial stage of the flow, developing up to moment the jet impinges onto the free surface. To explain this, consider the pressure distribution given in Fig.(7.21). At time $t = 0.1[s]$ and $t = 0.15[s]$ the vapour flowing around the front of the jet, flows around the surface of the jet sides. Since this surface is inclined with respect to the vertical direction, due to the process of the front deformation, the horizontal component of the velocity exerts a symmetric influence on the jet sides. This increases the pressure in the bulk of the jet. This pressure is seen as the elongated bright region in the pressure distribution at time $t = 0.1[s]$ and $t = 0.15[s]$ in Fig.(7.21). Reinforced by the gravitational force, the higher pressure accelerates the front region stretching the jet structure and causing the contraction.

All the time since the jet entered the domain phase transition occurs along the sides of the coolant. In Fig.(7.22) the solution is presented without phase transition, while in Fig.(7.23) and Fig.(7.24) phase transition has been activated. The occurrence of phase transition in the form of the velocity field divergence is illustrated in Fig.(7.24). Clearly, the region with nonzero divergence coincides with the layer of lowered temperature around the jet, see the series of pictures in Fig.(7.23). In general, the distribution of the velocity divergence is dominated by condensation except

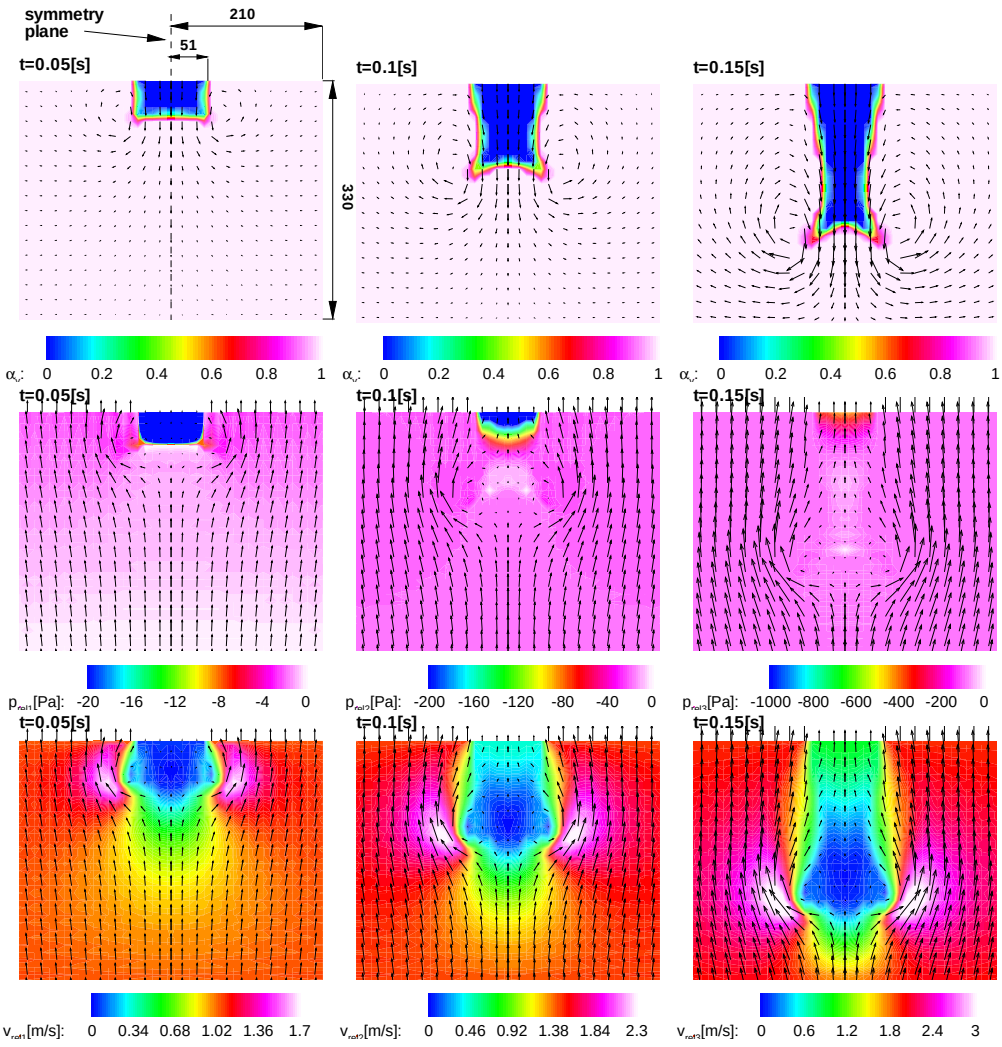


FIGURE 7.21: *Initial evolution of the jet front. Shown is the region above the free surface. The upper row of pictures - void fraction distribution with absolute velocity vectors; the middle row of pictures - relative static pressure* $|p - p_{ref}|$ *with relative velocity vectors; the third row of pictures - relative velocity magnitude* $|\vec{u} - \vec{u}_{ref}|$ *with relative velocity vectors. Note that the solution is symmetric and is computed in the right-hand side part of the domain only. The reference point for pressure and velocity is the point of highest pressure in the plane of symmetry. All dimensions are given in millimeters.*

in a few regions, where evaporation occurs.

The deformed front of the jet finally reaches the free surface. It happens at an instant right before $t = 0.25[s]$, see Fig.(7.23) and Fig.(7.22). Due to the cavity a portion of the vapour is encapsulated when the front tips of the jet reach the free surface. The enclosed gaseous structure is subsequently carried with the flow of the jet into the hot pool, flattened by the free surface meeting the jet, see pictures at $t = 0.25[s]$ in Fig.(7.23) and Fig.(7.22). This initial stage of the impact of the jet is characterised by a high intensity of mixing between the liquid and the encapsulated vapour. This is followed by a temperature drop in the bulk of the vapour. Thus, one may observe the intensive condensation visible as the region with the dark blue colour in Fig.(7.24) at time $0.25[s]$. The condensation results in a decrease of the vapour content in the region where the encapsulated vapour is squeezed out by the jet. This region is positioned out of the centre of the jet, at the left side of the wave induced by the impact of the jet on the free surface. The difference in the void fraction distribution can be recognized in Fig.(7.23) and Fig.(7.22) at time $t = 0.25[s]$. The void fraction distribution also differs at the right side of the wave. Apparently, the process of condensation has increased the contribution of the liquid in front of the wave crest. In the test case in which the phase transition is active, this has as result, that the vapour-liquid mixture touches the crest of the wave. The result of the numerical simulation without phase transition also reveals this structure, but now separated from the bulk of the liquid wave. The temperature field is also visibly affected by the phase transition. The layer next to the jet, above the impact region is warmer. Since solely condensation occurs, the higher temperature is caused by the release of latent heat contained in the vapour.

The further penetration of the coolant jet in the bulk of the hot liquid causes the formation of a meniscus adjacent to the impinging jet. This meniscus develops downwards entraining a sheet of vapour into the pool. At a depth of about two thirds from the undisturbed free surface level, the interface between the sheet and the bulk of the hot liquid becomes unstable. The gravitational force begins to deform the shape of the vapour sheet which finally collapses and encapsulates a portion of the vapour. The instant of the beginning of the sheet deformation is captured in Fig.(7.23) and Fig.(7.22) at time $t = 0.5[s]$.

The wave induced by the jet impact onto the free surface proceeds from the region of impact towards the outlet, flowing as the sheet-like structure on top of the surface. The crest of the wave is elongated and forms a tongue with a vapour-liquid mixture. The tongue, however, is different in the case with phase transition compared to the case without phase transition. The result of the case with phase transition reveals a smaller length of the tongue and a higher liquid content in it. Clearly, this is caused by the condensation of the vapour. The condensation intensity is depicted in Fig.(7.24) in the form of the divergence of the velocity field, equal to the production of vapour,

i.e. $\vec{\nabla}.\vec{u} < 0$ in the case of condensation. The condensation extends along the free surface far beyond the tip of the tongue. Apart from the vapour sheet adjacent to the jet, the highest intensity of the condensation is positioned in the tongue-like region on top of the free surface. This phase transition process affects effectively the temperature distribution along the surface, particularly in the frontal condensation region. The temperature at this place is substantially lower in the case without phase transition flow, compare Fig.(7.23) and Fig.(7.22) at time $t = 0.5[s]$.

Due to the features of the present method, which decreases interface diffusion, the mentioned tongue is represented as an integral structure with a higher liquid content rather than an assembly of tiny droplets, i.e. a spray. Thus, because of the weight of the structure the gravitational force lowers its position on top of the free surface. Comparing the rate at which the temperature wake develops towards the outlet, it is seen that in the case without phase transition, the rate exceeds that of the test case with phase transition. The reason lies in the momentum of the convected fluid. With respect to momentum conservation, the velocity of the liquid must become lower, when the mass of the convected fluid increases because of condensation of the vapour surrounding the moving fluid.

The subsequent stage of the flow reveals encapsulation of a gaseous structure by the deforming sheet of the vapour around the jet. The interface of the vapour with the hot liquid deforms due to the gravitational force. The process is similar to that observed during the water column collapse, see Sec.(7.2). The right boundary of the sheet impinges onto the side of the jet. The impingement causes a temporal increase of the static pressure at the point where the impingement takes place. The rise of the pressure reinforces the jet velocity downwards into the computational domain. The pressure also induces the upward flow which elevates the liquid adjacent to the jet. The upward stream forms a liquid column, which in a three dimensional case would be represented as a crown-like liquid structure around the jet. The tip of the column undergoes quite rapid condensation, thus the contribution of liquid in the vapour-liquid mixture at the top is larger for the case with phase transition. This is illustrated in Fig.(7.23) and Fig.(7.22) at time $t = 0.75[s]$. Due to the condensation the column top obtains a sharper shape of the interface. The process affects the temperature distribution of this structure. The temperature is higher for the case with phase transition since latent heat transfers to sensible heat.

One can observe an interesting behaviour of the temperature distribution in the layer flowing over the free surface in the result of the case without the phase transition. At the far right the temperature of the vapour increases at the outlet. The most probable reason is a change of the flow field in this region caused by the boundary condition which adjusts the velocity according to overall mass conservation. Apparently, the mass conservation requires a decrease of the outlet flux, hence an outlet velocity. Due to this the incoming flow is retarded rapidly at the boundary. Since it

is not allowed to pass the outlet entirely, the only remaining way is an upward motion. Consequently, the boundary condition constitutes an artificial semi-permeable boundary distorting the natural course of the flow.

At time $t = 0.75[s]$, one of the most intensive condensation processes appears in the wedge-like region of the vapour positioned between the mentioned upward moving water column and the coolant jet, see Fig.(7.24). Though at this instant the transition does not produce a visual difference in the void fraction distribution in this region, the difference in temperature is certainly distinguishable. The area of a lower temperature in the form of the green spot in the case without phase transition, is larger than in the result with phase transition. The lower corner of the wedge-like region may also be regarded as a residual of the meniscus mentioned earlier in this paragraph. This, say, secondary vapour sheet is induced due to entrainment of the liquid jet (Bonetto and Lahey, (1993)). In the course of the jet penetration into the bulk of the hot liquid, the secondary sheet becomes unstable. This leads to more or less periodic entrainment of vapour bubbles into the bulk under the free surface. The entrainment is represented by the void fraction wake that extends along the jet, below the free surface. The wake is clearly visible in Fig.(7.23) and Fig.(7.22) at time $t = 0.75[s]$. However, due to condensation, the entrained gaseous structures in the case with phase transition are smaller. The detail analysis of the entrainment effects will be given later in this paragraph.

The large gaseous structure, encapsulated by the collapse of the primary vapour sheet carried along with the coolant jet, experiences substantial deformation. This is caused by the strong vortex field reinforced primarily by the collapsing vapour sheet and secondarily by the jet reaching the bottom of the pool. It causes the static pressure to increase coupled with the appearance of a stagnation point. The result is the acceleration of the liquid on the bottom towards the outlet. The accelerated liquid stream runs right beneath the gaseous structure, propelling a large eddy. The eddy causes an instability of the structure interface leading to fragmentation in the case of the simulation without phase transition. The case with phase transition, however, does not show the fragmentation, but rather flattening and condensation at the rear (with respect to the flow direction towards the outlet) of the structure. The condensation occurring in the structure is intensive, see Fig.(7.24) at time $t = 0.75[s]$. The high rate of phase transition is caused by the cold liquid surrounding the gaseous structure, delivered by the large eddy induced by the jet motion. Clearly, the phase transition began right after the formation of the primary vapour sheet. Thus, the encapsulated amount of vapour was lower than in the case without phase transition. The condensation continues, thus at the instant of the large deformation, unlike in the case without phase transition, the size of the structure was sufficiently small to resist the fragmentation.

The last stage of the flow reported in Fig.(7.23), Fig.(7.22) and Fig.(7.24) is cap-

tured at time $t = 1[s]$. The simulation without phase transition shows the evolution of a lower temperature in the vapour at the outlet. The region with lower temperature appears to retreat towards the interior of the domain. This is caused by the convected fluid reaching the top of the domain. Since the outlet velocity is lower than that of the incoming flux, an upward motion of the fluid appears. This numerical occurrence has been explained above. Once the upward flux reaches the top, the flow is forced back into the domain. One can see the same phenomenon in the case with phase transition, however, it is less intensive. At time $t = 1[s]$ the entire free surface is covered by a layer of colder fluid which brings about the condensation. Right below this layer one can observe some white spots in the distribution of the temperature. These places of higher temperature appear in both test cases. Clearly, this is not a physical effect. The spots represent failures in mass conservation. The results of further calculations ($t = 1.045[s]$) show that in the case without phase transition this effect disappears. In the numerical simulation with phase transition, however, the temperature rise is maintained, see Fig.(7.27). This affects the velocity field, because the higher temperature causes unphysical evaporation. This is depicted on Fig.(7.28), where the divergence of the velocity field is shown in a different colour scale than in Fig.(7.24). This helps in distinguishing the regions of evaporation.

At the time $t = 1[s]$ the water column, generated because of the collapse of the primary vapour sheet, breaks and proceeds towards the outlet. The collapsed column assumes the shape of a wave on the free surface. The case with phase transition shows a tip of condensed liquid on the wave crest, whereas in the simulation without phase transition a sharp wave shape evolves. Clearly, this difference is caused by condensation. The condensation also changes the wedge-like gaseous structure which for the case with phase transition has a smaller area. The bottom corner of the wedge has a larger contribution from the liquid than in the case without phase transition. The vapour entrainment is visible in both cases. It is difficult to evaluate for which case the process is more intensive. One may only expect that in the case of phase transition the amount of vapour below the free surface will be lower due to the condensation. This is indeed the case, at least, at time $t = 1.045[s]$, see Fig.(7.27). The result without phase transition reveals a smooth, continuous vapour-liquid mixture wake extending downwards from the lower corner of the wedge-like meniscus adjacent to the jet. This structure gets thinner in the region closer to the bottom of the domain. A similar structure is observed in the case with condensation, however, it is not continuous and its thickness does not decrease in the downward direction.

At time $t = 1[s]$, the large gaseous structure, encapsulated during the collapse of the primary vapour sheet, has moved about one fourth of the domain length away from the symmetry plane. The structure remains surrounded by cold liquid. Due to the absence of condensation, the case without phase transition shows a vapour pattern blanketing the top of the structure. This is not the case for the simulation with phase

transition, where in the process of the phase transition the vapour pattern condensed. Also due to the condensation, the gaseous structure contains a higher amount of liquid than in the simulation without phase transition. One can also observe this at time $t = 1.045[s]$, see Fig.(7.27).

The subsequent part of this section is devoted to the qualitative evaluation of the computed void fraction distribution below the free surface. The basis for the analysis is the experiment carried out by Bonetto and Lahey (Bonetto and Lahey, (1993)). These authors proved empirically, that a jet penetrating the liquid in the vessel creates an annular meniscus or in other words, an annular thin gas sheet. This sheet becomes unstable and collapses, entraining air bubbles underneath the free surface. At the sheet bottom, the jet can be regarded as a purely one-phase stream. The bubble entrainment is coupled with the spreading of the gas (void fraction) in the region where the jet penetrates the bulk of the liquid. Consequently, beneath the bottom of the sheet one can observe a two-phase flow, where the distribution of the void fraction (bubble concentration and size) varies in the direction tangential and perpendicular to the flow.

The experimental results are given as the void fraction as function of the distance from the jet axis of symmetry and as function of the depth below the undisturbed free surface. The results are given on Fig.(7.25) and Fig.(7.26). Figure Fig.(7.25) shows three graphs. Each graph presents the void-fraction distribution at a different depth, $z$, measured from the undisturbed free surface. The process of the gas phase dispersion is observable in both directions, namely $r$ (the distance from the symmetry axis) and $z$ (the depth). The reason of the dispersion lies in turbulence of the flow which is expressed in terms of the turbulence intensity. The definition of this quantity is the relation between the local, instantaneous velocity fluctuations and the mean velocity of the flow. The turbulence intensity in the experiment has been reported as amounting to $3\%$. The turbulence of the flow is mainly responsible for the process of dispersion. A higher local velocity causes fragmentation of entrained bubbles. Since the velocity may occur not only in vertical direction the dispersed bubbles are spread in the direction perpendicular to the axis of symmetry as well as downwards in the vessel. The peak of the void fraction function, present at the depth $z = 1[mm]$, decreases, getting broader in the process. The process of dispersion leads gas towards the flow centre, namely the axis of symmetry. Consequently, the plot of $\alpha$ as function of $r$ at a depth of $z = 18[mm]$ and $z = 43[mm]$ has a value of $\alpha$ at the center different from zero. The value of the void fraction at the axis increases with $z$ in the downward direction. This process is clearly illustrated in Fig.(7.26) which shows the void fraction along the center line as function of depth $z$. The void fraction has a maximum at about $z = 40[mm]$. The reason that the function begins to decrease is the increase of the cross section of the jet, as it flows downwards into the vessel. The increase of the cross section is not compensated, by the rate of bubble spreading, thus

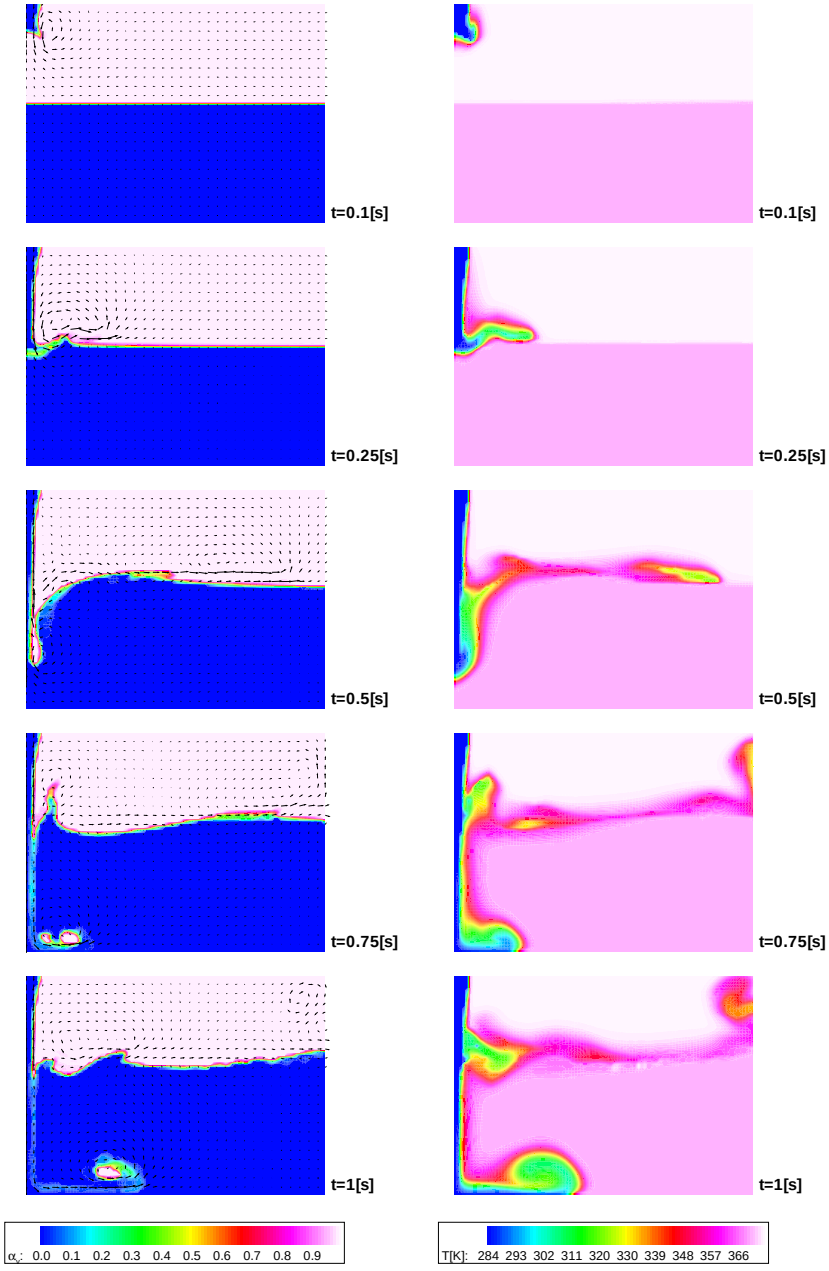


FIGURE 7.22: *Flow without phase transition. Distribution of void fraction and velocity vectors (left); distribution of temperature (right).*

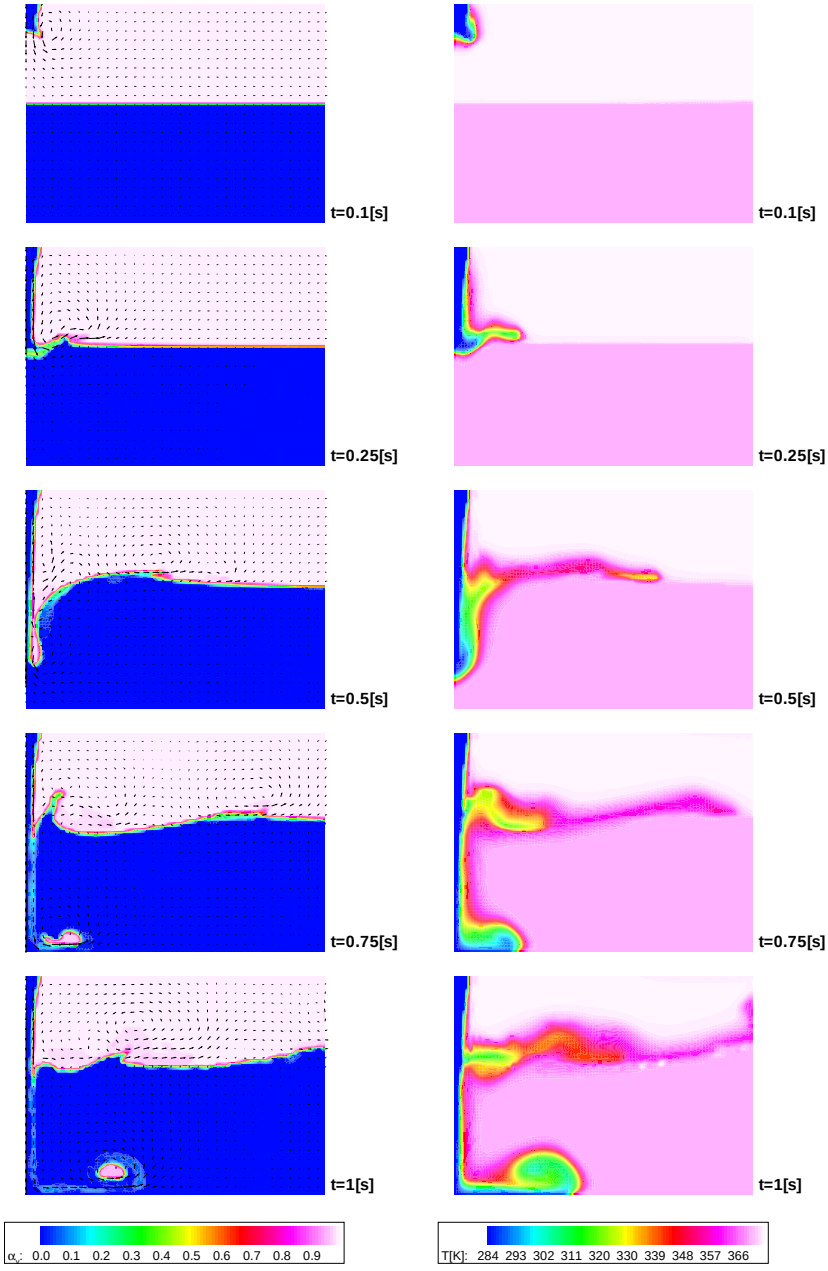


FIGURE 7.23: *Flow with phase transition. Distribution of void fraction and velocity vectors (left); distribution of temperature (right).*

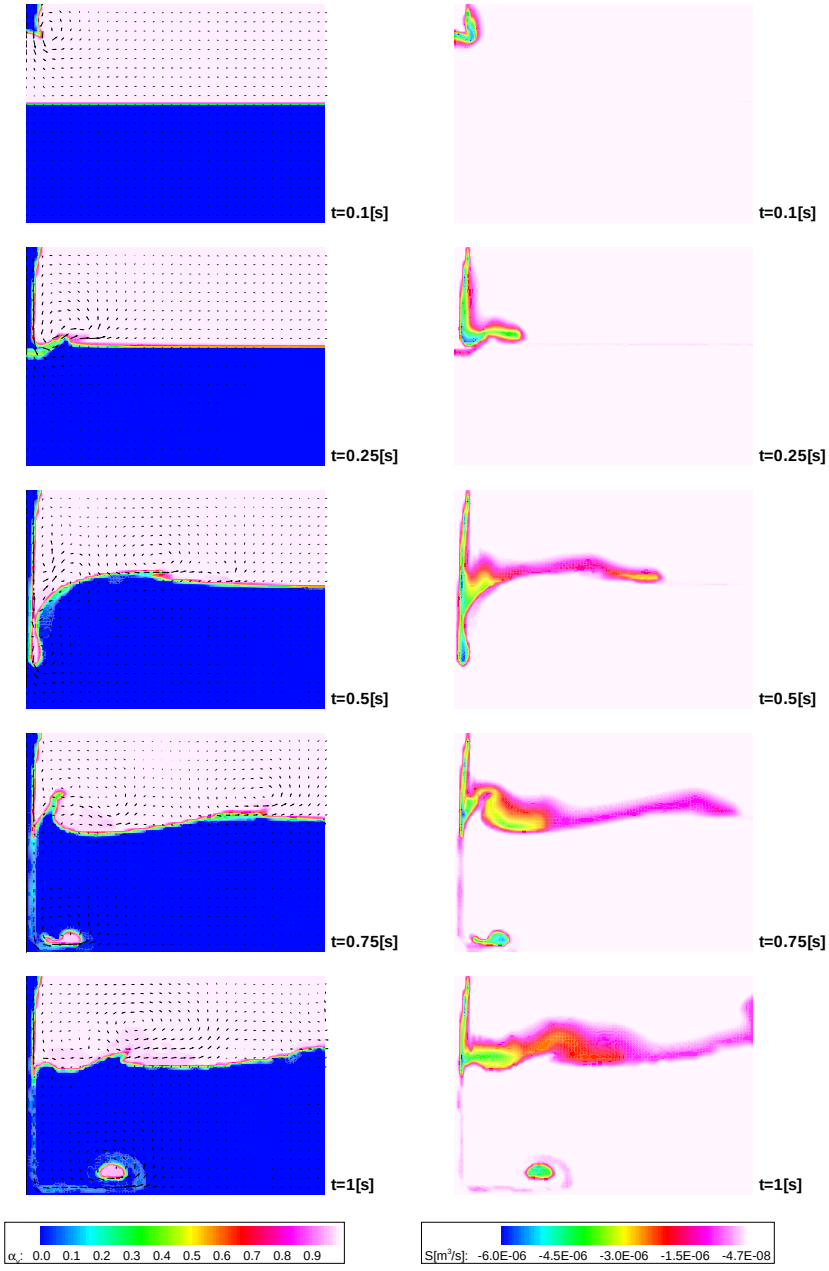


FIGURE 7.24: *Flow with phase transition. Distribution of void fraction and velocity vectors (left); distribution of velocity field divergence (right).*

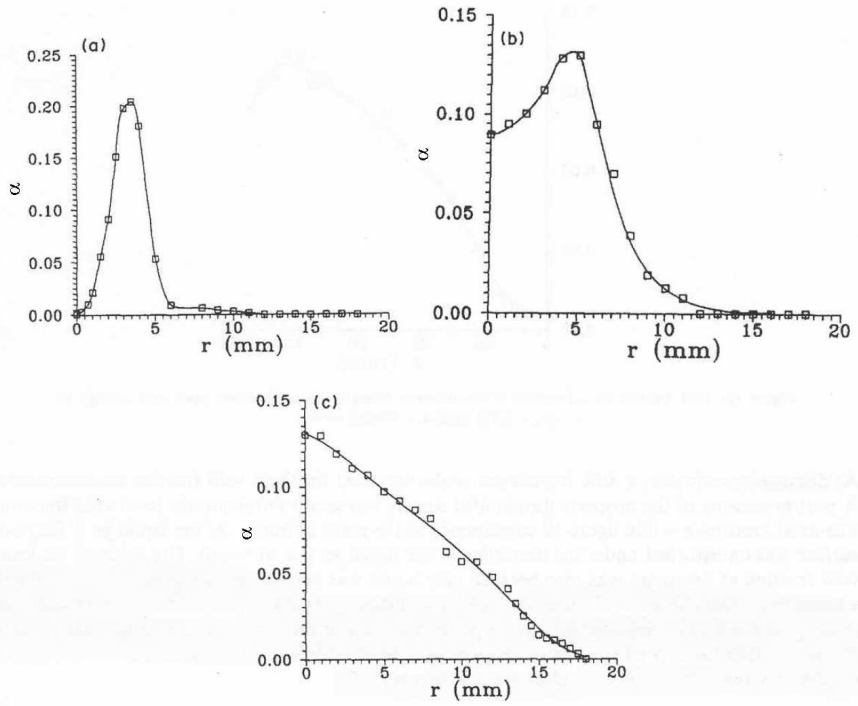


FIGURE 7.25: *Void fraction vs. distance from the symmetry axis.* $a)z = 1[mm]$*;* $b)z = 18[mm]$*;* $c)z = 43[mm]$*. Experiment by Bonetto and Lahey (Bonetto and Lahey, (1993)) for round jet of 5[mm] diameter.*

the void fraction decreases.

The results of the calculations for the two-dimensional computational setup are presented in Fig.(7.29) and Fig.(7.30). The first figure depicts the void fraction versus distance from the plane of symmetry, whereas the latter shows the void fraction as function of the depth from the undisturbed free surface. Values of the void fraction have been averaged in time similar to the procedure employed in the experiment. The time span of averaging begins at time $t = 0.8[s]$ and ends at $t = 1.049[s]$. It is assumed that the initial instant of data extraction is not affected by the process of the primary vapour sheet collapse. The levels at which data have been extracted are indicated in Fig.(7.27) by the horizontal dashed lines. The levels have been chosen according to the scale of the experimental vessel and that of the computational domain. Thus, the graphs $a)$ and $b)$ in Fig.(7.29) correspond to those in Fig.(7.25). Graph $c)$ in Fig.(7.29), however, is not equivalent to its experimental counterpart. In the experiment, the pool is much deeper than in the numerical simulation. Consequently, graph $c)$ in Fig.(7.29) represents the lowest possible level - the bottom in the

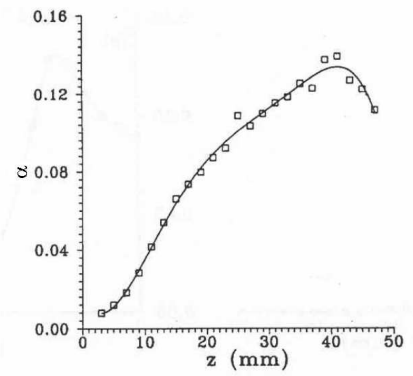


FIGURE 7.26: *Void fraction vs. depth measured from the level of the undisturbed free surface. Experiment by Bonetto and Lahey (Bonetto and Lahey, (1993)) for round jet of 5[mm] diameter.*

numerical simulation, while in the experiment Fig.(7.25 c) is for a level still far away from the bottom.

Graph $a)$ in Fig.(7.29) for depth $\hat{y} = 0.0116[m]$ has the same trend as its counterpart in Fig.(7.25). There is no vapour at the axis (plane) of symmetry. The void fraction level increases up to a maximum at about $x = 0.025[m]$. Then the void fraction decreases rapidly confirming the trend appearing in the experiment. Computed results are given for the case with phase transition and for the case without phase transition. As expected, due to condensation, the peak of the void fraction for the simulation with phase transition is lower than in case condensation is left out. Note that the jet has contracted to about half its width at the moment it hits the free surface.

The trend line for graph $b)$ differs however, from the corresponding one in the experiment. The most remarkable difference is the absence of vapour at the plane of symmetry. Furthermore, the void fraction in the case with phase transition as well as the one in the case without phase transition does not propagate much towards higher and lower values of $x$, contrary to the experiment, though some propagation takes place. Some of the differences will be due to the axi-symmetric jet spreading more rapidly towards its center than its two-dimensional counterpart. The lower rate of propagation causes the peaks to remain approximately as broad as in graph $a)$. The local velocity fluctuations with the Reynolds number in the jet, for the experiment and the numerical simulation, amounting to about $8e + 05$, cause dispersion of the void fraction in the horizontal direction. Since effects of turbulence are not handled in the model, one may not expect any substantial changes in the distribution in the horizontal direction. The resolution of the grid also influences dispersion of the void fraction. Since the grid is rather coarse relative to the scale of the jet width, the grid

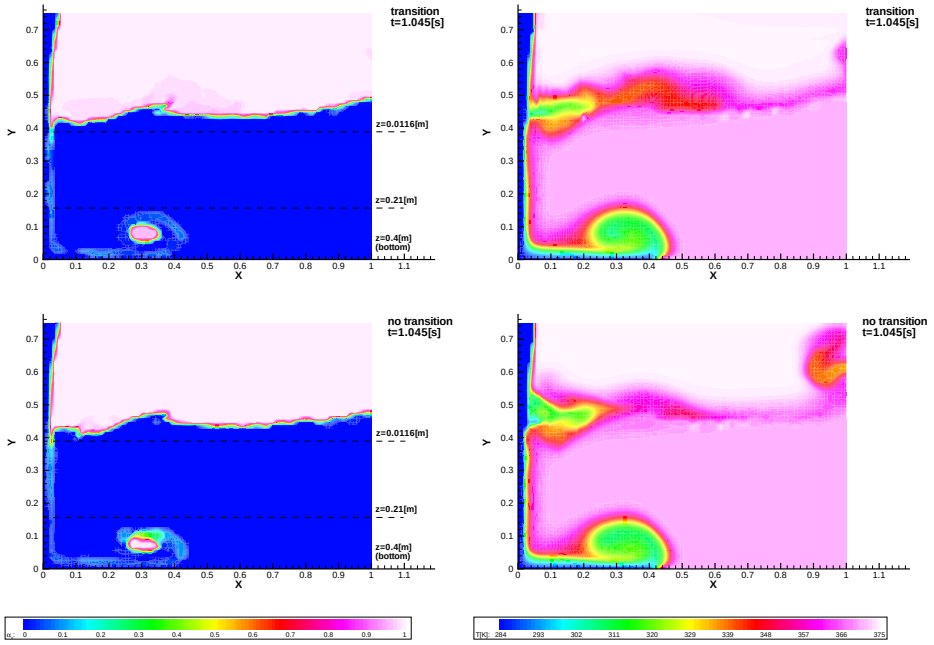


FIGURE 7.27: *Void fraction and temperature distribution at time t=1.045[s]. Simulation with phase transition (upper); simulation without phase transition (lower).*

resolution may be well to low to capture the phenomenon.
The distribution at the bottom of the domain has a completely different structure than the one in graph $c$) of Fig.(7.25) which is much further away from the bottom. Although a vapour contribution appears at the bottom of the domain, at the symmetry plane, its existence may have a different origin than in the experiment. The impinging jet encapsulates a portion of the vapour because of the presence of the cavity at the impinging jet front. Distorted and partially squeezed out of the jet front, the encapsulated gaseous structure is pushed down. Once the jet reaches the bottom, a stagnation point is established. A residual of the gaseous structure followed by the jet is trapped at the stagnation point. This gives a nonzero value of the void fraction at $x = 0[mm]$ in Fig.(7.29). The vapour contribution is present in the case of phase transition, as well as in the case without phase transition.

The bottom distribution of Fig.(7.29) shows also further increments of the void fraction. These represent the gaseous wake following the large gaseous structure, see Fig.(7.27). Surprisingly, the average value for the case without phase transition is lower than that for the case with phase transition. This is caused by the average mass of the wake, which is, because of condensation, larger for the simulation with phase transition. Due to this buoyancy forces cannot affect so much the vertical position of

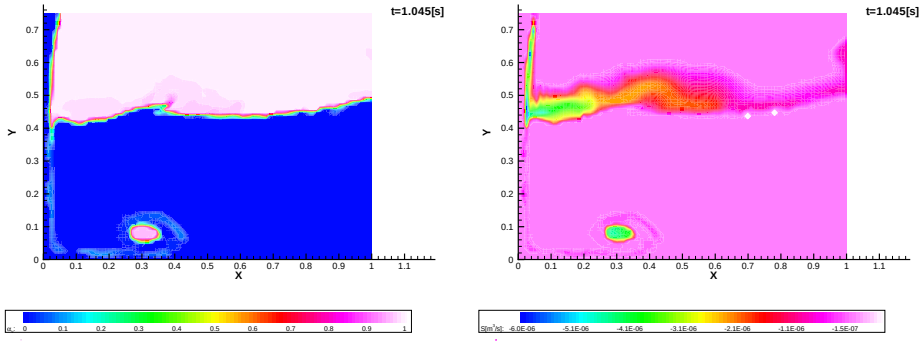


FIGURE 7.28: *Distribution of void fraction and divergence of velocity field at time t=1.045[s].*

the structure. Since the maximal void fraction is approximately in the middle of the wake, a lower position of the middle generates higher values of the void fraction at the bottom of the domain.

The distribution of the void fraction versus the distance from the free surface is shown in figure Fig.(7.30). The trend predicted by the case with phase transition and the one without phase transition remains in good agreement with that of the experiment. However, the void fraction in the numerical results, has a substantially lower level. The reason are the local flow fluctuations which are the driving force for the gas spreading in the experiment. As discussed, due to the model simplification omitting effects of turbulence, the vapour dispersion in the numerical simulation appears to be much less intensive than in the experiment. Consequently, the void fraction at the plane of symmetry in the numerical simulation is lower than that at the axis in the experiment. The distribution of the void fraction for the case with phase transition differs from the one for the case without phase transition. In the simulation with phase transition the vapour dispersion is more intensive, thus, the values of the void fraction are higher at smaller depths than in the simulation without phase transition. This is caused by the divergence of the velocity field which generates local disturbances causing vapour propagation in horizontal direction. A mechanism that causes the void fraction to decrease near the domain bottom is similar to that in the experiment. The reason is that the jet gets wider as the distance from the free surface increases. The void fraction propagation directed away from the symmetry axis brings about a decrease of the void fraction at the axis. In the numerical results, however, this effect is magnified by the jet impingement onto the bottom. This reinforces the jet widening.

Similar to the dam breaking problem, the gas-liquid interface is aligned monotonically. The interface remains sharp even in regions of a complex interface shape. The model is able to simulate phenomena associated with effects such as interface

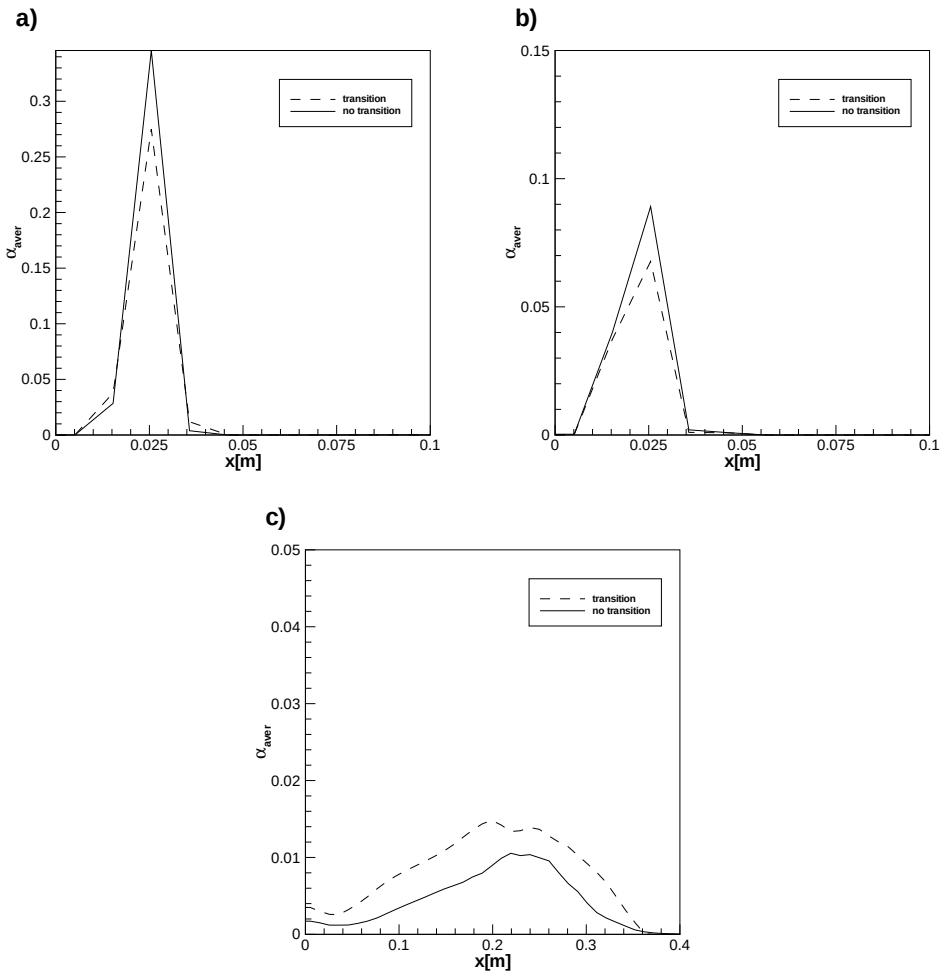


FIGURE 7.29: *Void fraction vs. distance from the symmetry plane, initial half-width jet is 0.05[m]. Numerical results.* $a)\hat{y} = 0.0116[m]$*;* $b)\hat{y} = 0.21[m]$*;* $c)\hat{y} = 0.4[m]$ *(bottom), with* $\hat{y} = y_{fs} - y$ *the distance from the undisturbed free surface.*

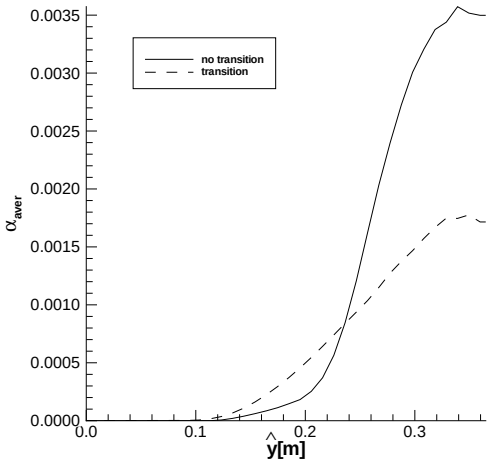


FIGURE 7.30: *Void fraction vs. depth measured from the level of the undisturbed free surface. Numerical results.*

instability. The numerical simulation reflects the basic features of the experimental result. These apply to the manner in which the gas is entrained in the bulk underneath the free surface. Appearance of an annular meniscus and unstable air sheet that form the basis for bubble entrainment into the bulk of the liquid, is confirmed by the numerical result. The numerical result also can handle vapour entrainment. However, because effects of turbulence have not been included in the model, the detail analysis of the computed void fraction distribution shows differences with that of the experiment. The numerical simulations are also aimed at showing the feasibility of the Energy of Fluid method. It is difficult to find an experiment that can be used for validating the model, which is indispensable for the development of the phase transition model. Furthermore, the experiment of (Bonetto and Lahey, (1993)) does not provide data on phase transition; it was primarily carried out for the purpose of studying air entrainment. Even if data were provided, the experiment constitutes a binary thermodynamic system, air-water. A system in which two or more species coexist cannot be treated by the phase transition model as it is presently implemented in the numerical algorithm. However, one can notice some thermodynamically and mechanically based phenomena, purely associated with the occurrence of phase transition, i.e. temperature rise caused by the release of latent heat. Another example is the change of momentum brought about by the change of the vapour-liquid mixture mass of convected structures due to condensation.

# DISCUSSION

8 CHAPTER

The presented algorithm is aimed at the prediction of multiphase flow with vapour-liquid phase transition. In this chapter the general features of the implemented methods are summarized and discussed in view of alternative methods. This will show advantages and disadvantages of the used phase transition model relative to other methods. Also some possible further developments of the algorithm are discussed.

## 8.1 Interface capturing

The algorithm assumes a single field approach (Banerjee, Hewitt, Zaleski, Tryggvason, Koumoutsakos, Yadigaroglu and Ishii, (2004)) in the form of the Volume of Fluid (VOF) method (Hirt and Nichols, (1981)). In this method a single set of governing equations describes the two phases present in the flow. The set of basic equations (continuity, momentum, energy) is complemented with an additional equation for the transport of an indicator which allows distinguishing the phases in the domain. This indicator can assume various forms (Unverdi and Tryggvason, (1992); Hirt and Nichols, (1981)). In the case of the VOF method it is the ratio of the volume of the gas and that of the gas-liquid mixture. No matter how this parameter is expressed, the common advantage of the single field approach is that information on the geometry of the interface does not need to be known *a priori*. The geometry of the interface is to be calculated in the course of the computation. This is the important feature that renders the method independent of, for example, empirical data bases for the particular type of flow, see Sec.(2.2). The single field approach does not require closure relations associated with the particular type of gas-liquid interface. Such relations are required in the alternative multi field approach. They constitute boundary conditions for this sort of models. Since the relations are strongly dependent on the geometry (topology) of the interface, it is difficult to evaluate or rather predict the flow quantities at the interface without exact information on interface position. Thus, in the case of complex flow geometries or complex dynamics of the flow, e.g. such as the jet impinging test case in Sec.(7.3), single field models have preference.

However, it is important to realize, that the single field model has also disadvantages. As mentioned in Sec.(2), once the flow is described with only a single set of equations, the model requires the continuity of all flow-field variables, including the void fraction. Consequently, the interface is not sharp but smeared out in space assuring continuity. It depends on the flow type whether or not such approach is accurate. In the case of the gas phase appearing in the form of a bubble cluster (foam) or the liquid phase in the form of a droplet cloud, one may assume that the model predicts the flow dynamics with acceptable accuracy. However, in the case of a sharp free surface, e.g. stratified, stratified wavy flows, see Sec.(2.2), the method can fail. Taking this into account numerical algorithms have been extended, see (Leonard, (1991)). The extensions allow increasing interface resolution up to the scale of a single control volume. A problem arises when the complex flow dynamics causes fragmentation of phasic structures e.g. a water column collapse or an impinging jet, see Sec.(7.2) and Sec.(7.3). Then, the structure of the flow cannot be uniquely classified as a flow with a sharp free surface or that with dispersed phasic structures. To tackle the problem, following (Leonard, (1997)) and (Ubbink, 1997), the current algorithm incorporates a switching procedure that blends algorithms for the prediction of sharp interfaces with those for smooth interfaces, see Sec.(6.2.4) and Sec.(6.3). This makes the algorithm suited for the prediction of complex flows. However, the tendency of the used methods to keep the interface sharp, sometimes deteriorates the solution. It applies particularly to regions where one expects a smooth distribution of the void fraction. Clearly, this is not a failure of the method, but rather requires adjustment of blending. To improve the procedure of blending, however, one needs to know whether or not dispersion of phasic structures takes place.

According to Zaleski (Scradovelli and Zaleski, (2003)) and Tryggvason (Unverdi and Tryggvason, (1992)) it is possible to determine the exact position of the interface. The methods of interface reconstruction or of grid adaptation, allow for assessment of further physical quantities. These quantities play the role of closure relations for other phenomena such as gas-liquid phase transition or phasic structure fragmentation. However, both of the mentioned approaches consider the detailed phasic structure of the flow, which includes individual phasic objects. Clearly, this limits the methods to cases where the interface geometry is not very complex and the number of phasic objects is not too large. The limitations are associated with the time required for the calculations. If the interface geometry is not sufficiently simple or the number of objects is too large, the methods may not be feasible from a practical point of view.

## 8.2 Phase transition

Methods for modelling phenomena of gas-liquid phase transition can be classified in two groups. The first group of methods treats the phase transition as a change of physical properties of the vapour-liquid mixture, without considering the dynamics of individual phasic structures appearing in the control volume because of the transition. To this group of methods belongs the Energy of Fluid (EOF) method incorporated in the current algorithm. The second class of methods focusses on the dynamics and considers the number and behaviour of phasic nuclei. In these methods the bubble or droplet growth model is considered.

Contrary to the EOF method, the second group of methods requires some initial data without which prediction of the phase transition is not possible. These data include the number of phasic nuclei present in the bulk of the continuous phase, their distribution, initial size and shape. For the sake of clarity, an example of the method will be briefly given below. The entire algorithm is comprehensively described in (Sauer, 2000). The model predicts the rate of expansion or shrinkage of vapour bubbles, dependent on the local thermodynamic conditions. Following (Sauer, 2000), the rate of the transition in terms of the void fraction reads

$$\frac{d\alpha}{dt} = (1-\alpha)\,\frac{4n_0\pi R^2}{1+n_0\frac{4}{3}\pi R^3}\frac{dR}{dt}, \tag{8.1}$$

where $R$ denotes the radius of the bubble, and $n_0$ denotes the concentration of nuclei in the bulk of the liquid (number of nuclei per unit of volume of the liquid). Evaluation of the rate of bubble size change, $dR/dt$, follows from a potential flow model of the expanding or contracting sphere surrounded by liquid. Neglecting surface tension and inertial effects and assuming that $dR/dt$ is constant in time, the relation between the velocity of the (growing) bubble boundary and pressure reads

$$\frac{dR}{dt} = sgn\,(p_g - p_l)\left(\frac{2\,|p_g - p_l|}{3\rho_l}\right)^{1/2}, \tag{8.2}$$

where $p_g$ is the pressure inside the bubble, whereas $p_l < p_g$ is the pressure in the ambient liquid. Relation (8.2) is termed the Rayleigh (Young, (1989)) equation. Clearly, (8.2) is applicable to phase transition in which the pressure plays the role of the driving force, e.g. cavitation. However, using thermodynamic relations the right hand side of (8.2) can also be expressed in terms of temperature. This would be more convenient for the temperature driven processes considered in this work. Many bubble growth models have been developed, in which temperature appears at the right hand side of (8.2), e.g. Plesset-Zwick or Mikic, see (Plesset and Zwick, (1954); Mikic, Rohsenow and Griffith, (1970)). The major advantage of the approach described is the direct relation between the phase change and the time rate of phase transition. This is developed on the basis of bubble dynamics. This feature of the model

eliminates the need of artificial manipulation of the phase transition rate, which is necessary in EOF methods. The EOF method assumes that the entire heat which exceeds the state of saturation is consumed in the phase transition during given time step, regardless of the time step duration. This tends to a thermodynamic equilibrium at the end of each time step. Thus, the approach does not give any information about the rate of the process. The rate is controlled only by changing the magnitude of the time step or by factorizing the magnitude of the divergence of the velocity field. The latter is, of course, a purely artificial manipulation which is not related to the phase transition dynamics. The magnitude of the velocity divergence factor can be estimated using time characteristics of the phase transition associated with a particular flow. Clearly, this limits the validity of the method to the range of available experimental data. One can, of course, assume that a large enough time step is sufficient to accomplish the transition process. This may happen in the case of absence or in the case of a low rate of convection. Nevertheless, without an experimental data base, this is only speculation. Since the current research is supposed to be an initial step of modelling the phase transition employing the EOF method, the factorization in the algorithm plays the role of a procedure which ensures numerical stability.

The bubble growth model requires a set of initial data. However, this type of model assumes usually many simplifications. This is mainly caused by some technical obstacles in extraction of experimental data (Yuan and Schnerr, (2003)). The shape of the growing bubble is assumed to be spherical regardless of its size. For a larger size, surface tension forces are smaller and the shape is controlled by the pressure gradient in the bubble surroundings. Usage of relation (8.2) requires the knowledge of the bubble concentration $n_0$. This parameter can only be attained by experimental measurement, but due to technical obstacles, bubbles of submicrometer scale can not be detected (Yuan and Schnerr, (2003)). The assumption of a homogeneous distribution of bubbles of the same initial radius may also not always be accurate.

The bubble growth model is difficult to implement for simulations in which the initial phase distribution consists of a two phase flow of a single substance, e.g. the jet impinging situation in Sec.(7.3). In such a situation the assumptions of equal initial bubble radius in the entire domain and of a homogeneous distribution of bubbles fail. Summarizing, EOF-like approaches appear to be favourable, since they do not demand the type of data discussed. Once one knows the phase change rate, the EOF method appears as an attractive method for the solution of multi-phase flows with phase transition.

## 8.3 Recommendation for future research

The present algorithm has some simplifications, that limit its ability to predict the flow. Some of the simplification are discussed here and possible solutions will be

proposed.

The first problem concerns the single field approach and the integration of flow field variables over the control volume. Since the model assumes continuity of variables all over the domain, physical quantities, including temperature, are averaged over the region that may include a sharp interface. The averaging allows preserving continuity and leads to interface spreading. For velocity and pressure one may assume continuity of function value across the interface (neglecting surface tension), this is not the case for temperature. Clearly, due to heat diffusion the temperature field is continuous across the free surface, however, the scale of the layer over which the temperature is equalized is much smaller than that of the control volume. The averaging distorts the real, steep variation of the temperature across the interface. The Energy of Fluid method uses the temperature as the driving force which governs the rate of phase transition. In the situation that the temperature is numerically changed during the process of averaging, the rate of phase transition departs from reality. This applies to the case of fluids remaining in rest as well as to these convected in the domain. Particularly the latter rises a question concerning the accuracy of the rate of phase transition. Suppose a one dimensional flow in a domain in which the interface is convected. The temperature at both sides of the interface keeps the fluids in a thermodynamic equilibrium. Neglecting heat diffusion (conduction), there is no observable phase change. However, due to the averaging the temperature of one of the fluids changes. Then one can observe a numerically induced evaporation or condensation. Since the temperature depends on the weight contribution of the fluid in the control volume, see (2.37), the higher contribution of the fluid the more the temperature of the vapour-liquid mixture depends on the incoming fluid. The weight contribution changes substantially only in the case of convection. Consequently, if one considers phase transition in the presence of convection, the transition rate will have a larger error than in the case of the transition occurring in a system remaining at rest. At this point of the discussion it is concluded, that the single field approach does not provide the proper accuracy of the temperature field. Since temperature is the driving force for the transition, the difficulty is clear. A cure can be found in the multi-field model applied to the energy equation, such that the temperature field is regarded separately for each phase. This must be coupled, however, with algorithms for interface reconstruction, since a single field model is employed for the rest of the governing equations. This solution is applicable only for a situation in which the interface characteristics are known in advance. In the case of a very complex, interface geometry this solution cannot be used, because the reconstruction process fails. This situation can take place in the case of bubble or droplet cloud formation. Consequently, the cure limits the applicability of the method.

The rate of phase transition also depends on the surface tension present at the interface. The current model does not take the surface tension into account. From a point

of view of the dynamics of phasic structures, surface tension is a very important factor influencing the rate of phase generation, particularly in the beginning of the transition. At this instant the surface tension exerts a strong influence on the shape of the structure, acting against gravitational forces (if the structure is attached to a boundary) and changing the thermodynamics of the system equilibrium, see Sec.(3.2). In the case of a multi-field approach for the energy equation, incorporation of the surface tension requires the reconstruction of the interface. Thus, it could be implemented and used only for cases with a relatively simple geometry of the interface.

The gas-liquid phase transition is always three-dimensional in nature. In the case of a bulk evaporation or condensation, the process of the transition begins with nucleation of phasic microstructures which are assumed to be spherical at the beginning of their existence. Phasic structures grow or shrink in three dimensions of space. Consequently, in this type of transition the flow problem is not two-dimensional. A possibility of the phase transition to be regarded as a two-dimensional phenomenon exists only in the case of surface evaporation or condensation that appears at the free surface. In such a situation one considers the phase change as a number of particles which are released from or absorbed by the surface. These phasic particles do not generate spherical clusters in the bulk of the phase, that grow in space and time. In a complex flow, however, such as that described in Sec.(7.3), surface as well as bulk phase transition can appear. Consequently, in order to relax the limitation of the algorithm, associated with its two-dimensionality, it is recommended to consider extension of the method to three dimensions.

# REFERENCES


Anghaie, S. and Ding, Z.: (1996), Numerical modelling of conduction-driven bulk evaporation and condensation processes with constant volume, *Int. J. Numerical Methods in Engineering* **39**, 219–233.

Anghaie, S. and Ding, Z.: (1997), Thermal hydraulic analysis of bulk evaporation and condensation in multiphase nuclear fuel cell, *Nucl. Tech.* **120**, 57–70.

Antoine, C.: (1888), Tensions des vapeurs; nouvelle relation entre les tensions et les températures, *C. R.* **107**, 681, 836.

Aulisa, E., Manservisi, S., Scradovelli, R. and Zaleski, S.: (2003), A geometrical area-preserving Volume-of-Fluid advection method, *J. Comput. Phys.* **192**, 355–364.

Banerjee, S. and Chan, A.: (1980), Separated flow model I. Analysis of the averaged and local instantaneous formulations, *Int. J. Multiphase Flow* **6**, 1–24.

Banerjee, S., Hewitt, G., Zaleski, S., Tryggvason, G., Koumoutsakos, P., Yadigaroglu, G. and Ishii, M.: (2004), Short courses. Modelling and computation of multiphase flows, Swiss Federal Institute of Technology (ETH), Zurich, Switzerland.

Banerjee, S., Takahira, H. and Horiuchi, T.: (2003), An improved three-dimensional level set method for gas-liquid two-phase flows, *Eighth Int. Symp. Gas-Liquid Two-Phase Flows*, ASME, Honolulu, Hawaii, USA.

Banerjee, S., Takahira, H. and Takahashi, M.: (2004), Numerical analysis of three dimensional bubble growth and detachment in a shear flow, *Fifth Int. Conf. Multiphase Flow*, The Japanese Society for Multiphase Flow, Yokohama, Japan.

Bankoff, S.: (1960), A variable density single-fluid model for two-phase flow with particular reference to steam-water flow, *J. Heat Trans.* **82**, 265–272.

Barnea, D.: (1986), Transition from annular flow and from dispersed-bubble flow - unified models for the whole range of pipe inclination, *Int. J. Multiphase Flow* **5**, 733–744.

Barnea, D.: (1987), A unified model for prediction of flow pattern transitions in the whole range of pipe inclination, *Int. J. Multiphase Flow* **13**, 1–12.

Beam, R. and Warming, R.: (1976), An implicit finite-difference algorithm for hyperbolic systems in conservation law form, *J. Comput. Phys.* **22**, 87–110.

Bell, J., Dawson, C. and Shubin, G.: (1988), An unsplit, higher order Godunov method for scalar conservation laws in multiple dimensions, *J. Comput. Phys.* **74**, 1–24.

Bonetto, F. and Lahey, R.: (1993), An experimental study on air carryunder due to a plunging liquid jet, *Int. J. Multiphase Flow* **19**, 281–294.

Brennen, C.: (2005), *Fundamentals of Multiphase Flow*, Cambridge University Press, Pasadena.

Brodkey, R.: (1967), *The Phenomena of Fluid Motions*, Addison-Wesley, London.

Caretto, L., Gosman, A., Patankar, S. and Spalding, D.: (1972), Two calculation procedures for steady, three-dimensional flows with recirculation, *Third Int. Conf. Numer. Methods Fluid Dyn.*, Vol. 2, Springer Verlag, Paris, France.

Collea, P.: (1990), Multidimentional upwind methods for hyperbolic conservation laws, *J. Comput. Phys.* **87**, 171–200.

Drew, D.: (1983), Mathematical modelling of two phase flow, *Ann. Rew. Fluid Mech.* **15**, 261–291.

Fromm, J.: (1968), A method for reducing dispersion in convective difference schemes, *J. Comput. Phys.* **3**, 176–189.

Harlow, F. and Welch, J.: (1965), Numerical calculation of time-dependent viscous incompressible flow of fluid with free surface, *Phys. Fluids* **8**, 2182–2189.

Hirt, C. and Nichols, B.: (1981), Volume of fluid (vof) method for the dynamics of free boundaries, *J. Comput. Phys* **39**, 201–225.

*http://highered.mcgraw-hill.com*: n.d.

Ishii, M. and Mishima, K.: (1984), Two-fluid model and hydrodynamic constitutive relations, *Nucl. Eng. Des.* **82**, 107–126.

Jameson, A., Schmidt, W. and Turkel, E.: (1981), Numerical solutions of the Euler equations by Finite Volume methods using Runge-Kutta time-stepping schemes, *AIAA* pp. Paper No.81–1259.

Kandlikar, S., Shoij, M. and Dhir, V.: (1999), *Handbook of Phase Change*, Taylor&Francis, Philadelphia.

Khosla, P. and Rubin, S.: (1974), A diagonally dominant second-order accurate implicit scheme, *Comput. Fluids* **2**, 207–209.

Koshizuka, S. and Oka, Y.: (1996), Moving-Particle semi-implicid method for fragmentation of incompressible fluid, *Nuc. Sci. Eng.* **123**, 421–434.

Kothe, D. and Mjolsness, R.: (1992), RIPPLE: A new method for incompressible flows with free surfaces, *AIAA Journal* **30**, 2694–2700.

Kuiken, G.: (1994), *Thermodynamics of Irreversible Processes*, John Wiley and Sons, New York.

Lafaurie, B., Nardone, C., Scardovelli, R., Zaleski, R. and Zanetti, G.: (1994), Modelling merging and fragmentation in multiphase flows with SURFER, *J. Comput. Phys.* **113**, 134–147.

Leonard, B.: (1979), A stable and accurate convective modelling procedure based on quadratic upstream interpolation, *Comp. Meth. Appl. Mech. Eng.* **19**, 59–98.

Leonard, B.: (1991), The ULTIMATE conservative difference scheme applied to unsteady one-dimensional advection, *Comp. Meth. Appl. Mech. Eng.* **88**, 17–74.

Leonard, B.: (1997), *Advances in Numerical Heat Transfer*, Vol. 1, Taylor&Francis, London, chapter Bounded higher-order upwind multidimensional finite-volume convection-diffusion algorithms, pp. 2–57.

Manhane, J., Gregory, G. and Azis, K.: (1974), A flow pattern map for gas-liquid flow in horizontal pipes, *Int. J. Multiphase Flow* **1**, 537–553.

Martin, J. and Moyce, W.: (1952), An experimental study of the collapse of liquid column on a rigid horizontal plane, *Philos. Trans. R. Soc. London Ser. A* **244**, 312–324.

Martinelli, R. and Nelson, D.: (1948), Prediction of pressure drop during forced circulation of boiling water, *Trans. ASME* **70**, 695–701.

Mikic, B., Rohsenow, W. and Griffith, P.: (1970), On bubble growth rate, *Int. J. Heat Mass Transfer* **13**, 657–666.

Nigmatulin, R.: (1979), Spatial averaging in the mechanics of heterogeneous and dispersed systems, *Int. J. Multiphase Flow* **5**, 353–385.

Osher, S. and Sethian, I.: (1988), Fronts propagating with curvature-dependent speed: algorithms based on Hamilton-Jacobi formulations, *J. Comput. Phys* **79**, 12–49.

Panton, R.: (1978), Flow properties for the continuum viewpoint of a non-equilibrium gas particle mixture, *Int. J. Fl. Mech.* **31**, 273–303.

Peng, D. and Robinson, D.: (1976), A new two-constant equation of state, *Ind. Eng. Chem. Fundamentals* **15**, 59–64.

Perić, M. and Ferziger, J.: (1996), *Computational Methods for Fluid Dynamics*, Springer Verlag, Berlin.

Plesset, M. and Zwick, S.: (1954), The growth of vapour bubble in superheated liquid, *J. Appl. Phys.* **25**, 493–500.

Pukett, E., Almgren, A., Bell, J., Marcus, D. and Rider, J.: (1997), A higher-order projection method for tracking fluid interfaces in variable density incompressible flows, *J. Comput. Phys.* **130**, 130–269.

Pulliam, T.: (1986), Artificial dissipation models for the Euler equations, *AIAA Journal* **24**, 1931–1940.

Ramaswamy, B. and Kawahara, M.: (1987), Lagrangian finite element analysis applied to viscous free surface fluid flow, *Int. J. Numer. Methods Fluids* **7**, 953–984.

Ramshaw, J. and Trapp, J.: (1976), A numerical technique for low-speed homogeneous two-phase flow with sharp interfaces, *J. Comput. Phys* **21**, 438–453.

Redlich, O. and Kwong, J.: (1949), On the thermodynamics of solution, *Chem. Rev.* **44**, 233–244.

Renardy, M. and Renardy, Y.: (1991), On the nature of boundary conditions for flows with moving free surfaces, *J. Comput. Phys* **93**, 325–335.

Rhie, C. and Chow, W.: (1983), A numerical study of the turbulent flow past an isolated airfoil with trailing edge separation, *AIAA* **21**, 1525–1532.

Richardson, S.: (1989), *Fluid mechanics*, Hemisphere, New York.

Rider, W. and Kothe, D.: (1998), Reconstructing volume tracking, *J. Comput. Phys.* **141**, 112–152.

Sauer, J.: 2000, *Instationär kavitierende Strömungen - ein neues Modell, basierend auf Front Capturing (VOF) und Blasendynamik*, Dissertation, Universität Karlsruhe, Karlsruhe.

Schmidt, E.: (1982), *Properties of Water and Steam in SI-units*, Springer Verlag, Berlin.

Scradovelli, R. and Zaleski, S.: (2001), Analytical relations connecting linear interfaces and volume fractions in rectangular grids, *J. Comput. Phys.* **164**, 228–237.

Scradovelli, R. and Zaleski, S.: (2003), Interface reconstruction with least-square fit and split Eulerian-Lagrangian advection, *Int. J. Numer. Meth. Fl.* **41**, 251–274.

Steger, J.: (1986), Artificial dissipation models for the Euler equations, *AIAA Journal* **24**, 1931–1940.

Stone, H.: (1968), Iterative solution of implicit approximations of multidimensional partial differential equations, *SIAM J. Numer. Anal.* **5**, 530–558.

Sussman, M., Fatemi, E. and Smereka, P.: (1998), An improved level set method for incompressible two-phase flows, *J. Comput. Phys* **27**, 663–680.

Sussman, M., Smereka, P. and Osher, S.: (1994), A level set approach for computing solutions to incompressible two-phase flow, *J. Comput. Phys* **114**, 146–159.

Tong, L.: (1965), *Boiling Heat Transfer and Two-phase Flow*, Wiley, New York.

Truesdell, C. and Toupin, R.: (1960), *The Classical Field Theories, Handbuch der Physik*, Vol. 3, Springer Verlag, Berlin.

Tryggvason, G., Bunner, B., Esmaeeli, A., Juric, D., Al-Rawahi, N., Tauber, W., Han, J., Nas, S. and Jan, Y.-J.: (2001), A front-tracking method for the computations of multiphase flow, *J. Comput. Phys* **169**, 708–759.

Ubbink, O.: 1997, *Numerical prediction of two fluid systems with sharp interfaces*, Dissertation, London University, London.

Unverdi, S. and Tryggvason, G.: (1992), A front-tracking method for viscous, incompressible, multifluid flows, *J. Comput. Phys* **100**, 25–37.

van der Waals, D.: 1873, *Over de continuiteit van den gas en vloeistoftoestand*, Dissertation, Universiteit Leiden, Leiden.

Versteeg, H. and Malalasekera, W.: (1995), *An introduction to computational fluid dynamics, the finite volume method*, Longman Scientific & Technical, Harlow, Essex, UK.

Volmer, M.: (1939), *Kinetic der Phasenbildung*, Theodor Steinkopff, Dresden.

Wilcox, D.: (1993), *Turbulence modeling for CFD*, DCW Industries, Inc., La Cañada, California.

Williams, S.: (1959), Spray combustion theory, *Combustion and Flame* **3**, 215–228.

Yih, C.: (1980), *Stratified Flows*, Academic Press, London.

Young, F.: (1989), *Cavitation*, McGraw-Hill, London.

Yuan, W. and Schnerr, G.: (2003), Numerical simulation of two-phase flow in injection nozzles: interaction of cavitation and external jet formation, *ASME J. Fluids Eng.* **125**, 963–969.

Zuber, N. and Findlay, J.: (1965), Average volumetric concentration in two-phase flow systems, *J. Heat Trans.* **87**, 453–468.

# CONSTANTS FOR PHYSICAL PROPERTIES

APPENDIX A

| **i→ j↓** | **0** | **1** | **2** | **3** | **4** | **5** |
|---|---|---|---|---|---|---|
| **0** | 0.501938 | 0.162888 | -0.130356 | 0.907919 | -0.551119 | 0.146543 |
| **1** | 0.235622 | 0.789393 | 0.673665 | 1.207552 | 0.0670665 | -0.084337 |
| **2** | -0.274637 | -0.743539 | -0.959456 | -0.687343 | -0.497089 | 0.195286 |
| **3** | 0.145831 | 0.263129 | 0.347247 | 0.213486 | 0.100754 | -0.032932 |
| **4** | -0.0270448 | -0.0253093 | -0.0267758 | -0.0822904 | 0.0602253 | -0.0202595 |

TABLE 1.1: *Values of the constant $b_{ij}$ for Eq.(4.56) (Schmidt, (1982)).*

| **Index** | **a** $[W/Km]$ | **b** $[W/Km]$ | **B** | **C** | **d** $[W/Km]$ |
|---|---|---|---|---|---|
| **0** | $1.02811 \cdot 10^{-2}$ | $-3.97070 \cdot 10^{-1}$ | – | – | – |
| **1** | $2.99621 \cdot 10^{-2}$ | $4.00302 \cdot 10^{-1}$ | $-1.71587 \cdot 10^{-1}$ | $6.42857 \cdot 10^{-1}$ | $7.01309 \cdot 10^{-2}$ |
| **2** | $1.56146 \cdot 10^{-2}$ | 1.06 | 2.39219 | -4.11717 | $1.18520 \cdot 10^{-2}$ |
| **3** | $-4.22464 \cdot 10^{-3}$ | – | – | -6.17937 | $1.69937 \cdot 10^{-3}$ |
| **4** | – | – | – | $3.08976 \cdot 10^{-3}$ | -1.02 |
| **5** | – | – | – | $8.22994 \cdot 10^{-2}$ | – |
| **6** | – | – | – | $1.00932 \cdot 10^{1}$ | – |

TABLE 1.2: *Values of constants used in Eq.(4.59) (Schmidt, (1982)).*

| **k** | **0** | **1** | **2** | **3** |
|---|---|---|---|---|
| $\mathbf{a_k}$ | 0.0181583 | 0.0177624 | 0.0105287 | -0.0036744 |

TABLE 1.3: *Values of the constant $a_k$ for Eq.(4.57) (Schmidt, (1982)).*

# DERIVATION OF SOME NUMERICAL FORMULAS

B APPENDIX

For the sake of simplicity, in all subsections of this appendix, superscripts denoting an iteration level will be left out.

## B.1 Momentum equation

### B.1.1 Viscous terms

#### Symmetry boundary

In this case the component of the viscous stress tangential to the plane of symmetry equals zero and one has to deal with the normal component only. Therefore

$$\bar{\bar{\tau}}\vec{n} = \left[\left(\bar{\bar{\tau}}\vec{n}\right).\vec{n}\right]\vec{n} = \tau_{nn}\vec{n}. \tag{B.1}$$

The x-component of the viscous stress component normal to the boundary of the control volume for the symmetry plane reads

$$\tau_{nn}S_{x_{n,sym}}. \tag{B.2}$$

The stress $\tau_{nn}$, is expressed by

$$\bar{\bar{\tau}}_{nn} \cong 2\mu_{sym}\frac{u_{n_B} - u_{n_P}}{|\delta\vec{n}|} - \frac{2}{3}\mu_{sym}\left(\vec{\nabla}.\vec{u}\right)_{sym}, \tag{B.3}$$

where $u_{n_B}$ and $u_{n_P}$ are velocities in the direction normal to the plane of symmetry, at points $B$ and $P$, respectively (see Fig.(B.1)). Term $|\delta\vec{n}|$ is the distance between node $P$ adjacent to the boundary and the boundary itself, see Fig.(B.1). Its value is calculated according to

$$\begin{aligned}|\delta\vec{n}| = \vec{d}.\vec{n} = \left(d_x\vec{e}_x, \quad d_y\vec{e}_y\right)\left(S_{x_{n,sym}}, \quad S_{y_{n,sym}}\right)^T\frac{1}{|\vec{n}S|} = \\ \frac{d_xS_{x_{n,sym}} + d_yS_{y_{n,sym}}}{|\vec{n}S|}.\end{aligned} \tag{B.4}$$

Since there is no flux through the boundary, velocity $u_{n_B}$ is zero. Velocity $u_{n_P}$ is evaluated

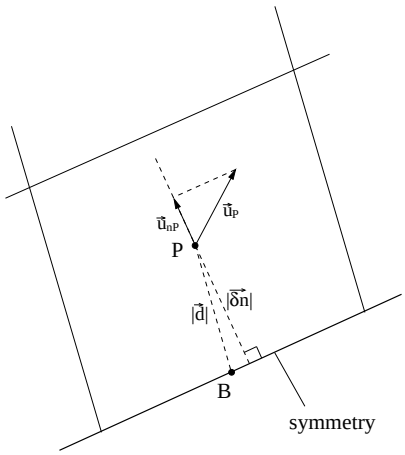


FIGURE B.1: *Symmetry boundary.*

using

$$u_{nP} = \vec{u}_P.\vec{n} = \left(u_P\vec{e}_x, \quad v_P\vec{e}_y\right)\left(S_{x_{n,sym}}, \quad S_{y_{n,sym}}\right)^T \frac{1}{|\vec{n}S|} = \frac{u_P S_{x_{n,sym}} + v_P S_{y_{n,sym}}}{|\vec{n}S|}. \tag{B.5}$$

Substituting (B.4) and (B.5) in (B.3), bearing in mind the assumption of non-permeability of the boundary, yields

$$\tau_{nn} \cong -2\mu_{sym}\frac{u_P S_{x_{n,sym}} + v_P S_{y_{n,sym}}}{d_x S_{x_{n,sym}} + d_y S_{y_{n,sym}}} - \frac{2}{3}\mu_{sym}\left(\vec{\nabla}.\vec{u}\right)_{sym}. \tag{B.6}$$

Substitution of (B.6) in (B.2) gives the formula for viscous forces at the symmetry boundary for the horizontal direction

$$\begin{aligned}&\tau_{nn}S_{x_{n,sym}} \cong \\ &-2\mu_{sym}\frac{u_P S_{x_{n,sym}} + v_P S_{y_{n,sym}}}{d_x S_{x_{n,sym}} + d_y S_{y_{n,sym}}} S_{x_{n,sym}} - \frac{2}{3}\mu_{sym}\left(\vec{\nabla}.\vec{u}\right)_{sym} S_{x_{n,sym}} = \\ &\left(-2\mu_{sym}\frac{u_P}{d_x S_{x_{n,sym}} + d_y S_{y_{n,sym}}} S^2_{x_{n,sym}} - 2\mu_{sym}\frac{v_P}{d_x S_{x_{n,sym}} + d_y S_{y_{n,sym}}} S_{x_{n,sym}} S_{y_{n,sym}}\right) \\ &-\frac{2}{3}\mu_{sym}\left(\vec{\nabla}.\vec{u}\right)_{sym} S_{x_{n,sym}}.\end{aligned} \tag{B.7}$$

The formula for the vertical direction is found analogously.

**Rigid boundary**

In this case the component of the viscous stress normal to the rigid boundary equals zero and one has to deal with the tangential component only. Therefore

$$\bar{\bar{\tau}}\vec{n} = \left[\left(\bar{\bar{\tau}}\vec{n}\right).\vec{t}\right]\vec{t} = \tau_{nt}\vec{t}. \tag{B.8}$$

The x-component of the force of the shear stress for the rigid boundary in Cartesian coordinate system reads

$$\tau_{nt} S_{x_{wal}}. \tag{B.9}$$

Shear stress $\tau_{nt}$ is expressed as

$$\tau_{nt} \cong \mu_{wal} \frac{u_{t_B} - u_{t_P}}{|\delta\vec{n}|} - \frac{2}{3}\mu_{wal}\left(\vec{\nabla}.\vec{u}\right)_{wal}, \tag{B.10}$$

where $u_{t_B}$ and $u_{t_P}$ are velocities in the direction tangential to the rigid boundary, at nodes $B$ and $P$, respectively (see Fig.(B.2)). Term $|\delta\vec{n}|$ is the distance between node $P$ adjacent to the boundary and the boundary itself, see Fig(B.2). Its value is calculated according to (B.4). Since one assumes the no-slip boundary condition at the wall, velocity $u_{t_B}$ is zero. Velocity

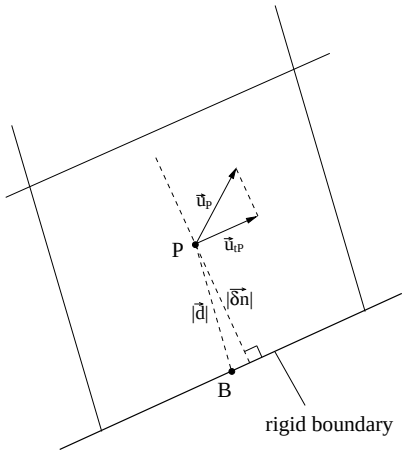


FIGURE B.2: *Rigid boundary.*

$u_{t_P}$ is evaluated using

$$u_{t_P} = \vec{u}_P.\vec{t} = \left(u_P\vec{e}_x, \quad v_P\vec{e}_y\right)\left(S_{x_{wal}}, \quad S_{y_{wal}}\right)^T \frac{1}{\left|\vec{S}\right|} = \frac{u_P S_{x_{wal}} + v_P S_{y_{wal}}}{\left|\vec{S}\right|}. \tag{B.11}$$

Substituting (B.4) and (B.11) in (B.10), bearing in mind the assumption of the no-slip boundary condition, yields

$$\tau_{nt} \cong -\mu_{wal} \frac{u_P S_{x_{wal}} + v_P S_{y_{wal}}}{d_x S_{x_{n,wal}} + d_y S_{y_{n,wal}}} - \frac{2}{3}\mu_{wal}\left(\vec{\nabla}.\vec{u}\right)_{wal}. \tag{B.12}$$

Substitution of (B.12) in (B.9) and incorporation of the divergence of the velocity field gives the formula for the viscous forces at the rigid boundary for the horizontal direction

$$\tau_{nt}S_{x_{wal}} \cong -\mu_{wal}\frac{u_P S_{x_{wal}} + v_P S_{y_{wal}}}{d_x S_{x_{n,wal}} + d_y S_{y_{n,wal}}} S_{i_{wal}} - \frac{2}{3}\mu_{wal}\left(\vec{\nabla}.\vec{u}\right)_{wal} S_{x_{n,wal}} =$$
$$\left(-\mu_{wal}\frac{u_P}{d_x S_{x_{n,wal}} + d_y S_{y_{n,wal}}} S^2_{x_{wal}} - \mu_{wal}\frac{v_P}{d_x S_{x_{n,wal}} + d_y S_{y_{n,wal}}} S_{x_{wal}} S_{y_{wal}}\right) \quad \text{(B.13)}$$
$$-\frac{2}{3}\mu_{wal}\left(\vec{\nabla}.\vec{u}\right)_{wal} S_{x_{n,wal}}.$$

The formula for the vertical direction is derived analogously.

## B.2 Energy equation

The energy equation is considered in the form given in (4.35).

### B.2.1 Heat conduction term

According to (5.43), the heat conduction term for a single boundary of the control volume may be expressed as

$$\lambda_{nb}\left(\vec{\nabla}T\right).\vec{n}S. \quad \text{(B.14)}$$

Since the vector connecting nodes $P$ and $N$ is not necessarily in the direction normal to the control volume boundary, the vector of the temperature gradient may be expressed as the vectorial summation

$$\left(\vec{\nabla}T\right)_n = \left(\vec{\nabla}T\right)_d + \left(\left(\vec{\nabla}T\right)_n - \left(\vec{\nabla}T\right)_d\right), \quad \text{(B.15)}$$

see Fig.(B.3). Substituting (B.15) in (B.14)yields

$$\lambda_{nb}\left(\vec{\nabla}T\right).\vec{n}S = \lambda_{nb}\left(\vec{\nabla}T\right)_d.\vec{n}S + \lambda_{nb}\left(\left(\vec{\nabla}T\right)_n.\vec{n}S - \left(\vec{\nabla}T\right)_d.\vec{n}S\right), \quad \text{(B.16)}$$

The value of $\lambda_{nb}\left(\vec{\nabla}T\right)_d.\vec{n}S$ may be expressed as

$$\lambda_{nb}\left(\nabla T\right)_d\left|\vec{n}S\right| \cong \lambda_{nb}\frac{T_{NB} - T_P}{\left|\vec{d}\right|}\left|\vec{n}S\right|. \quad \text{(B.17)}$$

The same term may be written in the form

$$\lambda_{nb}\left(\nabla T\right)_d\left|\vec{n}S\right| \cong \lambda_{nb}\left(\left(\frac{\delta T}{\delta x}\right)_{nb}\frac{d_x}{\left|\vec{d}\right|} + \left(\frac{\delta T}{\delta y}\right)_{nb}\frac{d_y}{\left|\vec{d}\right|}\right)\left|\vec{n}S\right|, \quad \text{(B.18)}$$

where gradient $\left(\delta T/\delta x\right)_{nb}$ or $\left(\delta T/\delta y\right)_{nb}$ is to be evaluated using 5.34. Term $\lambda_{nb}\left(\vec{\nabla}T\right)_n.\vec{n}S_{nb}$ may be expressed as

$$\lambda_{nb}\left(\vec{\nabla}T\right)_n.\vec{n}S \cong \lambda_{nb}\left(\left(\frac{\delta T}{\delta x}\right)_{nb}\vec{e}_x,\ \ \left(\frac{\delta T}{\delta y}\right)_{nb}\vec{e}_y\right)\left(S_{x_n}\vec{e}_x,\ \ S_{y_n}\vec{e}_y\right)^T =$$
$$\left(\frac{\delta T}{\delta x}\right)_{nb}S_{x_n} + \left(\frac{\delta T}{\delta y}\right)_{nb}S_{y_n}. \quad \text{(B.19)}$$

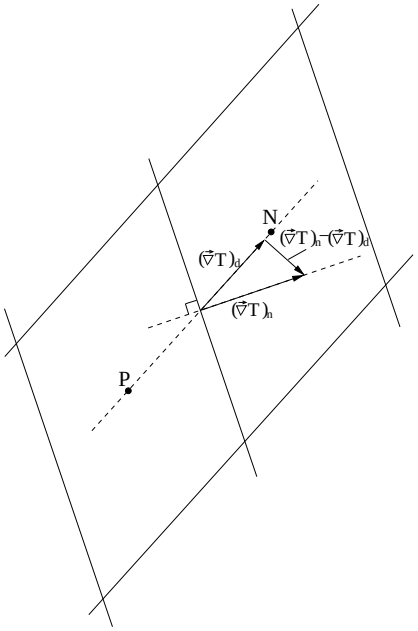


FIGURE B.3: *Temperature gradient vectors.*

Substitution of (B.17), (B.18) and (B.19) in (B.16) yields the formula for the heat conduction at the control volume boundary, namely

$$\begin{aligned}\lambda_{nb}\left(\vec{\nabla}T\right).\vec{n}S \cong \lambda_{nb}\frac{T_{NB}-T_P}{\left|\vec{d}\right|}\left|\vec{n}S\right| + \\ \lambda_{nb}\left(\left(\left(\frac{\delta T}{\delta x}\right)_{nb}S_{x_n}+\left(\frac{\delta T}{\delta y}\right)_{nb}S_{y_n}\right)-\left(\left(\frac{\delta T}{\delta x}\right)_{nb}d_x+\left(\frac{\delta T}{\delta y}\right)_{nb}d_y\right)\frac{\left|\vec{n}S\right|}{\left|\vec{d}\right|}\right).\end{aligned} \tag{B.20}$$

### B.2.2 Viscous term: Rayleigh dissipation function

The Rayleigh dissipation function is, according to (5.46), expressed by

$$\int_{\Omega}\left(\overline{\overline{\tau}}\,\vec{\nabla}\right).\vec{u}\,d\Omega \cong \left(\overline{\overline{\tau}}\,\vec{\nabla}\right).\vec{u}\,\Omega. \tag{B.21}$$

For the sake of simplicity, the subscript indicating the considered node of the control volume has been dropped. The tensor of viscous stresses reads

$$\overline{\overline{\tau}} = \begin{pmatrix}\tau_{xx} & \tau_{xy}\\ \tau_{yx} & \tau_{yy}\end{pmatrix}. \tag{B.22}$$

The individual elements of matrix (B.22) read

$$\begin{aligned} \tau_{xx} &\cong 2\mu\frac{\delta u}{\delta x} - \frac{2}{3}\mu\left(\frac{\delta u}{\delta x} + \frac{\delta v}{\delta y}\right), \quad \tau_{xy} \cong \mu\left(\frac{\delta u}{\delta y} + \frac{\delta v}{\delta x}\right), \\ \tau_{yx} &\cong \mu\left(\frac{\delta v}{\delta x} + \frac{\delta u}{\delta y}\right), \qquad\qquad \tau_{yy} \cong 2\mu\frac{\delta v}{\delta y} - \frac{2}{3}\mu\left(\frac{\delta u}{\delta x} + \frac{\delta v}{\delta y}\right). \end{aligned} \tag{B.23}$$

All gradients in (B.23) are approximated using (5.8). Expansion of the Rayleigh dissipation function gives

$$\left(\vec{\overline{\tau}}\,\vec{\nabla}\right).\vec{u} = \left(\left(\tau_{xx}\frac{\delta}{\delta x} + \tau_{xy}\frac{\delta}{\delta y}\right)\vec{e}_x, \quad \left(\tau_{yx}\frac{\delta}{\delta x} + \tau_{yy}\frac{\delta}{\delta y}\right)\vec{e}_y\right)\left(u\vec{e}_x, \quad v\vec{e}_y\right)^T. \tag{B.24}$$

Substitution of (B.23) to (B.24) leads to the relation

$$\begin{aligned} &\left(\vec{\overline{\tau}}\,\vec{\nabla}\right).\vec{u} \cong 2\mu\left(\left(\frac{\delta u}{\delta x}\right)^2 + \left(\frac{\delta v}{\delta y}\right)^2\right) + \mu\left(\left(\frac{\delta u}{\delta y}\right)^2 + 2\frac{\delta u}{\delta y}\frac{\delta v}{\delta x} + \left(\frac{\delta v}{\delta x}\right)^2\right) - \\ &\frac{2}{3}\mu\left(\left(\frac{\delta u}{\delta x}\right)^2 + 2\frac{\delta u}{\delta x}\frac{\delta v}{\delta y} + \left(\frac{\delta v}{\delta y}\right)^2\right), \end{aligned} \tag{B.25}$$

which subsequently substituted in (B.21)yields the final form for the viscous forces, namely

$$\begin{aligned} &\left(\vec{\overline{\tau}}\,\vec{\nabla}\right).\vec{u}\,\Omega \cong \\ &2\mu\left(\left(\frac{\delta u}{\delta x}\right)^2 + \left(\frac{\delta v}{\delta y}\right)^2\right)\Omega + \mu\left(\left(\frac{\delta u}{\delta y} + \frac{\delta v}{\delta x}\right)^2 - \frac{2}{3}\left(\frac{\delta u}{\delta x} + \frac{\delta v}{\delta y}\right)^2\right)\Omega. \end{aligned} \tag{B.26}$$

## B.3 Pressure correction equation

The left-hand side of (5.64), containing the gradient of the pressure correction, may be written, for a single boundary of the control volume, as

$$\begin{aligned} &\left(\frac{\Omega}{A}\right)_{nb}\vec{\nabla}p'.\vec{n}S = \left(\frac{\Omega}{A}\right)_{nb}\vec{\nabla}p'.\left[\frac{\vec{d}}{\left(\vec{d}.\vec{n}\right)} + \frac{\vec{d}\times\left(\vec{n}\times\vec{d}\right)}{\left(\vec{d}.\vec{n}\right)}\right] \cong \\ &\left(\frac{\Omega}{A}\right)_{nb}\frac{p'_{NB} - p'_P}{\left|\vec{d}_n\right|}\left|\vec{n}S\right|, \end{aligned} \tag{B.27}$$

where the second part in the expression for $\vec{n}$ has been neglected. Distance $\left(\vec{d}.\vec{n}\right)$ originates from the projection of vector $\vec{d}$ connecting nodes $P$ and $N$, onto the direction normal to the boundary of the control volume, see Fig.(B.4). $\left(\vec{d}.\vec{n}\right)$ follows from

$$\left(\vec{d}.\vec{n}\right) = \frac{\vec{d}\cdot\vec{n}S}{S} = \frac{d_x S_{x_n} + d_y S_{y_n}}{|\vec{n}S|}. \tag{B.28}$$

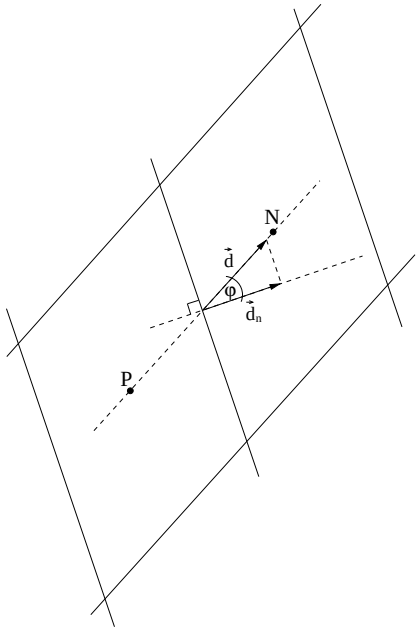


FIGURE B.4: *Projection of vector $\vec{d}$ on the direction normal to the boundary of control volume $P$.*

Substitution of (B.28) in (B.27) reveals

$$\begin{aligned}&\left(\frac{\Omega}{A}\right)_{nb}\vec{\nabla}p'.\vec{n}S \cong \left(\frac{\Omega}{A}\right)_{nb}\frac{p'_{NB}-p'_P}{\left(\vec{d}.\vec{n}\right)}\left|\vec{n}S\right| = \\ &\left(\frac{\Omega}{A}\right)_{nb}\frac{p'_{NB}-p'_P}{d_xS_{x_n}+d_yS_{y_n}}\left|\vec{n}S\right|^2 = \left(\frac{\Omega}{A}\right)_{nb}\left(p'_{NB}-p'_P\right)\frac{S_{x_n}^2+S_{y_n}^2}{d_xS_{x_n}+d_yS_{y_n}}.\end{aligned} \tag{B.29}$$

The pressure gradient present in (5.65), namely

$$\begin{aligned}&\left(\frac{\Omega}{A}\right)_{nb}\vec{\nabla}p.\vec{n}S \cong \left(\frac{\Omega}{A}\right)_{nb}\frac{p_{NB}-p_P}{d_xS_{x_n}+d_yS_{y_n}}\left|\vec{n}S\right|^2 = \\ &\left(\frac{\Omega}{A}\right)_{nb}\left(p_{NB}-p_P\right)\frac{S_{x_n}^2+S_{y_n}^2}{d_xS_{x_n}+d_yS_{y_n}},\end{aligned} \tag{B.30}$$

is obtained in the same manner. The second expression in (5.65) may be expressed as

$$\begin{aligned}&\left(\vec{\nabla}p\right).\vec{n}S \cong \left(\vec{\nabla}p\right).\frac{\vec{d}S}{\left(\vec{d}.\vec{n}\right)} = \left(\vec{\nabla}p\right).\frac{\vec{d}S^2}{\left(\vec{d}.\vec{n}S\right)} = \\ &\left(\left(\frac{\delta p}{\delta x}\right)_{nb}\vec{d}_x,\ \left(\frac{\delta p}{\delta y}\right)_{nb}\vec{d}_y\right).\vec{n}S.\end{aligned} \tag{B.31}$$

Gradients $(\delta p/\delta x)_{nb}$ or $(\delta p/\delta y)_{nb}$ are calculated using (5.34). Finally, combination of (B.31) and (B.30) yields

$$S_{corr_P} = \left(\frac{\Omega}{A}\right)_{nb} \left(\frac{S_{x_n}^2 + S_{y_n}^2}{d_x S_{x_n} + d_y S_{y_n}}\right)_{nb} \left((p_{NB} - p_P) - \left(\left(\frac{\delta p}{\delta x}\right)_{nb} d_x + \left(\frac{\delta p}{\delta y}\right)_{nb} d_y\right)\right). \tag{B.32}$$

# SUMMARY

Multiphase flows are usually accompanied by thermodynamic effects. These effects are associated with gas-liquid phase transition which can occur in a single fluid system as well as in systems comprising more than one species. Appearance of the transition in a system has substantial thermal and mechanical consequences, such as transfer of mass, momentum as well as energy and change in the temperature field.

Flows coupled with phase change occur abundantly in nature. They are responsible for atmospheric phenomena such as cloud formation, absorption of gases (including green house ones) by sea water and many other phenomena of a global or local scale, which influences everyday life. Multiphase flows are also often present in many industrial applications in which their physical features are advantageous or disadvantageous. Installations in the oil production industry and energy production plants are examples of installations in which multi-phase flows with phase transition appear. Phase transition is a desired phenomenon in vapour generation systems such as power plant boilers or water cooled nuclear reactors; as well as indirect or direct contact vapour condensers or mass transfer equipment used e.g. for humidification. Phase transition can also be an undesired phenomenon. It occurs in pumps and on ship propellers where because the pressure decreases considerably at the suction side of the impeller or propeller blade, cavitation appears. This sort of transition can cause oscillations and may threaten the structural integrity of the impeller or propeller.

Two driving mechanisms for phase transition inside a fluid can be distinguished. The first is variation of the pressure leading to cavitation, whereas the second one is heat transfer (temperature) resulting in boiling and evaporation/condensation.

For any kind of transition prediction of the flow is vital for designing industrial system components and their efficient and reliable operation. Over the past decades researchers put much effort in the development of algorithms capable of numerically simulate multiphase flows with phase transition. The present study concerns the development of a method for the prediction of multiphase flow with temperature-driven phase transition for which the geometry of the gas-liquid interface is not known in advance. A single substance is considered consisting of incompressible phases.

The gas-liquid interface in multiphase flows, with or without phase transition, involves a discontinuity in the physical properties of the flow at the interface. This leads to difficulties in preserving convergence in numerical algorithms for predicting single phase flows. The key point of the present algorithm developed is the single field approach in the form of the Volume of Fluid (VOF) method. The approach regards the gas-liquid flow as one field, smearing out the discontinuity in the flow field quantities. The two phases are to be recognized by a Heav-

iside step function. The argument of this function is the void fraction which is the ratio of the volume of gas in the control volume and the volume of the infinitesimal control volume itself. The void fraction distribution is obtained from a transport equation with additional terms to satisfy mass conservation. The partial differential equation for the void fraction is solved separately for each of the coordinate directions using a split operator method. Since flow quantities are smoothed across the interface, a special numerical algorithm has been incorporated in order to maintain a high resolution of the interface. The algorithm comprises the procedure of blending of two algorithms from literature: the Universal Limiter (ULTIMATE) and the Quadratic Upstream Interpolation Estimated (QUICKEST). The blending procedure was initially devised for one-dimensional computational domains. In order to extend the capability of the method to multi-dimensional flows, Compressive Interface Capturing Scheme for Arbitrary Meshes (CICSAM) has been incorporated. This allows the calculation of flows in two or three dimensional domains without jeopardizing interface resolution.

The set of governing equations is solved using a pressure correction algorithm adapted to multiphase flow problems. The algorithm is based on the Semi Implicit Method for Pressure-Linked Equations (SIMPLE). SIMPLE has been improved to handle the present collocated, spatial discretization. The improvement concerns the artificial dissipation incorporated in the momentum equation. This leads to the damping of unphysical oscillations resulting from the collocated scheme.

The model for phase transition is based on the Energy of Fluid (EOF) method. The algorithm utilizes the portion of the enthalpy of the fluid exceeding that at the state of saturation. This portion of the enthalpy is then related to the latent heat necessary to change the state of aggregation of the entire mass of the substance in the control volume. This relation allows the evaluation of the volumetric amount of the substance which will transfer from vapour to liquid or vice versa. The volumetric amount is related to the magnitude of the divergence of the velocity field, which appears as source term in the right-hand side of the governing equation for the void fraction.

Validation of the algorithm has been carried out for different flow types. The first group of tests concerns the single phase flow around hydrofoil NACA 0015 in a parallel flow, aimed at the assessment of the effects of the added artificial dissipation. The results show that the method employing a central difference scheme with added dissipation gives the best results. The subsequent simulations concerned a two phase flow without phase transition. The standard dam breaking problem has been used for the qualitative and quantitative evaluation of the capability to capture a rapidly changing gas-liquid interface. It is shown that mass conservation has been improved by modification of the transport equation for the void fraction. Finally, feasibility of the EOF method has been assessed with the simulation of a jet of liquid coolant impinging on a free surface separating a hot liquid and its vapour present in the space above the free surface.

# SAMENVATTING

In meerfasen stromingen treden vaak thermodynamische effecten op. Deze effecten houden verband met de faseovergang van gas naar vloeistof of omgekeerd. Faseovergang komt voor in stromend medium dat uit een enkele stof bestaat als in stromend medium dat uit verschillende stoffen bestaat. Fase overgang gaat gepaard met overdracht van massa, impuls en energie en met veranderingen in het temperatuurveld.

In de natuur komen meerfasen stromingen met faseovergang veelvuldig voor. Deze stromingen bepalen atmosferische verschijnselen als wolkenvorming, absorptie van gassen (inclusief broeikasgassen) door zeewater en vele andere verschijnselen op globale of lokale schaal, die een invloed hebben op het dagelijkse leven. Meerfasen stromingen komen ook veelvuldig voor in industrile toepassingen, waar hun fysische kenmerken zowel voor- als nadelig kunnen zijn. Installaties in de olieproducerende industrie en elektriciteitscentrales zijn voorbeelden van industrile installaties waarin meerfasen stromingen met faseovergang optreden. Faseovergang is een gewenst fenomeen in dampgeneratie systemen zoals boilers in centrales of in watergekoelde nucleaire reactors, zowel als in direct- of indirect-contact condensors van massaoverdracht installaties als bevochtigers of drogers. Faseovergang kan ook een nadelig verschijnsel zijn. Dit komt voor in pompen en bij scheepsschroeven, waar, ten gevolge van de aanzienlijke afname van de druk aan de zuigzijde van de impeller van de pomp en het blad van de schroef, cavitatie optreedt. Dit type faseovergang leidt tot trillingen en kan de integriteit van de constructie van de pomp en scheepsschroef bedreigen.

Men kan onderscheid maken tussen twee bepalende mechanismen voor faseovergang binnen in een medium. Het eerste mechanisme is de variatie van de druk in een stroming die leidt tot cavitatie op plaatsen waar de druk onder de dampdruk komt. Het tweede mechanisme is warmteoverdracht, waar bijvoorbeeld bij voortdurende toevoer van warmte (energie) aan vloeistof de kooktemperatuur wordt bereikt en de vloeistof overgaat in damp, of omgekeerd bij het ontrekken van energie aan damp de kooktemperatuur wordt bereikt en damp tot vloeistof condenseert. Bij het ontwerpen van (componenten van) industrile systemen waarin het gedrag van meerfasen stromingen met faseovergang bepalend is voor een efficint en betrouwbaar gebruik, is de voorspelling van de stroming essentieel. Gedurende de laatste decades hebben onderzoekers veel genvesteerd in de ontwikkeling van algoritmes voor de numerieke simulatie van meerfasen stromingen met en zonder faseovergang. De huidige studie betreft de ontwikkeling van een methode voor de voorspelling van meerfasen stromingen met temperatuurgedreven faseovergang, waarin de geometrie van het gasvloeistof interface a priori onbekend is. De beperking hierbij is dat een medium bestaande uit een enkele stof wordt beschouwd bestaande uit onsamendrukbare fasen.

Het gasvloeistof interface in meerfasen stromingen, al dan met faseovergang, vormt in de stroming een discontinuteit in de fysische eigenschappen van de stroming. Dit leidt tot moeilijkheden in het behouden van de convergentie van numerieke algoritmes die zijn ontwikkeld voor het voorspellen van stromingen van fluda bestaande uit een enkele fase. De kern van het algoritme ontwikkeld in dit proefschrift is de zogenaamde single-field formulering in de vorm van de Volume-of-Fluid (VOF) methode. In deze formulering wordt de gasvloeistof stroming opgevat als een enkelvoudig veld, waarbij de discontinuteit in de stromingsgrootheden wordt uitgesmeerd. Vervolgens worden de twee fasen gedentificeerd met behulp van een Heaviside stapfunctie. Het argument van deze functie is de lokale waarde van de dampfractie (void fraction), het quotint van het volume aan gas in en het totale volume van een infinitesimaal controle volume. De ruimtelijke verdeling van de dampfractie volgt uit een transportvergelijking met extra termen om het behoud van massa te waarborgen. De partile differentiaal vergelijking voor de dampfractie wordt met een splitoperator techniek gesplitst in elk van de cordinaatrichtingen. Het resulterende veld van stromingsgrootheden is continu over het interface, waarna de resolutie van het interface wordt verkregen door middel van een speciale numerieke procedure. Deze procedure bestaat uit een combinatie van twee algoritmes uit de literatuur: het Universal Limiter (ULTIMATE) algoritme en het Quadratic Upstream Interpolation Estimated (QUICKEST) algoritme. Oorspronkelijk was deze procedure ontwikkeld voor eendimensionale rekengebieden. Ten behoeve van de uitbreiding naar meerdimensionale stromingen is er het Compressive Interface Capturing Scheme for Arbitrary Meshes (CICSAM) aan toegevoegd. Met het resulterende algoritme is het mogelijk om stromingen in twee- en driedimensionale gebieden te berekenen met behoud van de resolutie van het interface.

Het set van beschrijvende vergelijkingen wordt opgelost met een drukcorrectie methode, aangepast voor meerfasen stromingen. Het algoritme is gebaseerd op de numerieke procedure die algemeen wordt aangeduid als de Semi Implicit Method for Pressure Linked Equations (SIMPLE) procedure. Deze procedure is verbeterd ten behoeve van de huidige gecolloceerde ruimtelijke discretisatie methode. De verbetering bestaat er uit dat kunstmatige dissipatie is toegevoegd aan de impulsvergelijking. Dit resulteert in demping van de niet-fysische oscillaties die optreden in de gecolloceerde discretisatie formulering. Het model voor faseovergang is gebaseerd op de Energy-of-Fluid (EOF) methode. Dit algoritme maakt gebruik van het deel van de enthalpie van het medium dat uitgaat boven dat van de verzadigingstoestand. Dit deel van de enthalpie wordt vervolgens gerelateerd aan de latente warmte benodigd om de aggregatietoestand van het medium in het controle volume te veranderen. Daarmee kan dan het volume worden bepaald van het deel van de massa van het medium in het controle volume dat van fase verandert. Dit volume is direct gerelateerd aan de grootte van de divergentie van het snelheidsveld, welke als bronterm verschijnt in de transportvergelijking voor de dampfractie. De validatie van de ontwikkelde methode is uitgevoerd aan de hand van verschillende testgevallen. Het eerste testgeval betreft de een-fase stroming om het NACA0015 profiel in een parallelstroming, gericht op de beoordeling van de effecten van de toegevoegde artificile dissipatie. De resultaten geven aan dat de methode met een centraal schema met toegevoegde artificile dissipatie het beste presteert. Het tweede testgeval betreft een tweefasen stroming zonder faseovergang. Het standaard dambreuk probleem is gebruikt voor een kwalitatieve en kwantitatieve evaluatie van de mogelijkheden van de huidige methode om een snelveranderend gasvloeistof interface numeriek te simuleren. De resultaten laten zien dat de modificaties aan de transportvergelijking voor de dampfractie resulteren in

een verbeterd behoud van massa. Tenslotte is de haalbaarheid van de EOF methode beoordeeld voor het testgeval van een straal van koelvloeistof die het vrije oppervlak treft dat het interface vormt tussen een hete vloeistof en de zich daarboven bevindende damp. Dit testgeval laat zien dat dit soort complexe stromingen met de huidige methode numeriek kan worden gesimuleerd.

# ACKNOWLEDGMENT

This research and the thesis is the result of work performed in the past four and half years in the research group of Engineering Fluid Dynamics in the Faculty of Engineering Technology at University of Twente. Completion of this research, however, would not have been possible without the help of people who contributed to this work professionally as well as otherwise. I would like to express my gratitude to all of them here.

In the first place I would like to thank Harry Hoeijmakers who was one of the supervisors of this Ph.D. project. Thanks to his support and guidance I have been led through all the details of the research subject. This created the base for further research and development. Harry, your broad knowledge and experience headed me in the right direction during seeking answers for questions which arose in the course of the project. Our fruitful discussions considerably supported the development of my work and contributed effectively in completion of the thesis. Your interest concerned not only the scientific background, but also many things outside the objective of the project. This generated a friendly and motivating atmosphere which substantially supported my scientific activity. Thus, I would like to express my great appreciation.

The scope of the Ph.D. programme could not have been achieved without the research group of Fluid Mechanics of the University of Karlsruhe and its head, prof. G.H. Schnerr. I would like to express my special gratitude to prof. Schnerr for his guidance, advices and supervising. Thanks to him, I had the opportunity to visit Karlsruhe University and work with his research group. Here, I also would like to express my appreciation to the members of his group, especially Esra Sorgüven who devoted a lot of effort and time to provide me with the details of the computer code which was the basic tool in my project.

I very much would like to thank ECN/NRG in Petten, The Netherlands who supported the ECN/NRG JMBC professorship of professor Schnerr, which resulted in my project. Thanks also to professor G. Ooms of the J.M. Burgers Center, Research School for Fluid Mechanics in The Netherlands for the organizational support given during the establishment of the JMBC chair of professor Schnerr. From NRG I would like to thank Ed Komen, Victor Wichers and Sander Willemsen. Furthermore, I would like to thank the former Twente Institute of Mechanics (TIM), now Institute of Mechanics, Processes and Control Twente (IMPACT) for their support of the project.

I also would like to thank the current and former staff of the research group of Engineering Fluid Dynamics at University of Twente for the friendly atmosphere and enjoyable working environment. Here, I would like to express my special thanks to my roommates Remco Westra, Philip Kelleners and Jeroen Dillingh for many discussion which not necessarily con-

cerned our scientific activity, but rather provided a friendly atmosphere. Furthermore, I would like to thank Wouter den Breeijen who kept the computer network of the group running, in spite of my not deliberate actions causing sometimes server problems. Special thanks goes to Yvonne Weber, the former secretary, who helped me considerably in the beginning of my stay in The Netherlands. Thanks to her help and practical information, I could quickly adapt to the new country and its culture.

I must also express my great gratitude to my parents, brother and grand mother, who supported me from a distance and always served invaluable help and advise.

Finally, I would like to thank my wife Agnieszka for supportive attitude, patience and understanding.